

**ÉCOLE DOCTORALE DE PHYSIQUE, CHIMIE-PHYSIQUE (182)**

**Institut de Physique et Chimie des Matériaux de Strasbourg**

**THÈSE** présentée par :

**Joanna Lucie Paulette WOLFF**

soutenue le : 29 Novembre 2024

pour obtenir le grade de : **Docteur de l'université de Strasbourg**

Discipline / Spécialité : Physique / Nanophysique

**Suspended antiferromagnetic van der Waals membranes:  
optical spectroscopy and nanomechanics to probe and  
control their magnetic properties**

**THÈSE dirigée par :**

**M. BERCIAUD Stéphane**  
**M. GLOPPE Arnaud**

Université de Strasbourg, IPCMS  
CNRS, Université de Strasbourg, IPCMS

**RAPPORTEURS :**

**M. FAUGERAS Clément**  
**M. JACQUES Vincent**

CNRS, LNCMI-Grenoble  
CNRS, Université de Montpellier, L2C

**AUTRES MEMBRES DU JURY :**

**M. POGGIO Martino**  
**M. GENET Cyriaque**  
**Mme. MERCIER DE LEPINAY Laure**

Université de Bâle  
CNRS, Université de Strasbourg, ISIS  
Université d'Aalto



---

# Contents

---

<b>Remerciements</b>	<b>5</b>
<b>Résumé en français</b>	<b>9</b>
<b>Introduction</b>	<b>43</b>
<b>1 Optical spectroscopy and nanomechanics of few-layer antiferromagnetic membranes</b>	<b>53</b>
1.1 Transition metal phosphorus trisulfides $MPS_3$ ( $M=Fe,Ni$ )	53
1.1.1 Crystalline structure	53
1.1.2 Magnetic properties	55
1.1.3 Mechanical properties	58
1.1.4 Thermal properties	61
1.2 Sample fabrication	64
1.2.1 Substrate micro-patterning	64
1.2.2 Micro-mechanical cleavage	64
1.2.3 Transfer techniques	67
1.2.4 Sample list	71
1.3 Experimental setup	73
1.3.1 The heart of the setup: the cryostat	73
1.3.2 Around the cryostat: Optical excitation path and signal collection	75
1.3.3 Setup interfacing and auto-positioning	78
1.4 Raman spectroscopy of $MPS_3$	80
1.4.1 Raman scattering processes	80
1.4.2 Phonons dispersion curves	82
1.4.3 Raman tensor and selection rules	84
1.4.4 Interpretation of $MPS_3$ typical spectrum	87
1.5 Nano-optomechanics of suspended van der Waals materials	92
1.5.1 Dynamics of a circular suspended film	92
1.5.2 Detection of the membrane Brownian motion	97
1.5.3 Driven motion	102

---

<b>2</b>	<b>Study of magnetic phase transitions</b>	<b>111</b>
2.1	FePS <sub>3</sub> phase transition . . . . .	111
2.1.1	Probed by nanomechanical measurements . . . . .	111
2.1.2	Probed by Raman spectroscopy . . . . .	117
2.2	NiPS <sub>3</sub> phase transition . . . . .	124
2.2.1	Probed by nanomechanical measurements . . . . .	124
2.2.2	Probed by Raman spectroscopy . . . . .	128
<b>3</b>	<b>Towards strain-tuning of mechanical and magnetic properties in suspended homo- and heterostructures</b>	<b>137</b>
3.1	Strain-induced effects on a homostructure nanomechanics . . . . .	137
3.1.1	Tuning of the membrane's mechanical parameters . . . . .	138
3.1.2	Estimation of gate voltage-induced deflection and strain . . . . .	142
3.2	Influence of strain on NiPS <sub>3</sub> magnetic phase transition . . . . .	146
3.2.1	Seen by Landau theory of phase transitions . . . . .	146
3.2.2	Probed by nanomechanical measurements . . . . .	148
3.2.3	Probed by Raman spectroscopy . . . . .	152
3.3	Magnetic heterostructure nanomechanics . . . . .	155
3.3.1	Mechanical response evolution for an applied gate voltage . . . . .	155
3.3.2	Modification of the membrane spatial profile . . . . .	158
3.3.3	Consequences on the magnetic phase transition . . . . .	162
<b>4</b>	<b>Investigation of NiPS<sub>3</sub> photoluminescence: strain-tuning and fine structure</b>	<b>167</b>
4.1	An intriguing photoluminescence . . . . .	167
4.1.1	Characteristic properties . . . . .	167
4.1.2	Insights into its origins . . . . .	170
4.2	Study of few-layer NiPS <sub>3</sub> photoluminescence main peak . . . . .	173
4.2.1	Evolution with strain . . . . .	173
4.2.2	A non-trivial polarization dependence . . . . .	176
4.3	Identification of magnetic domains and characterization of a satellite peak . . . . .	185
4.3.1	Imaging magnetic domains . . . . .	185
4.3.2	Exploration of satellite peak S <sub>3</sub> behavior . . . . .	189
	<b>Conclusion &amp; perspectives</b>	<b>193</b>
<b>A</b>	<b>Propagation of uncertainties</b>	<b>199</b>
<b>B</b>	<b>Fit with a Voigt profile</b>	<b>201</b>
	<b>Bibliography</b>	<b>203</b>

---

# Remerciements

---

Une thèse est une aventure humaine et collective, pour qu'elle se passe au mieux le soutien et le travail de nombreuses personnes sont nécessaires. Je tiens donc à remercier toutes celles et ceux qui, de près ou de loin, en ont fait partie.

Tout d'abord, l'équipe administrative de l'IPCMS, notamment Catherine et Stéphanie pour leur aide lors de la préparation des événements entre doctorants, et surtout un grand merci à Véronique qui est aux petits soins pour tous les membres du DMONS et qui participe à la cohésion du département avec l'organisation des traditionnels barbecues et galettes des rois.

Merci à Yves pour sa gestion efficace du département et sa rapidité à trouver deux écrans identiques pour chaque étudiant.

Mon travail de thèse n'aurait pas pu se faire sans le support technique de l'IPCMS. Merci à Jérémy et Lorry pour leurs contributions précieuses concernant la partie électronique du setup; merci à Virginie pour son aide dans tous nos problèmes liés à des fuites ou des pompes; et enfin merci à Michi pour son dévouement à la conception de programmes et d'interfaces pour la cartographie de nos échantillons.

J'ai eu la chance de pouvoir compter sur le personnel de la salle blanche STNano pour l'élaboration des substrats de mes échantillons. Un grand merci à Romain, Sabine, Hicham, Ulrich et plus récemment Ali, pour leur aide et leurs conseils.

Une thèse ce n'est pas que du travail, mais aussi des moments conviviaux avec les autres membres du laboratoire. Pour cela j'aimerais en premier lieu remercier l'ADDEPT pour l'organisation de nombreux événements, notamment le tournoi Mario Kart et le très célèbre tournoi annuel de pétanque, ainsi que celui qui en a été le président pendant la majorité de ma thèse, Xavier, merci pour ton enthousiasme, ta bienveillance et ta volonté de rassembler les membres du laboratoire. J'en profite aussi pour remercier tous mes coéquipiers des tournois de pétanque.

J'ai également eu l'honneur et la responsabilité de tenir le business café du bureau 1053 (aka place du café #2), merci à tous ceux qui, en venant chercher un café, s'arrêtaient régulièrement pour demander de mes nouvelles ou me partager des ragots.

Parmi les adeptes de la machine à café, j'aimerais exprimer mon affection à deux équipes en particulier. First, the STM team, with its temporary members Tomáš, Katharina and Anna (thank you for the shared cakes!), its newly permanent member Song, et merci à Guillaume pour son soutien durant ces trois années. Ensuite, l'équipe méso, avec qui j'ai partagé de nombreuses

discussions autour de l'enseignement à la fac de physique. D'abord Gaëtan et Thomas qui ont été présents pendant la majeure partie de ma thèse, puis Florian et Maxime (bonne chance pour la suite de votre thèse !), merci à Dietmar pour ta gentillesse et ton écoute, et un merci spécial à Guillaume pour avoir un été un super prof, avoir largement contribué au bénéfice du business café, et surtout pour m'avoir bien fait rire avec ses blagues potaches pendant mes années de thèse. J'ai aussi eu la chance de représenter les doctorants au conseil d'institut de l'IPCMS pendant un court mandat d'un an, je tiens à remercier mon suppléant, Romain, pour son aide à la co-organisation des soirées des doctorants. Merci également à Ronan et Krystyna pour leur enthousiasme concernant ces événements et leur bonne humeur communicative.

I would also like to thank the PhD students present in the DMONS department from the beginning of my PhD thesis with whom I had the pleasure of sharing time: Ankita, with memories of our trip to the March meeting, Satakshi, José and Gyandeeep; et aussi ceux arrivés plus récemment qui ont égayé la fin de ma thèse: grand Quentin, Davy, Thomas et bien sûr Louis qui a été mon camarade de bureau pendant quelques mois et avec qui j'ai toujours eu beaucoup de plaisir à discuter par la suite.

Durant ma thèse, j'ai eu l'opportunité de co-encadrer la préparation aux montages à la prépa agrég de Strasbourg, après y avoir été moi-même étudiante. Merci tout particulièrement à Marguerite, Thierry, Yannick, François F. et François S. pour leur soutien durant la préparation au concours et leur accompagnement lors de la formation des étudiants.

Les personnes qui ont été les plus importantes pour moi durant ma thèse sont évidemment les membres de mon équipe. Merci à Étienne, un vétéran de l'équipe, de retour pendant quelques mois avant son départ pour les États-Unis, pour la transmission de son art de la fabrication d'échantillons. Merci à Luis, pour son optimisme à toute épreuve et son soutien, notamment lors de mes déboires avec le CIA durant de mon stage de master. Viennent ensuite Loïc et Aditi, les doctorants avec qui j'ai eu le plaisir et l'honneur de partager la majeure partie de ma thèse. Loïc, merci de m'avoir éclairé le chemin de la physique depuis la L1 MPA jusqu'à la thèse, en passant par ce stage de M1 où je suis également tombée dans les filets de Stéphane. Merci pour ton sourire au quotidien, pour avoir pu partager nos frustrations et nos joies, et pour le montage du setup de l'attocube qui est au top. Tu es un expérimentateur de talent, je te souhaite de trouver un poste où tu puisse t'éclater et qui nous permettra, je l'espère, d'à nouveau collaborer un jour. Aditi, we started as colleagues and ended up as friends. Thank you so much for your company during those three years, I had such a great time discussing with you about French and Indian cultures, but also lab gossips and many other things. I hope to see you soon, and that we keep in touch for many years to come. Quentin a ensuite rejoint notre équipe, d'abord comme stagiaire de master 1, puis de master 2 et enfin, en thèse. Merci pour ton soutien moral et pour m'avoir épaulée pendant ces trois années, bon courage pour la fin de ta thèse ! Je tiens aussi à remercier Jules qui est passé deux fois par notre équipe en tant que stagiaire avant de partir faire sa thèse à Paris. J'ai beaucoup apprécié travailler avec toi et je te souhaite le meilleur pour la suite ! Enfin, plus récemment, de nouveaux membres ont été accueillis dans l'équipe. D'abord Élise, qui est

arrivée en stage de master 2 et continue désormais en thèse, merci beaucoup pour ta gentillesse et nos nombreuses discussions, je suis très heureuse d'avoir partagé cette dernière année avec toi. Je te souhaite bonne chance pour la suite de ta thèse, et surtout la fin des problèmes techniques. Ensuite plusieurs doctorants et post-doctorants co-encadrés par Stéphane nous ont rejoints : Manas Pratim, Fabio, Sankesh et Tamaghna, I wish you all the very best with your projects! Finally, Sotos joined as a post-doc, thank you so much for your great advice and for all the efforts you have already put in to improve our work environment! It was a pleasure to work and discuss with you during these few months. I know you will take good care of the team after I am gone, and I really hope you find a permanent position that makes you fulfilled.

Cette thèse n'aurait bien sûr pas pu exister, ni aboutir sans le concours de mes deux directeurs de thèse. Stéphane, merci de m'avoir transmis le goût pour la recherche expérimentale lors de ce stage d'été de M1. Ta bienveillance, la cohésion de l'équipe et ces journées ensoleillées d'été passées à faire de la spectroscopie dans le noir, m'ont donné envie de revenir pour mon stage de M2, après mon passage par l'agrégation. Merci de m'avoir fait confiance pour cette thèse, et merci encore pour ton soutien, ton écoute et tes conseils avisés durant ces nombreuses années (sept si on compte depuis le M1 !). Arnaud, il n'y a pas assez de quelques phrases pour décrire tout ce que tu m'as apporté durant cette thèse. Tu m'as énormément appris, que ce soit en termes de manip, de code Python ou de comment réaliser une présentation efficace et esthétique, pour que je devienne autonome et puisse voler de mes propres ailes. Merci d'avoir cru en moi pendant ces quatre années passées ensemble, d'avoir eu les mots justes pour me remotiver quand j'en avais besoin et de m'avoir soutenue dans mes projets et mes envies. Je vous souhaite à tous les deux le meilleur pour vos projets à venir, accompagnés de nombreux doctorants et post-docs au moins aussi talentueux et motivés que moi !

Finalement, j'aimerais remercier mes amis qui ont contribué à me changer les idées durant ces trois années de thèse, en particulier Camille et Morgane, merci les filles pour votre précieux soutien et votre franchise. Un grand merci aussi aux membres de ma famille qui m'ont encouragée dans cette aventure et se sont montrés curieux de mes nano-tambours magnétiques, en particulier ceux qui sont venus assister à ma soutenance, votre présence m'a beaucoup touchée. Merci à ma maman pour avoir éveillé ma curiosité au monde et m'avoir motivée à suivre mes rêves. Merci à mon papa pour avoir eu confiance en moi et avoir apporté du fun à ma vie.

Le plus important pour la fin, merci à Florian, pour ton soutien indéfectible et ta patience au quotidien, sans toi je n'aurais pas eu le courage de commencer cette thèse, ni la détermination pour la finir. Merci pour tous les beaux moments passés ensemble et pour les aventures à venir.



---

# Résumé en français

---

## Introduction

Le magnétisme est une propriété de la matière qui suscite la curiosité depuis des siècles, déjà en 800 avant J.C., les Grecs étudiaient l'attraction du fer et de l'acier par la magnétite ( $\text{Fe}_3\text{O}_4$ ) qui était minée dans la province de Magnésie en Asie mineure [1]. Les progrès dans la compréhension du magnétisme ont mené à plusieurs innovations technologiques comme le compas, permettant l'exploration des océans, ou l'électroaimant, conduisant à la fabrication de générateurs de courant continu.

D'un point de vue fondamental, les expériences pionnières réalisées par Michael Faraday à partir de 1831 aboutirent à la classification des matériaux comme ferromagnétiques (qui sont facilement aimantés et attirés par un champ magnétique), paramagnétiques (qui sont plus faiblement attirés par un champ magnétique) et diamagnétiques (qui sont repoussés par le champ). Plus tard, en 1895, Pierre Curie démontra que les matériaux ferromagnétiques subissent une transition de phase pour devenir paramagnétiques au delà d'une température nommée d'après lui température de Curie  $T_C$ . La compréhension fondamentale du magnétisme a été rendue possible par l'avènement de la mécanique quantique et de la relativité, notamment grâce à la découverte en 1925 par Georges Uhlenbeck et Samuel Goudmsit du moment angulaire de spin, un nouveau degré de liberté électronique qui peut seulement prendre les valeurs  $\pm\hbar/2$  avec  $\hbar$  la constante de Planck réduite, étant à l'origine des propriétés magnétiques de la matière [2, 3]. En 1932, Louis Néel mis en avant l'idée de matériaux antiferromagnétiques où les moments magnétiques sont arrangés en deux-sous réseaux anti-alignés afin d'expliquer les propriétés de certains alliages [4]. Dans ces matériaux, la température de transition vers la phase paramagnétique porte le nom de température de Néel  $T_N$ . Un autre concept, crucial pour l'essor des technologies magnétiques, est celui de domaines magnétiques, postulé par Pierre Weiss en 1907 et observés en 1949 par H. J. Williams *et al.* [5], il s'agit de régions d'un matériau magnétique où tous les moments magnétiques sont orientés dans la même direction. Les domaines magnétiques sont à la base de l'enregistrement magnétique, d'abord développé pour enregistrer de l'audio sur un film plastique recouvert d'une couche magnétique flexible, disponible notamment sous la forme de cassette audio aux alentours de 1963, puis pour l'enregistrement digital sur disque dur. Grâce aux avancées dans le domaine de la fabrication de films minces conduisant à la miniaturisation des composants magnétiques, la

densité d'informations enregistrées avait ainsi augmenté d'un facteur  $10^8$  entre l'introduction du premier disque dur en 1956 et 2008 [6], soulevant au passage la question de savoir ce qu'il advient des propriétés magnétiques de ces objets de dimensions réduites.

Des prédictions théoriques concernant l'existence ou l'absence d'un ordre magnétique à longue portée dans un système magnétique ont été faites et dépendent de sa dimension d'espace  $D$  et de sa dimension de spin  $n$  [7–9]. La dimension d'espace correspond au nombre de directions selon lesquelles il existe des interactions magnétiques non nulles entre les spins. Le cas le plus courant est celui d'interactions magnétiques dans un cristal ( $D = 3$ ), mais dans certains cas les interactions entre spins sont confinées dans un plan ( $D = 2$ ) ou le long d'une chaîne de spins ( $D = 1$ ). La dimension de spin est le nombre d'axes selon lesquels les spins sont libres de s'orienter et permet de déterminer le modèle théorique adéquat pour décrire le système. Dans le cas d'une dimension de spin  $n = 1$  les spins ne peuvent s'orienter seulement vers le haut ou le bas le long d'un axe et le système est alors décrit par le modèle d'Ising. Pour caractériser un système de dimension de spin  $n = 2$ , où les spins peuvent s'orienter dans un plan, le modèle XY est un modèle de référence. Enfin dans le cas  $n = 3$ , c'est le modèle plus général de Heisenberg qui est employé. Nous nous intéressons ici au cas de dimension d'espace  $D = 2$ , où un ordre magnétique à longue portée a été prédit dans certains cas, notamment dans celui du modèle d'Ising.

Dès le début des années 60, des cristaux présentant une configuration magnétique quasi bidimensionnelle ont été étudiés. Un exemple marquant est celui de  $K_2NiF_4$  qui possède une structure telle que les interactions magnétiques entre les plans atomiques s'annulent et qu'un ordre magnétique à longue portée subsiste seulement à l'intérieur de ces plans [10]. Dans les années 80, suite aux progrès dans la croissance de films minces, des monocouches de fer, cobalt ou nickel ont pu être étudiées, présentant une transition de phase de type Ising et prouvant ainsi l'existence d'un ordre magnétique à la limite bidimensionnelle [11–13]. Plus récemment, une autre famille de cristaux au caractère bidimensionnel a fait l'objet d'un effort soutenu de recherche au niveau international avec pour but l'étude du magnétisme dans des systèmes à faible nombre de couches atomiques : les matériaux de van der Waals magnétiques.

Les matériaux de van der Waals sont des matériaux lamellaires dont les atomes sont liés dans un même plan par des liaisons fortes, covalentes ou ioniques, et hors du plan par des interactions de van der Waals. Grâce à ces interactions plus faibles dans la direction hors du plan, ces matériaux peuvent être exfoliés mécaniquement jusqu'à la limite monocouche, comme cela a été réalisé pour la première fois en 2004 dans le cas du graphène, qui est une monocouche de graphite. Cet accomplissement a ouvert la voie à l'isolation d'une monocouche d'un matériau de van der Waals magnétique, qui constituerait un aimant bidimensionnel. La persistance d'un ordre magnétique a été démontrée expérimentalement en 2016 dans le cas d'une monocouche d'un matériau de van der Waals antiferromagnétique [14] et en 2017 pour un matériau ferromagnétique [15].

Au cours des années qui ont suivi, le nombre de matériaux de van der Waals magnétiques étudiés a considérablement augmenté, offrant une grande diversité de configurations magnétiques exploitables.

Les matériaux de van der Waals magnétiques peuvent également être combinés à d'autres matériaux de van der Waals, formant des hétérostructures, sans désaccord de réseau de part leur maintien par des forces de van der Waals. Les couches magnétiques, généralement sensibles à l'air, peuvent ainsi être encapsulées par du nitrure de bore hexagonal (hBN), qui est un isolant, ou associées à des matériaux semi-conducteurs émettant de la lumière comme les dichalcogénures de métaux de transition (TMDs) afin d'étudier des effets de proximité magnétique. De plus, les matériaux de van der Waals peuvent être suspendus au dessous de trous micrométriques pour obtenir des résonateurs sous forme de nano-tambours. Cette géométrie d'échantillon permet d'accéder aux propriétés intrinsèques du matériau, sans effets provenant du substrat, ainsi que d'analyser l'évolution de ses propriétés sous contrainte. D'autre part, un couplage est attendu entre les degrés de liberté magnétique et mécanique des aimants de van der Waals suspendus, comme cela a été montré précédemment dans le cas de nano-résonateurs hybrides magnéto-optomécaniques [17].

Les matériaux de van der Waals magnétiques offrent donc une plateforme idéale pour étudier le magnétisme à la limite bidimensionnelle (voir Fig. 1).

Ce projet de thèse marque le début de l'étude des matériaux de van der Waals magnétiques dans l'équipe de recherche qui travaillait précédemment sur des homo- ou hétérostructures constituées de graphène et de dichalcogénures de métaux de transition [18–20]. Nous avons commencé à travailler avec des composés de la famille des trisulfures de phosphore de métaux de transitions ( $\text{MPS}_3$ ), qui offrent des configurations antiferromagnétiques variées. Notre approche consiste à suspendre des flocons de ces matériaux ayant une épaisseur de quelques couches atomiques, éventuellement intégrés dans une hétérostructure, sur des trous de taille micrométrique afin de former les nano-résonateurs évoqués précédemment (voir Fig. 2). Nous explorerons ici les propriétés de ces nano-résonateurs magnétiques par le prisme de la nano-optomécanique et des spectroscopies optiques, combinées sur le même

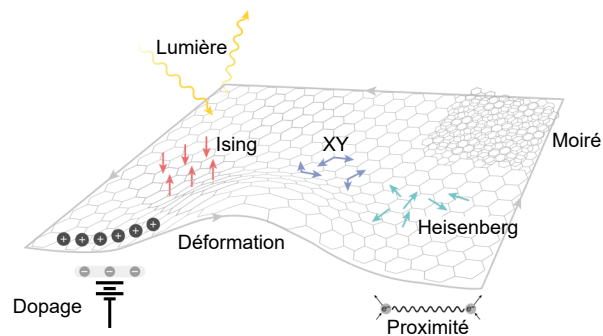


**Figure 1:** Illustration du large éventail de degrés de liberté offerts par les matériaux magnétiques de van der Waals. Adapté de [16].

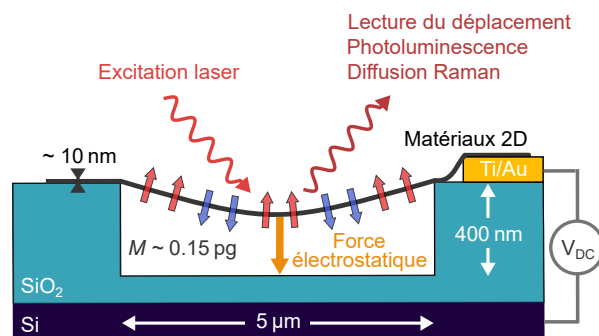


**Figure 2:** Interactions et degrés de liberté dans un nano-tambour magnétique.

dispositif expérimental.

Le premier objectif de ce projet sera de réaliser ces échantillons en forme de nano-tambours par des techniques de nanofabrication en salle blanche. Ensuite, nous sonderons les propriétés magnétiques des ces couches antiferromagnétiques suspendues, notamment leurs transitions de phase magnétiques, avant d'explorer leur contrôle par l'application d'une contrainte. Par ailleurs, nous analyserons également la nanomécanique d'hétérostructures de van der Waals magnétiques en fonction d'une déformation induite ainsi que les propriétés intrigantes de l'émission de lumière de NiPS<sub>3</sub>.

Ce résumé est composé de quatre parties qui correspondent aux quatre chapitres de la thèse.

Une première partie introduit les concepts essentiels à la compréhension du reste des travaux, comme les propriétés principales des matériaux étudiés, les techniques de nanofabrication employées ou encore une introduction aux méthodes expérimentales.

Une deuxième partie présente la détection des transitions de phase magnétiques dans des échantillons suspendus de quelques couches de FePS<sub>3</sub> et NiPS<sub>3</sub> à la fois en utilisant la spectroscopie Raman et des mesures de nanomécanique.

Une troisième partie est dédiée à l'évolution des propriétés mécaniques et magnétiques en fonction de la contrainte appliquée pour une homostructure de NiPS<sub>3</sub> et une hétérostructure contenant FePS<sub>3</sub>.

Une dernière partie est consacrée à l'exploration des propriétés de la photoluminescence de NiPS<sub>3</sub>, notamment son comportement sous contrainte et la résolution spatiale de sa polarisation permettant d'imager des domaines antiferromagnétiques.

## Spectroscopie optique et nanomécanique de membranes anti-ferromagnétiques à quelques couches atomiques

Dans cette partie, nous introduisons les méthodes et les concepts qui seront utiles à la compréhension des résultats obtenus durant cette thèse.

### Matériaux magnétiques de van der Waals étudiés

Pour cette première étude réalisée dans l'équipe sur des matériaux de van der Waals magnétiques, nous avons choisi d'étudier les trisulfures de phosphore de métaux de transition ( $MPS_3$ ). Les composés appartenant à cette famille présentent un ordre antiferromagnétique pour des températures inférieures à leur température de Néel. Ils présentent l'avantage d'être stables dans des conditions ambiantes, contrairement à la plupart des matériaux de van der Waals magnétiques qui doivent être manipulés sous atmosphère inerte.

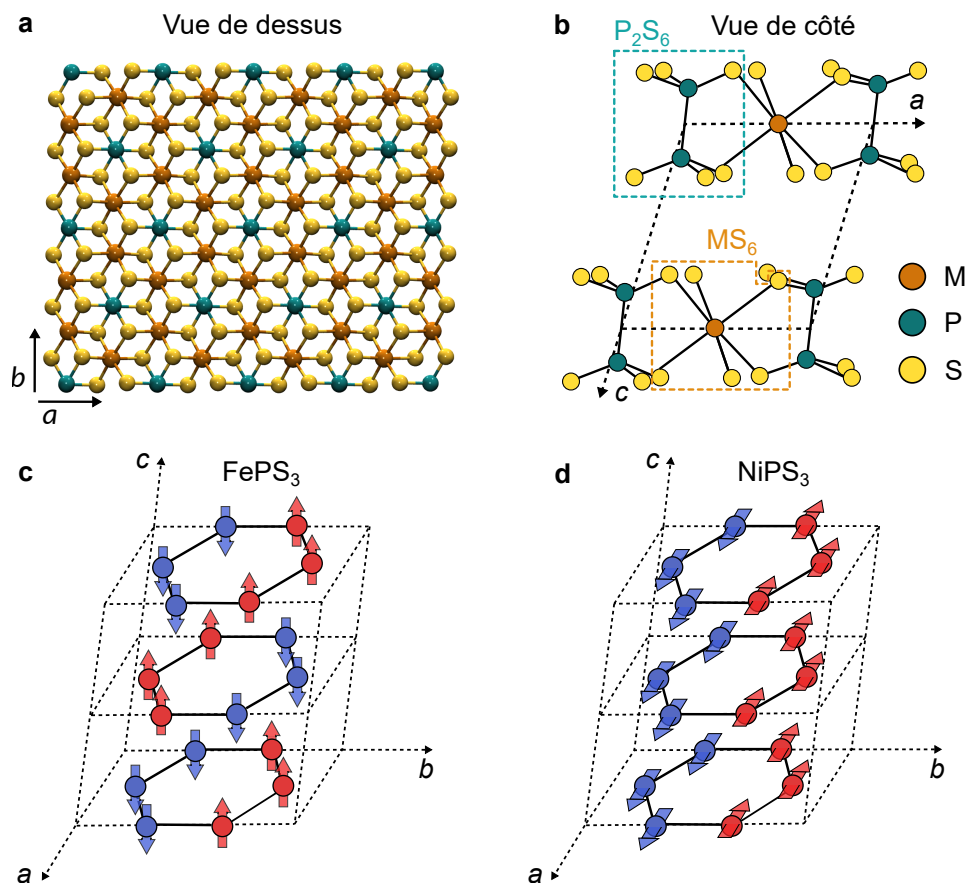


**Figure 3: Structures cristalline et magnétique de  $FePS_3$  et  $NiPS_3$ .** a. Structure cristalline d'une monocouche de  $MPS_3$  vue du dessus. b. Schéma de la structure cristalline de deux couches de  $MPS_3$  vues de côté. Les pointillés verts indiquent une cellule  $P_2S_6$  tandis que les pointillés oranges indiquent une cellule  $MS_6$ . Adapté de [21]. c,d. Schéma de la structure magnétique de  $FePS_3$  et  $NiPS_3$ , respectivement. Les spins des atomes de métaux de transition sont représentés par des flèches. Adapté de [22].

Les  $MPS_3$  possèdent une structure cristalline commune (voir Fig. 3 a,b) dans laquelle les atomes

de métaux de transition forment un réseau en nid d'abeille. Les couches atomiques constituant ces matériaux peuvent être vues comme une alternance de cellules non-magnétiques ( $P_2S_6$ ) et de cellules contenant un atome de métal de transition ( $MS_6$ ). Ces couches sont empilées suivant une structure monoclinique, ce qui se traduit par une brisure de la symétrie spatiale dans la direction hors du plan.

Durant ce projet, nous avons travaillé sur deux matériaux :  $FePS_3$  et  $NiPS_3$ , possédant chacun un ordre magnétique d'orientation différente (voir Fig. 3 c,d).  $FePS_3$  est un matériau antiferromagnétique inter- et intracouche de type Ising, présentant des spins orientés hors du plan, avec une température de Néel d'environ 118 K pour un cristal massif. D'autre part,  $NiPS_3$  est aussi un matériau antiferromagnétique intracouche mais possède un ordre ferromagnétique intercouche. Ses spins sont orientés dans le plan  $ab$  le long d'un axe facile d'aimantation qui est préférentiellement l'axe cristallin  $a$  dans le cas d'un cristal massif. Sa température de Néel est de 155 K pour un cristal massif. De plus,  $NiPS_3$  présente une émission lumineuse à l'origine encore débattue que nous analyserons plus en détails dans la dernière section de ce résumé.

## Fabrication d'homo et d'hétérostructures magnétiques suspendues

Afin d'obtenir les membranes magnétiques suspendues de quelques couches d'épaisseur que nous désirons étudier, nous fabriquons des échantillons en salle blanche.

Des flocons de matériaux de van der Waals sont exfoliés mécaniquement à partir de cristaux massifs avant d'être transférés sur des substrats de Si/SiO<sub>2</sub> possédant des électrodes et des trous préalablement implémentés par des techniques de nanofabrication (lithographie laser, dépôt de métaux et gravure ionique réactive).

Le transfert est réalisé grâce à une station de transfert motorisée (voir Fig. 4 a) placée dans une boîte à gants afin de pouvoir manipuler des matériaux sensibles à l'air sans risque de dégradation.

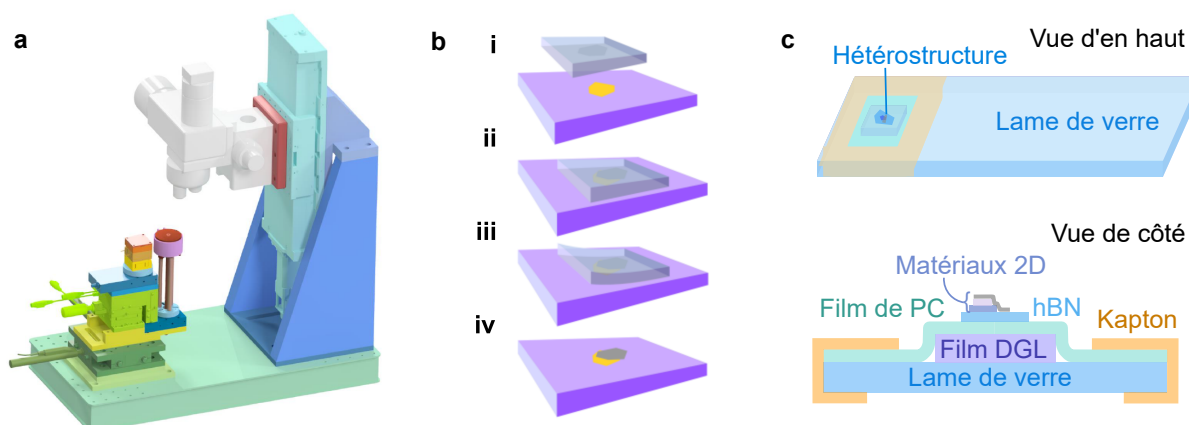


**Figure 4: Techniques employées pour le transfert de matériaux 2D.** **a.** Vue 3D de la station de transfert motorisée. **b. i-iv.** Étapes du transfert sur un substrat par la méthode «all-dry». Adapté de [23]. **c.** Schémas d'un stamp utilisé pour la méthode «pick-up» intégrant une hétérostructure de van der Waals prête à être transférée.

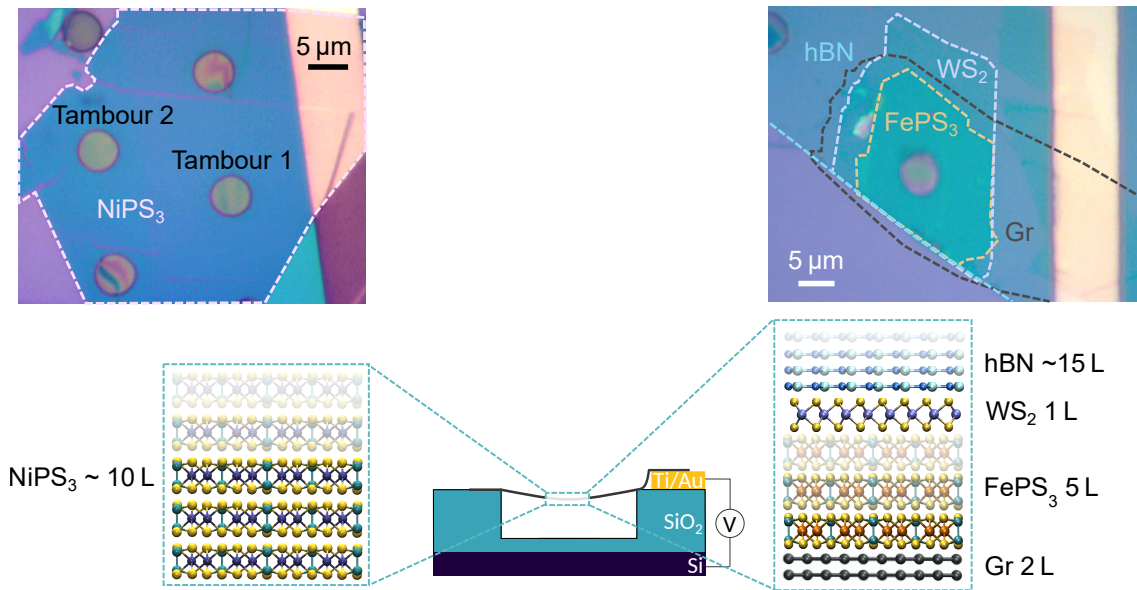


**Figure 5: Images optiques et schémas de la composition de deux échantillons parmi ceux étudiés.** A gauche, une homostructure de  $\text{NiPS}_3$  d'environ 10 couches possédant deux nano-tambours intacts, apparaissant comme deux disques jaunes : *Tambour 1* et *Tambour 2*. A droite, une hétérostructure comprenant du nitrure de bore hexagonal (hBN), une monocouche de  $\text{WS}_2$ , un flocon de 5 couches de  $\text{FePS}_3$  et une bicouche de graphène (Gr).

Deux techniques de transfert peuvent être employées afin d'obtenir des membranes suspendues :

- la méthode dite «all-dry» où le flocon de matériau 2D est exfolié sur un film de polymère *DGL* puis directement transféré sur le trou (voir Fig. 4 b). Cette technique est privilégiée pour les homostructures ou les hétérostructures contenant seulement deux matériaux.
- la méthode dite du «pick-up» où les flocons de matériaux 2D sont d'abord exfoliés sur des substrat de Si/SiO<sub>2</sub> avant d'être récupérés un à un sur un «stamp» constitué d'un film de PC (polybisphénol A carbonate) et d'un film *DGL* (voir Fig. 4 c). L'hétérostructure ainsi formée est déposée sur le trou en faisant fondre le film de PC. Cette technique est privilégiée pour les hétérostructures contenant plus de deux matériaux.

Deux exemples d'échantillons suspendus et contactés obtenus par ces méthodes et étudiés durant la thèse sont présentés en Figure 5. L'homostructure d'environ 10 couches de  $\text{NiPS}_3$  a été obtenue par la méthode all-dry tandis que l'hétérostructure comprenant un flocon de  $\text{FePS}_3$  de 5 couches encapsulé par du nitrure de bore hexagonal, une monocouche de  $\text{WS}_2$  et une bicouche de graphène a été réalisée par la méthode du pick-up.

Une fois les échantillons fabriqués, ceux-ci sont fixés dans un chip carrier et contactés par pontage avec un fil d'or.

## Dispositif expérimental

Une fois contacté, l'échantillon est inséré dans un cryostat avec accès optique afin de réaliser des mesures à des températures inférieures à la température de Néel des matériaux étudiés.

Le cryostat principalement utilisé pour ces travaux de thèse est un cryostat fonctionnant en cycle fermé d'hélium offrant une grande stabilité en température. L'échantillon y est placé au sommet d'un empilement de positionneurs piézoélectriques permettant une résolution spatiale des propriétés physiques (voir Fig. 6). Le cryostat inclut également un objectif de microscope cryo-compatible assurant une haute stabilité spatiale des mesures.

Autour de ce cryostat est construite une expérience d'optique qui peut être décomposée en plusieurs parties (voir Fig. 7) :

- deux lignes d'excitation laser de longueurs d'onde respectives 532 et 633 nm dont la puissance peut-être variée grâce à des couples lame demi-onde et cube semi-réfléchissant polarisant.
- une illumination en lumière blanche permettant de faire l'image optique de l'échantillon sur une caméra.
- une ligne de détection pour la spectroscopie optique (spectroscopie Raman et de photoluminescence) comprenant un sténopé, qui permet le filtrage spatial de la lumière réfléchie par l'échantillon, et un filtre optique passe-haut pour son filtrage spectral. Cette lumière est ensuite focalisée dans un spectromètre comprenant un monochromateur et une caméra CCD.
- une ligne de détection pour l'optomécanique comprenant un circulateur formé par un couple lame quart d'onde et cube semi-réfléchissant polarisant permettant de diriger la lumière réfléchie par l'échantillon vers une photodiode à avalanche (APD). Le signal collecté peut ensuite être envoyé soit vers un analyseur de spectre dans le cas de la détection du mouvement Brownien de la membrane, soit vers un analyseur de réseau pour la détection de son mouvement forcé.

La spectroscopie optique et la détection optomécanique sont ainsi réunies sur un même dispositif expérimental, ce qui permet de réaliser ces deux types de mesures dans des conditions identiques.

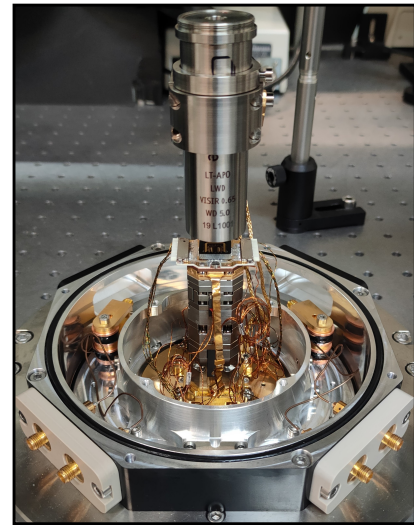
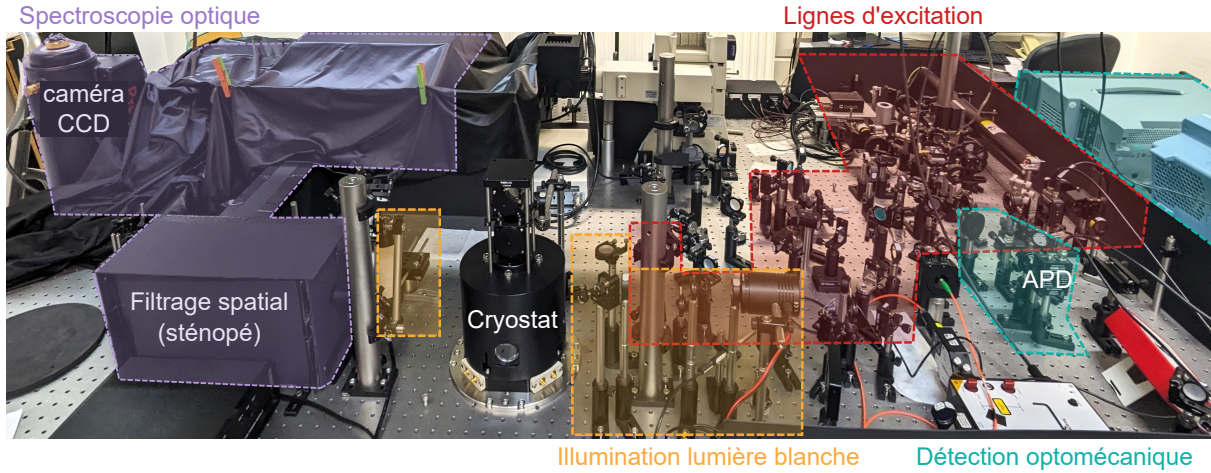


Figure 6: Intérieur du cryostat.



**Figure 7:** Dispositif expérimental où les différentes parties le composant sont mises en évidence par différentes couleurs : rouge pour les lignes d'excitation laser, jaune pour l'illumination en lumière blanche, violet pour la spectroscopie optique et bleu pour la détection optomécanique.

Durant ma thèse, l'interfaçage des instruments faisant partie du dispositif expérimental a été poursuivi en utilisant le protocole VISA (Virtual Instrument Software Architecture) et Python comme langage de programmation. Cela a notamment permis l'implémentation d'un positionnement automatique sur la membrane, afin de corriger la dérive spatiale induite par le changement de température nécessaire pour sonder la transition de phase.

### Spectroscopie Raman des $\text{MPS}_3$

La spectroscopie Raman est une spectroscopie optique qui utilise la diffusion inélastique de la lumière afin de sonder les excitations élémentaires d'un cristal comme les phonons ou les magnons. Dans cette partie, nous nous concentrerons uniquement sur les phonons, qui sont les quanta des modes normaux de vibration des atomes du réseau cristallin. A partir des relations sur la conservation de l'énergie et du moment lors du processus de diffusion, il est possible de montrer que seuls les phonons avec un vecteur d'ordre proche de zéro, donc proches du point  $\Gamma$  de la zone de Brillouin, peuvent être sondés en spectroscopie Raman.

Le nombre de phonons attendu pour une maille cristalline donnée est  $3N$  avec  $N$  le nombre d'atomes dans la maille élémentaire, ce qui donne 30 phonons dans le cas des trisulfures de phosphore de métaux de transition. La symétrie de ces modes peut être déterminée grâce à la théorie des groupes. Dû à leur empilement monoclinique, le groupe ponctuel de symétrie des  $\text{MPS}_3$  est  $C_{2h}$ . La représentation irréductible correspondante est alors

$$\Gamma_{C_{2h}} = 8A_g + 6A_u + 7B_g + 9B_u. \quad (1)$$

Les labels A, B indiquent des modes de phonon symétriques, anti-symétriques, respectivement, par rapport à l'axe principal du cristal. Tandis que les indices g, u correspondent à des modes symétrique, anti-symétriques, respectivement, par rapport au centre d'inversion de la maille

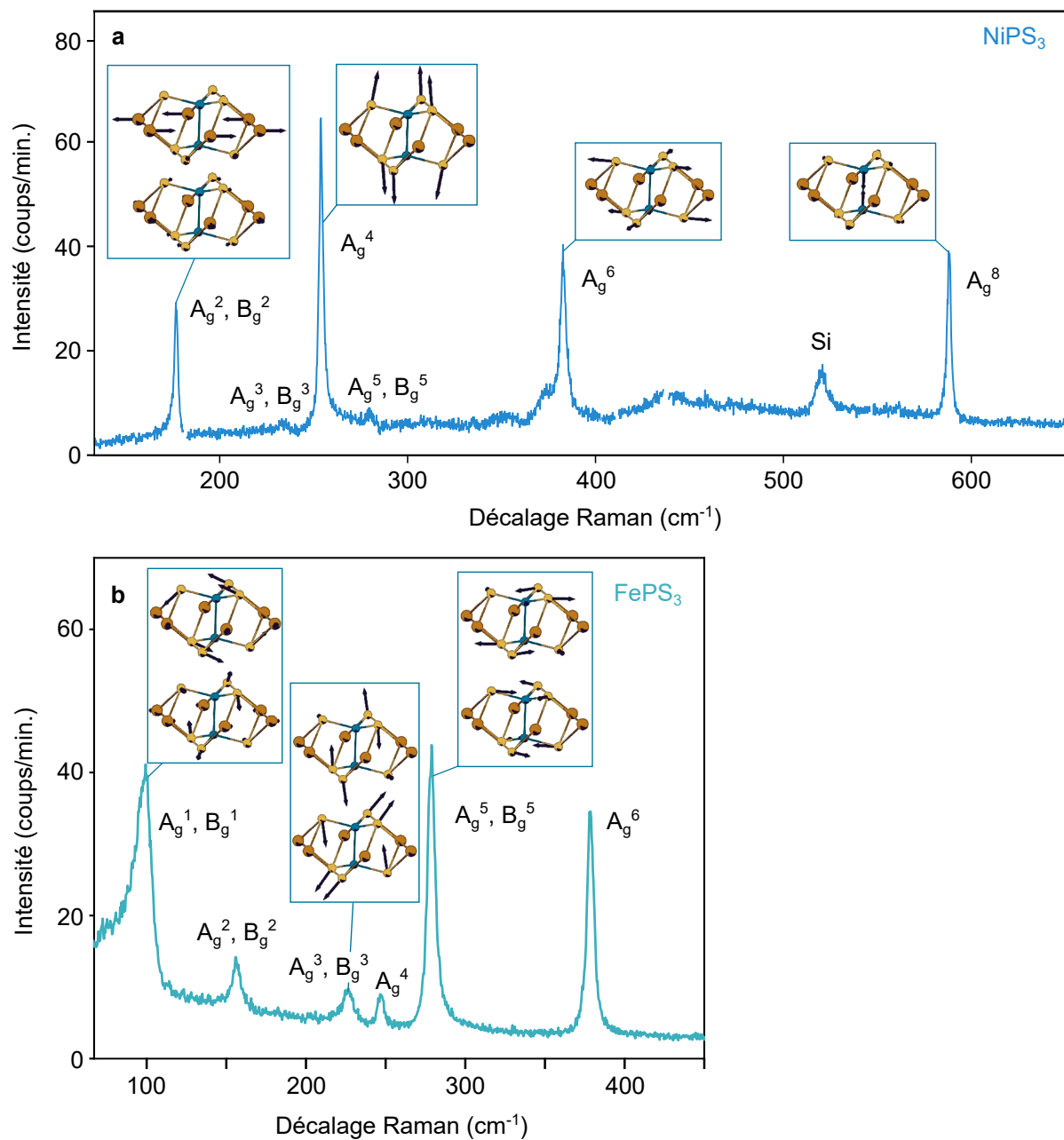


**Figure 8: Modes actifs-Raman mesurés expérimentalement à température ambiante sur des cristaux massifs et schéma des modes de vibration associés.** a. Spectre Raman de  $\text{NiPS}_3$  pour une longueur d'onde laser de 632.8 nm. Le pic intitulé "Si" provient du substrat. b. Spectre Raman de  $\text{FePS}_3$  pour une longueur d'onde laser de 532.1 nm. Les pics sont désignés par les symétries du mode de phonon correspondant. Les schémas des modes de vibration pour une maille de  $\text{MPS}_3$  sont adaptés de [24]: ceux correspondant à des modes de phonon d'exposant pair sont indiqués sur le spectre de  $\text{NiPS}_3$ , tandis que ceux correspondant à des modes de phonon d'exposant impair sont indiqués sur le spectre de  $\text{FePS}_3$ .

élémentaire. Selon les règles de sélection de la diffusion Raman, seuls les modes avec un indice "g" sont actifs-Raman et peuvent donc être détectés, ce qui réduit de moitié le nombre de phonons possiblement visibles dans le spectre Raman des  $\text{MPS}_3$ .

Les modes normaux de vibration correspondants, ainsi que leurs fréquences, peuvent être calculés et assignés aux pics observés dans les spectres Raman mesurés expérimentalement [14, 24, 25]. En observant les spectres de  $\text{FePS}_3$  et  $\text{NiPS}_3$  obtenus à température ambiante (voir Fig. 8) nous remarquons que quatre pics correspondent à des modes doublement dégénérés ( $A_g, B_g$ ) et trois pics à des modes  $A_g$ . Les modes de vibration ayant un décalage Raman supérieur à  $200 \text{ cm}^{-1}$  impliquent seulement le mouvement des atomes de soufre et de phosphore de la cellule  $\text{P}_2\text{S}_6$ , alors que les modes ( $A_g^1, B_g^1$ ) et ( $A_g^2, B_g^2$ ) font intervenir le mouvement d'atomes de métaux de transition. Ce sont donc ces deux pics à plus basse fréquence qui vont nous intéresser pour sonder la transition de phase magnétique de  $\text{FePS}_3$  et  $\text{NiPS}_3$  lors de mesures à des températures plus basses.

## Nano-optomécanique de matériaux de van der Waals suspendus

### Dynamique d'un film mince circulaire suspendu

L'optomécanique est le domaine de la physique consacré à l'étude des interactions entre la lumière et les degrés de libertés mécaniques. Dans cette sous-partie, le degré de liberté mécanique considéré est le mouvement hors du plan d'un nanorésonateur constitué d'un flocon de matériau de van der Waals suspendu au-dessous d'un trou.

Le déplacement de ce film mince dans la direction  $z$  peut être décrit par un champ scalaire  $\xi(r, \varphi)$  et décomposé en une superposition linéaire de ses modes propres selon

$$\xi(r, \varphi, t) = \sum_n z_n(t) u_n(r, \varphi) \quad (2)$$

où  $u_n(r, \varphi)$  est le profil spatial du n-ième mode et  $z_n(t)$  une fonction décrivant la dépendance temporelle du mouvement du n-ième mode du résonateur.

Les profils spatiaux des modes propres peuvent être calculés en minimisant l'énergie totale du film mince suspendu ainsi qu'en prenant en compte les conditions aux limites pour un film fixé aux bords du trou. L'expression obtenue pour le mode  $(m, n)$  est alors

$$u_{mn}(r, \varphi) = A_m \cos(m\varphi) J_m \left( \frac{\alpha_{mn} r}{R} \right) \quad (3)$$

avec  $J_m$  la fonction de Bessel sphérique du premier type d'ordre  $m$ ,  $\alpha_{mn}$  sa n-ième racine,  $R$  le rayon du film et  $A_m$  une constante de normalisation telle que la valeur maximale de  $u_{mn}$  est égale à l'unité. Les profils théoriques ainsi obtenus pour les six premiers modes mécaniques sont illustrés en Figure 9.

D'autre part, nous pouvons également déterminer la dépendance temporelle du déplacement

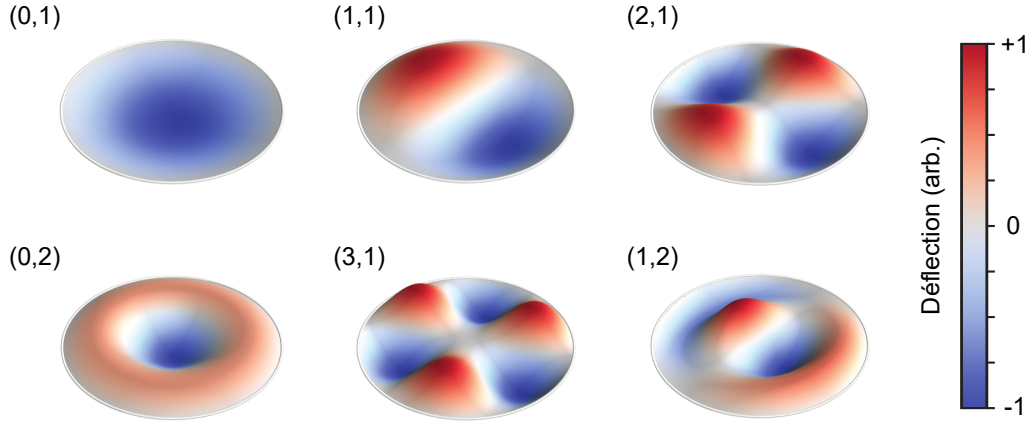


**Figure 9:** Profils spatiaux des modes propres d'un film mince circulaire calculés à partir de l'Équation (3).

hors du plan pour le point de déflexion maximale  $z_n(t)$ . La dynamique d'un point du film mince pour le mode  $(m, n)$  peut être décrite par celle d'un oscillateur harmonique amorti forcé dont l'équation du mouvement est

$$\ddot{z}(t) + \Gamma_m \dot{z}(t) + \Omega_m^2 z(t) = \frac{F(t)}{M_{\text{eff}}} \quad (4)$$

où  $\Omega_m$  et  $\Gamma_m$  sont la pulsation à résonance et l'amortissement du mode mécanique, respectivement. Le facteur de qualité du mode mécanique est défini comme  $Q = \Omega_m/\Gamma_m$ .  $F(t)$  est une force dépendant du temps ressentie par le résonateur et  $M_{\text{eff}}$  est la masse effective du mode  $(m, n)$ , traduisant le fait que seule une fraction de la masse totale du film participe au mouvement de ce mode donné.

Dans l'espace de Fourier, le déplacement de la membrane en réponse à la force ressentie s'écrit, en ne considérant que les termes linéaires,

$$z[\Omega] = \chi_m[\Omega] F[\Omega] \quad (5)$$

où l'on a défini la susceptibilité mécanique par

$$\chi_m[\Omega] = \frac{1}{M_{\text{eff}}(\Omega_m^2 - \Omega^2 - i\Gamma_m\Omega)}. \quad (6)$$

La réponse mécanique  $z[\Omega]$  possède donc un profil proche d'une Lorentzienne avec un pic à la fréquence de résonance  $f_m$  et une largeur à mi-hauteur  $\Gamma_m$ . Ce déplacement hors du plan  $z$  est la grandeur à laquelle nous avons accès expérimentalement.

### Détection interférométrique des mouvements Brownien et forcé

Pour détecter le mouvement de la membrane hors du plan, un laser est focalisé sur l'échantillon et est réfléchi à la fois par la membrane mais aussi par le silicium au fond du substrat, formant ainsi une cavité Fabry-Pérot (voir Fig. 10). Le déplacement de la membrane dans la cavité modifie

l'intensité lumineuse réfléchi de deux manières : la position de la membrane contrôle la taille de la cavité et donc le profil d'interférences dans celle-ci, de plus le matériau 2D absorbe une partie de la lumière qui est proportionnelle à l'intensité lumineuse dans la cavité lors de son déplacement.

Le mouvement de la membrane est donc encodé dans la lumière réfléchi qui est collectée par une photodiode à avalanche et ensuite transmise à un analyseur de spectre ou un analyseur de réseau.

Si nous n'appliquons aucune force sur la membrane, elle sera uniquement soumise aux fluctuations thermiques qui sont modélisées par la force de Langevin  $F_{th}$  et nous détecterons alors son mouvement Brownien. La densité spectrale de bruit de déplacement  $S_z$  peut être exprimée comme

$$S_z[\Omega] = |\chi_m[\Omega]|^2 S_{F_{th}} \quad (7)$$

où  $\chi_m$  est la susceptibilité mécanique définie à l'Équation (6) et  $S_{F_{th}}$  est la densité spectrale de la force de Langevin qui vaut

$$S_{F_{th}}[\Omega] = 2M_{eff}\Gamma_m k_B T \quad (8)$$

avec  $k_B$  la constante de Boltzmann.

L'analyseur de spectre mesure la densité spectrale de bruit  $S_V$  en sortie de la photodiode, il est possible de remonter à la densité spectrale de bruit de déplacement en calibrant le signal grâce à l'Équation (7) évaluée à résonance. Un spectre calibré du mouvement Brownien d'une membrane d'environ dix couches de FePS<sub>3</sub> est présenté en Figure 11 a, on peut y voir le mode fondamental de vibration à 4.7 MHz ainsi que deux modes d'ordre supérieur.

Comme la densité spectrale de bruit de déplacement est proportionnelle à la température, le temps d'acquisition nécessaire pour obtenir un spectre de mouvement Brownien avec un rapport signal sur bruit suffisant augmente lorsque l'on diminue la température, pour atteindre environ 15 minutes par spectre aux alentours de la température de Néel des matériaux étudiés. Afin de réduire ce temps d'acquisition, en vue de sonder la transition de phase magnétique de ces matériaux, nous allons donc forcer le mouvement de la membrane.

Pour cela, une somme d'une tension alternative, dont la fréquence est variée autour de la fréquence de résonance de la membrane, et d'une tension continue est appliquée à l'électrode en contact avec le matériau 2D, tandis que le fond du substrat est mis à la masse (voir Fig. 10). La membrane et le fond du substrat peuvent donc être considérées comme les deux plaques d'un condensateur

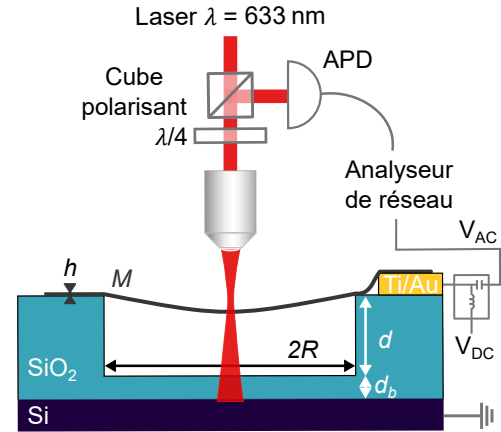


**Figure 10: Schéma simplifié de la détection interférométrique et de l'actuation électrostatique.** Une somme de tensions continue  $V_{DC}$  et alternative  $V_{AC}$  est appliquée à l'électrode en contact avec la membrane, le fond du substrat étant à la masse, formant un condensateur.

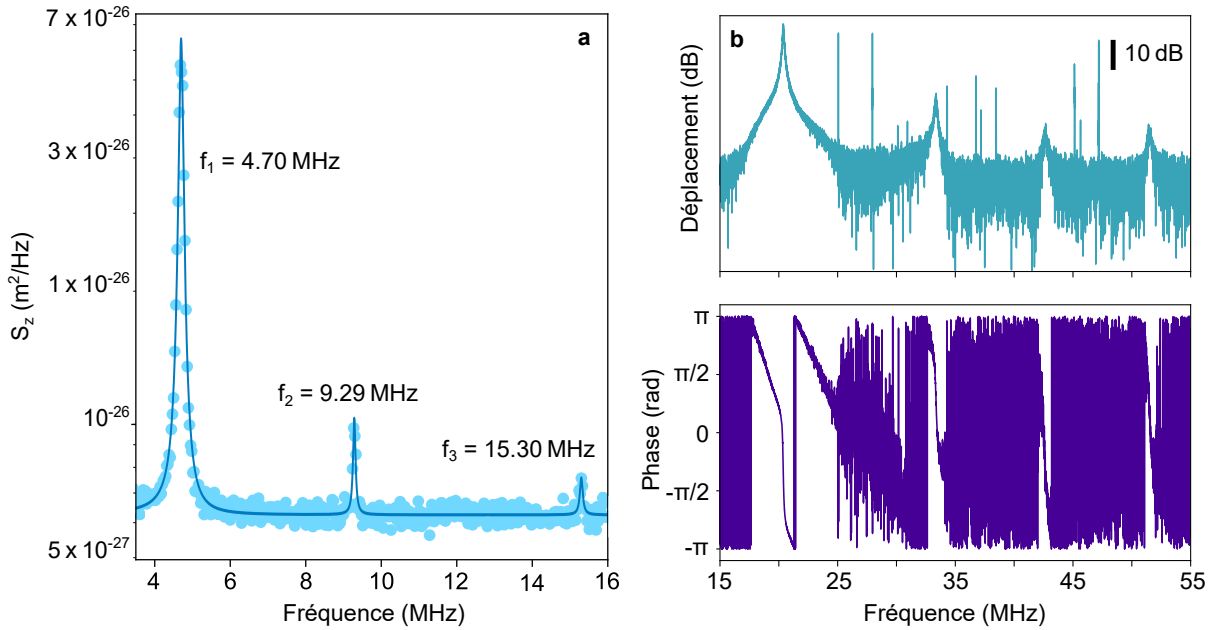


**Figure 11: Réponses mécaniques de membranes suspendues avec et sans actuation électrostatique.** **a.** Spectre de mouvement Brownien à température ambiante d’une membrane d’environ 10 couches de  $\text{FePS}_3$  présentant trois modes mécaniques. Les points correspondent aux données expérimentales et la ligne continue à un ajustement selon le modèle de l’Équation (6). **b.** Réponse mécanique à une actuation électrostatique ( $V_{\text{DC}} = 13.5$  V,  $V_{\text{AC}} = 22.5$  mV) mesurée à une température de 109 K pour une hétérostructure suspendue comprenant cinq couches de  $\text{FePS}_3$ .

entre lesquelles s’exerce une force électrostatique

$$F_{\text{el}} \propto (V_{\text{DC}}^2 + 2V_{\text{AC}}V_{\text{DC}} \cos(\Omega t)). \quad (9)$$

Cette force possède une partie statique, proportionnelle à  $V_{\text{DC}}^2$ , qui tend à attirer la membrane vers le fond du substrat et une partie dépendante du temps qui force le mouvement de la membrane. Un spectre de la réponse mécanique à une actuation électrostatique pour une hétérostructure comprenant cinq couches de  $\text{FePS}_3$  (voir Fig. 5) est présenté en Figure 11 b. Le temps typique d’acquisition pour un tel spectre est d’environ une minute.

Il est aussi possible de forcer le mouvement du résonateur en utilisant un second laser modulé en intensité autour de la fréquence de résonance de la membrane. Son déplacement forcé est alors induit à la fois par la pression de radiation et des forces optothermiques.

## Étude des transition de phase magnétiques

Dans cette partie, nous présentons la méthodologie que nous avons développée durant cette thèse pour sonder les transitions de phase magnétiques de matériaux de van der Waals suspendus. D'abord nous montrons les résultats obtenus par des mesures de nanomécanique suivant une méthode proposée séparément par Šiškins *et al.* [26] et Jiang *et al.* [27] en 2020, puis ceux obtenus par la spectroscopie Raman, qui est devenue ces dernières années une technique standard pour sonder localement l'ordre magnétique dans les matériaux 2D.

### Sondées par des mesures de nanomécanique

#### FePS<sub>3</sub>

Nous étudions d'abord la transition de la phase paramagnétique vers la phase antiferromagnétique d'une hétérostructure suspendue comportant cinq couches de FePS<sub>3</sub> encapsulées par une quinzaine de couches de nitrure de bore, une monocouche de WS<sub>2</sub> et une bicouche de graphène (voir Fig. 5). Pour mettre en évidence cette transition de phase magnétique, nous suivons l'évolution du mode mécanique fondamental du nanorésonateur pour des températures autour de la température de Néel de FePS<sub>3</sub> en cristal massif (118 K).

Nous observons que la fréquence de résonance du mode mécanique augmente lorsque la température diminue ce qui correspond à une contraction de la membrane (voir Fig. 12 a). Cependant, entre 101 et 118 K, la fréquence de résonance décroît plus rapidement, indiquant la gamme de température où la transition de phase magnétique se produit. En effet, la variation de la fréquence de résonance est liée à la capacité thermique  $c_v$  de la membrane par [26]

$$c_v(T) \propto -\frac{df_m^2(T)}{dT}. \quad (10)$$

La capacité thermique est discontinue à la transition de phase ce qui se traduit par un pic dans son évolution avec la température provenant de sa contribution magnétique, comme cela a été mesuré par Takano *et al.* en 2004 dans le cas d'un cristal massif de FePS<sub>3</sub> [28]. En traçant la grandeur  $-df_m^2(T)/dT$  nous observons en effet un pic dont le sommet nous permet d'estimer une température de Néel d'environ 109 K pour cet échantillon de FePS<sub>3</sub> (voir Fig. 12 b).

La transition de phase magnétique est aussi visible comme un point d'inflexion dans l'évolution de l'inverse du facteur de qualité avec la température (voir Fig. 12 c). Cette caractéristique est attribuée à une augmentation de la contribution de l'amortissement thermoélastique lors de la transition de phase [29] et nous offre un deuxième indicateur de celle-ci.

#### NiPS<sub>3</sub>

Le même protocole est appliqué pour sonder la transition de phase magnétique d'une homostructure suspendue de dix couches de NiPS<sub>3</sub>.

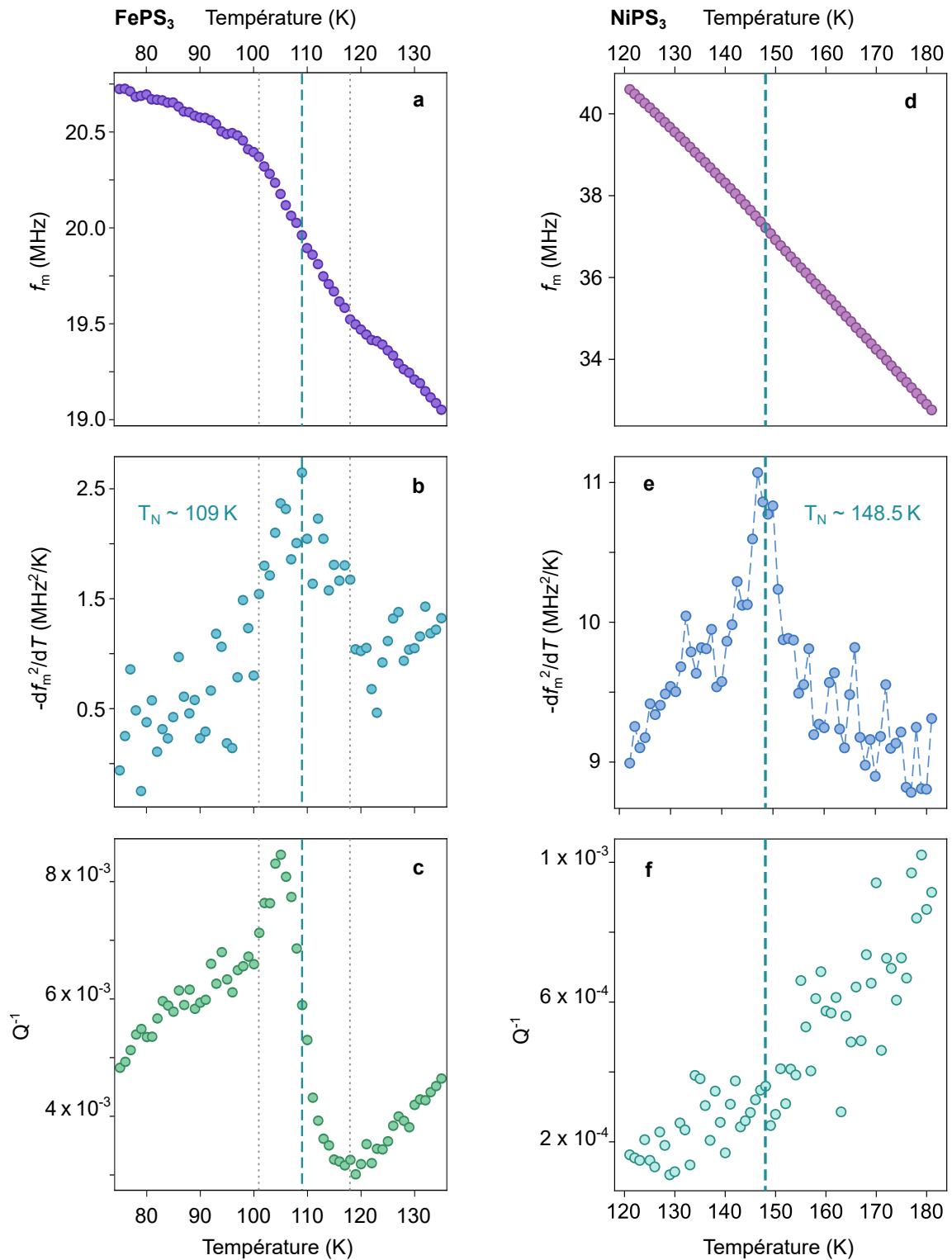


**Figure 12: Évolution avec la température des paramètres du mode mécanique fondamental d’une hétérostructure comprenant cinq couches de  $\text{FePS}_3$  et une homostructure d’environ dix couches de  $\text{NiPS}_3$  et estimation de leurs températures de Néel  $T_N$  respectives.** Les panneaux de gauche correspondent au nanorésonateur de  $\text{FePS}_3$  tandis que ceux de droite au nanorésonateur de  $\text{NiPS}_3$ . **a, d.** Fréquences de résonance en fonction de la température. **b, e.** Opposé de la dérivée par rapport à la température du carré de la fréquence de résonance. La température de Néel de l’échantillon est définie par le maximum du pic mesuré. **c, f.** Inverse du facteur de qualité en fonction de la température. Un point d’inflexion est visible à la température de Néel dans le cas du résonateur comprenant  $\text{FePS}_3$ . Les pointillés bleus indiquent la température de Néel estimée.

Nous observons que le changement de pente à la transition de phase dans l'évolution de la fréquence de résonance avec la température est plus faible que dans le cas de l'hétérostructure comprenant FePS<sub>3</sub> (voir Fig. 12 d). Cependant, un pic est bien visible dans  $-df_m^2(T)/dT$ , nous permettant d'estimer une température de Néel d'environ 148.5 K pour cet échantillon de NiPS<sub>3</sub>. Concernant l'inverse du facteur de qualité, le point d'inflexion présent dans le cas de FePS<sub>3</sub> n'est pas visible, suggérant une contribution plus faible de l'amortissement thermoélastique pour NiPS<sub>3</sub>.

## Sondées par spectroscopie Raman

Pour détecter la transition entre la phase paramagnétique et antiferromagnétique dans FePS<sub>3</sub> et NiPS<sub>3</sub>, nous analysons l'évolution de leurs spectres Raman en fonction de la température en nous focalisant sur les modes de phonon à basse fréquence qui impliquent des atomes de métaux de transition.

### FePS<sub>3</sub>

Nous étudions l'hétérostructure comprenant cinq couches de FePS<sub>3</sub> déjà mentionnée dans la partie nanomécanique. Les modes de phonon provenant de la monocouche de WS<sub>2</sub> sont donc également visibles dans le spectre Raman de cette hétérostructure (voir Fig. 13 a), en plus des modes de phonon appartenant à FePS<sub>3</sub>.

Le principal changement visible dans le spectre Raman de FePS<sub>3</sub> lors d'une diminution de la température est l'apparition, aux alentours de 113 K, d'un pic que nous appellerons P<sub>1</sub> avec un décalage Raman d'environ 88 cm<sup>-1</sup>. Ce pic est attribué à un phonon de repliement de zone. En effet, lors de la transition de phase magnétique, la taille de la maille élémentaire double afin de prendre en compte l'ordre antiferromagnétique (voir Fig. 13 b). Cela se traduit dans l'espace réciproque par une réduction de moitié de la taille de la zone de Brillouin, ce qui induit un repliement du point *M* sur le point  $\Gamma$  dans le cas de FePS<sub>3</sub>. Or, comme les phonons sondés en spectroscopie Raman sont ceux localisés au point  $\Gamma$ , cela permet de détecter des modes de phonon supplémentaires comme celui dont provient le pic P<sub>1</sub>. L'apparition du pic P<sub>1</sub> est donc bien liée à l'émergence d'un ordre antiferromagnétique.

Pour déterminer quantitativement la température de Néel de FePS<sub>3</sub> dans cet échantillon, nous calculons l'intensité intégrée du pic P<sub>1</sub> en fonction de la température (voir Fig. 13 c). Celle-ci est constante pour des températures inférieures à la température de transition de phase après laquelle l'intensité intégrée commence à croître. Cette augmentation peut être ajustée par un modèle de diffusion Raman dépendant du spin développé par Suzuki *et al.* en 1973 [30], nous permettant d'estimer une température de Néel d'environ 115 K pour cet échantillon.

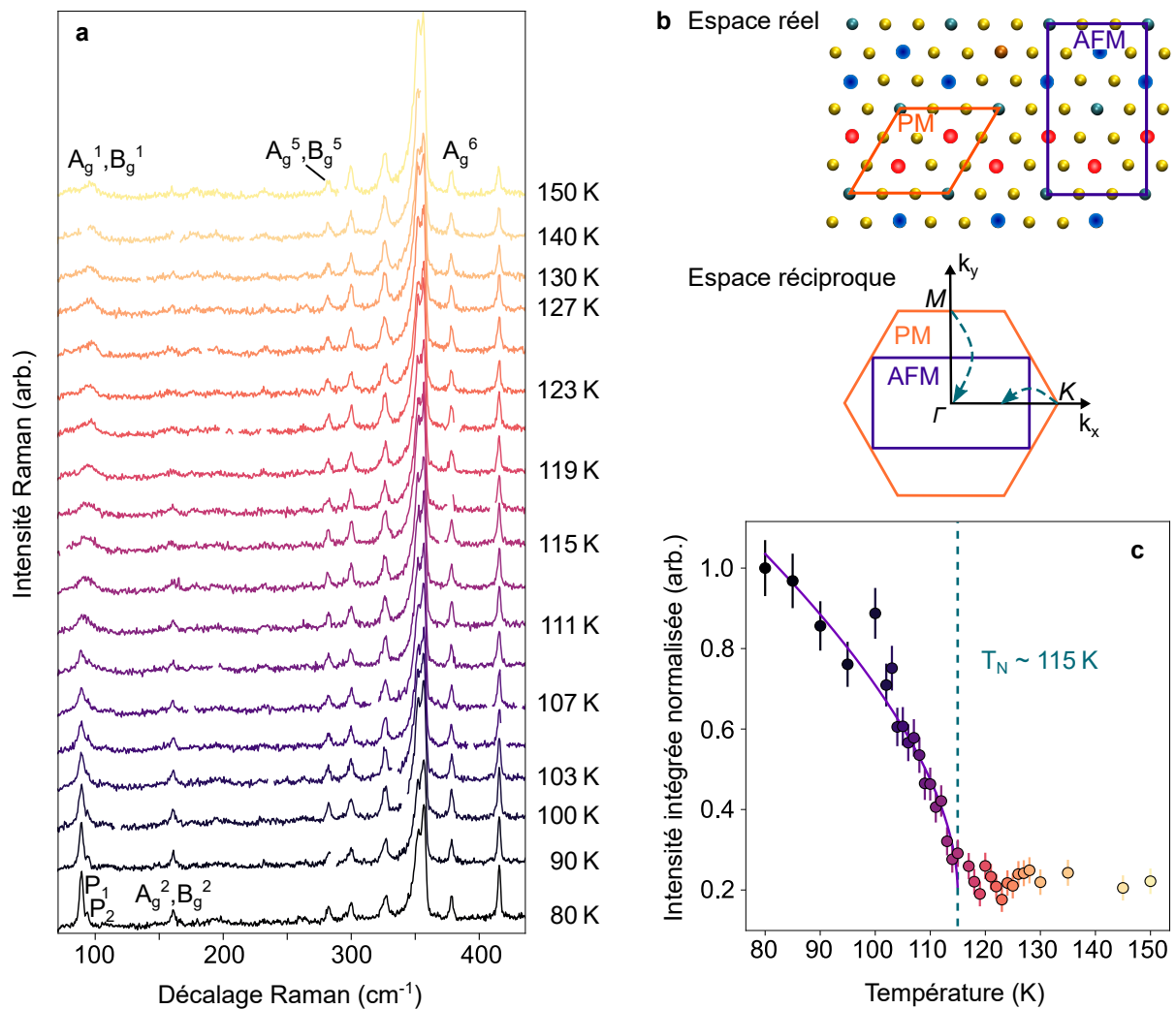


**Figure 13: Détection de la transition de phase magnétique de  $\text{FePS}_3$  par la spectroscopie Raman.** **a.** Spectres Raman d'une hétérostructure comprenant cinq couches de  $\text{FePS}_3$ , une monocouche de  $\text{WS}_2$ , une bicouche de graphène et une quinzaine de couches de nitrure de bore pour des températures comprises entre 80 et 150 K. Les pics avec un label proviennent de  $\text{FePS}_3$ , tandis que les pics sans label proviennent de  $\text{WS}_2$ . **b.** Schéma illustrant le concept de phonon de repliement de zone. Le panneau du haut montre la structure cristalline d'une couche de  $\text{FePS}_3$  vue de dessus avec en rouge les atomes de fer ayant un spin orienté vers le haut et en bleu ceux ayant un spin vers le bas. La maille élémentaire paramagnétique (PM) est tracée en orange tandis que celle antiferromagnétique (AFM) est tracée en violet. Le panneau du bas présente les zones de Brillouin correspondantes pour les phases paramagnétique (orange) et antiferromagnétique (violet) avec leurs points de symétrie. Les flèches de couleur cyan indiquent les directions de repliement de la zone de Brillouin paramagnétique lors de sa transition en la zone de Brillouin antiferromagnétique. **c.** Évolution de l'intensité intégrée normalisée du pic  $P_1$  en fonction de la température. Les points correspondent aux données et la ligne continue à un ajustement utilisant le modèle de Suzuki *et al.* [30] pour des températures inférieures à la température de Néel qui est ainsi estimée à 115 K.

## NiPS<sub>3</sub>

Nous considérons ensuite une homostructure suspendue de NiPS<sub>3</sub> d'environ 13 couches. Le spectre Raman de NiPS<sub>3</sub> ne contenant aucun phonon de repliement de zone dans la gamme de décalage Raman considérée, nous utilisons des mesures résolues en polarisation linéaire pour sonder la transition de phase magnétique.

La polarisation de la lumière incidente est fixée et la polarisation de collection est variée entre une configuration parallèle (co-polarisation  $\parallel$ ) et une configuration orthogonale (polarisation croisée  $\perp$ ) à la polarisation incidente. Les mesures co-polarisées permettent de sonder les modes de symétrie  $A_g$  uniquement, tandis que les mesures en polarisation croisée détectent uniquement les modes de symétrie  $B_g$  (voir Fig 15 a). Il est ainsi possible de détecter séparément les composantes  $A_g$  et  $B_g$  des modes dégénérés ( $A_g$ ,  $B_g$ ). Cela nous permet de mettre en évidence la levée de dégénérescence du mode ( $A_g^2$ ,  $B_g^2$ ) induite par l'émergence de l'ordre magnétique. En effet, l'ordre magnétique dans le plan de NiPS<sub>3</sub> n'affecte pas les modes  $A_g^2$  et  $B_g^2$  de la même manière (voir Fig. 14). Les deux modes n'ont donc plus la même fréquence dans la phase antiferromagnétique.

Nous observons effectivement que les fréquences de ces deux modes ont une évolution différente avec la température après la transition de phase magnétique qui semble se produire aux alentours de 150 K (voir Fig. 15 b). La modification de la fréquence d'un mode Raman induite par l'établissement d'un ordre magnétique a été modélisée par Baltensperger et Helman en 1968 et s'exprime comme [31, 32]

$$\Delta\omega_{\text{mag}} \propto (T_N - T)^{2\beta} \quad (11)$$

où  $\beta$  est un exposant critique. La contribution magnétique au décalage en fréquence du mode  $B_g^2$  est obtenue en soustrayant à l'évolution de sa fréquence avec la température celle d'un mode Raman de référence provenant du substrat. Un ajustement par le modèle de l'Équation (11) nous donne une température de Néel de 147 K et une valeur de l'exposant critique  $\beta$  de 0.37 (voir Fig. 15 c).

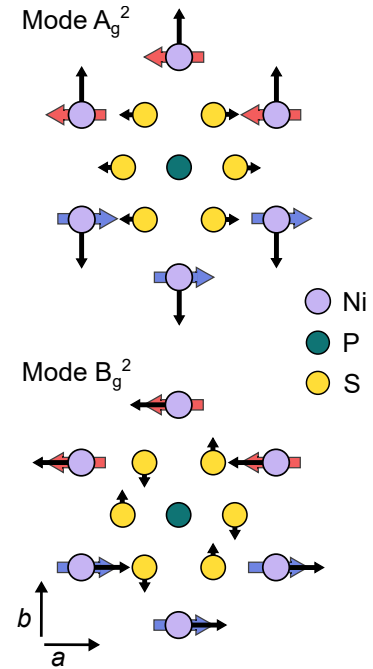


**Figure 14:** Schéma représentant les déplacements atomiques des modes de phonon  $A_g^2$  (haut) et  $B_g^2$  (bas) dans une maille cristalline de NiPS<sub>3</sub> vue du dessus. Les flèches noires indiquent le mouvement des atomes, tandis que les flèches rouges et bleues indiquent la direction des spins. Les déplacements atomiques sont extraits de [24].

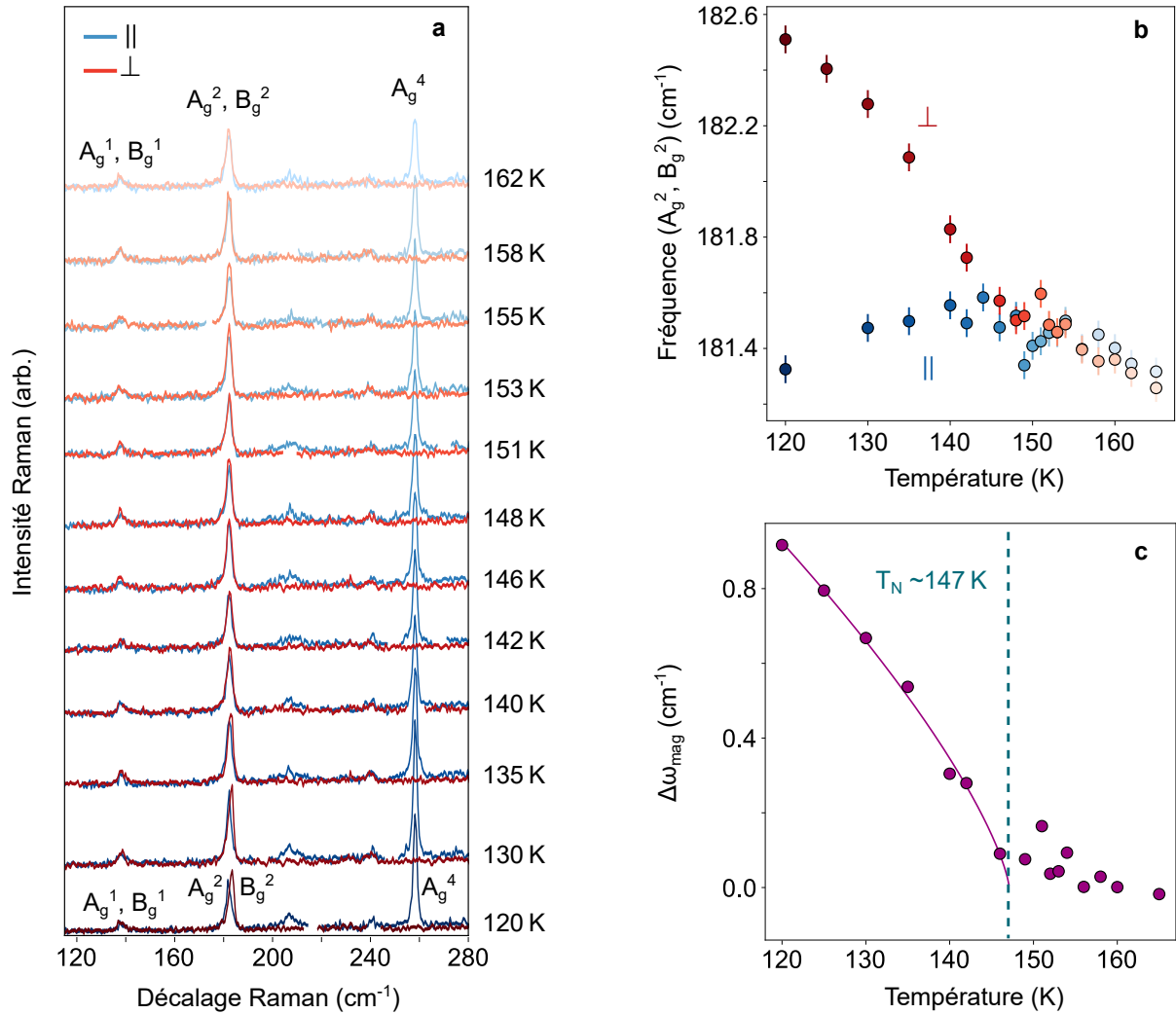


**Figure 15: Détection de la transition de phase magnétique de NiPS<sub>3</sub> par des mesures de spectroscopie Raman résolues en polarisation.** **a.** Spectres Raman d'une homostructure suspendue d'environ 13 couches de NiPS<sub>3</sub> pour des températures comprises entre 120 et 162 K en co-polarisation || (bleu) et en polarisation croisée ⊥ (rouge). **b.** Évolution de la fréquence des modes A<sub>g</sub><sup>2</sup> (points bleus) et B<sub>g</sub><sup>2</sup> (points rouges) en fonction de la température. **c.** Contribution magnétique au décalage en fréquence de B<sub>g</sub><sup>2</sup> en fonction de la température. La contribution magnétique est obtenue en soustrayant à l'évolution de B<sub>g</sub><sup>2</sup> avec la température celle d'un pic de référence provenant du substrat. La ligne continue est un ajustement par un modèle développé par Baltensperger *et al.* [31] prédisant le décalage en fréquence induit par l'ordre magnétique, résultant en une température de Néel d'environ 147 K.

## Vers le contrôle par la contrainte des propriétés mécaniques et magnétiques dans des homo- et hétérostructures suspendues

Dans cette partie, nous explorons comment la déformation de la membrane, induite par une tension de grille appliquée entre cette dernière et le substrat, affecte ses propriétés mécaniques et magnétiques. Nous analysons d'abord le cas d'une homostructure suspendue, avant d'explorer la nanomécanique d'une hétérostructure.

### Effets de la contrainte sur la nanomécanique d'une homostructure suspendue

#### Évolution des paramètres mécaniques de la membrane

Nous développons d'abord un modèle capacitif pour une membrane, considérée comme un conducteur parfait, afin de décrire qualitativement les effets d'une tension de grille sur ses propriétés mécaniques.

La membrane et le silicium au fond du substrat sont considérés comme les deux plaques d'un condensateur entre lesquelles est appliquée une tension de grille  $V_g$ , dont seulement la composante continue  $V_{DC}$  nous intéresse dans cette partie. Une force électrostatique  $F_{el}^{stat}$  dirigée vers le substrat est ainsi exercée sur la membrane induisant une déflexion  $\xi(r)$ . Pour des déflexions très faibles devant la profondeur du trou, la force électrostatique et la déflexion au centre de la membrane  $\xi_0$  dépendent de la tension appliquée comme

$$F_{el}^{stat} \propto \xi_0 \propto V_{DC}^2. \quad (12)$$

La contrainte induite est alors exprimée par

$$\varepsilon = \frac{2}{3} \left( \frac{\xi_0}{R} \right)^2 \propto V_{DC}^4 \quad (13)$$

avec  $R$  le rayon de la membrane.

Expérimentalement, nous pouvons étudier l'influence de la tension de grille sur les modes mécaniques de la membrane en suivant sa réponse mécanique forcée en fonction de  $V_{DC}$  (voir Fig. 16). Dans le cas d'une membrane suspendue de dix couches de NiPS<sub>3</sub>, nous observons d'abord une diminution de sa fréquence de résonance jusqu'à 24.7 V, ce qui correspond à une

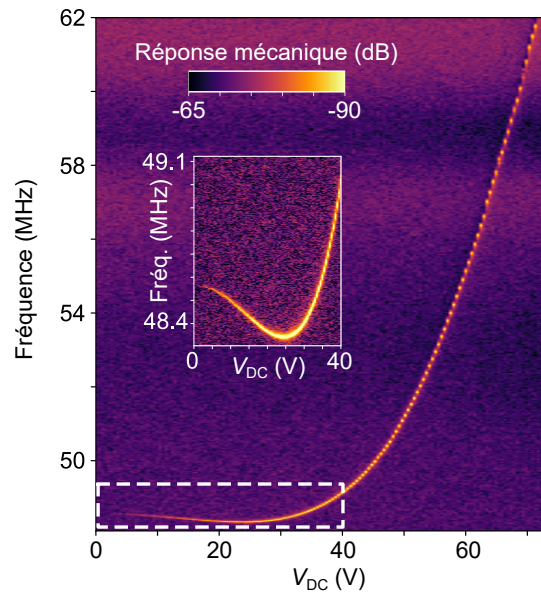


**Figure 16: Spectre de réponse mécanique d'une homostructure suspendue de dix couches de NiPS<sub>3</sub> en fonction de la tension de grille  $V_{DC}$  mesurée à 5.5 K. L'insert montre un zoom sur la région de basse tension indiquée par un rectangle en pointillés.**

relaxation de la contrainte initialement présente dans la membrane. Puis la fréquence augmente de façon quadratique traduisant un raidissement de la membrane. Ce comportement est celui attendu pour une membrane de matériau 2D suspendue [33]. En raison des approximations utilisées dans ce modèle, notamment le fait que la membrane est constituée d'un matériau conducteur alors que NiPS<sub>3</sub> est un semi-conducteur à grand gap, nous ne pouvons pas déduire de ces mesures des valeurs quantitatives pour la déflexion et la contrainte induites. Nous utiliserons pour cela un autre modèle basé sur la réflectance de la cavité.

### Estimation de la déflexion et de la contrainte induites

La réflectance de la cavité formée par la membrane et le silicium au fond du substrat peut-être modélisée en fonction la déflexion de la membrane (voir Fig. 17 b). Pour cela, nous considérons les matériaux présents dans la cavité comme des milieux d'indices optiques différents et calculons le coefficient de réflexion équivalent de cette structure.

Nous comparons cette réflectance calculée à l'évolution de la tension de sortie de la photodiode mesurée expérimentalement, qui est proportionnelle à l'intensité lumineuse réfléchie, pour une augmentation de la tension de grille de 75 V (voir Fig. 17 a). Une variation de la réflectance de 62 % en est déduite ce qui correspond à une déflexion  $\xi_0 \sim 111$  nm. En utilisant l'Équation (13), nous obtenons une contrainte d'environ 0.13 % pour une tension de grille de 75 V.

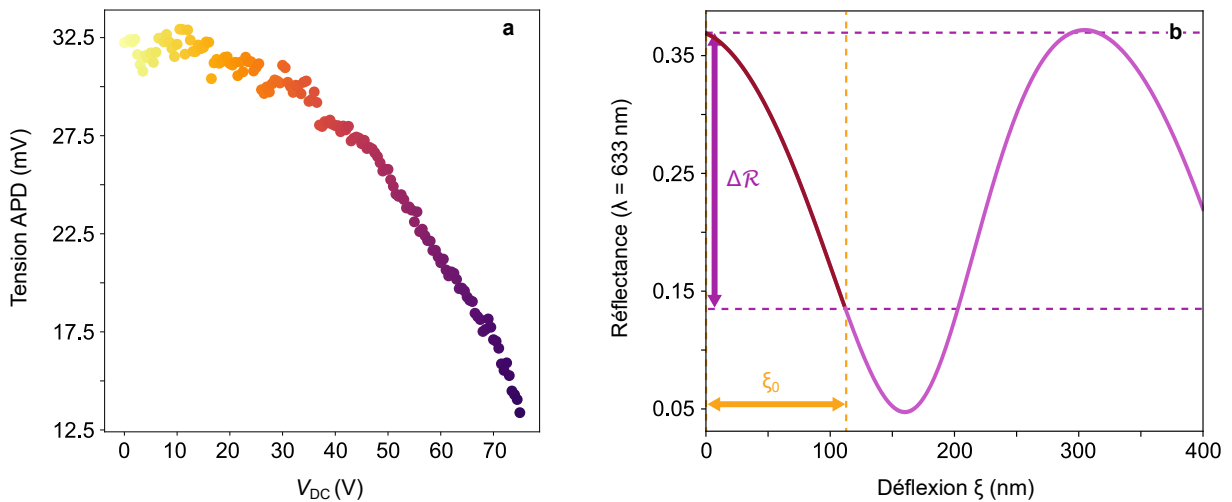


**Figure 17: Estimation de la variation de déflexion d'une membrane de dix couches de NiPS<sub>3</sub> pour une augmentation de la tension de grille de 75 V et une température de 5 K. a.** Diminution de la tension moyenne de sortie de la photodiode (APD) en fonction de l'augmentation de la tension de grille. **b.** Réflectance calculée  $\mathcal{R}$  en fonction de la déflexion de la membrane  $\xi$  pour dix couches de NiPS<sub>3</sub> séparées d'un substrat Si/SiO<sub>2</sub> par 400 nm de vide.  $\Delta \mathcal{R}$  est la variation de réflectance pour une rampe de tension de 0 à 75 V estimée en utilisant la variation du signal de sortie de la photodiode.  $\xi_0$  représente la variation de déflexion correspondante. La partie en rouge de la courbe est celle parcourue par la membrane pendant la rampe en tension.

## Influence de la contrainte sur la transition de phase magnétique de NiPS<sub>3</sub>

Précédemment, nous avons sondé la transition de phase magnétique de NiPS<sub>3</sub> par des mesures de nanomécanique pour une tension de grille donnée. Dans cette section, nous reproduisons le même protocole de mesure mais pour des tensions de grille plus élevées et donc une contrainte plus importante induite dans la membrane.

Nous constatons que le sommet du pic dans  $df_m^2/dT$ , indiquant la température de Néel, situé à 149.5 K pour une tension de grille de 18 V, se décale vers les températures plus basses pour atteindre environ 146.5 K à 40 V (voir Fig. 18). Nous observons ainsi une diminution de la température de Néel d'approximativement 3 K pour une augmentation de 22 V de la tension de grille, ce qui correspond à une contrainte d'environ 0.02 %. Cette constatation est en accord avec la théorie de Landau des transitions de phase [34], qui prédit qu'une contrainte induit, par des effets de magnétostriction, une augmentation ou une diminution de la température de Néel d'un matériau antiferromagnétique.

Pour des tensions de grille supérieures à 40 V une instabilité mécanique émerge, induisant des variations aléatoires de la fréquence de résonance de quelques dizaines de kHz, rendant impossible la détection de la transition de phase, comme on peut le constater à 50 V en Figure 18.

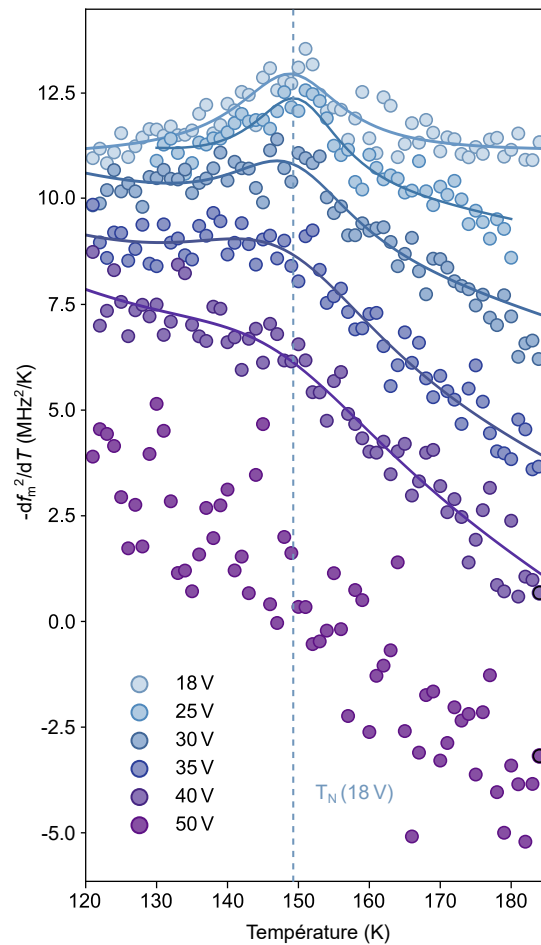


**Figure 18: Diminution de la température de Néel sondée par des mesures de nanomécanique sur une homostructure suspendue de 13 couches de NiPS<sub>3</sub> pour des tensions de grille de 18 à 50 V.** Opposé de la dérivée par rapport à la température de la fréquence de résonance au carré  $-df_m^2/dT$  en fonction de la température. Les points correspondent aux données expérimentales et les lignes continues à des guides pour les yeux. La ligne en pointillés indique la température de Néel à la tension de grille la plus faible (18 V).

## Nanomécanique d'une hétérostructure magnétique

Dans cette sous-partie nous explorons l'évolution des propriétés mécaniques en fonction de la tension de grille dans le cas de l'hétérostructure contenant cinq couches de FePS<sub>3</sub> encapsulées par une quinzaine de couches de nitrure de bore hexagonal, une monocouche de WS<sub>2</sub> et une bicouche de graphène.

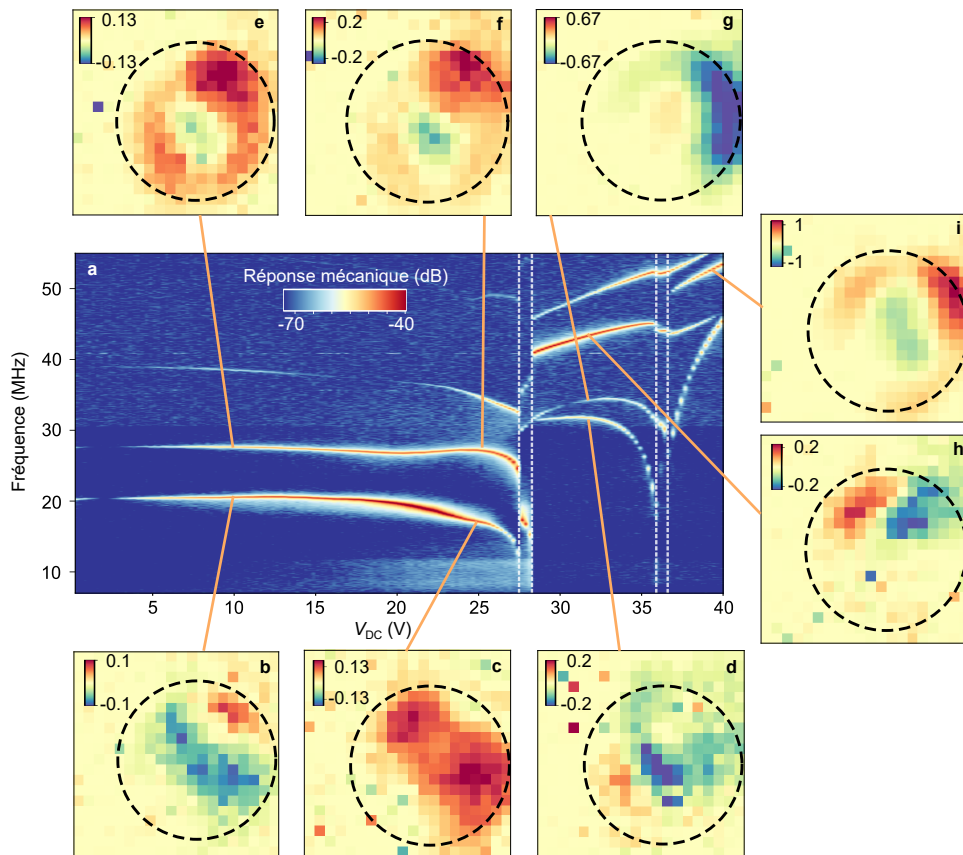


**Figure 19: Réponse mécanique et reconstruction des profils spatiaux des modes mécaniques en fonction de la tension de grille pour une hétérostructure contenant cinq couches de  $\text{FePS}_3$  à 130 K.** **a.** Réponse mécanique pour une augmentation de la tension de grille de 0 à 40 V. **b-d.** Reconstruction des profils spatiaux du mode de plus basse fréquence à 10 V, 25 V et 32 V. **e-g.** Reconstruction des profils spatiaux du deuxième mode ayant la fréquence la plus basse à 10 V, 25 V et 32 V. **h,i.** Reconstruction des profils spatiaux du troisième mode ayant la fréquence la plus basse à 32 V et 39 V. La quantité affichée est  $z[\Omega_m] \sin(\phi_{0,m})$  ce qui correspond à l'amplitude du mode normalisée par l'amplitude maximale, multipliée par le sinus de la phase à résonance. Les cercles en pointillés représentent la région suspendue qui mesure 5  $\mu\text{m}$  de diamètre.

Nous constatons que la réponse mécanique de ce résonateur en fonction de la tension de grille est très différente de celle observée pour une homostructure de  $\text{NiPS}_3$  (voir Figs. 16 et 19 a). Dans le cas de l'hétérostructure, pour une augmentation de la tension de grille, nous observons d'abord une diminution de la fréquence de résonance jusqu'à 27.4 V, ce qui traduit une importante pré-contrainte. Ensuite, deux régions présentant des discontinuités sont visibles autour de 28 et 36.2 V, associées à une modification drastique des profils spatiaux des modes mécaniques de la membrane (voir Fig. 19 b-i). Cette évolution avec la tension de grille est reproductible, notamment pour des tensions négatives. Dans le cas d'une diminution de la tension de grille de  $\pm 40$  à 0 V une hystérèse est présente entre 34.9 et 13.3 V, elle aussi reproductible.

Ces signatures sont vraisemblablement causées par l'empilement successif des quatre flocons de matériaux 2D d'épaisseurs différentes résultant en une importante pré-contrainte dans la membrane ainsi formée. Lors de l'application d'une tension de grille, et donc d'une force,

sur l'hétérostructure, la pré-contrainte peut être redistribuée, induisant une modification de la fréquence et de la forme des modes mécaniques. Ce rééquilibrage de la contrainte peut aller jusqu'à une délamination entre deux matériaux formant l'hétérostructure, comme cela a été montré par Sangani *et al.* [35] après l'observation de discontinuités similaires dans l'évolution de la fréquence de résonance avec la tension de grille d'une hétérostructure hBN/graphène.

## Analyse de la photoluminescence de NiPS<sub>3</sub> : contrôle par la contrainte et domaines magnétiques

### Introduction à la photoluminescence de NiPS<sub>3</sub>

L'émission de lumière d'un cristal de NiPS<sub>3</sub> a été mise en évidence pour la première fois en 2020 par Kang *et al.* [36] et apparaît à une énergie de 1.4771 eV ce qui correspond à une longueur d'onde de 840.0 nm (voir Fig. 20 a). La largeur du pic de photoluminescence, entre 500 et 300  $\mu$ eV, est plus faible que celle rencontrée dans d'autres matériaux de van der Waals comme les dichalcogénures de métaux de transition (TMD), impliquant une plus grande cohérence de l'émission.

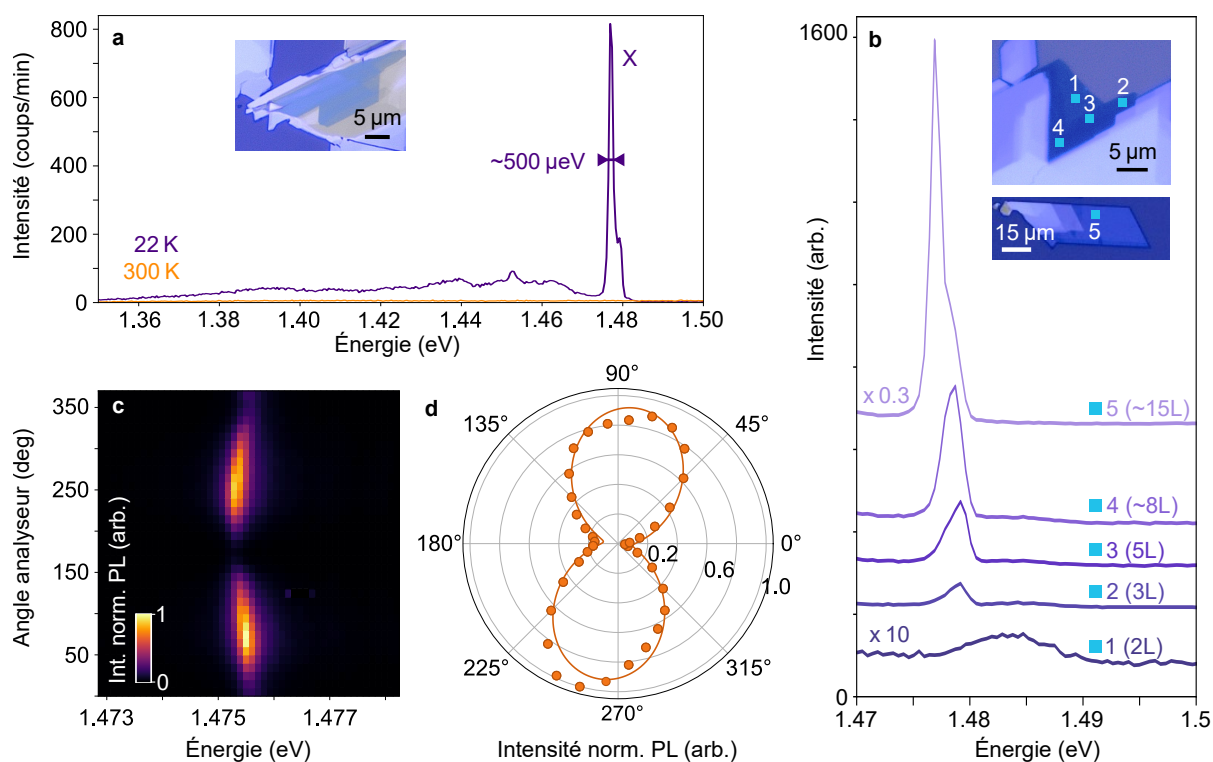


**Figure 20: Illustration des propriétés caractéristiques de la photoluminescence de NiPS<sub>3</sub>.** a. Spectres de photoluminescence mesurés à température ambiante (orange) et à 22 K (violet) sur un flocon supporté de NiPS<sub>3</sub> montré en insert. Le pic principal de photoluminescence (PL) est noté X. b. Evolution du pic principal de photoluminescence en fonction de l'épaisseur du flocon de NiPS<sub>3</sub> indiquée entre parenthèses. Les spectres ont été mesurés à différents endroits du même échantillon, indiqués par un carré bleu sur l'image en insert. Les spectres sont décalés verticalement par souci de clarté. c. Spectres de photoluminescence pour des angles de collection entre 0 et 360° mesurés sur un flocon de NiPS<sub>3</sub> de plusieurs centaines de nanomètres d'épaisseur à 5.5 K. d. Intensité normalisée de la photoluminescence en fonction de l'angle de l'analyseur. Les points correspondent aux données expérimentales et la ligne continue à un ajustement qui nous donne un angle de polarisation linéaire de 262.6° pour cet échantillon.

Plusieurs propriétés de la photoluminescence de NiPS<sub>3</sub> semblent indiquer une corrélation avec l'ordre antiferromagnétique : il a été observé que l'émission lumineuse apparaît progressivement

sous 120 K, c'est à dire dans la phase magnétique de NiPS<sub>3</sub>; de plus son intensité diminue pour des flocons plus fins que dix couches et disparaît complètement à la limite monocouche, pour laquelle la présence d'un ordre magnétique est toujours débattue [36, 37] (voir Fig. 20 b).

Il apparaît également que la photoluminescence de NiPS<sub>3</sub> est polarisée linéairement (voir Fig. 20 c,d), cette direction de polarisation a été récemment démontrée comme orthogonale à celle du vecteur de Néel [38–40], offrant la possibilité de remonter à la direction des spins dans un flocon de NiPS<sub>3</sub>.

Plusieurs hypothèses concernant l'origine de cette émission lumineuse ont été émises, notamment celle énoncée premièrement par Kang *et al.* d'un exciton dit de "Zhang-Rice" qui correspond à une transition d'un état triplet vers un état singlet de l'atome de nickel et de ses ligands soufrés [36]. Une autre possibilité est celle de transitions entre orbitales *d* internes à l'atome de nickel [41, 42]. Enfin, une étude plus récente suggère que l'émission lumineuse pourrait provenir de défauts structurels, en l'occurrence d'atomes de soufre manquants [38]. Toutes parviennent à expliquer une partie des propriétés de la photoluminescence de NiPS<sub>3</sub> mais aucune n'en justifie la totalité, invitant à des investigations supplémentaires sur ce matériau.

Dans un premier temps, nous étudions l'effet de l'application d'une contrainte sur la photoluminescence de NiPS<sub>3</sub>, puis nous nous intéressons à ses propriétés de polarisation, notamment résolues spatialement, dans le but d'imager d'éventuels domaines magnétiques.

### **Effet de la contrainte sur le pic principal de photoluminescence pour un faible nombre de couches de NiPS<sub>3</sub>**

Pour étudier l'évolution de l'émission de lumière de NiPS<sub>3</sub> avec la contrainte, nous appliquons une tension de grille variant entre 0 et 80 V entre la membrane et le fond du substrat. Nous comparons les résultats obtenus sur un nano-tambour, à ceux obtenus sur une partie du flocon qui est supportée (voir insert de la Figure 21 b).

Dans le cas de la région suspendue, nous constatons une diminution de l'intensité et de l'énergie de la photoluminescence lors d'une augmentation de la tension de grille (voir Fig. 21 a). Cet effet étant absent dans la région supportée, cela indique qu'il est vraisemblablement dû à la contrainte induite par la tension de grille.

La diminution d'énergie de la photoluminescence peut être ajustée par une fonction proportionnelle à la tension de grille à la puissance quatre (voir Fig. 21 b), ce qui correspond à la même dépendance en la tension de grille que celle de la contrainte. Nous en déduisons que la diminution d'énergie est proportionnelle à la contrainte appliquée avec un décalage de 1 meV/%. D'autre part, la diminution de l'intensité est ajustée par une fonction proportionnelle à la tension de grille au carré (voir Fig. 21 c) et est donc proportionnelle à la déflexion de la membrane induite par la tension de grille. Nous observons également un élargissement du pic de photoluminescence à partir de 60 V, probablement en raison d'une contrainte inhomogène dans la région illuminée par le laser (voir Fig. 21 d).

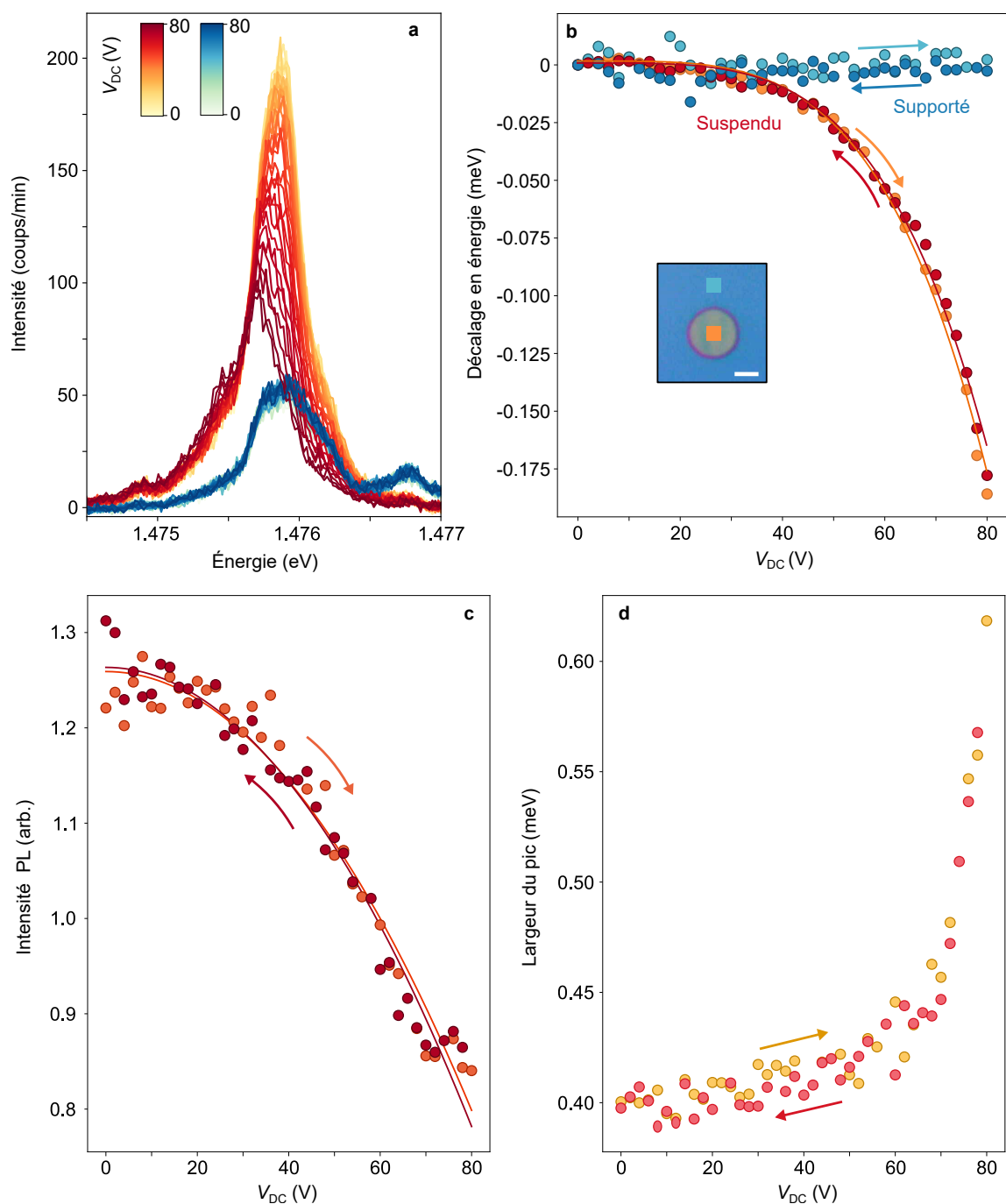


**Figure 21: Modifications des propriétés de la photoluminescence induites par une variation de la tension de grille pour une homostructure suspendue de dix couches de NiPS<sub>3</sub>.** **a.** Spectres du pic principal de photoluminescence obtenus pour des tensions de grilles comprises entre 0 et 80 V. Les spectres dont les couleurs vont du jaune au rouge sont mesurés sur une région suspendue de l'échantillon, tandis que les spectres dont les couleurs vont du vert au bleu sont mesurés sur une région supportée. **b.** Décalage en énergie de la photoluminescence en fonction d'une augmentation et d'une diminution de la tension de grille  $V_{DC}$  dans une région suspendue (orange/rouge) et une région supportée (bleu clair/bleu foncé). Les points sont les données expérimentales et les lignes continues un ajustement proportionnel à  $V_{DC}^4$ . En insert est montrée une image optique du nano-tambour considéré avec des carrés indiquant les points de mesure, la barre d'échelle est de 2.5  $\mu\text{m}$ . **c.** Intensité du pic de photoluminescence en fonction d'une tension de grille croissante (rouge clair) et décroissante (rouge foncé). Les lignes continues sont un ajustement proportionnel à  $V_{DC}^2$ . **d.** Largeur du pic de photoluminescence en fonction d'une tension de grille croissante (jaune) et décroissante (corail).

Des cartes de la photoluminescence de NiPS<sub>3</sub> ont également été réalisées à 0 et 75 V afin de résoudre l'étendue spatiale des modifications observées avec l'augmentation de la tension de grille. En effectuant la soustraction de ces deux cartes pour l'intensité intégrée, l'énergie et la largeur du pic, nous observons que les variations sont localisées sur la région suspendue (voir Fig. 22 pour le cas de l'énergie).

L'ensemble de ces éléments nous permet de conclure que la déformation mécanique de la membrane induite par la tension de grille permet de modifier et contrôler l'énergie et l'intensité de la photoluminescence de NiPS<sub>3</sub>.

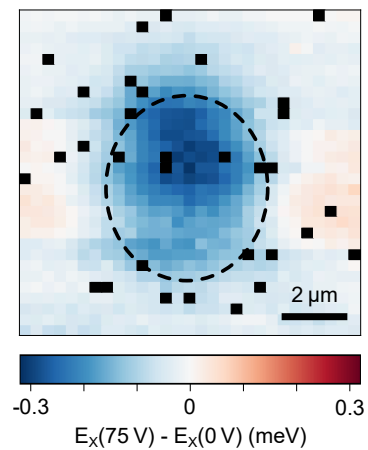


**Figure 22: Carte de la différence en énergie du pic X de photoluminescence entre 75 et 0 V.** Le cercle en pointillés représente la région suspendue. Les pixels noirs correspondent à des spectres rendus inutilisables par des pics provenant de rayons cosmiques.

## Dépendance en polarisation et visualisation de domaines magnétiques

Dans la première partie de ce résumé, nous avons vu que dans un cristal massif de NiPS<sub>3</sub> les spins sont orientés préférentiellement le long de l'axe cristallin  $a$  suite à la brisure de symétrie dans la direction hors du plan causée par l'empilement monoclinique (voir Fig. 3 c). La photoluminescence étant polarisée linéairement selon un axe orthogonal aux spins, sa direction préférentielle de polarisation est l'axe cristallin  $b$ . Cependant, pour des flocons possédant un nombre plus faible de couches (à partir d'environ dix couches [43]), l'effet de l'empilement monoclinique est réduit et trois directions d'orientation des spins coexistent à 60° l'une de l'autre (voir Fig. 23), induisant la présence de domaines magnétiques qui ont été mis en évidence pour la première fois en 2024 [43–45]. Trois orientations sont donc également possibles pour la polarisation de la photoluminescence, dont la détermination permet de remonter à l'orientation des spins dans la région sondée et donc d'imager ces domaines magnétiques.

Pour cela, nous réalisons trois cartes de photoluminescence, avec des angles de collection espacés de 60° afin de couvrir les trois directions possibles des chaînes de spin, d'un échantillon de NiPS<sub>3</sub> d'environ dix couches (voir Fig. 24).

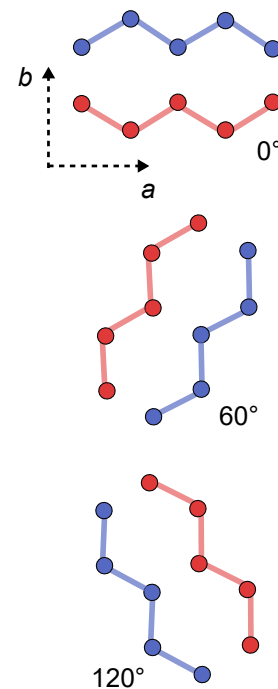


**Figure 23: Schéma des trois orientations possibles des chaînes de spin dans NiPS<sub>3</sub>.**

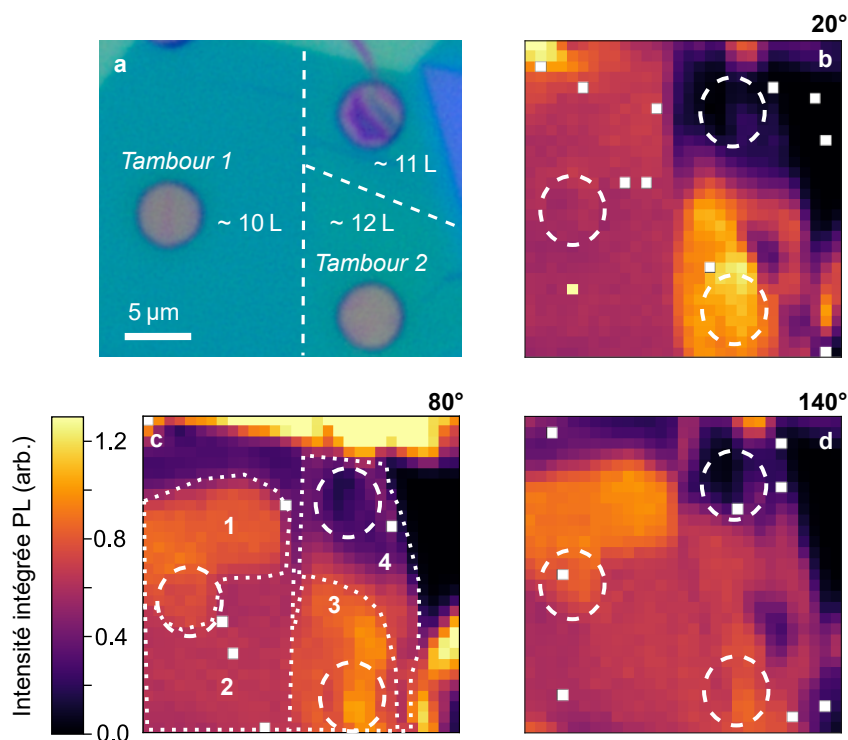


**Figure 24: Cartes de l'intensité intégrée de la photoluminescence d'un échantillon de  $\text{NiPS}_3$  pour des angles de collection espacés de  $60^\circ$ .** **a.** Image optique de la zone cartographiée présentant trois épaisseurs différentes (de 10 à 12 couches) et deux régions suspendues (*Tambour 1* et *Tambour 2*). **b-d.** Cartes d'intensité intégrée de la photoluminescence pour des angles de collection de  $20^\circ$ ,  $80^\circ$  et  $140^\circ$ , respectivement. Les cercles en pointillés correspondent aux nano-tambours d'un diamètre de  $5 \mu\text{m}$ . Sur la carte **c** quatre régions globalement homogènes sont délimitées et numérotées.

Quatre régions possédant une dépendance différente en l'angle de collection, et donc une polarisation différente, sont identifiées. Les régions **3** et **4** peuvent être attribuées à des régions de l'échantillon n'ayant pas le même nombre de couches ce qui pourrait expliquer que leurs chaînes de spin n'aient pas la même orientation. Alors que les régions **1** et **2** sont localisées sur une même partie du flocon possédant dix couches et peuvent donc être vues comme deux domaines antiferromagnétiques distincts.

Nous nous focalisons sur les régions **1** et **3**, où la photoluminescence semble présenter une direction de polarisation bien définie, pour y déterminer l'orientation des chaînes de spin. Des mesures de photoluminescence en fonction de l'angle de collection sont mises en relation avec des mesures de la polarisation des modes Raman  $A_g^2$  et  $B_g^2$ , utilisés précédemment pour sonder la transition de phase magnétique et donc sensibles à l'ordre magnétique (voir Fig. 25). Nous constatons que la direction de la polarisation de la photoluminescence est la même que la direction de polarisation du mode  $B_g^2$  et orthogonale à celle du mode  $A_g^2$ , ce qui nous permet de déterminer une orientation des spins à environ  $37^\circ$  pour la région **1** et  $118^\circ$  pour la région **3**. Nous remarquons que l'angle entre ces deux domaines est de  $81^\circ$ , ce qui est loin des  $60^\circ$  attendus et invite à des études plus approfondies sur d'autres échantillons.

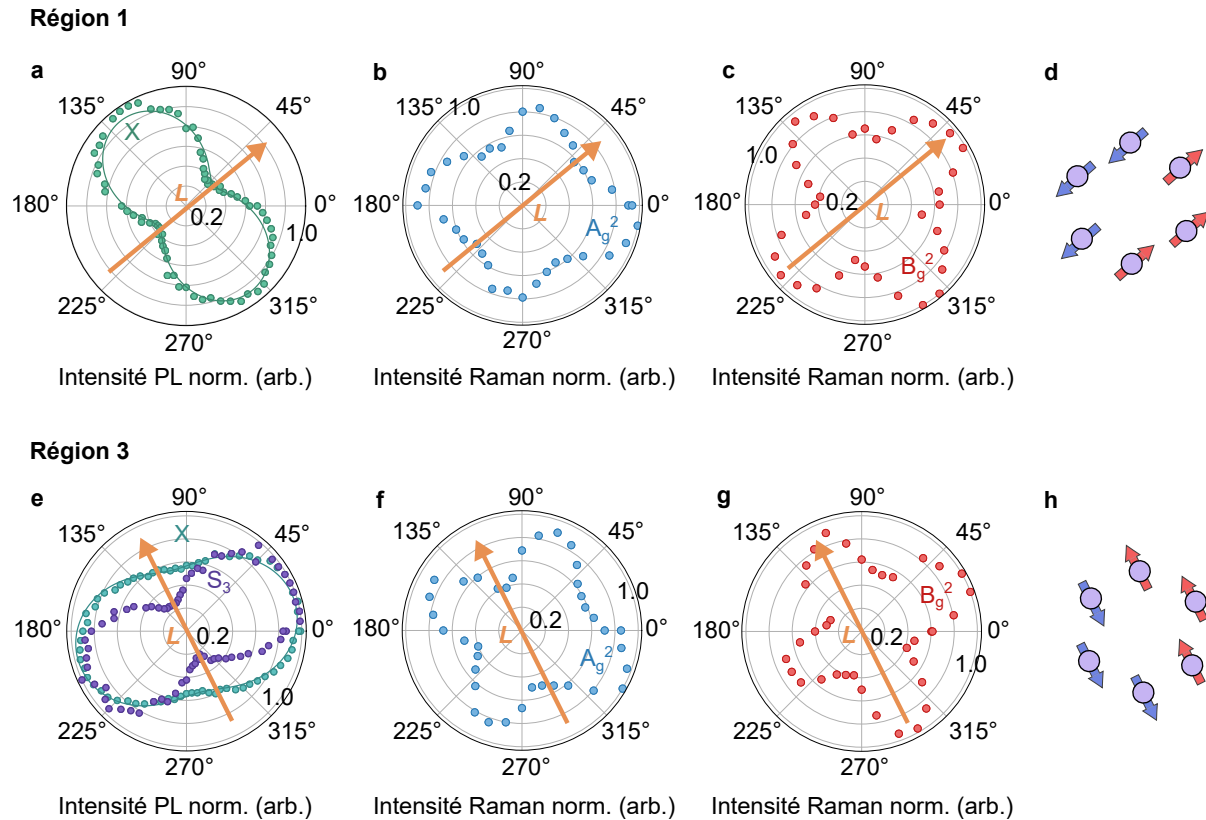


**Figure 25: Détermination de l'orientation des chaînes de spin dans deux des régions présentées en Figure 24 en combinant spectroscopie Raman et photoluminescence.** a,e. Intensité normalisée en fonction de l'angle de collection pour le pic principal de photoluminescence X et pour le pic secondaire  $S_3$ , respectivement. b, f. Intensité normalisée du mode Raman  $A_g^2$  en fonction de l'angle de collection et de l'angle incident qui sont égaux et variés simultanément. c, g. Intensité normalisée du mode Raman  $B_g^2$  en fonction de l'angle de collection et de l'angle incident qui sont égaux et variés simultanément. d, h. Schéma d'une cellule hexagonale d'atomes de nickel dans  $NiPS_3$ , illustrant l'orientation des spins dans la région de l'échantillon correspondante. Les flèches oranges représentent la direction du vecteur de Néel  $L$ , déterminée en comparant la polarisation de la photoluminescence avec celle des modes Raman.

## Conclusion

Durant ce travail de thèse, nous avons étudié des nano-résonateurs composés de matériaux magnétiques de van der Waals, à savoir  $\text{FePS}_3$  et  $\text{NiPS}_3$ , à faible nombre de couches, sous forme d'homo- ou d'hétérostructures, suspendus au dessus de trous micrométriques. Cette plateforme polyvalente nous a permis de sonder optiquement les interactions entre leurs degrés de liberté mécaniques et magnétiques.

Dans une première partie, nous avons démontré notre capacité à nano-fabriquer des échantillons suspendus à bas nombre de couches à partir de matériaux de van der Waals magnétiques. Une hétérostructure suspendue élaborée, composée de quatre matériaux différents, a été réalisée, notamment grâce à une station de transfert motorisée fabriquée au laboratoire.

Dans une deuxième partie, nous avons effectué la détection de transitions de phase magnétiques dans des échantillons suspendus de matériaux de van der Waals magnétiques. La clé de ce succès a été la correction automatique de la dérive spatiale induite durant les rampes en température, ce qui nous a permis d'effectuer des mesures autonomes durant plusieurs jours. Nous avons d'abord sondé la transition de phase magnétique d'un flocon de cinq couches de  $\text{FePS}_3$  inclus dans une hétérostructure en combinant deux méthodes, l'une basée sur la spectroscopie Raman et l'autre sur des mesures de nanomécanique, développées précédemment séparément sur  $\text{FePS}_3$  seul. Ensuite nous avons démontré la détection de la transition de phase magnétique de deux échantillons suspendus de  $\text{NiPS}_3$  de dix et treize couches par des mesures de nanomécanique. La transition de phase magnétique a été confirmée par spectroscopie Raman sur les mêmes échantillons. Les températures de Néel obtenues par ces deux approches sont en bon accord pour les deux matériaux étudiés, prouvant la fiabilité de ces méthodes pour sonder la transition de phase magnétique de matériaux de van der Waals magnétiques suspendus.

Dans une troisième partie, nous avons présenté nos résultats en vue du contrôle par la contrainte des propriétés magnétiques de matériaux de van der Waals magnétiques suspendus. En induisant une contrainte estimée aux alentours de 0.02 %, nous avons observé une diminution d'environ 3 K de la température de Néel sondée par des mesures de nanomécanique.

Nous avons également documenté les effets d'une augmentation de la force électrostatique appliquée à l'hétérostructure contenant  $\text{FePS}_3$  via une tension de grille continue. Nous avons constaté des discontinuités abruptes dans l'évolution de la fréquence de résonance de la membrane avec la tension de grille, concomitantes avec une modification drastique des profils spatiaux des modes mécaniques. Nous en avons conclu que ces caractéristiques pouvaient provenir soit d'une redistribution d'une importante pré-contrainte, pouvant induire une délamination de deux couches composant l'hétérostructure, lors de l'augmentation de la tension de grille.

Dans une quatrième et dernière partie, nous avons exploré l'émission de lumière de  $\text{NiPS}_3$  qui a été démontrée comme corrélée à l'ordre magnétique [38, 39, 46]. Nous avons établi un décalage de l'énergie de la photoluminescence de 1 meV/% dû à la contrainte induite par une tension de grille.

D'autre part, nous avons imagé des domaines magnétique dans un échantillon de dix couches de NiPS<sub>3</sub> en utilisant l'orthogonalité entre la direction de polarisation de la photoluminescence et celle de l'ordre magnétique. Les orientations de deux de ces domaines ont été confirmées par des mesures de spectroscopie Raman résolues en polarisation. Enfin, nous avons également observé des pics secondaires dans le spectre de photoluminescence dont le comportement en fonction de la contrainte et de la position diffère de celui du pic principal. L'ensemble de ces observations pourrait permettre d'apporter un nouvel éclairage sur les origines de la photoluminescence de NiPS<sub>3</sub> qui sont encore soumises à débat.

Dans le cadre de ce travail de thèse, nous avons réussi à sonder les propriétés magnétiques, et ouvert la voie vers leur contrôle, dans des nano-résonateurs de matériaux de van der Waals magnétiques. Il reste encore de nombreuses directions à explorer et de degrés de libertés à exploiter dans ces systèmes très riches, notamment en se rapprochant de leur limite bidimensionnelle.

Nous avons également commencé à explorer d'autres axes de recherche prometteurs liés à ce sujet. Des mesures préliminaires ont été effectuées sur une hétérostructure suspendue comprenant NiPS<sub>3</sub> et du graphène épais de quelques couches servant de contact électrique, dans le but d'augmenter la contrainte induite par la tension de grille et d'utiliser les modes Raman du graphène comme jauge de contrainte. Nous avons également acquis et installé un nouveau cryostat incluant un aimant supraconducteur de 7 T qui nous permettra prochainement de réaliser des mesures sous champ. D'autre part nous travaillons toujours à améliorer la détection de la transition de phase magnétique en implémentant la méthode dite de "friction froide" utilisée en optomécanique [47–49], ce qui nous permet de diminuer l'amortissement effectif du mode mécanique du résonateur. Enfin, à plus long terme, nous visons à explorer les effets de proximité magnétique entre les matériaux de van der Waals magnétiques et des monocouches de dichalcogénures de métaux de transition [50, 51] et d'explorer leur contrôle par la contrainte.



---

# Introduction

---

## General introduction

### Historical breakthroughs in magnetism

Magnetism is a property of matter that has sparked curiosity for ages, already in 800 B.C. the Greeks were investigating the attraction of iron and steel by lodestone ( $\text{Fe}_3\text{O}_4$ ) that was mined in Magnesia, a city in minor Asia, that is said to have given the material its name "magnet" [1]. The route towards the comprehension of magnetism led to several technological breakthroughs, the first of them being the invention of the compass, heading to the exploration and mapping of the oceans during the xv<sup>th</sup> century.

In 1820, the Danish scientist Hans Christian Oersted demonstrated publicly the deviation of a magnetic needle by the current flowing in a copper wire, implying that this current was creating a magnetic field, that was the sparkle for the electromagnetic revolution [52]. The first iron-cored electromagnet was built in 1825 by William Sturgeon, and six years later, the electromagnetic induction (the creation of an electric current by a varying magnetic field) was discovered by Michael Faraday. Subsequently, in 1832, the principle of an electrical generator was demonstrated by André-Marie Ampère and the instrument maker Hypolyte Pixii, but it was not until 1854 that an industrial DC generator was produced by Siemens brother's workshop. To complete these breakthroughs, the building of the first system of electric distribution in New York by Thomas Edison in 1882, added to Nikola Tesla's AC system that enabled long-range transmission at high voltages led to electricity distribution and electrification of the communications [53].

On a more fundamental point of view, Faraday realized pioneering experiments culminating in the classification of magnetic materials into ferromagnetic (that are easily magnetized and drawn towards a magnetic field), paramagnetic (that are more weakly attracted by the field) and diamagnetic (that are repelled by the field) as well as introducing the idea of lines of force underlying the concept of electric and magnetic fields [54]. This work greatly inspired James Clerk Maxwell to establish his well-known equations in 1865, defining the relation between electric and magnetic fields through the distributions of electric charge and current densities in surrounding space [55]. A key consequence of these equations being the existence of electromagnetic waves traveling at the speed of light  $c$  in the vacuum. Later, in 1895, Pierre Curie established his law

---

for paramagnetism and demonstrated that ferromagnets undergo a phase transition, becoming paramagnets, above a given temperature named after him the Curie temperature  $T_c$ . Pierre Weiss, by extending Langevin's theory of paramagnetism to ferromagnetism and postulating a "molecular field", was able, twelve years later, to obtain an expression of the Curie temperature below which a spontaneous magnetization appears [56].

It was only with the advent of quantum mechanics and relativity that the fundamental understanding of magnetism in condensed matter was made possible. The first step was, in 1915, the demonstration by Albert Einstein and Wander Johannes de Haas that the magnetization inversion of a ferromagnetic cylinder makes it rotate, confirming the proportionality between magnetic and angular momenta (see Fig. 26 a-d) [57]. The angular momentum quantization was then established in 1922 by Otto Stern and Walter Gerlach. In their experiment, two distinct spots are formed when deflecting a beam of silver atoms by a non-uniform magnetic field as seen in Figure 26 e, accounting for two discrete possible states, unlike the continuum expected in classical physics, confirming the Bohr-Sommerfeld model [58]. The efforts of Georges Uhlenbeck and Samuel A. Goudmsit in understanding the fine structure of the hydrogen atom spectrum led them, in 1925, to the discovery of spin angular momentum, a new electronic degree of freedom, which can only take the values  $\pm \frac{\hbar}{2}$ , with  $\hbar$  the reduced Planck constant [2, 3]. They were then able to explain the Zeeman effect by attributing the value of a Bohr magneton  $\mu_B = \frac{e\hbar}{2m_e} = 9.274 \times 10^{-24} \text{ A.m}^2$ , with  $e$  and  $m_e$  the electronic charge and mass, to the electron magnetic momentum from which originates the magnetic properties of solids. The spin theoretical confirmation had to await 1928 and the rewriting of Schrödinger equation in a relativistically invariant form by Paul Dirac, predicting the electron spin in term of the spinor matrices  $2 \times 2$  proposed by Wolfgang Pauli the year before [59, 60]. In 1929, taking into account the electrons indistinguishability and Pauli exclusion principle, Werner Heisenberg and Dirac modeled the magnetic interaction between two spin vectors  $\mathbf{S}_i$  and  $\mathbf{S}_j$  by the exchange Hamiltonian  $-2J\mathbf{S}_i \cdot \mathbf{S}_j$ , where  $J$  is the exchange constant [61, 62]. Using this Hamiltonian, Felix Bloch and John C. Slater described spin waves as being the elementary excitations of an array of atoms coupled by the exchange interaction a year later [63, 64].

Nevertheless, the following technological breakthroughs did not arise from this fundamental understanding, but from more phenomenological considerations. In 1932, starting from the model proposed by Weiss in 1907, Louis Néel put forward the idea of antiferromagnetism, in which the magnetic moments are arranged in two anti-aligned sublattices, to describe the magnetic properties of some alloys [4]. Later, in 1948, he investigated ferrites like lodestone, which led him to derive ferrimagnetism, where the two sublattices are not fully compensated [66]. Ferrites have proven to have a significant impact on technological advances, for example, Ni-Zn ferrites contributed to the development of radio communications, Mg ferrites were used in early computer memories or  $\text{BaFe}_{12}\text{O}_{19}$  which was the first permanent magnet that could be manufactured into any desired shape without self-demagnetization and is used in small DC motors [53]. Another crucial idea to the growth of magnetic technologies is that of magnetic domains. Postulated by

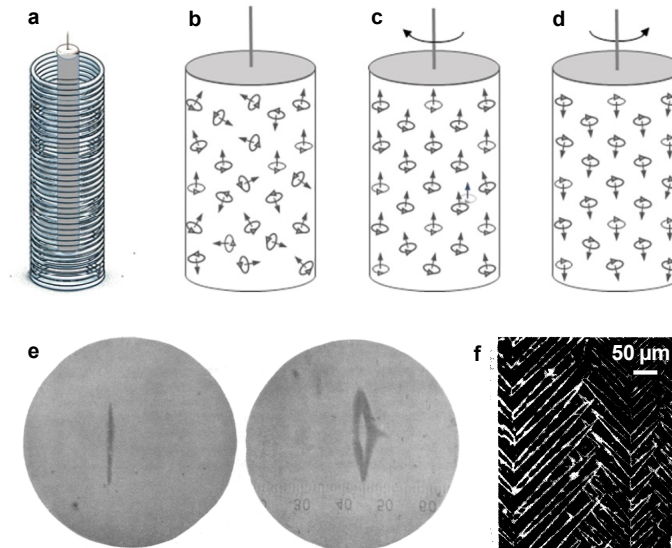


**Figure 26: Illustrations of groundbreaking experiments in magnetism history.** **a.** Scheme of the Einstein-de Haas experiment, displaying a magnetic rod used as a torsion pendulum. **b-d.** Principle of the Einstein-de Haas experiment. **b.** Without magnetic field the magnetic moments are randomly oriented. **c.** A magnetic field is applied in one direction, aligning the magnetic moments and making the cylinder rotates to conserve angular momentum. **d.** The direction of the magnetic field is reversed making the cylinder rotates in the opposite direction. Adapted from [65]. **e.** Pictures of the Stern-Gerlach experiment results without (left) and with (right) magnetic field. Adapted from [58]. **f.** Picture of the powder patterns representing the magnetic domains observed by Williams and co-authors. Adapted from [5].

Weiss in 1907, these are regions of a magnetic material in which all the magnetic moments are oriented in the same direction. Between them, the magnetization rotates continuously forming domain walls, a concept introduced by Bloch in 1932 [67]. The magnetic domains of a material were directly observed for the first time in 1949 by H. J. Williams and co-authors using a liquid suspension of magnetite colloidal particles applied on the polished surface of iron containing 3.8 % in mass of silicon [5]. They were able to observe a "powder pattern" formed by the magnetite particles gathered along the domain walls (see Fig. 26 f). The hysteresis cycle of magnetic materials could then be interpreted in terms of motion and rotation of domain walls.

Another significant breakthrough was magnetic recording, that was first developed to record audio on plastic tape recovered with a flexible magnetic layer during World War II, before becoming accessible to the consumers in the form of audio cassette around 1963. Later on, the digital recording on hard disk experienced rapid progress with the advent of magnetic thin films stacking, resulting in an increase by a factor  $10^8$  of the recorded information density between the introduction of the first hard drive in 1956 and 2008 [6]. This quest of space optimization led to increasingly advanced miniaturization of magnetic components, raising the question of what happen to magnetic properties of objects with reduced dimensionality.

---

## Magnetism and dimensionality

The model proposed by Wilhelm Lenz and Ernst Ising in 1925 was the first to put forward the crucial role of dimensionality in relation to the existence of a magnetic order in materials. Their objective was to explain experimental results on paramagnetism and ferromagnetism, notably those obtained by Curie. As did Weiss, they applied statistical mechanics to elementary magnets on a lattice, but Lenz proposed to consider only two possible orientations for their magnetic moments, one at  $0^\circ$  and the other at  $180^\circ$  [68]. Ising added to it the idea of a force vanishing quickly with the distance between the micromagnets, so he could take into account only the nearest neighbors interactions. Under those assumptions, he made the calculations for a linear chain of elementary magnets, a one-dimensional system, and obtained the Curie law in the paramagnetic case. In addition, he demonstrated that the system displayed no spontaneous magnetization, i.e. no ferromagnetic order. He concluded that these results were also valid in the two- and three-dimensional cases and thus, that the model was not able to describe properly ferromagnetism [69, 70]. Nevertheless, the Lenz-Ising model has not been totally forgotten, despite being regarded as unrealistic compared to the Heisenberg model, which takes into account the electron spin angular momentum. Indeed, in 1941, Hendrick A. Kramers and Gregory H. Wannier carried an exact derivation of the two-dimensional Lenz-Ising model by the means of transfer matrices, establishing an expression for the Curie temperature, but were not able to prove the existence of the Curie point [71]. A more complete solution to the model was developed in 1944 by Lars Onsager, who derived the evolution of the specific heat as a function of the temperature and found that it goes to infinity at the Curie point, with an expression of the Curie temperature in accordance with the one found previously by Kramers and Wannier [7]. This result confirmed the existence of a ferromagnetic order for the two-dimensional Lenz-Ising model without a magnetic field and contributed greatly to relaunch its popularity in the scientific community.

Concerning the isotropic Heisenberg model, in 1966, N. David Mermin and Herbert Wagner applied to ferro- and antiferromagnetism Pierre Hohenberg's idea of using a Bogoliubov inequality to rule-out long-range order like superfluidity or superconductivity in one- and two-dimensional systems [72]. In this way, they proved the absence of spontaneous magnetization, or sublattice magnetization, in a one- or two-dimensional isotropic Heisenberg model with finite range interactions at a temperature  $T$  [8]. This theorem was mainly understood as the impossibility of a magnetic order existence in one and two dimensions in general, forgetting about the Ising case, considered as a theoretical simplification [73].

Another model that raised interest was the XY model, in which the spins are free to rotate within a plane and can be considered as a two-dimensional Heisenberg model. In 1971, Vadim Berezinskii showed that, despite the destruction of long range magnetic order by spin-wave excitations in a two-dimensional lattice within this model, a phase transition must occur. To achieve this result, he took into account topological defects that he described as spin "fluctuation deflections" taking the form of vortices [74]. The description of this topological phase transition was completed two

years later by John M. Kosterlitz and David T. Thouless, giving it the name "BKT" transition. They depicted it as the dislocation of bound pairs of vortices into free vortices above the transition temperature  $T_{\text{BKT}}$  (see Fig. 27 a), resulting in an abrupt change in the magnetic susceptibility of the system [9]. In their paper, topological phase transitions were also predicted in the case of two-dimensional crystals and superfluids, and indeed, the first validation of Kosterlitz and Thouless picture came in 1978 from experiments performed on the superfluid transition of two-dimensional helium films [75].

At that period, similarities were observed between the critical point behavior of phase transitions in various systems such as fluids, magnets, alloys or ferroelectrics, giving rise to a common description based on critical exponents [76, 77]. These exponents characterize the asymptotic evolution of the order parameter, or other relevant quantities like the susceptibility or the specific heat, when approaching a critical point. In the case of the ferromagnetic transition, the order parameter is the spontaneous magnetization  $M_s$  and the critical exponent  $\beta$  is defined as  $M_s \sim (T - T_c)^\beta$ , one can also define the exponents  $\gamma$  and  $\alpha$  accounting for the critical behavior of the magnetic susceptibility  $\chi_m$  and magnetic specific heat  $C_m$ , respectively. Since the Lenz-Ising model was the only one solved analytically in two dimensions, the exact values for the critical exponents could be extracted, whereas only approached values were determined in the other cases of magnetic models. The great strength of this description is the concept of universality class, specified by the space and spin dimensionalities  $(D, n)$  of the system [52, 73]. The space dimensionality is the number of directions along which non-zero magnetic interactions exist between the spins, while the spin dimension is the number of axes along which spins are free to orient themselves, that is related to the Ising, XY or Heisenberg nature of the system. All the materials belonging to the same class possess the same behavior when approaching the phase transition, regardless of their lattice or composition, so by measuring the critical exponents of a magnetic material it is then possible to trace back the magnetic model that describes it the best. This classification allows to predict if a system could present or not a long-range magnetic order (see Table 1).

	$D = 1$	$D = 2$	$D = 3$
$n = 1$ (Ising)	×	✓	✓
$n = 2$ (XY)	×	~	✓
$n = 3$ (Heisenberg)	×	×	✓

**Table 1:** Overview of the presence or absence of a long-range magnetic order in a system, depending on its space  $D$  and spin  $n$  dimensionalities. The case  $D = 2$  and  $n = 2$  is special since it corresponds to the topological BKT transition that presents a short-range order, hence the symbol ~.

Actually, quasi-2D magnetic order began to be investigated experimentally from 1962 [10]. It was found in bulk crystals whose magnetic atomic planes were isolated from one another by canceling of the magnetic interactions or intercalation of non-magnetic layers. This cancellation results in the absence of long-range order in the direction perpendicular to the planes, whereas

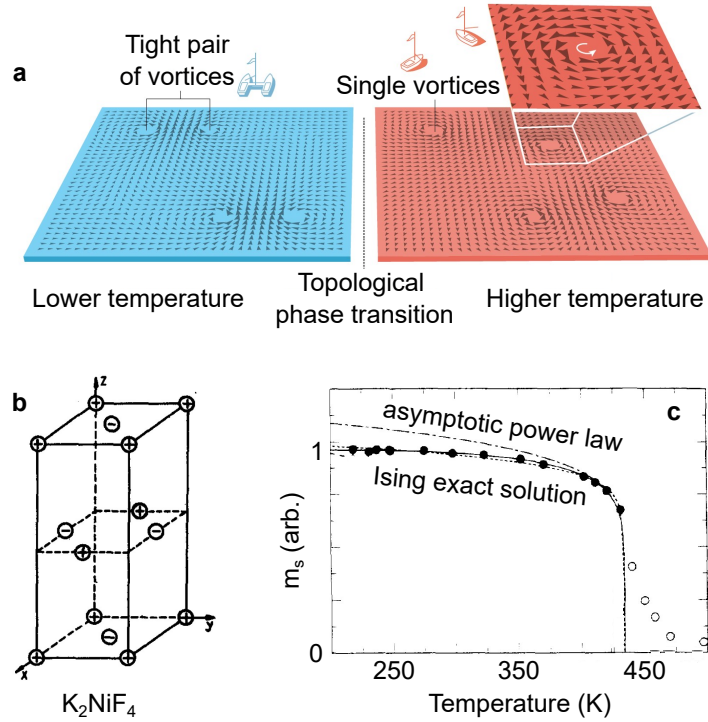


**Figure 27: Illustrations of 2D magnetism.** **a.** Artist view of the two phases of the topological BKT phase transition. Adapted from [80]. **b.** Magnetic unit cell of  $K_2NiF_4$  displaying Ni ion planes whose magnetic interactions cancel each other out, from [10]. **c.** Saturation magnetization  $m_s$  as a function of the temperature of a monolayer Co film encapsulated by two Cu thin films. The data (dots) are better fitted by the exact solution to the Ising model (solid lines) than the asymptotic power law (dashed lines). Adapted from [11].

long-range correlations are preserved within the planes. The most seminal example being  $K_2NiF_4$ , which contains planes of antiferromagnetically-coupled nickel ions perpendicular to the  $z$  axis (see Fig. 27 b). Each nickel ion in a plane has eight nearest-neighbors in surrounding planes, four of them having a spin up and the four others having a spin down, resulting in a canceling of the magnetic interactions between the nickel atomic planes. The absence of interactions between these planes has been demonstrated using neutron scattering, that allows to access the materials magnetic structure, indicating the two-dimensional nature of the magnetic interactions in that compound ( $D = 2$ ) [10, 78]. Moreover, a critical exponent  $\beta = 0.14$  close to the one of  $\beta_{\text{Ising}}^{2D} = 0.125$  expected for the 2D Ising model was estimated from sub-lattice magnetization ( $n=1$ ) [78]. Similar proofs of quasi-2D magnetism have been reported in multiple bulk crystals compounds [79], giving first insights on the interpretation of magnetism in two dimensions.

The development of epitaxial thin film growth in the eighties made possible the exploration of the magnetic order in mono- or bilayer thin films from magnetic transition metals like Fe, Co or Ni, grown on non-magnetic substrates [81]. Monolayer thin films are free from the influence of the interlayer coupling present in the bulk crystals, and so, are closer to a true two-dimensional structure. They were therefore expected to be examples of two-dimensional Heisenberg ferromagnets ( $D = 2, n = 2$ ), and so, to not show a long range magnetic order. However,

magnetic phase transitions have been demonstrated in Fe, Co and Ni monolayers grown on various substrates [11–13]. This apparent contradiction with the Mermin-Wagner theorem has been explained by the presence of uniaxial anisotropy in ultrathin films as a result of the local symmetry breaking at the thin film interfaces [82, 83]. Indeed, Bander and Mills used renormalization group theory to demonstrate that an uniaxial anisotropy, no matter how small, always produces a magnetic phase transition of an Ising character [81]. A Co monolayer encapsulated between Cu layers has even been proven to be a pure 2D Ising system, showing a saturation magnetization following the exact Ising solution with a critical exponent  $\beta = 0.125 = \beta_{\text{Ising}}^{2\text{D}}$  (see Fig. 27 c) [11]. The absence of long-range magnetic order corresponding to the XY model, and the associated BKT transition, are then highly unlikely to be observed experimentally in thin films since it would require a zero anisotropy [73]. The study of magnetic phenomena in thin films is now more oriented towards the interactions occurring in stacks of thin films that is an expanding research field [84]: from a fundamental point of view, with the imaging and control of magnetic spin textures like domain walls or skyrmions [85, 86] or more oriented towards applications, with the design and improvement of spintronic devices [87–89].

## Van der Waals magnets: a versatile platform to study 2D magnetism

Van der Waals materials are layered materials whose atoms are bound in-plane by strong bounds, that can be covalent or ionic, and out-of-plane by weaker van der Waals interactions. Due to this weak inter-plane coupling, some of their compounds, notably the chromium trihalides ( $\text{CrX}_3$ ) and the transition metal phosphorus trisulfides ( $\text{MPS}_3$ ) families, were already considered as two-dimensional magnets in their bulk form from the 70's [79, 90, 91]. However, contrarily to the case of  $\text{K}_2\text{NiF}_4$ , their out-of-plane interactions are not negligible and can lead to a magnetic behavior closer to 3D or 2D depending on the compounds [79, 92, 93].

Thanks to these weak out-of-plane interactions, the atomic planes of van der Waals materials can be mechanically cleaved until the monolayer limit, as first shown in the case of graphene in 2004 [94]. This achievement offered the perspective to isolate a magnetic van der Waals monolayer that would constitute a true two-dimensional magnet, raising the question of the existence of a long-range magnetic order in such a system. The persistence of a magnetic order in a  $\text{FePS}_3$  monolayer was finally demonstrated experimentally in 2016 by two different teams [14, 95].  $\text{FePS}_3$  is an Ising antiferromagnet ( $n = 1, D = 2$ ) in which a long-range magnetic order was expected. The next year came the proof of a long range magnetic order existence in a  $\text{CrI}_3$  ferromagnetic monolayer that is also described by the Ising model [15].

In the following years, the number of studied magnetic van der Waals materials blossomed, creating a vast portfolio to be exploited [96–98]. To highlight the diversity of the magnetic configurations offered by these materials, we focus on the two families mentioned above, namely the chromium trihalides ( $\text{CrX}_3$ ), that are intralayer ferromagnets and the transition metal phosphorus trisulfides ( $\text{MPS}_3$ ), that are intralayer antiferromagnets (see Fig. 28 a,b). For a compound with a

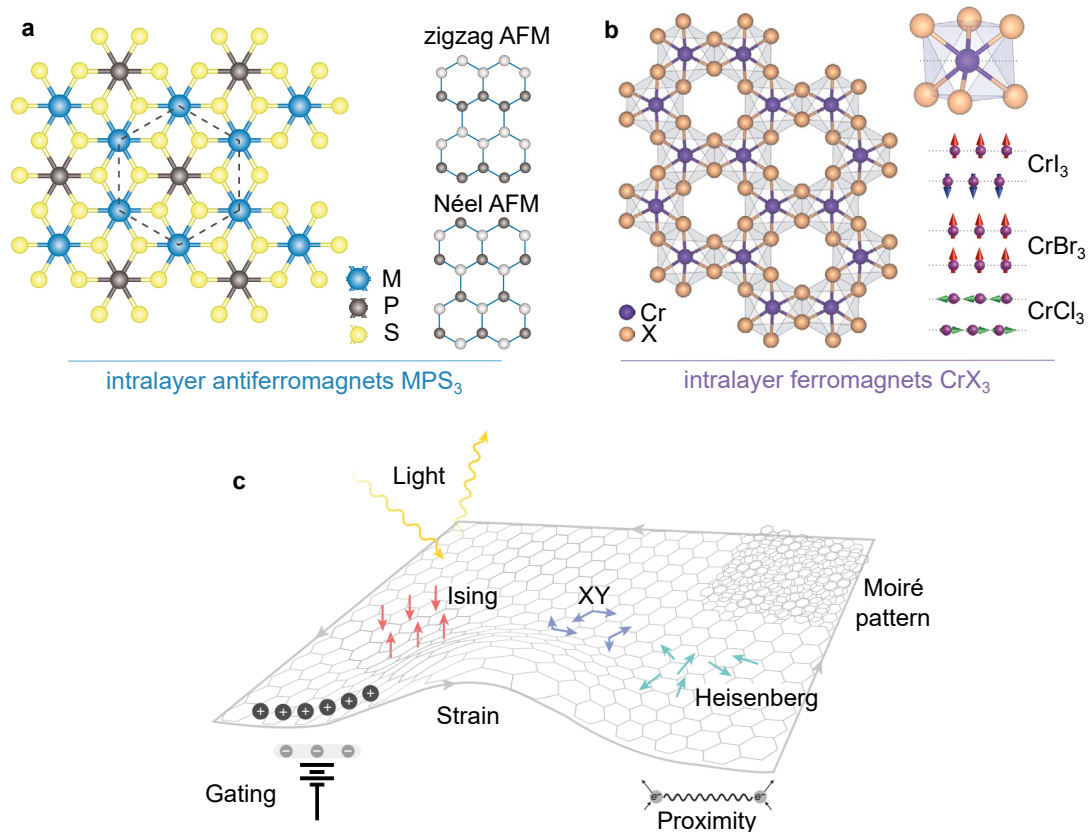


**Figure 28: The versatile playground of van der Waals 2D magnets.** **a.** Top view of the crystalline structure and in-plane magnetic configuration of antiferromagnetic  $MPS_3$  compounds. Adapted from [97]. **b.** Top view of the crystalline structure and side view of inter- and intralayer magnetic configurations of  $CrX_3$  compounds. Adapted from [98]. **c.** Illustration of the wide range of degrees of freedom offered by van der Waals 2D magnets. Adapted from [16].

different transition metal ion for the  $MPS_3$  ( $M = Fe, Ni, Mn, Co$ ) or a different halogen ion for the  $CrX_3$  ( $X = I, Br, Cl$ ), the resulting magnetic configurations can be very distinct. For example,  $NiPS_3$  and  $FePS_3$  present a zigzag magnetic order, while a Néel order type has been reported in  $MnPS_3$  [22]. The magnetic order orientation can also be changed, with an out-of-plane easy axis for  $CrI_3$  and  $CrBr_3$ , whereas  $CrCl_3$  spins are oriented within the plane. Additionally, the interlayer coupling can be different, the one in  $CrCl_3$  being antiferromagnetic, while it is ferromagnetic in  $CrBr_3$ .

Van der Waals 2D magnets benefit from the many degrees of freedom characteristic from this class of materials (see Fig. 28 c). Their physical properties can be easily tuned by strain or doping [99, 100], offering an ideal platform to study and control the magnetism in two-dimensions. They can also be combined to other types of van der Waals materials in van der Waals heterostructures, without any lattice mismatch issues since these are held by van der Waals forces. Air sensitive 2D magnetic layers can then be encapsulated by insulating hexagonal boron nitride (hBN) to protect their properties. Moreover, van der Waals heterostructures offer the opportunity to study proximity effects between 2D magnetic materials and light-emitting 2D semi-conductors like transition metal dichalcogenides (TMD) [101, 102].

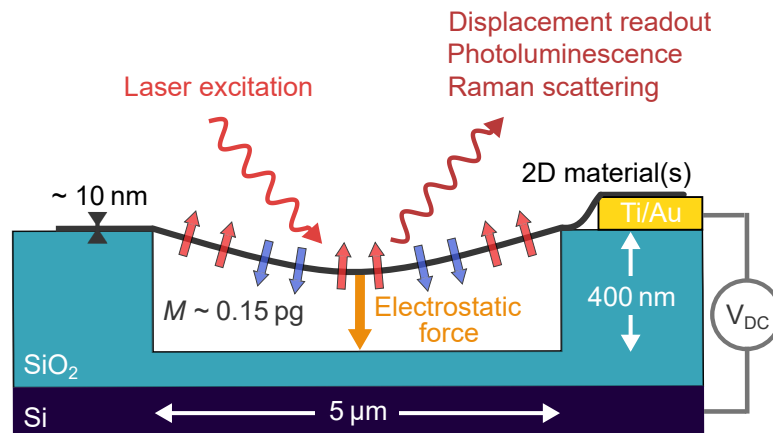


**Figure 29:** Interactions and degrees of freedoms in a magnetic drum-like nano-resonator.

2D magnetic van der Waals layers can also be suspended over micrometric holes to form drum-like nano-resonators. The first free-standing graphene nano-resonator was demonstrated in 2007 by Bunch *et al.* [103], followed in 2013 by the first nanomechanical measurements on suspended TMD nanodrums made of MoS<sub>2</sub> layers [104, 105]. This drum-like geometry allows to access to the intrinsic material properties, free from substrate effects, and to investigate their tuning by strain [106, 107]. From the perspective of suspended 2D magnets, we could expect a coupling between magnetic and mechanical degrees of freedom as already shown on hybrid magneto-optomechanical resonators [17].

### Approach adopted in this thesis

This PhD project marks the beginning of investigations on magnetic van der Waals materials in the team. We decided to start to work with compounds from the transition metal phosphorus trisulfides (MPS<sub>3</sub>) family, that provide a diversity of magnetic configurations and have the great advantage to be air-stable for a few days [14], which is not the case of the members of the chromium trihalides family (CrX<sub>3</sub>) that we plan to investigate in the future. Our approach consists in suspending few-layer flakes of these materials, eventually embedded in a van der Waals heterostructure, over micrometer size holes to obtain the drum-like resonators mentioned previously (see Fig. 29). Previous works of the team have already been carried out in this scope, on suspended homo- or heterostructures constituted of graphene and semi-conducting transition metal dichalcogenides (TMD) [18–20]. We will explore the properties of these suspended magnetic nano-resonators through the perspective of nano-optomechanics and optical spectroscopies combined on the same experimental setup.

The first objective will be to fabricate these drum-like samples by nanofabrication techniques in a cleanroom. Then, we aim at probing the magnetic properties in these 2D antiferromagnets, notably their magnetic phase transitions, before heading towards the control of these properties via an applied strain. On the way, we will also explore the nanomechanical behavior of magnetic van der Waals heterostructures with strain and the intriguing properties of NiPS<sub>3</sub> light emission.

---

## Manuscript organization

This manuscript is divided into four chapters.

Chapter 1 introduces the concepts that will be useful for the understanding of the rest of the manuscript. In a first part, the main properties of the transition metal phosphorus trisulfides ( $\text{MPS}_3$ ) studied compounds are reviewed. The sample fabrication process and experimental setup are then presented, followed by an introduction to the fundamentals of Raman spectroscopy, which is further applied to the case of the  $\text{MPS}_3$  compounds at room temperature. This chapter ends with a description of the nano-mechanical behavior of the studied drum-like resonators.

Chapter 2 presents the detection of magnetic phase transitions in a suspended  $\text{FePS}_3$ -based heterostructure and a  $\text{NiPS}_3$  homostructure by both Raman spectroscopy and nanomechanical measurements. The principle of the phase transition identification is reviewed for the two methods. Raman spectroscopy and nanomechanics results obtained for temperatures around the expected Néel temperature of these materials are discussed. The Néel temperatures of  $\text{FePS}_3$  and  $\text{NiPS}_3$  samples are estimated by both methods.

Chapter 3 is dedicated to an investigation of mechanical and magnetic properties evolution with applied strain for a  $\text{NiPS}_3$  homostructure and a  $\text{FePS}_3$ -based heterostructure. The magnetic phase transition is probed in the few-layer  $\text{NiPS}_3$  homostructure by Raman spectroscopy and nanomechanical measurements for different strain values. The influence of strain on the Néel temperature is estimated. The  $\text{FePS}_3$ -based heterostructure nanomechanical behavior with strain is studied and linked to the results obtained on the detection of its magnetic phase transition for various strains.

Chapter 4 is focused on the exploration of  $\text{NiPS}_3$  photoluminescence properties. The characteristic features and possible origins of this light emission are reviewed. Results obtained at low temperatures shed light on the behavior of the photoluminescence with strain. The polarization of the light emission is determined, and spatially-resolved measurements are carried out to reveal antiferromagnetic domains. Special attention is paid to monitor the behavior of secondary emission lines present in the photoluminescence spectrum.

# Chapter 1

---

## Optical spectroscopy and nanomechanics of few-layer antiferromagnetic membranes

---

In this chapter, we will introduce concepts and methods that will be useful throughout the development of the manuscript. First, we will review some meaningful properties of the materials studied during this thesis. Then we will detail how few-layer suspended samples can be fabricated out of their bulk crystals, before presenting the setup on which these samples will be measured. The last two parts will be dedicated to the introduction to two approaches to investigate these samples, respectively Raman spectroscopy and nano-optomechanics.

### 1.1 Transition metal phosphorus trisulfides $MPS_3$ ( $M=Fe,Ni$ )

During this PhD project we focused our study on the van der Waals material family of the transition metal phosphorus trisulfides  $MPS_3$ . These materials offer the great advantage to be air-stable for a few days at room temperature [14], contrarily to most of van der Waals magnets that need to be handled under a controlled atmosphere. Four members of this family present a magnetic order at low temperatures:  $FePS_3$ ,  $MnPS_3$ ,  $NiPS_3$  and  $CoPS_3$  [108], in this thesis we will focus on two of them:  $FePS_3$  and  $NiPS_3$ . To get more familiar with their properties, we will first review the crystalline structure of the  $MPS_3$  family materials and the magnetic ordering in  $FePS_3$  and  $NiPS_3$ . Then we will introduce their mechanical properties by defining the Hooke's law in the case of these materials. Finally we will discuss their thermal properties, namely their specific heat and thermal expansion coefficient, and compare them to the ones of other van der Waals materials.

#### 1.1.1 Crystalline structure

All the members of the  $MPS_3$  family present the same crystalline structure shown on Figure 1.1 [22]. The transition metal atoms are arranged in a honeycomb lattice, while the phosphorus

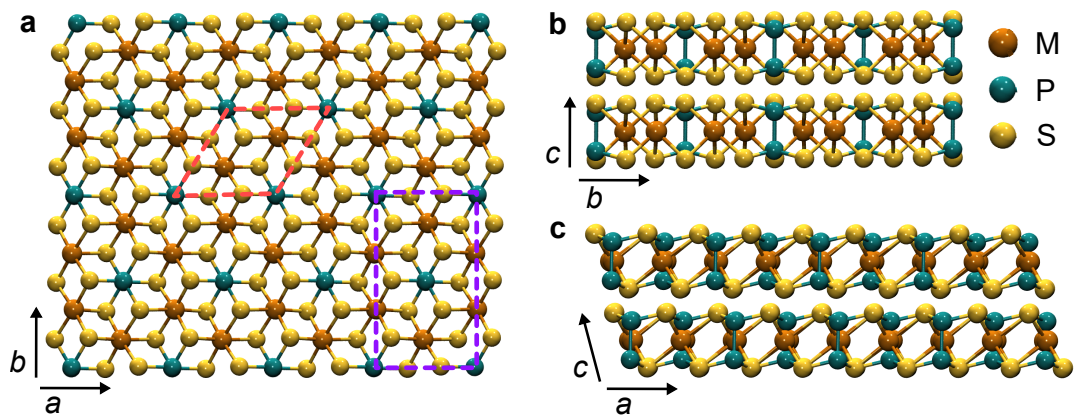


**Figure 1.1:  $MPS_3$  crystalline structure seen along their three crystalline axes  $a$ ,  $b$  and  $c$ .** **a.** Top view of a  $MPS_3$  monolayer. The orange, purple dashed lines represents the paramagnetic, antiferromagnetic unit cell, respectively. **b.** Side view of a  $MPS_3$  bilayer perpendicular to the  $a$  axis. **c.** Side view of a  $MPS_3$  bilayer perpendicular to the  $b$  axis.

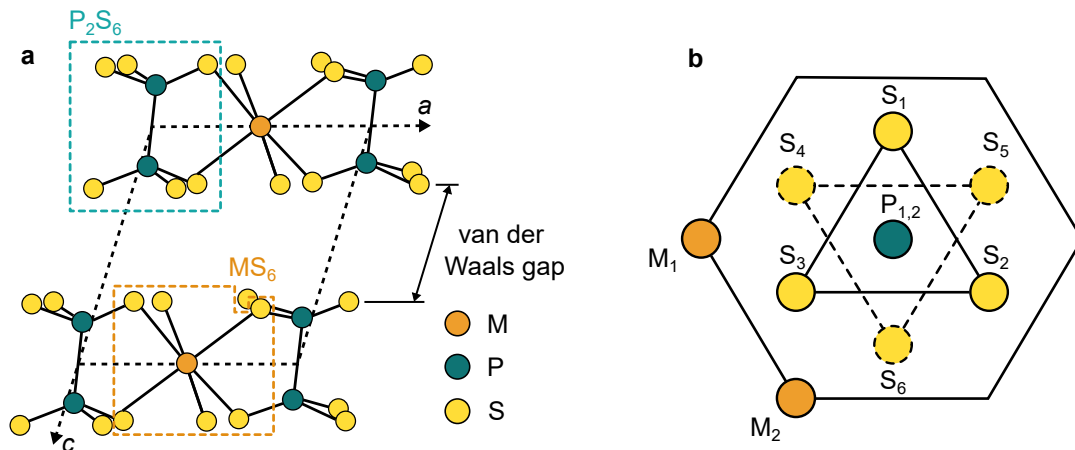


**Figure 1.2: Elementary units of  $MPS_3$  crystalline structure.** **a.** Scheme of two  $MPS_3$  atomic layers seen along the  $b$  axis. The dotted lines indicates the  $a$  and  $c$  crystalline axes. The green, orange dashed box represents the  $P_2S_6$ ,  $MS_6$  units, respectively. Adapted from [21]. **b.** Scheme of  $MPS_3$  paramagnetic unit cell, seen from top, containing ten atoms.  $P_{1,2}$  represents two phosphorus atoms one on top of the other. The dashed lines and contour indicate sulfur atoms that are located on a lower level along the  $c$  axis. Adapted from [25].

atoms are located on hexagonal lattice sites (see Fig. 1.1 a). Each transition metal atom is bound to six sulfur atoms in an octahedral geometry, forming  $MS_6$  units (see Fig. 1.2 a). On the other hand, each phosphorus atom is bound to three sulfur atoms and one other phosphorus atom. These are constituting  $P_2S_6$  units in a dumbbell shape with three sulfur and one phosphorus atoms on each side of the P-P bound (see Fig. 1.2 a). The  $MPS_3$  layers are thus made up of an alternation of these two types of units.

As we can see on Figures 1.1 c and 1.2 a, there is a shift in the layer stacking, resulting from a  $ABC\ ABC$  stacking of the sulfur planes along the  $c$  axis [25], implying an out-of-plane anisotropy. The  $MPS_3$  have therefore a monoclinic symmetry with space group  $C_{2/m}$  [22].

The transition metal atoms of each member of the  $MPS_3$  family have a different radius, so their bound length and angle between bounds will not be the same [22, 109], resulting in different lattice constants that are displayed in Table 1.1.

A representation of the  $MPS_3$  paramagnetic unit cell is displayed on Figure 1.2 b, we note that it contains ten atoms, two of which are transition metal atoms.

	$a$	$b$	$c$	vdW gap	Ref.
FePS <sub>3</sub>	5.947	10.300	6.722	3.25	[22, 110]
NiPS <sub>3</sub>	5.812	10.070	6.632	3.26	[22, 110]

**Table 1.1:** Lattice constants of FePS<sub>3</sub> and NiPS<sub>3</sub> from X-ray diffraction measurements and calculated van der Waals gaps. All the values are given in angström.

## 1.1.2 Magnetic properties

### Magnetic structure

Both FePS<sub>3</sub> and NiPS<sub>3</sub> are intralayer *zigzag* antiferromagnetic materials. This type of magnetic order is characterized by antiferromagnetically coupled spin chains, that are made of ferromagnetically coupled spins along the *zigzag* axis of the honeycomb transition metal lattice (see Fig. 1.3 c,d).

However they present different spin orientations and interlayer couplings (see Fig. 1.3 a, b). FePS<sub>3</sub> has an out-of-plane easy axis, so its spins are oriented perpendicularly to the  $ab$  plane, making it well described by the Ising model [111]. Whereas NiPS<sub>3</sub> has an in-plane easy-axis, with its spins oriented in the  $ab$  plane along the  $a$  axis, with a small out-of-plane component [111, 112], and has been reported to follow an XXZ model [113, 114]. The coupling between FePS<sub>3</sub> layers is antiferromagnetic whereas NiPS<sub>3</sub> shows an interlayer ferromagnetic coupling [22].

The sizes of FePS<sub>3</sub> and NiPS<sub>3</sub> unit cells are modified in their antiferromagnetic phase. Indeed, as we showed in the previous subsection, the paramagnetic unit cell contains two transition metal atoms along the *zigzag* direction which belong to the same spin chain. To take into account the existence of the two spin chains with opposite spin direction, the size of the magnetic cell has to

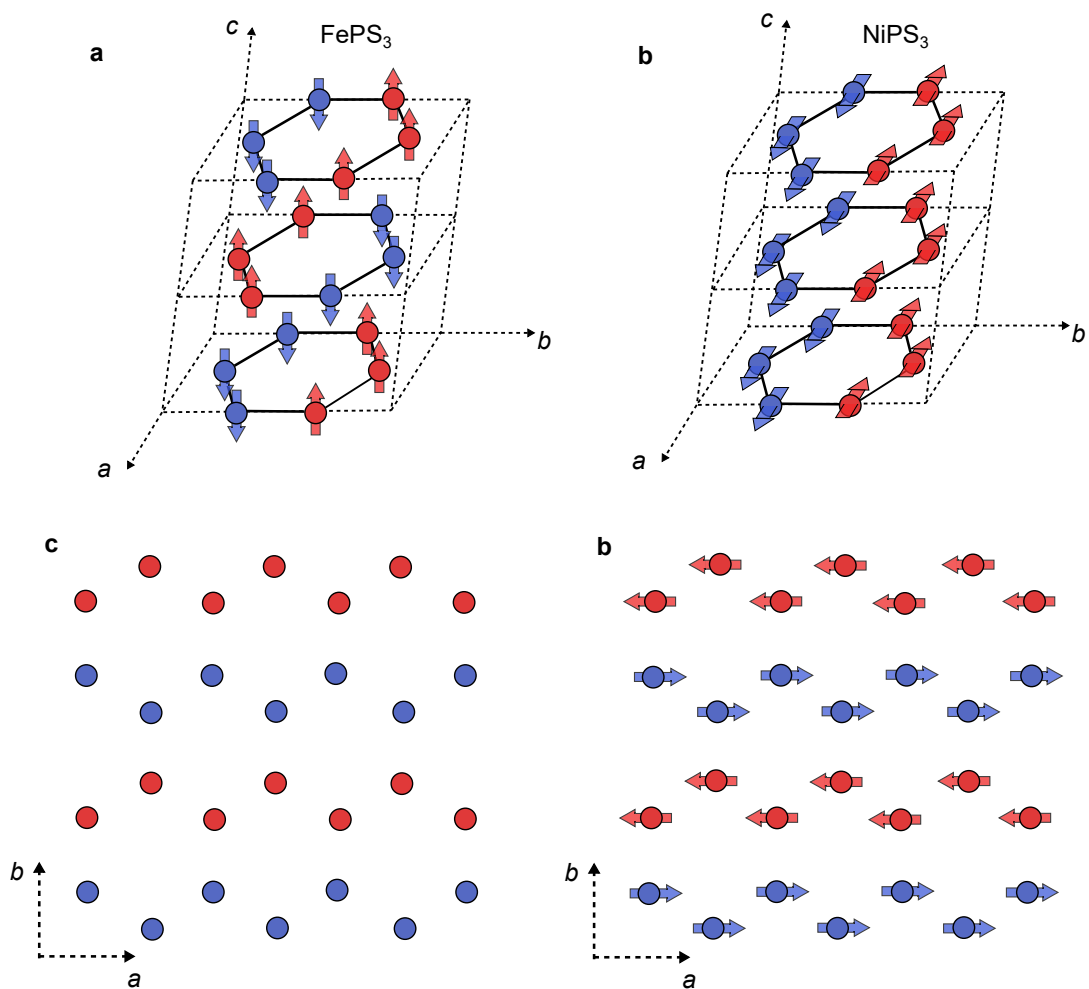


**Figure 1.3: Schemes of magnetic ordering in  $FePS_3$  and  $NiPS_3$ .** a,b. Magnetic structure shown for three layers of  $FePS_3$ ,  $NiPS_3$ , respectively. The arrows represent the spin directions. Adapted from [22]. c,d. Top view of the magnetic ordering in a  $FePS_3$ ,  $NiPS_3$  atomic layer, respectively. Only transition metal atoms are displayed for clarity.

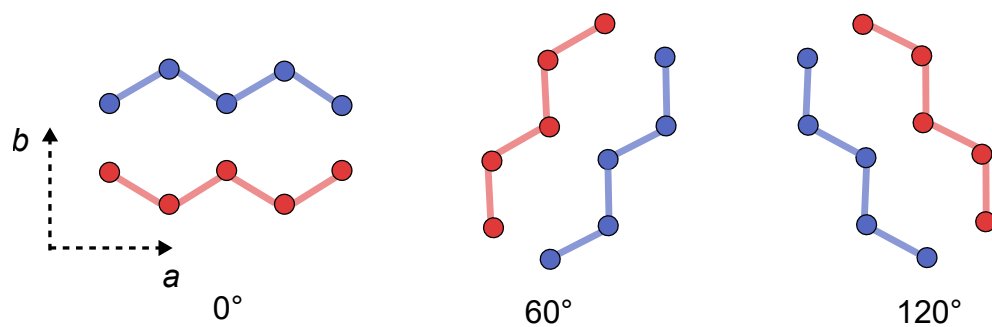


**Figure 1.4: Scheme of the three possible spin chains orientation in zigzag  $MPS_3$  antiferromagnets.**

be doubled in the  $ab$  plane (see Fig. 1.1 a). In the case of  $\text{FePS}_3$ , the unit cell size has also to be doubled along the  $c$  axis to consider the antiferromagnetic coupling between the  $ab$  planes.

### Magnetic phase transitions

$\text{FePS}_3$  paramagnetic to antiferromagnetic phase transition in bulk crystals has been reported at a Néel temperature of  $T_N \sim 118$  K by calorimetry [28], Raman spectroscopy [14] and magnetization [115] measurements. The persistence of a magnetic order to the monolayer limit was proved in 2016 using Raman spectroscopy [14], in good agreement with what is expected from the Ising model. There is no clear trend in the variation of  $\text{FePS}_3$  Néel temperature with decreasing thickness and it has been predicted to remain constant from first-principle calculations [116]. However, lower Néel temperatures ranging from 108 to 116 K are reported for exfoliated layers with a thickness between one and about 80 layers [14, 117, 118].

The Néel temperature of  $\text{NiPS}_3$  bulk crystals has been reported as  $T_N \sim 155$  K from nuclear magnetic resonance [119], Raman spectroscopy [32] and magnetic susceptibility [120] measurements. The presence of a magnetic order in monolayer  $\text{NiPS}_3$  is still debated, a first Raman spectroscopy study of 2019 claimed its absence [32] in agreement with recent linear dichroism measurements [44], whereas a work from 2023 combining Raman and ultrafast spectroscopy showed signs of a phase transition at the monolayer limit [121]. In both cases the magnetic phase transition is still detected in bilayer flakes. A decrease in Néel temperature for a number of layers lower than five has been measured by Raman spectroscopy and linear dichroism [32, 44] and predicted from first principle calculations [116].

### Three-state nematicity

Actually, due to the three-fold rotational symmetry of a  $\text{MPS}_3$  monolayer, the magnetic spin chains are not necessarily oriented along the  $a$  axis, but can present three different orientations at  $60^\circ$  from each other (see Fig. 1.4). These three possible antiferromagnetic orders are referred as a three-state Potts nematicity [43, 44]. The coexistence of several magnetic order orientations naturally leads to the presence of antiferromagnetic domains characterized by a given spin chain direction.

In bulk  $\text{MPS}_3$  compounds, the monoclinic stacking imposes a preferred direction for the spin chains orientation that has been reported to be the  $a$  axis [36, 43]. This restriction is attenuated as the monolayer limit is approached, leading to the observation of the three spin chains orientations and their corresponding antiferromagnetic domains, first, on exfoliated  $\text{FePS}_3$  flakes down to the monolayer using linear dichroism and second harmonic generation [122, 123], before being recently observed on  $\text{NiPS}_3$  until the bilayer limit thanks to linearly-polarized photoluminescence, Raman spectroscopy and linear dichroism measurements [38, 43, 44].

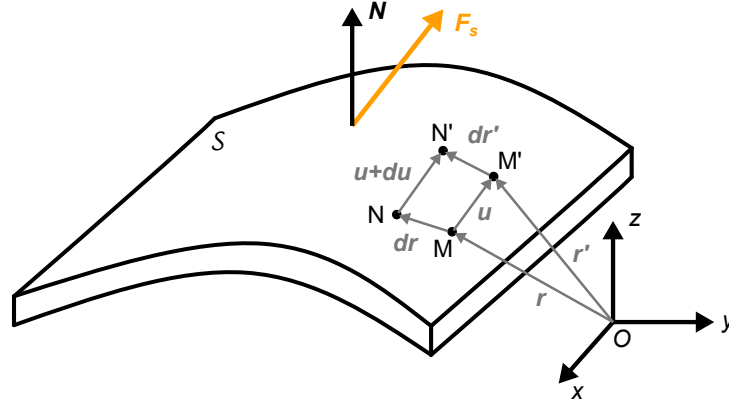


**Figure 1.5:** Scheme of a solid undergoing deformation. The two infinitesimally close points  $M$  and  $N$  belong to the non-deformed solid whereas  $M'$  and  $N'$  points are the corresponding points of the solid after deformation. The displacement of the point  $M$  induced by the deformation is described by the vector  $\mathbf{u}$ . The points  $M$  and  $M'$  are located by the vectors  $\mathbf{r}$  and  $\mathbf{r}'$ , respectively in the  $(Oxyz)$  frame. The unit vector  $\mathbf{N}$  represents the normal to the surface  $S$  and  $\mathbf{F}_s$  stands for the resultant of surface forces exerted on the surface  $S$ .

### 1.1.3 Mechanical properties

The mechanical properties of a material can be derived by considering its response to a deformation, that is described using the elasticity theory of continuous media [124]. Within this formalism, the deformation of a three-dimensional solid is linked to the resulting internal stress by the generalized Hooke's law that involves the elastic constants of the material. We will consider only linear deformations of the medium and so neglect the second-order terms.

#### Generalized Hooke's law

A deformation of a material with an initial volume  $\mathcal{V}$  to a final volume  $\mathcal{V}'$  induces a displacement field  $\mathbf{u}$  for the particles composing the medium. It is illustrated on Figure 1.5 by the displacement of the reference point  $M$  to the position of the point  $M'$ . The point  $N$  infinitesimally close to  $M$  undergoes a displacement  $\mathbf{u} + d\mathbf{u}$  with  $d\mathbf{u} = d\mathbf{r}' - d\mathbf{r}$  towards the point  $N'$ . The matrix of the linear strain tensor  $\bar{\epsilon}$  is then set in the form [125, 126]

$$\bar{\epsilon} = \begin{pmatrix} \epsilon_{xx} & \epsilon_{xy} & \epsilon_{xz} \\ \epsilon_{xy} & \epsilon_{yy} & \epsilon_{yz} \\ \epsilon_{xz} & \epsilon_{yz} & \epsilon_{zz} \end{pmatrix} \quad \text{with} \quad \epsilon_{ij} = \frac{1}{2} \left( \frac{\partial u_i}{\partial r_j} + \frac{\partial u_j}{\partial r_i} \right) \quad (1.1)$$

where  $i, j = x, y, z$  and  $u_i, r_i$  are the projections of the corresponding vector on the axis  $i$ . We note that the strain tensor is a second rank symmetric tensor, where the diagonal components  $\epsilon_{ii}$  relate to extensions of the material, while the non-diagonal components  $\epsilon_{ij}$  are referred to as shearing strains.

The stress field in the material is identified to the field of internal forces that maintains the mechanical equilibrium of the solid subjected to external forces. The stress tensor  $\bar{T}$  is thus

defined by

$$\mathbf{F}_s = \mathbf{N} \cdot \bar{\mathcal{T}} \quad \text{with} \quad \bar{\mathcal{T}} = \begin{pmatrix} \sigma_x & \tau_{xy} & \tau_{xz} \\ \tau_{xy} & \sigma_y & \tau_{yz} \\ \tau_{xz} & \tau_{yz} & \sigma_z \end{pmatrix} \quad (1.2)$$

with  $\mathbf{N}$  the unit vector normal to the surface  $\mathcal{S}$  and  $\mathbf{F}_s$  the resultant of surface forces exerted on the solid [125] (see 1.5). The stress tensor is also a second rank symmetric tensor, with diagonal components  $\sigma_i$  called normal stresses and off-diagonal components  $\tau_{ij}$  called shear stresses.

The stress and strain tensors are related through the generalized Hooke's law as

$$\bar{\mathcal{T}} = \bar{\mathcal{C}}\bar{\varepsilon} \quad (1.3)$$

where  $\bar{\mathcal{C}}$  is the fourth rank elasticity tensor with components  $C_{ijkl}$ . Since the stress and strain tensors are both symmetrical, so is the elasticity tensor, reducing its number of independent components to 21 [127].

### MPS<sub>3</sub> elasticity tensor

As discussed in the previous section, the members of the MPS<sub>3</sub> family present a monoclinic symmetry. The corresponding elastic tensor comprises 13 independent constants and the Hooke's law writes [126, 128]

$$\begin{pmatrix} \sigma_x \\ \sigma_y \\ \sigma_z \\ \tau_{yz} \\ \tau_{xz} \\ \tau_{xy} \end{pmatrix} = \begin{pmatrix} C_{11} & C_{12} & C_{13} & 0 & 0 & C_{16} \\ C_{12} & C_{22} & C_{23} & 0 & 0 & C_{26} \\ C_{13} & C_{23} & C_{33} & 0 & 0 & C_{36} \\ 0 & 0 & 0 & C_{44} & C_{45} & 0 \\ 0 & 0 & 0 & C_{45} & C_{55} & 0 \\ C_{16} & C_{26} & C_{36} & 0 & 0 & C_{66} \end{pmatrix} \begin{pmatrix} \varepsilon_{xx} \\ \varepsilon_{yy} \\ \varepsilon_{zz} \\ 2\varepsilon_{yz} \\ 2\varepsilon_{xz} \\ 2\varepsilon_{xy} \end{pmatrix} \quad (1.4)$$

where  $x$ ,  $y$  and  $z$  are orthogonal axes which coincide with principal axes of the crystal. The asymmetry induced by the monoclinic staking results in non zero terms ( $C_{16}$ ,  $C_{26}$ ,  $C_{36}$  and  $C_{45}$ ) compared to an isotropic material, leading to additional shear stress.

However, this elastic tensor being rather complicated, its elastic constants have not being computed for now in the case of the MPS<sub>3</sub> family. Only the case of monolayers MPS<sub>3</sub> has being investigated [24, 129], we will thus restrict ourselves to this situation in the following.

Since we are now dealing with a monolayer, the components in the  $z$  direction can be omitted. A monolayer of transition metal phosphorus trisulfides possesses an isotropic hexagonal symmetry and can then be described as graphene [24, 129], whose elastic tensor only comprises two independent constants in two dimensions. The Hooke's law can then be written as follows

$$\begin{pmatrix} \tilde{\sigma}_x \\ \tilde{\sigma}_y \\ \tilde{\tau}_{xy} \end{pmatrix} = \begin{pmatrix} \tilde{C}_{11} & \tilde{C}_{12} & 0 \\ \tilde{C}_{12} & \tilde{C}_{11} & 0 \\ 0 & 0 & (\tilde{C}_{11} - \tilde{C}_{12})/2 \end{pmatrix} \begin{pmatrix} \tilde{\varepsilon}_{xx} \\ \tilde{\varepsilon}_{yy} \\ 2\tilde{\varepsilon}_{xy} \end{pmatrix}. \quad (1.5)$$

with the tilded variables corresponding to the two-dimensional case. The constants  $\tilde{C}_{11}$  and  $\tilde{C}_{12}$  are relating the normal strains to the elongations of the material, whereas the term  $\tilde{C}_{\text{shear}} = (\tilde{C}_{11} - \tilde{C}_{12})/2$  is relating the shear stress to shear strain. The remaining elastic constants can be expressed in terms of the two-dimensional in-plane Young's modulus  $E_{2D}$  and the Poisson ratio  $\nu$  as [24, 130]

$$\tilde{C}_{11} = \frac{E_{2D}}{1 - \nu} \quad \text{and} \quad \tilde{C}_{12} = \frac{\nu E_{2D}}{1 - \nu^2}. \quad (1.6)$$

The Young's modulus quantifies the stress created in the material upon deformation, while the Poisson ratio is a measure of how much the material deforms in a direction perpendicular to the applied stress.

### FePS<sub>3</sub> and NiPS<sub>3</sub> elastic parameters

The elastic constants  $\tilde{C}_{11}$  and  $\tilde{C}_{12}$  of FePS<sub>3</sub> and NiPS<sub>3</sub> monolayers have been calculated using DFT simulations by Hashemi *et al.* [24], allowing to obtain their two-dimensional Young's modulus and Poisson ratio by inverting the relations of Equation (1.6). Their values are shown in Table 1.2 along with those of MnPS<sub>3</sub> and other 2D materials for comparison. We note that among the MPS<sub>3</sub>, NiPS<sub>3</sub> is the one with the highest Young's modulus even though it remains lower than that of MoS<sub>2</sub> or WS<sub>2</sub> and far below that of graphene. Nevertheless, the values of Young's modulus and Poisson ratio among the MPS<sub>3</sub> family are of the same order of magnitude.

	$\tilde{C}_{11}$	$\tilde{C}_{12}$	$\tilde{C}_{\text{shear}}$	$E_{2D}$	$\nu$	Ref.
FePS <sub>3</sub>	72.7	22.1	25.0	79.4	0.304	[24]
NiPS <sub>3</sub>	87.0	23.1	31.9	93.1	0.265	[24]
MnPS <sub>3</sub>	61.7	20.2	20.8	68.3	0.327	[24]
MoS <sub>2</sub>	137.9	36.0	50.9	147.3	0.262	[24]
WS <sub>2</sub>				137	0.22	[131]
graphene	352.6	59.6	146.5	362.67	0.17	[24]
hBN	334.7	89.2	163.3	310.9	0.267	[132]

**Table 1.2:** Elastic constants for FePS<sub>3</sub>, NiPS<sub>3</sub> and MnPS<sub>3</sub> calculated in [24] compared to the ones of MoS<sub>2</sub>, WS<sub>2</sub>, graphene and hexagonal boron nitride (hBN). The elastic constants  $\tilde{C}_{11}$ ,  $\tilde{C}_{12}$ ,  $\tilde{C}_{\text{shear}}$  and the two-dimensional Young's modulus  $E_{2D}$  are in the units of N/m, while the Poisson ratio  $\nu$  is dimensionless.

We can recover a three-dimensional Young's modulus  $E$  by dividing the two-dimensional quantity by the interlayer distance  $t$ , giving  $E = E_{2D}/t$  [26]. Considering  $t = 0.67$  nm for FePS<sub>3</sub> and  $t = 0.66$  nm for NiPS<sub>3</sub> [110], we obtain  $E_{\text{FePS}_3} = 119$  GPa and  $E_{\text{NiPS}_3} = 141$  GPa. However,

by using these quantities calculated for  $\text{MPS}_3$  monolayers in the case of few-layer flakes we are neglecting the shear stresses induced by the monoclinic stacking.

Two useful quantities can be derived from the Young's modulus and the Poisson ratio. First, the bulk modulus  $K = E/3(1 - 2\nu)$  [127], whose values are  $K = 100$  GPa for  $\text{NiPS}_3$  and  $K = 102$  GPa for  $\text{FePS}_3$ , that will become relevant when computing thermodynamics properties of those materials. Second, the bending rigidity

$$\kappa = Eh^3/12(1 - \nu^2) \quad (1.7)$$

that describes the out-of-plane properties of thin plates with a thickness  $h$  and will be employed when describing the dynamics of few-layer suspended flakes.

## 1.1.4 Thermal properties

### Specific heat

The specific heat capacity  $c_v$  of a solid is defined as [133]

$$c_v(T) = \left. \frac{\partial u}{\partial T} \right|_V \quad (1.8)$$

with  $u$  its thermal energy density. It represents the increase of thermal energy stored in a molar unit of the solid for a temperature increase  $dT$  while maintaining a fixed volume or pressure<sup>1</sup>.

There are multiple terms contributing to the specific heat, but here we will focus on the two main terms in the case of  $\text{FePS}_3$  and  $\text{NiPS}_3$ , the lattice contribution to the specific heat  $C_L$  and the magnetic contribution  $C_M$ . The lattice specific heat can be expressed thanks to the Debye model as [134]

$$C_L(T) = \frac{12\pi^2}{5} n k_B \left( \frac{T}{\Theta_D} \right)^3 \quad (1.9)$$

where  $n = N/V$  is the number of atoms (or ions) per volume and  $k_B$  is the Boltzmann constant. This expression for the lattice specific heat is valid for temperatures  $T$  below the Debye temperature  $\Theta_D$  which is 263 K for  $\text{FePS}_3$ .

On the other hand, the magnetic contribution to the specific heat will appear as a peak at the critical temperature of the material, translating the singularity expected from the critical exponent description as  $C_M(T) \sim (T - T_c)^{-\alpha}$ , with  $\alpha$  the corresponding critical exponent.

The specific heat is an important quantity in the frame of this work, as it is the one we have access to through nanomechanical measurements as a function of temperature. The specific heat of bulk  $\text{FePS}_3$  and  $\text{NiPS}_3$  have been measured experimentally in the work of Takano *et al.* [28] and Pistawala *et al.* [135], respectively (see Fig. 1.6).

On Figure 1.6 a and on the inset of Figure 1.6 b, we see that all the specific heat curves share the

<sup>1</sup> For a solid, the specific heat at constant volume  $c_v$  is approximately equal to the specific heat at constant pressure  $c_p$ .

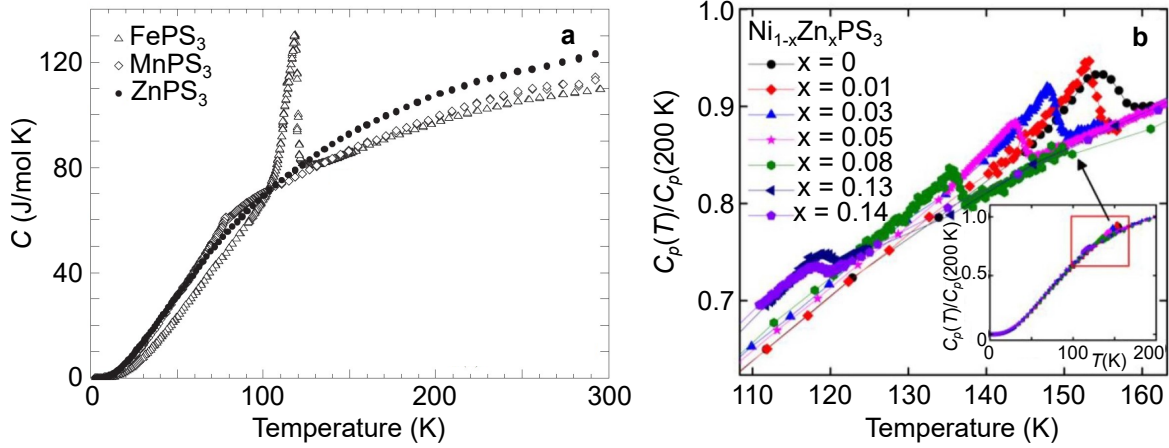


**Figure 1.6: Bulk  $FePS_3$  and  $NiPS_3$  specific heat evolution with temperature.** **a.** Specific heat of  $FePS_3$  (triangles),  $MnPS_3$  (diamonds) and  $ZnPS_3$  (dots) as a function of temperature. The specific heat of  $FePS_3$  presents a peak at its Néel temperature. Adapted from [28]. **b.** Normalized specific heat of  $Ni_{1-x}Zn_xPS_3$  for different Zn-doping ( $x$ ) as a function of temperature around  $T_N(x)$ . The inset shows the temperature evolution of the specific heat in the range 2-200 K. Adapted from [135].

same overall behavior that originates from the lattice contribution. The main difference comes from the magnetic contribution resulting in a sharp and intense peak in  $FePS_3$  specific heat at its Néel temperature, whereas only a small bump is visible in  $NiPS_3$  specific heat evolution (black dots on Figure 1.6 b). These distinct behaviors are attributed to their different magnetic anisotropy values,  $FePS_3$  presenting an out-of-plane magnetic order with a large anisotropy, whereas  $NiPS_3$  presents an in-plane magnetic order with a lower anisotropy [28, 116]. We can note that the peaks does not look like the expect singularity at the phase transition but are quite broad, around 8 K width. An early study of 1894 on  $FePS_3$  bulk crystals by Mössbauer spectroscopy has shown the coexistence of paramagnetic and antiferromagnetic phases between 110 and 120 K [91], which indicates that the magnetic phase transition is not instantaneous at the Néel temperature and could explain the width of the peak observed in the magnetic specific heat.

### Thermal expansion coefficient

The thermal expansion coefficient  $\alpha$  quantifies the contraction or dilatation of a material upon temperature variation. It is a crucial quantity to describe the evolution of the materials mechanical properties with temperature that will occur when probing the magnetic phase transition. We will use here the linear thermal expansion coefficient  $\alpha_L$  that characterizes the change in length  $L$  of the material in a given direction, defined as [134]

$$\alpha_L(T) = \frac{1}{L} \frac{dL}{dT}. \quad (1.10)$$

In a crystal, the thermal expansion coefficients are usually defined along the crystalline axes  $a$ ,  $b$  and  $c$  (see Fig. 1.1).

Material	$\alpha_L$ (300 K)	$\alpha_L(T)$	Reference
FePS <sub>3</sub>	12.7	7.5 (115 K)	[138],[26]
WS <sub>2</sub>	6	7 (160 K)	[136]
Graphene	-7	-4.5 (115 K)	[137]
h-BN	-2.7	-1.28 (114.5 K)	[139]
SiO <sub>2</sub>	0.5	-0.5 (115 K)	[141]
Silicon	2.7	-0.14 (115 K)	[142]

**Table 1.3:** Thermal expansion coefficients of various materials at room and low temperatures derived from experimental measurements except for both h-BN values and FePS<sub>3</sub> value at low temperature that are calculated. All the values are in  $10^{-6} \text{ K}^{-1}$ .

The evolution of thermal expansion coefficients as a function of temperature for 2D materials can be measured experimentally, for example using Raman spectroscopy or optomechanics [136–138], or calculated by numerical simulations [139, 140]. In the case of FePS<sub>3</sub>, a thermal expansion coefficient has been estimated from optomechanical measurements at room temperature [138] and its evolution at lower temperatures can be calculated using the thermodynamic relation [26, 134]

$$\alpha_L(T) = \frac{\gamma_D c_v(T)}{3KV_M} \quad (1.11)$$

that links the thermal expansion coefficient to the specific heat through the Grüneisen parameter  $\gamma_D$ .  $K$  is the material bulk modulus defined in Section 1.1.3,  $V_M$  is its molar volume and  $c_v$  is supposed equal to the lattice specific heat from the Debye model (see Eq. 1.9) with the Debye temperature  $\Theta_D(\text{FePS}_3) = 236 \text{ K}$  estimated in [28].

The thermal expansion coefficients of FePS<sub>3</sub> at room temperature and in a temperature range close to its Néel temperature are compared to those of other materials that are part of the samples studied in this manuscript in Table 1.3. We see that the thermal expansion coefficients of FePS<sub>3</sub> and WS<sub>2</sub> are positive on all the considered temperature range, that implies that they contract for decreasing temperatures, whereas those of graphene and h-BN are negative, meaning that they will expand for decreasing temperatures. We also note that the coefficients of FePS<sub>3</sub>, WS<sub>2</sub> and graphene are much larger than those of h-BN, SiO<sub>2</sub> and Si at the considered temperatures.

## 1.2 Sample fabrication

In order to obtain a suspended and contacted sample as required for our measurements (see Fig. 29), we first need to pattern substrates by nanofabrication techniques in a cleanroom. The materials of interest are micro-mechanically cleaved to get few-layer flakes that are then transferred on an aforementioned substrate. This procedure will be explained in details in the following Section.

### 1.2.1 Substrate micro-patterning

The two features we want to achieve on these substrates are electrodes to ensure the electrical contact, and holes over which to suspend the flakes of magnetic material.

We use conventional p-doped Si/SiO<sub>2</sub> wafers with 500 nm of SiO<sub>2</sub> to be able to etch deep enough holes. Multiple substrates of 4×4 mm (36 substrates for a 3-inch diameter wafer) are patterned on the same wafer to be cut just before use.

All the following nanofabrication steps, illustrated in Figure 1.7, were performed in the cleanroom STnano at IPCMS.

First, the electrodes are drawn by laser lithography (*Heidelberg μPG101*). For this purpose, the wafer is covered with a UV-sensitive resist by spin-coating (2) and illuminated by a 375 nm laser, only on the electrodes pattern (3). The wafer is then immersed into a developer to remove the light-activated regions of the resist (4) (see Fig. 1.8 a). Afterward, 3 nm of titanium and 47 nm of gold are deposited on it in an e-beam evaporator (*Plassys MEB550S*) (5). The excess of gold present on the non-illuminated region (i.e. on the remaining resist) is removed in acetone during the lift-off process, leaving only the electrodes on the wafer (6). The hole pattern is subsequently lithographed by the same process as the electrodes (7-8). The tricky part here, being to align carefully the hole design with the electrodes already present on the wafer, both separated by 12 μm<sup>2</sup>, so they do not overlap (see Fig. 1.8 c). After the development, the resist is removed only on the illuminated hole pattern, the rest of it protecting the substrate from the etching (9). The holes are etched by reactive ion etching (RIE) using argon and CHF<sub>3</sub> to a depth of 400 nm (10). After removing the remaining resist in acetone the substrates are ready to be cut and used (11) (see Fig. 1.8 b).

### 1.2.2 Micro-mechanical cleavage

Van der Waals materials can be cleaved quite easily to the monolayer limit by mechanical exfoliation [94].

In order to obtain high-quality few-layer flakes, we exfoliate starting from bulk FePS<sub>3</sub> and NiPS<sub>3</sub> crystals grown commercially and bought at *2D Semiconductors* (Fig. 1.9 a) or grown in the team

---

<sup>2</sup> Two versions of the substrates will be used in this work, one with a 12 μm space between electrodes and holes and a 4 μm space for the other version.

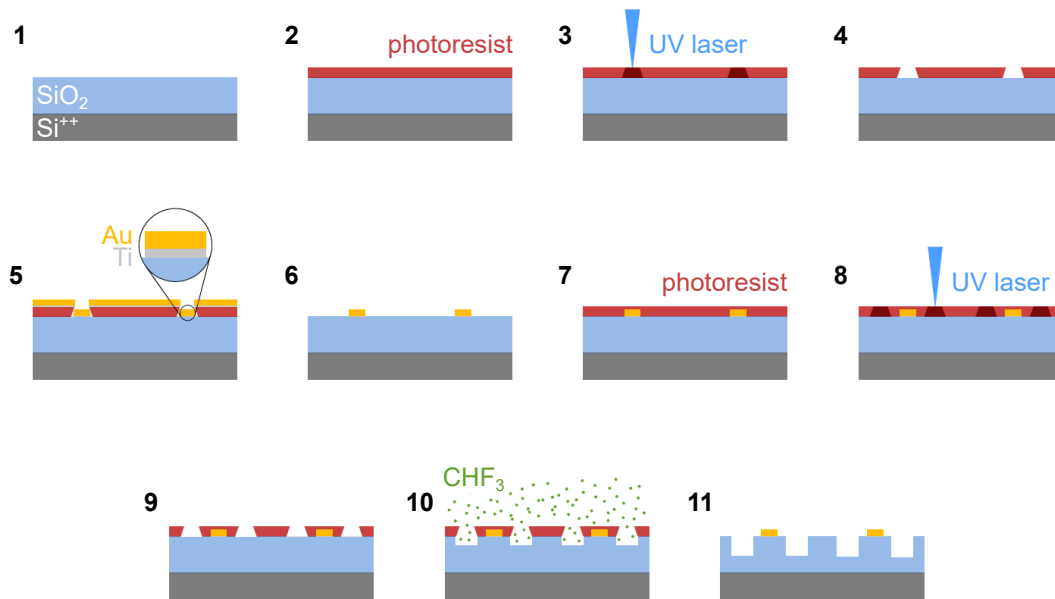


**Figure 1.7: Schematic of the substrate micro-patterning process.** 1-4 Laser lithography of the electrodes design. 5-6 Metallic thin film deposition forming the electrodes. 7-9 Laser lithography of the hole design. 10-11 Reactive ion etching of the holes. Adapted from [20].

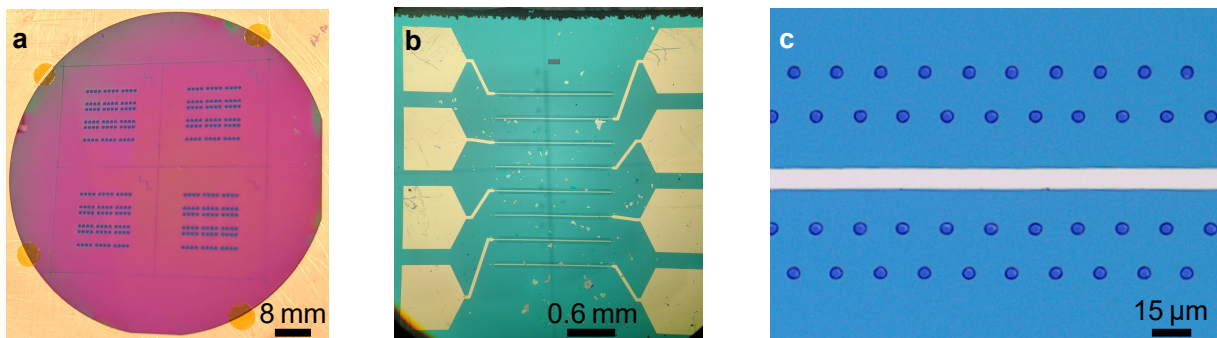


**Figure 1.8: Optical pictures of the substrates during and after the patterning process.** a. A wafer after the development of the electrode design. The electrode pattern is blue and the resist is pink. b. A final  $4 \times 4$  mm cut substrate seen through a binocular magnifier. Adapted from [20]. c. One electrode and its adjacent  $5 \mu\text{m}$ -diameter holes.

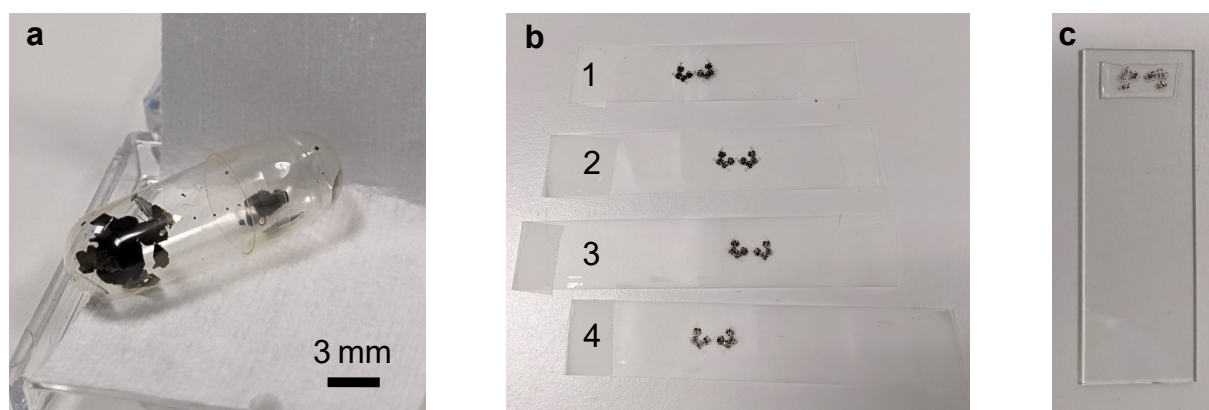


**Figure 1.9: Optical pictures of the exfoliation process.** **a.** Typical  $\text{FePS}_3$  crystals as received from *2D Semiconductors* that are used for exfoliation. **b.** Scotch tapes showing the progressive cleavage of  $\text{NiPS}_3$ , from the bulk crystal start (1) to the final exfoliation (4). **c.** A polymer film stamp on a glass slide after tape #4 removal.

of Damien Voiry at IEM in Montpellier.

For the cleavage process, we first place a piece of the bulk crystal on an scotch tape, then we fold it once to increase the surface and thus the chance to find suitable layers. Contrarily to graphene, for those materials, multiple folding of the scotch tape lead to a lower yield of thin layers, therefore we do not repeat the operation. To thin down the flakes, we apply a second scotch tape on the first one with a gentle pressure to eliminate eventual bubbles, before separating them slowly so that some of the material remains on both of them. We repeat this process until some transparent gray regions appears within the flakes (see Fig. 1.9 b), indicating good probabilities to find thin enough layers. The tape is then stuck and massaged for few minutes on the desired substrate to deposit the flakes.

Two types of substrates are commonly used:  $\text{Si}/\text{SiO}_2$  (usually with 90 nm of oxide for a better contrast) or *DGL* films from *Gel-Pak* (retention x4, 6.5 mil thickness) that is a polymer film similar to polydimethylsiloxane (PDMS). For  $\text{Si}/\text{SiO}_2$ , the substrate and scotch tape can be heated at  $100^\circ\text{C}$  during 1 minute to increase the yield of thin layers, in the case of magnetic materials the heating step has to be done in a glovebox to prevent their oxidation. The adhesive tape has then to be removed as slowly as possible from the substrate to reduce the tape residues. Whereas for *DGL* films, no heating is needed and the tape has to be peeled off fast to get unbroken flakes (Fig. 1.9 c).

The choice of substrate is determined by the exfoliated material and the selected transfer technique. The *DGL* films are preferred for magnetic materials and TMDs because it gives larger flakes than on  $\text{Si}/\text{SiO}_2$ . Whereas it is easier to see graphene and hBN monolayers on  $\text{Si}/\text{SiO}_2$  thanks to a better optical contrast.

The exfoliation process being non-deterministic, multiple substrates have to be carefully checked under a microscope in search of a suitable flake measuring at least  $8\ \mu\text{m} \times 8\ \mu\text{m}$  to cover the hole and consisting from one to fifteen atomic layers depending on the material and its use. At this stage, the flake thickness is determined by optical contrast. Once the ideal layer has been found,

it can be transferred on a patterned substrate.

### 1.2.3 Transfer techniques

Two transfer techniques were employed during this PhD work: the all-dry transfer and the PC method.

#### All-dry transfer

The all-dry transfer technique, popularized in 2014 by Castellanos-Gomez and co-authors [23] and now widely used in the 2D materials community, is based on the viscoelastic properties of the *DGL* films presented previously.

The last scotch tape of the exfoliation is peeled off on a stamp made from one of these films as depicted in Figure 1.9 c. A square of about  $4\text{ mm} \times 4\text{ mm}$  has to be cut around the chosen flake so the film is smaller than the substrate to be transferred to, and the first point of contact between the two will not be too far from the layer to transfer. The stamp can also be pre-cut in squares before the scotch tape deposition to avoid damaging the flake during the cutting of the film.

The transfer of the flake (Fig. 1.11 b) on a prepatterned substrate is then performed using a transfer station. Two of these are available in the cleanroom, one motorized, which was mainly used and will be described here, and one manual, operating in a similar way [143]. The motorized transfer station was designed and assembled in the lab at the beginning of my PhD, it is placed in a glovebox filled with nitrogen or argon for the transfer of air-sensitive materials (see Fig. 1.10).

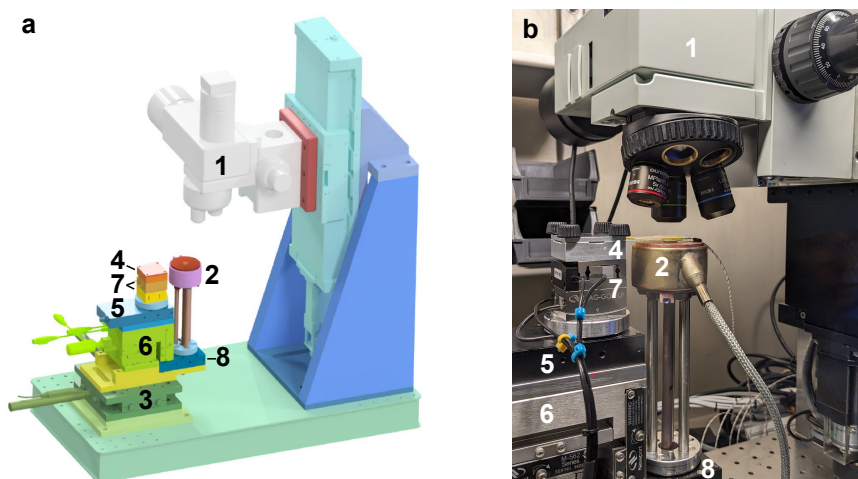


**Figure 1.10: The motorized transfer station.** The labels 1-8 represents different parts of the transfer station and are described in the main text.

The process is monitored through a microscope equipped with three microscope objectives ( $5\times$ ,  $20\times$  and  $50\times$ ) (1) and connected to a camera (CMOS *LC30 Olympus*). The prepatterned substrate is vacuum-fixed on the heating stage (2) using a pump, it can be positioned in *XY* directions with respect to the microscope using a combination of a linear stage and motorized actuators (*Newport M-401 XY Linear Stage & CONEX-TRB12CC*) (3) that are moving the entire stage. The substrate

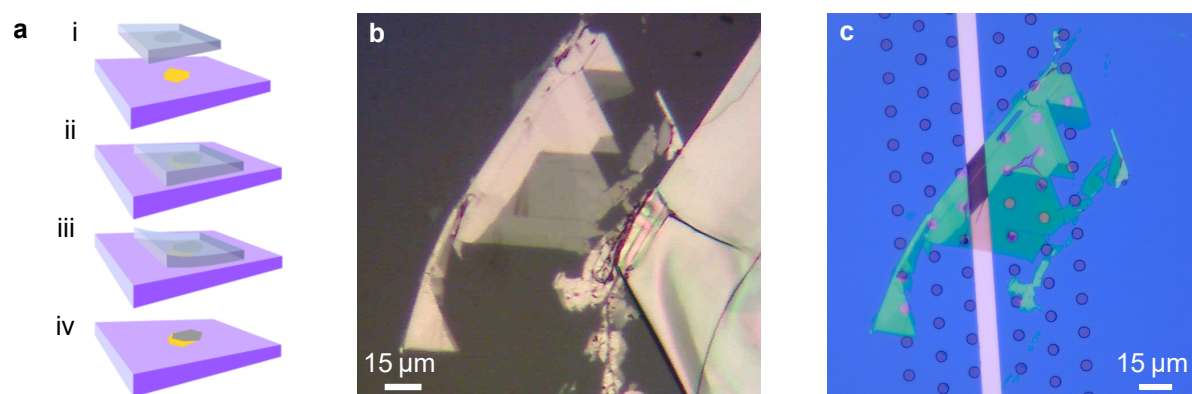


**Figure 1.11: The all-dry transfer method.** **a.** Schematic of the all-dry transfer method. The labels i-iv represent the successive transfer steps. In our case, the yellow flake already present on the substrate can be thought of as a hole. Adapted from [23]. **b.** Optical image of a NiPS<sub>3</sub> flake on *DGL* film before transfer. **c.** Optical image of the same NiPS<sub>3</sub> flake after its all-dry transfer on a prepatterned Si/SiO<sub>2</sub> substrate.

is then scanned to choose an intact electrode and hole(s), usually towards its center. Then, the glass slide is slid and clamped in its holder (4) with its stamp oriented towards the substrate. To help in this task, the upper stage can be automatically rotated by 90° from the loading to the transfer positions using a motorized rotation stage (*Newport PR50CC*) (5). The glass slide and its stamp can be moved in XYZ with respect to the substrate by a combination of linear stage and piezo actuators (*Newport M-562 & PZA12*) (6) to align precisely the flake with the chosen hole and electrode. If necessary, two goniometers (*Newport CONEX-AG-GON-LP/UP*) (7) ensure the rotation of the glass slide around its longest and shortest axis to adjust the approach angle. The angle between the flake and the substrate can also be adjusted by a rotation stage attached to the substrate stage (8) similar to that of the glass slide stage (5).

Once the alignment between the flake and the hole is adequate, the stamp is lowered towards the substrate (see Fig. 1.11 a i). A realignment is usually performed just before the *DGL* film stamp is brought into contact with the substrate. The contact point between the two is performed at 40 °C. The substrate is then heated until the film expands and gently deposits the flake over the hole(s) (ii). The heater is then switched off so the film contracts and removes smoothly (iii) leaving the suspended membrane (iv). To avoid breaking of the flake over the hole it is crucial to lay and retract the *DGL* film as slowly as possible. The glass slide can finally be lifted and removed to finish the transfer. The flake is now suspended over holes and contacted to an electrode (see Fig. 1.11 c).

This method is quick to set up, rather efficient and does not involve any solvent, but is only profitable for making homostructures or heterostructures composed of only two different layers. For each layer one transfer is required and there is a chance to damage the whole structure at each of them. Another limitation is that the transferred material has to adhere sufficiently to the substrate, for example graphene sticks quite poorly to the gold electrodes so it often breaks or stays on the *DGL* film. The solution to those challenges is to perform the transfer with the PC method.

### Transfer with the PC method

The PC method, also called pick-up technique, is more challenging to implement but extremely powerful to fabricate sophisticated van der Waals heterostructures. The different layers are stacked one by one on a polybisphenol A carbonate (PC) film before being deposited on a prepatterned substrate by melting of this film.

First the PC stamp has to be fabricated. A small *DGL* film square of about  $2\text{ mm} \times 2\text{ mm}$  is placed on a glass slide and recovered by a labmade PC film [144] stretched over a hole in a kapton tape (that can resist high temperatures) (see Fig. 1.12 a i-ii). The stamp is then heated to  $200\text{ }^\circ\text{C}$  on a hot plate for 30 seconds to adhere the PC film to the *DGL* film, no bubble or wrinkles should be present between the two, otherwise the film may tear during transfer. The PC stamp is now ready for use.

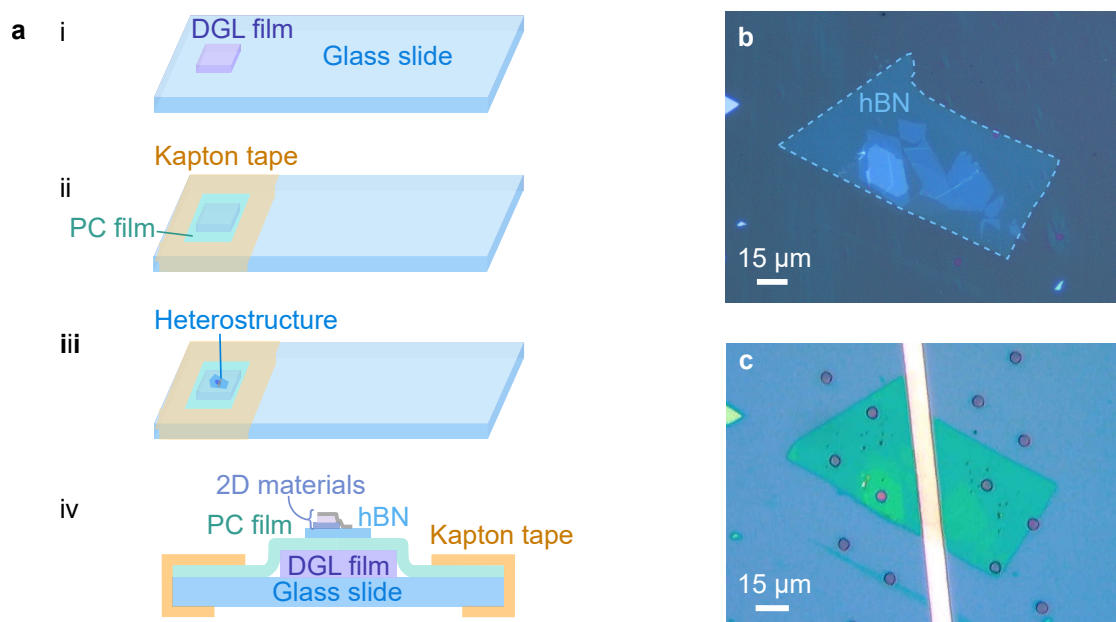


**Figure 1.12: The PC transfer method.** a. Schematic of the PC transfer method. i-ii. Fabrication of the PC stamp. iii. The stamp after the heterostructure pick-up. iv. Side view of iii. b. Optical picture of a heterostructure on the PC film after pick-up. c. The same heterostructure after transfer on a prepatterned substrate and removal of the PC film.

A flake of the desired material can then be picked up by the PC film. Usually, the first flake of the heterostructure is hBN, because it will protect the other materials from the PC residues and overall from the chloroform used to dissolve the PC film at the end of the process.

The glass slide with the PC stamp is clamped in its holder in the transfer station, the substrate with the hBN flake to pick up is fixed on the heating stage. The PC film is brought carefully into contact with the flake and the substrate is heated to  $80\text{ }^\circ\text{C}$  to reach the film glass transition. If some bubbles are still present the temperature can be increased to  $100\text{ }^\circ\text{C}$  to make them disappear. The film is then removed from the substrate, taking with it the hBN flake, using the Z translation of the piezo motors. It has to be done slowly but continuously, as stopping could cause the flake to crack. This pick-up step is repeated for each layer to be included in the heterostructure (see

Fig. 1.12 **a** iii-iv and **b**). When the heterostructure is formed on the PC stamp the final transfer step can be performed. A prepatterned substrate is placed on the heating stage and the PC film is brought into contact. The deposition of the flake is made by the *DGL* film dilatation with the increase of temperature to suspend the heterostructure delicately over a hole as for the all-dry technique. But here, we increase the temperature to 180 °C to melt the PC film. When the glass slide is withdrawn, only the *DGL* film stays on it, the melted PC and the heterostructure being deposited on the substrate. Finally, the sample is left during a night in a sealed vial of chloroform to dissolve the PC film (see Fig. 1.12 **c**).

Important note: for some magnetic materials, in our case FePS<sub>3</sub>, the pick-up by a hBN flake was not successful. A solution found is to perform the pick up of the magnetic material with a TMD monolayer, here WS<sub>2</sub>, instead of hBN. A monolayer TMD is then added to the heterostructure between the hBN and the magnetic material. This procedure was employed for the sample *Fantadwich* (see 1.2.4).

One of the drawbacks of these two transfer methods is the presence of hydrocarbon residues between and on the layers in the finished sample due to the use of polymers in the fabrication process. This issue is notably addressed by the team of R. Gorbachev in [145], where they use, instead of a PC film stamp on a glass slide, a polymer-free gold-coated silicon nitride cantilever to perform the transfer. Another point of attention is the strain induced by the transfer process in the sample, including the formation of wrinkles more or less pronounced on the suspended flakes leading to non-ideal membranes. A possible solution would be to anneal the suspended samples to reduce or even suppress the wrinkles [146, 147], however this was not tried here for concern of damaging the air-sensitive magnetic materials.

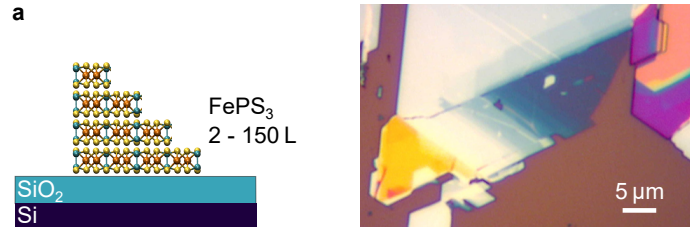
## 1.2.4 Sample list

We describe here all the samples discussed in the manuscript.

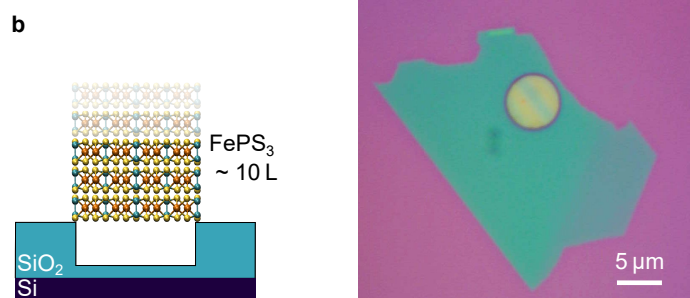
### FePS<sub>3</sub> samples

*Ocean*: supported FePS<sub>3</sub> flakes in a staircase geometry with a thickness from 2 (dark blue) to  $\sim 150$  (pink) layers.

Referred to in sub-section 1.4.4.



*Whale*: suspended FePS<sub>3</sub> flake of approximately 10 layers, not contacted. Referred to in sub-sections 1.5.2 and 1.5.3.



*Fantadwich*: suspended and contacted FePS<sub>3</sub>-based heterostructure. It is composed of (from bottom to top) a bilayer graphene, 5 layers of FePS<sub>3</sub>, a WS<sub>2</sub> monolayer and approximately 15 layers of hexagonal boron nitride. The graphene is employed to obtain a better conduction from the electrode. As explained previously (1.2.3) the WS<sub>2</sub> monolayer is used to pick up the FePS<sub>3</sub> flake.

Referred to in sub-section 1.5.3, section 2.1, and section 3.3.

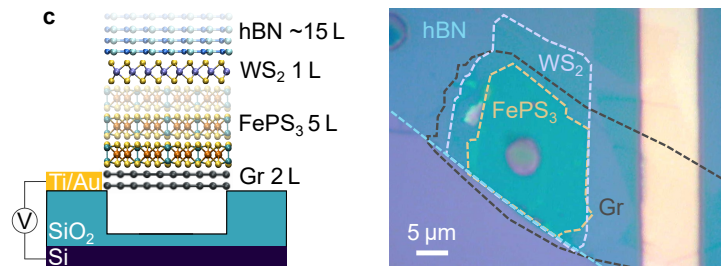
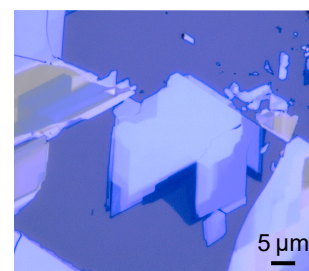
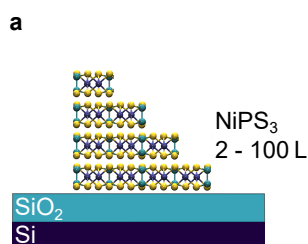


**Figure 1.13:** Scheme (left) and optical picture (right) of the samples **a. Ocean**, **b. Whale** and **c. Fantadwich**. The schemes are not to scale and are only intended to show the different layers composing the sample.

### NiPS<sub>3</sub> samples

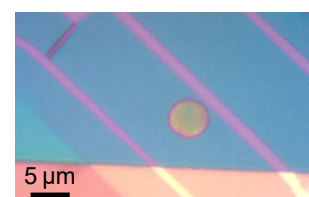
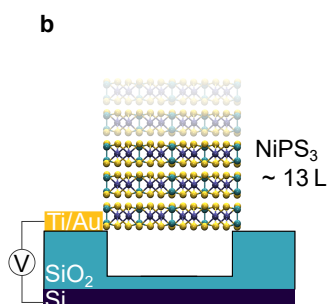
*PacMan*: supported NiPS<sub>3</sub> flakes in a staircase geometry with a thickness from 2 (dark violet) to ~ 100 (green) layers.

Referred to in sub-section 1.4.4 and sub-section 4.1.1.



*Mordor*: suspended and contacted NiPS<sub>3</sub> flake of approximately 13 layers.

Referred to in sub-section 1.5.3, section 2.2 and section 3.2.2.



*Balor*: suspended and contacted NiPS<sub>3</sub> flake of approximately 10 layers. Two drums can be measured: drum 1 and drum 2.

Referred to in subsection 2.2.1, section 3.1, section 4.2 and section 4.3.

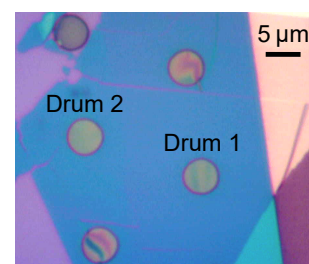
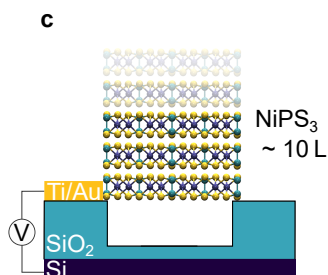


**Figure 1.14:** Scheme (left) and optical picture (right) of the samples a. *PacMan*, b. *Mordor* and c. *Balor*. The schemes are not to scale and are only intended to show the different layers composing the sample.

## 1.3 Experimental setup

In the previous part, we have seen how the samples are fabricated, we will now take a look at the experimental setup to carry out measurements on them. To perform these experiments around or below the phase transition temperatures of  $\text{FePS}_3$  and  $\text{NiPS}_3$  the samples are placed in a cryostat.

### 1.3.1 The heart of the setup: the cryostat

Two different cryostats in two separate rooms are used within the team. One is a helium closed-cycle *attodry 800* from *attocube* integrated into an optical table, the other is a continuous flow cryostat from *Cryo Industries of America* (CIA) that operates with liquid helium.

#### The CIA cryostat

The sample is inserted into the cryostat head in contact with a cold finger (see Fig. 1.15 a). A socket for electrically contacted samples is present but not used in the case of the picture, where the sample is not fixed in a chip carrier. The cryostat is then closed and firmly mounted on a platform that can be moved by mechanical translations (1) in the XYZ directions (see Fig. 1.15 b). The vacuum is made via a valve (2) by primary and turbo pumps. When a pressure of  $10^{-4}$  mbar is reached, the liquid helium can be pumped from a bottle through the cryostat. The temperature is controlled by a *cryo-con 32B* and can reach around 10 K. A window at the bottom of the cryostat head (3) ensures an optical access for the light coming from the rest of the setup, that is focused by a *Mitutoyo M Plan APO NIR B 50x* objective (4) with a numerical aperture (N.A.) of 0.65 and a 10 mm working distance. The objective can be moved finely (with 0.5 nm resolution) by a XY piezostage (5) (*Physik Instrumente P-527*) to perform spatially-resolved measurements on the sample.

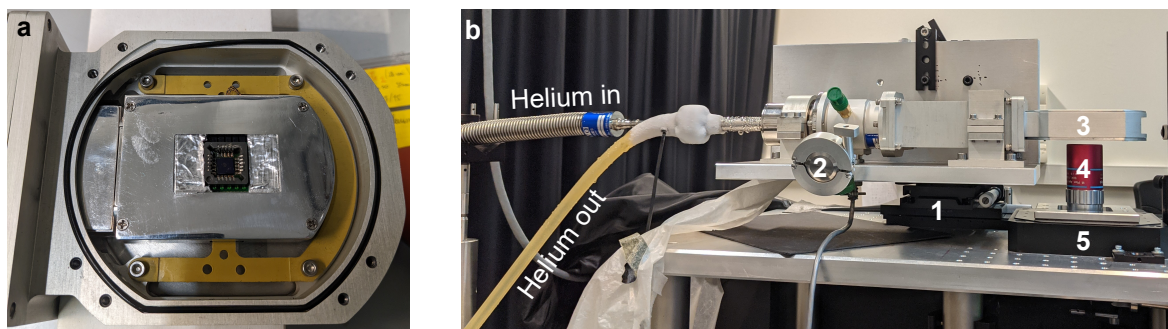


**Figure 1.15: Optical pictures of the CIA cryostat.** a. Head interior containing a sample. b. The cryostat in operation. The labels on the picture indicate: 1 the mechanical translations in the XYZ directions, 2 the valve used to pump the cryostat, 3 the head of the cryostat where the sample sits, 4 the 50 $\times$  microscope objective and 5 the XY piezostage.

Swapping sample in this cryostat is easy and quick, making it ideal for a first characterization. It was used in this way to study the supported samples *Ocean* and *PacMan* and the suspended

sample *Whale* (see Sample list 1.2.4). However, considering its poor spatial stability at low temperatures (drift greater than 2 micrometers after one hour), partly due to the fact that the microscope objective is at room temperature, and the difficulty to maintain a defined temperature, its use is not relevant to perform long measurement campaigns at intermediate temperatures as it will be needed to probe the phase transitions of  $\text{FePS}_3$  and  $\text{NiPS}_3$ .

### The attoDRY 800 cryostat

The attoDRY 800 cryostat was installed at the end of 2020 and is composed of a *Sumitomo RDK-101D* cryocooler (A) (Fig. 1.16 a) inserted in an *attocube*-designed receptacle (B) allowing it to be embedded in an optical table for space optimization (see Fig. 1.16 b). It operates in a helium closed-cycle, resulting in a great thermal stability with weeks of operation at its base temperature.

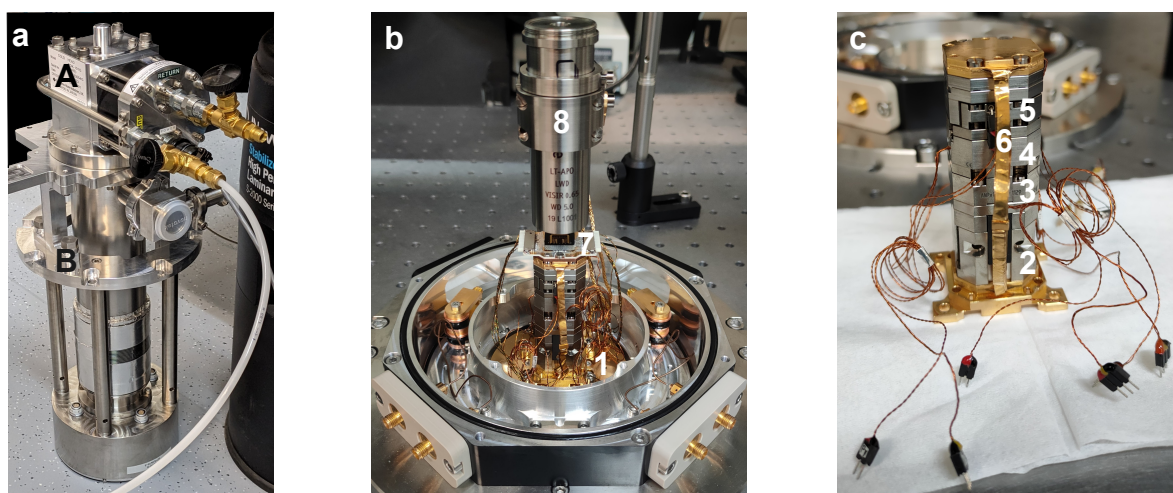


**Figure 1.16: Optical pictures of the attodry cryostat and its components.** a. The cryostat out of its housing during a maintenance. The labels represent: A the *Sumitomo* cryocooler and B the receptacle for embedding it in the optical table. b. Inside of the open sample chamber of the cryostat. The labels represent: 1 the base plate, 7 the sample holder with a printed circuit board (PCB) and 8 the cryo-compatible microscope objective. c. Unplugged nanopositioners and thermal coupler stack. The labels represent: 2 the z positioner, 3,4 the x and y positioners respectively, 5 the xy scanner and 6 the thermal coupler.

The visible part of the cooling system is the base plate (1) maintained at 4 K. On it, is fixed the stack of *attocube* cryo-compatible piezoelectric positioners detailed on Figure 1.16 c. The first three from the bottom are linear nanopositioners with resistive readout and a maximum resolution of 200 nm: (2) being an *ANPz102* with 4.8 mm travel range used as z positioner and (3,4) being *ANPx101* with 5 mm travel range used as x and y positioners. The top one (5) is a xy scanner *ANSxy100lr* with sub-nanometer resolution and a  $30 \times 30 \mu\text{m}$  scanning range at 4 K that becomes  $50 \times 50 \mu\text{m}$  range at room temperature. The linear nanopositioners are used to search for the desired flake on the sample and adjust the focus, while the scanners allows to realize precise mapping of a sample region. The thermal link between the cold plate (1) and the top of the stack, where the sample sits, is realized by an *attocube Thermal Coupler (ATC)* (6) composed of two

thermally connected copper plates. The top plate is equipped with a temperature sensor and a heater. This configuration allows to reach temperatures at the sample between 4 to 250 K with a precision of at least 100 mK that are stable for days while the cryostat is running.

On top of the ATC upper plate is screwed a modified sample holder with a printed circuit board (PCB) (7) designed by Jérémy Thoraval, a research engineer at IPCMS. To electrically contact our samples, they are glued with silver paint and wire-bonded in a commercial chip carrier that can be mounted into the PCB, connecting it to the breakout box of the cryostat. The breakout box is used to choose the pin of the chip carrier, that will correspond to the sample electrode or the bottom of the substrate, on which to apply an electric voltage. Above the sample holder stands a cryo-compatible long working distance *attocube* microscope objective (*LT-APO/LWD*) (8) with 0.65 N.A. and 5 mm working distance for illumination and light collection. The combination between the closed-cycle technology, a cryo-compatible microscope objective and the titanium-built piezo positioners results in a spatial stability way higher than the one of the *CIA* cryostat, no drift being visible after few days of measurement at the same spot.

Before a cool-down is launched, the cryostat is closed by a thermal shield and a vacuum shroud (see Fig. 1.17) and pumped by a primary and turbo pumps until  $10^{-4}$  mbar. This cryostat was used for measurements campaigns on the samples *Fantadwich*, *Mordor* and *Balor* (see Sample list 1.2.4).

### 1.3.2 Around the cryostat: Optical excitation path and signal collection

This subsection describes the setup shown in Figures 1.17 and 1.18 built around the *attodry* cryostat, the setup including the *CIA* cryostat is designed in a similar fashion.

This setup was designed and mounted by L. Moczko a previous PhD student of the team, after the installation of the *attodry 800* cryostat, for similar measurements to those performed in this work but on different systems.

#### Illumination path

Two continuous lasers are used to probe the sample: a 632.8 nm helium-neon (*LASOS LGK 7665 P18*) with 18 mW power, and a 532 nm diode laser (*Cobolt Samba 0532-04-01*) with 50 mW power. The power arriving at the sample is reduced to values ranging from 1 to 500  $\mu$ W by varying the angle of a half-wave plate ( $\lambda/2$ ), which modifies the light intensity coming out of a polarized beam splitter (PBS) placed after it, and by adding neutral densities on the laser path. On the green laser path, an acousto-optic modulator (*AA MT350-A0,2-VIS*) allows light intensity modulation at a given frequency, that is used to optically drive the membrane motion. The two lenses between the mirrors  $M_5$  and  $M_6$  are forming a beam expander, so the laser spot diameter matches the one of the microscope objective opening to benefit fully of its numerical aperture and get a smaller laser spot size (see Eq. 1.12). Moreover, this beam expander is slightly defocused to correct the focus difference at the sample between the green and red lasers in order to measure

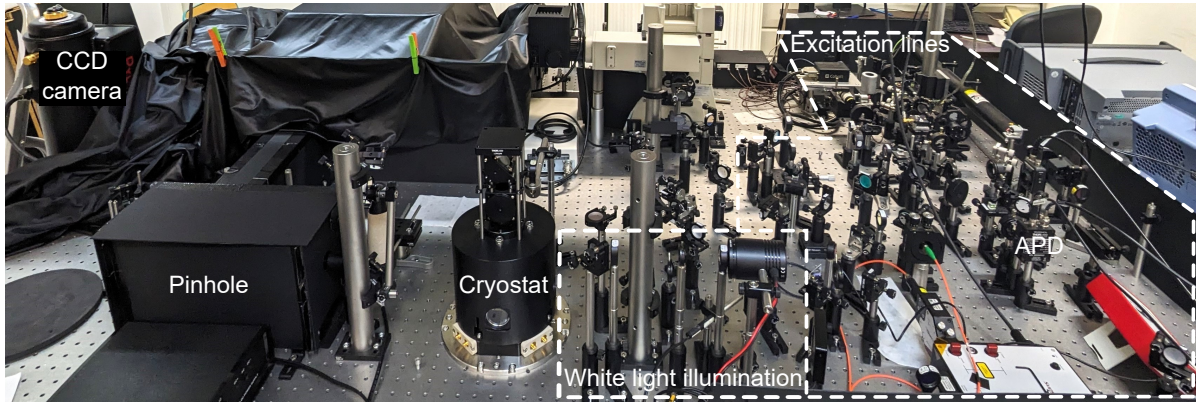


**Figure 1.17:** Optical picture of the experimental setup built around the *attodry* cryostat.

with both of them at the same time.

For the light to pass straight through the microscope objective, the laser beams have to be aligned using two mirrors:  $M_2$  and  $M_3$  for the 633 nm laser and  $M_5$  and DM 532 for the green laser. DM 532 (*Semrock LPD02-532RU-25x36x1.1*) is a dichroic mirror coated to reflect only at a wavelength of 532 nm, so the red laser beam can pass through. The laser beams are thus focused on the sample, resulting in a diffraction-limited spot with a minimum lateral spotsizes  $\Delta x$  given by the Abbe diffraction limit for an optical microscope [148]

$$\Delta x = 0.61 \frac{\lambda}{\text{NA}} \quad (1.12)$$

with  $\lambda$  the wavelength and NA the objective numerical aperture. Considering the case of the 633 nm laser with the 0.65 N.A. microscope objective in the *attodry* cryostat, we could reach an optimal spotsizes of 595 nm.

A white light source is used to image the sample, its path substitutes that of the laser thanks to flippable elements (represented by a curved double arrow on the scheme of Figure 1.18). The light source is first spatially filtered by an assembly of two lenses and an iris, before being focused at the bottom focal plane of the microscope objective to obtain a large and uniform illumination of the sample. The collected light is then sent to a camera via a flip mirror.

### Signal collection for optical spectroscopy

The light reflected, scattered and emitted by the sample is collected by the same microscope objective used for illumination and transmitted through the 50/50 beam splitter. It is then spatially filtered by a 125  $\mu\text{m}$  pinhole conjugated with the focal point on the sample, allowing to reduce unwanted contributions to the signal coming from the substrate. A long-pass filter (LPF), at 532 (*Semrock LP03-532RE-25*) or 633 nm (*Semrock LP03-633RE-25*), placed in front of the spectrometer is greatly reducing the laser line intensity to avoid saturating the CCD camera. The filtered light is then collimated and sent to a monochromator (*Acton SP2500*) to obtain the spectral decomposition of the light around a given wavelength. Three gratings with a different

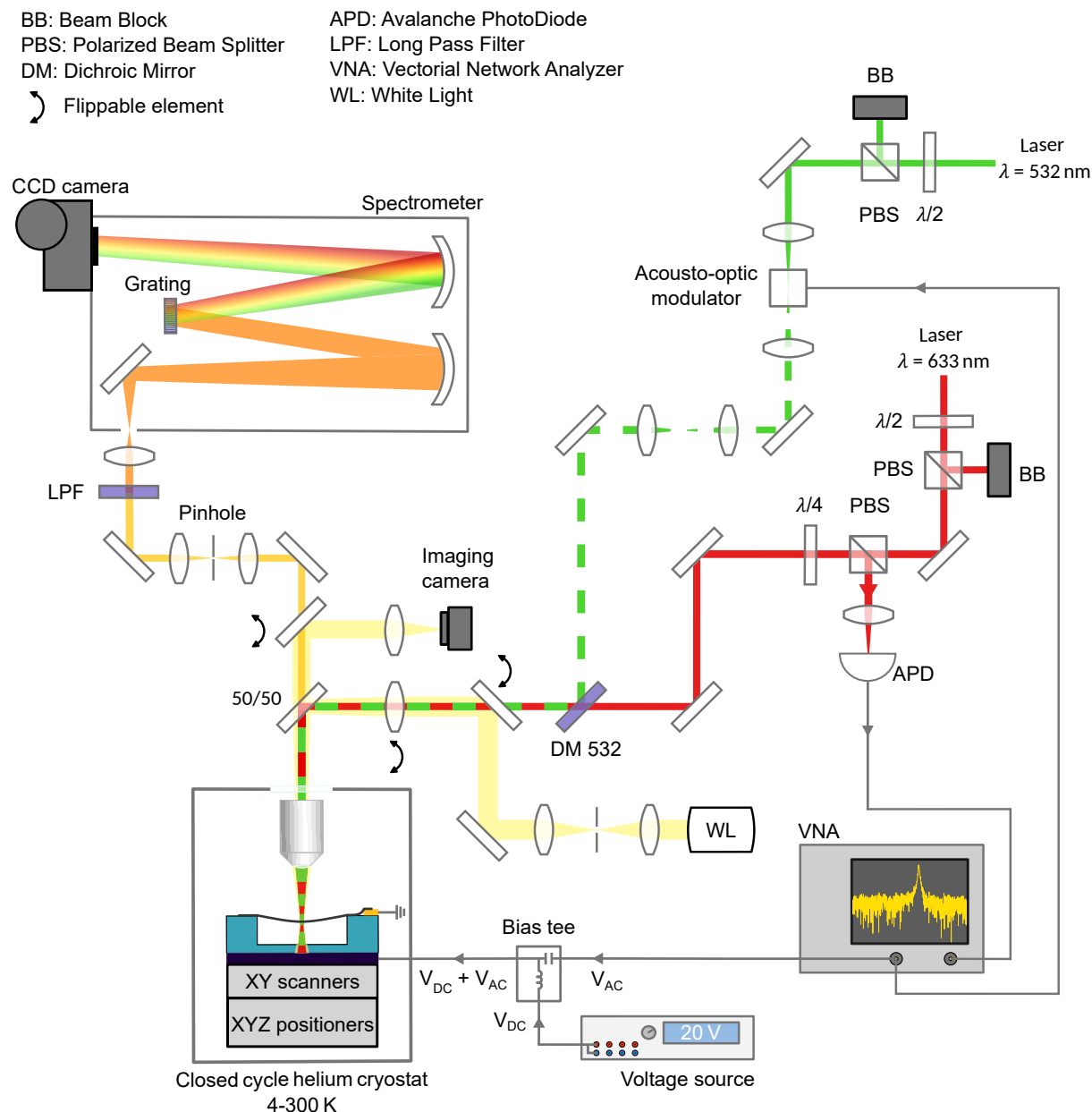


**Figure 1.18:** Detailed schematic of the experimental setup built around the attody cryostat.

number of grooves are available: 150 gr/mm, 600 gr/mm and 1800 gr/mm. The higher the number of grooves, the greater the spectral resolution but the smaller the spectral range and the longer the acquisition time. The diffracted light is finally collected on a nitrogen-cooled CCD camera (*Princeton Instrument PyLoN VIS/NIR 1340 $\times$ 100*).

### Polarization-resolved measurements

Polarization-resolved measurements are discussed in Section 2.2.2 and extensively in Chapter 4. To realize those experiments, the laser light polarization is defined by a polarizer added after the dichroic mirror (DM 532) and can be rotated using a half-wave plate placed right after the polarizer. An analyzer, that selects a given polarization of the light scattered or emitted by

the sample, is placed between the pinhole and the long-pass filter. Finally, the grating being polarization-sensitive, a half-wave plate, placed after the analyzer, ensures that the light always enters the spectrometer with the same polarization.

Three types of polarization-resolved measurements were performed during this PhD work. First in subsection 2.2.2, the spectra taken in co-polarization (same incident and collection polarizations) and cross-polarization (orthogonal incident and collection polarizations) are compared. In subsection 4.2.2, the polarization of the emitted light is determined by fixing the incident polarization and rotating by  $360^\circ$  the collection polarization. Finally in section 4.3, both incident and collection polarization are rotated simultaneously.

#### Signal collection for nanomechanics

The motion of the membrane is detected by optical interferometry between the light reflected by both the membrane and the substrate (more information in Section 1.5.2). This light is collected thanks to a circulator formed by a PBS and a quarter-wave plate ( $\lambda/4$ ) on the path of the 633 nm laser. On the outward path, the light acquires a circular polarization passing through the quarter-wave plate, whose handedness is then reversed by reflection on the sample. On the return path, the light polarization is thus relinearized by the quarter-wave plate with a polarization orthogonal to the incident one. As a result, the light coming back from the sample is reflected by the PBS (and no more transmitted) and focused on an avalanche photodiode (*Thorlabs APD 430A2/M*). The resulting electric signal is sent to a vector network analyzer (VNA) (*Keysight ENA E5080B*) or, in a previous version of the setup, to a lock-in amplifier (*Zurich Instrument ZI-HFLI*). The VNA RF source allows to drive the motion of the membrane by applying an alternative voltage ( $V_{AC}$ ), added to a continuous voltage ( $V_{DC}$ ) coming from a power supply (*Rohde & Schwarz NGP800*) by a lab-made bias tee, to the substrate or the electrode of the sample. In order to probe the Brownian motion of the membrane the signal coming out from the photodiode can also be sent to a spectrum analyzer (*Rohde & Schwarz FSL3*). The output voltage of the photodiode is simultaneously acquired by an oscilloscope (*Rohde & Schwarz RTB2004*) to perform DC reflectivity maps of the sample.

#### 1.3.3 Setup interfacing and auto-positioning

During my PhD, we developed the interfacing of the setup using the *VISA* (Virtual Instrument Software Architecture) standard and Python as a programming language and achieved the control of all our measurement devices (except the monochromator). This was crucial for the implementation of an auto-positioning on the membrane that was needed for the temperature ramps performed in Chapters 2 and 3. The position on a given spot of the membrane is maintained, despite the spatial drift between two values of temperature, by reconstructing the membrane contour on a laser reflectivity map. Indeed, when illuminated by the red laser, the suspended area has a higher reflectivity than the supported one (see Fig. 1.19 a). The center of the membrane is first found by

successively fitting a Gaussian function to  $x$  and  $y$  sections in the middle of the photodiode output voltage map and extracting its center coordinates and linewidth (see Fig. 1.19 **b**). The radius  $r$  of the apparent membrane is then estimated as the average distance to the center of reflectivity values being equal to a given percentage of the maximum reflectivity. Knowing the coordinates of the membrane center and its radius allows to position on the desired spot. We thus corrected linear drifts of about 7 V along  $x$  and 8 V along  $y$  which correspond to around 2.3  $\mu\text{m}$  and 2.7  $\mu\text{m}$ , respectively, for a 60 K temperature shift shown as an illustration in Figure 1.19.

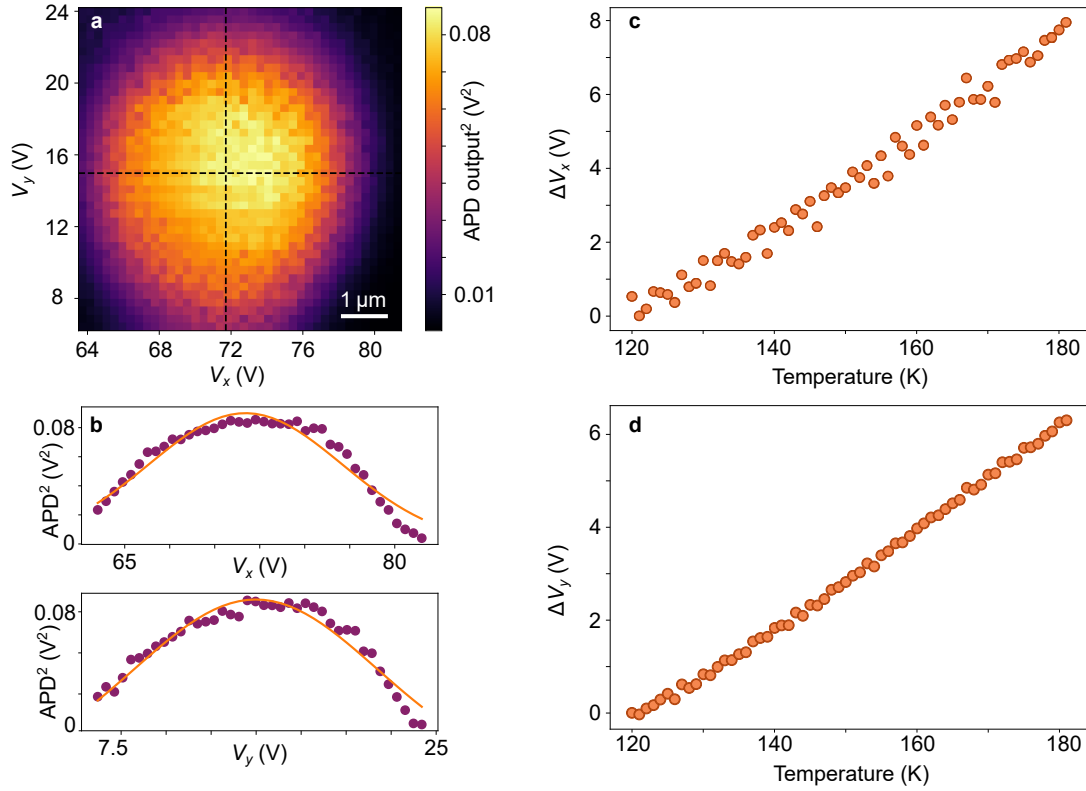


**Figure 1.19: The auto-positioning procedure.** **a.** Map of the photodiode output voltage (proportional to the laser reflectivity) squared for a suspended sample. The voltages  $V_x$ ,  $V_y$  are the ones applied to the scanners. The dotted lines indicates the center of the membrane (15.0 V, 71.7 V) found using the Gaussian fit. **b.** Reflectivity profiles along the dotted lines indicated on **a**. The dots are the data and the solid lines are the Gaussian fits. **c,d.** Voltage correction applied to the scanner along  $x,y$ -axis, respectively, as a function of temperature.

Moreover, motorized polarizer rotators (*standa 8MPR16-1*) were added to the setup for automated polarization and laser power ramps. The interfacing of the setup combined with the temperature stability of the cryostat and the spatial stability of both made it possible to launch autonomous measurements over several days.

## 1.4 Raman spectroscopy of $\text{MPS}_3$

Raman spectroscopy uses inelastic light scattering that has been first observed by C.V. Raman and K.S. Krishnan in 1928 using sunlight [149], leading to the Nobel prize for Raman in 1930. Raman scattering has become a standard powerful spectroscopic tool whether in chemistry to identify substances from their distinctive spectral patterns, or in condensed matter physics to characterize lattice vibrations and so, access physical properties of a sample like crystal orientation, phase transitions or doping.

### 1.4.1 Raman scattering processes

The incident light on a sample is mainly transmitted or absorbed by it, with only a tiny proportion scattered by crystal inhomogeneities. The dominant scattering process is the elastic scattering, called *Rayleigh* scattering, in which the energy of a scattered photon is the same as the energy of an incident one. On the other hand, inelastic scattering occurs when the incident photon interacts with a dynamic scatterer that modifies its energy. It is a weak process, only one photon over  $10^6 - 10^8$  which scatters is Raman scattered [150]. Here, we will describe the process for scattering of a photon by lattice vibrations, the quantum of which is called phonon, but it can also be inelastically scattered by spin-waves [151] or electronic states, the later corresponding to electronic Raman scattering [152].

Raman scattering is usually performed with visible light at frequencies between 350 - 750 THz that correspond to  $10\,000 - 30\,000\text{ cm}^{-1}$  or 1 - 4 eV, whereas the phonon frequencies are ranging from 3 - 30 THz ( $100 - 1\,000\text{ cm}^{-1}$  or 10 - 100 meV) [151], the discrepancy between these values results in a very weak photon-phonon interaction. The interaction between an incident photon and a phonon is thus essentially mediated by electrons.

The microscopic processes behind Rayleigh and first-order Raman scattering are depicted on Figure 1.20 and their descriptions are based on [153, 154].

For the Rayleigh process, an incident photon of frequency  $\omega_i$  is creating an electron-hole pair and excites the system from its ground state  $|G\rangle$  to a virtual state  $|V\rangle$ . The virtual state not being a stationary state of the system, the electron-hole pair recombines quickly, emitting a photon of frequency  $\omega_s = \omega_i$ . This process is responsible for the most intense central line at the incident frequency (i.e. the laser frequency) on the spectrum depicted on Figure 1.21.

For each one-phonon Raman process, an incident photon is also absorbed and a scattered photon emitted but, in addition, a phonon is involved in the scattering process. The incident photon can either undergo a *Stokes* process, leading to the creation of a phonon and the emission of a photon with a lower energy  $\hbar\omega_s = \hbar\omega_i - \hbar\Omega$  than the incident one. Otherwise, the incident photon can find the system into an excited vibrational state  $|E_v\rangle$  thanks to an absorbed phonon leading to the emission of a scattered photon with a higher energy  $\hbar\omega_s = \hbar\omega_i + \hbar\Omega$  than the incident one, corresponding to the *anti-Stokes* process. Scattering processes are instantaneous so the

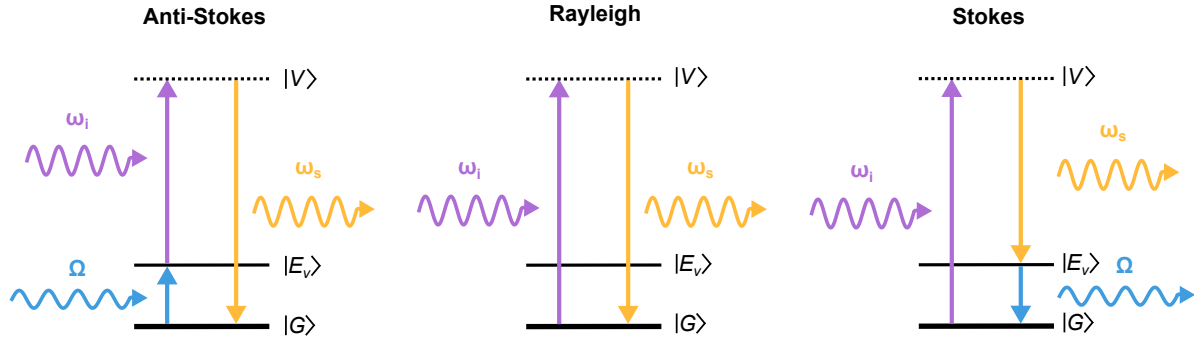


**Figure 1.20:** Scheme from left to right of anti-Stokes, Rayleigh and Stokes microscopic processes. Three energy levels are represented:  $|G\rangle$  is the ground state,  $|E_v\rangle$  is an excited vibrational state and  $|V\rangle$  is a virtual state. In purple are the transitions corresponding to the incident photon, in orange to the scattered photon and in blue to the phonon. Adapted from [155].

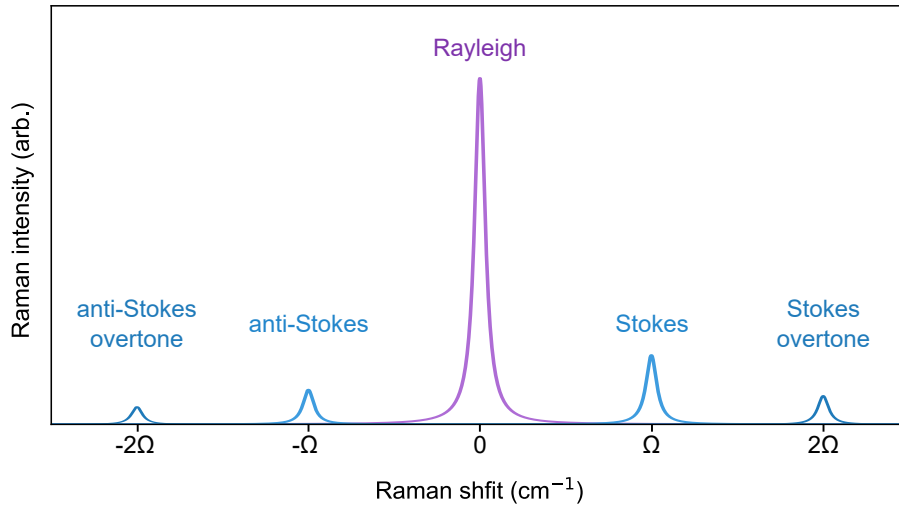


**Figure 1.21:** Schematic of a typical Raman spectrum representing its Rayleigh, first-order and second-order Stokes and anti-Stokes lines. Adapted from [155].

transitions described above can occur in any time order. In the general case, and in the context of this thesis, the virtual state  $|V\rangle$  is not a real state of the system, however, the excitation frequency can be chosen to match an electronic transition and give rise to *resonant* Raman scattering in which the intensities are strongly enhanced.

A schematic of a typical Raman spectrum is displayed on Figure 1.21, it is usually plotted as a function of the Raman shift  $\delta = \omega_i - \omega_s$ , that is the difference between the frequencies of incident and scattered light, and expressed as a wavenumber in  $\text{cm}^{-1}$ . The Stokes and anti-Stokes components are evenly spaced by  $\pm\Omega$  on either side of the laser line (corresponding to the Rayleigh peak). The integrated intensities  $I_S$  and  $I_{AS}$  of these two components are different and their ratio can be computed using the Boltzmann distribution. The Stokes integrated intensity is proportional to  $n_v + 1$ , with  $n_v$  the average number of phonons given by the Bose-Einstein distribution

$$n_v = \frac{1}{\exp(\hbar\Omega/k_B T) - 1}, \quad (1.13)$$

whereas the anti-Stokes integrated intensity is proportional to  $n_v$  [153]. The ratio of the integrated intensities is then  $I_{AS}/I_S = \exp(-\hbar\Omega/k_B T) \sim 10^{-1} - 10^{-4}$  at room temperature for the above-mentioned phonon frequencies, implying that the anti-Stokes component is weaker than the Stokes one, this ratio tends to zero at 10 K. As a consequence, generally, and as will be the case in this manuscript, only the Stokes part of the Raman spectrum is measured. Nevertheless, the ratio between Stokes and anti-Stokes peak intensities can be used to determine the phonons temperature.

In the above scattering processes, the conservation of both energy and momentum are leading to

$$\begin{cases} \omega_i &= \omega_s \pm \Omega \\ \mathbf{k}_i &= \mathbf{k}_s \pm \mathbf{q} \end{cases} \quad (1.14)$$

with  $\mathbf{k}_i$ ,  $\mathbf{k}_s$  and  $\mathbf{q}$  the wavevectors of the incident light, scattered light and phonon, respectively. The + corresponds to the Stokes process (i.e. the emission of a phonon) and the - to the anti-Stokes process (i.e. the absorption of a phonon). Considering visible light, these relations impose a maximal value for the phonon wavevector of around  $10^6$ - $10^7$  m<sup>-1</sup>, that is way smaller than the size of the Brillouin zone ( $2\pi/a \sim 1.06 \times 10^{10}$  m<sup>-1</sup> with  $a$  being around 5.94 Å for FePS<sub>3</sub> [110]). As a consequence, the phonons probed by first-order Raman spectroscopy are the ones at the center of the Brillouin zone (i.e. at the  $\Gamma$  point) and with a near-zero wavevector  $\mathbf{q} \sim \mathbf{0}$ .

Nevertheless, second-order Raman scattering processes (i.e. two phonons scattering) can also occur [151]. It can be either two successive first-order Raman processes, implying that both of them have to fulfill Eq 1.14 and the frequency shift of the second-order peak should be the sum or the difference of the shift in the first-order spectra. If the two involved phonons belong to the same branches the obtained feature is called an overtone, the overtones of all phonons with  $\mathbf{q} = \mathbf{0}$  are Raman-active (see Fig. 1.21). Or, another possibility is that the light can interact with two phonons in a single event. The sum of the two phonons wavevectors has then to be close to zero to fulfill the conservation equations, but they can individually span the entire Brillouin zone.

Now we know that zone-center phonons are probed using first-order Raman spectroscopy, we will discuss Raman activity, i.e. which phonon modes can we expect to detect with Raman spectroscopy and how do these modes depend on the polarization conditions.

## 1.4.2 Phonons dispersion curves

The atomic vibrations of the lattice depend on its crystalline structure. Considering a Bravais lattice we can focus only on its unit cell, the one of the MPS<sub>3</sub> being depicted on Figure 1.2 b. We first recall that it contains  $N = 10$  atoms that will results in  $3N = 30$  phonon modes. To obtain an indication on the symmetry of these modes, the symmetries of the unit cell are classified using group theory to attribute a point group to it. We will not go into the details of group theory here, more information can be found in [155, 156]. A MPS<sub>3</sub> monolayer in its paramagnetic phase

	$E$	$2C_3$	$3C_2$	$i$	$2S_6$	$3\sigma_h$
$A_{1g}$	1	1	1	1	1	1
$A_{2g}$	1	1	-1	1	1	-1
$E_g$	2	-1	0	2	-1	0
$A_{1u}$	1	1	1	-1	-1	-1
$A_{2u}$	1	1	-1	-1	-1	1
$E_{1u}$	2	-1	0	-2	1	0

**Table 1.4:** Character table of the  $D_{3d}$  point group. Extracted from [24]

	$E$	$3C_2$	$i$	$3\sigma_h$
$A_g$	1	1	1	1
$B_g$	1	-1	1	-1
$A_u$	1	1	-1	-1
$B_u$	1	-1	-1	1

**Table 1.5:** Character table of the  $C_{2h}$  point group. Extracted from [24]

possessing, among others, a 3-fold rotational symmetry and an inversion center, is assigned to the point group  $D_{3d}$ . However, if we consider a few-layer flake, the monoclinic stacking of the planes breaks the symmetry along the  $c$  axis (see Fig. 1.1 c) and the corresponding point group becomes  $C_{2h}$  [25].

To each point group is associated a character table (see Tables 1.4 & 1.5) linking the symmetry operations of the group (top row labels) to its irreducible representations (left-hand column). Each phonon mode can be characterized by an irreducible representation. The characters are equal to +1 or -1 depending whether the lattice vibration is symmetric or anti-symmetric, respectively, under the symmetry operation [155]. The symmetry operations common to both point groups are  $E$  the identity,  $C_n$  a clockwise rotation around an axis by  $\frac{2\pi}{n}$ , here  $n = 2$  so a  $\pi$  rotation,  $i$  an inversion and  $\sigma_h$  a reflection about a plane perpendicular to the principle axis of the unit cell. The  $D_{3d}$  point group is of a higher symmetry than the  $C_{2h}$ , so it possesses two additional symmetry operations that are  $C_3$  clockwise rotations of  $\frac{2\pi}{3}$  and  $S_6$  rotations of  $\frac{\pi}{3}$  followed by a reflection through a plane perpendicular to the rotation axis.

There are as many irreducible representations of the point group as there are symmetry classes in it, i.e. 4 for the  $C_{2h}$  point group and 6 for the  $D_{3d}$  point group. The labels  $A$  and  $B$  indicate a phonon symmetric, anti-symmetric, respectively, to the principal axis  $C_n$ , whereas a label  $E$  designates a doubly degenerate vibrational mode. Since these modes are doubly degenerate a  $\pm 2$  or a 0 can appear in their row of the character table. The subscripts  $g$  (from 'gerade') and  $u$  (from 'ungerade') correspond to symmetric, anti-symmetric modes, respectively, with regard to the inversion center of the unit cell.

Using these character tables, the 30 zone-center phonons of  $MPS_3$  can be classified by their

irreducible representation  $\Gamma$  as

$$\Gamma_{D_{3d}} = 3A_{1g} + 2A_{2g} + A_{1u} + 4A_{2u} + 5E_g + 5E_u \quad (1.15)$$

for a monolayer [25] and as

$$\Gamma_{C_{2h}} = 8A_g + 6A_u + 7B_g + 9B_u \quad (1.16)$$

for a multilayer [157].

To obtain an estimation of the lattice vibration modes frequencies, phonons dispersion curves (i.e. phonon frequency plotted as a function of its wavevector) can be calculated by a force-constant model [153] like in a 1988 paper from Bernasconi *et al.* [25] or more recently, simulated using first-principle calculations like in the work of Hashemi *et al.* [24] or Kagar *et al.* [157]. The phonon dispersion curves thus obtained for non-magnetic and antiferromagnetically-ordered bulk  $\text{FePS}_3$  and  $\text{NiPS}_3$  are shown in Figure 1.22.

The distribution in frequency of the phonon modes is similar in all cases and is typical from the  $\text{MPS}_3$  family in general [24]. We observe first a high density of phonons with frequencies below  $300 \text{ cm}^{-1}$ , including three with a frequency close to zero at the  $\Gamma$  point that are the acoustic phonons. Then between  $350$  and  $450 \text{ cm}^{-1}$  we find two relatively flat bands, before a more dense region between  $500$  and  $600 \text{ cm}^{-1}$ . As we can see from the projection of the phonon eigenvector to each of the atoms in Figure 1.22 d, the lattice vibrations with frequencies above  $300 \text{ cm}^{-1}$  involves essentially sulfur and phosphorus atoms from the  $\text{P}_2\text{S}_6$  structure (see Fig. 1.2 a). While phonons with lower frequencies include motion of the sulfur and transition metal atoms. We also observe a doubling of phonon modes number for antiferromagnetic  $\text{FePS}_3$  and  $\text{NiPS}_3$  induced by the doubling of the unit cell in the antiferromagnetic phase (see Fig. 1.1 a and Sec. 1.1.2).

Nevertheless, only some of these phonons are detected by Raman spectroscopy due to selection rules that will be detailed in the following.

### 1.4.3 Raman tensor and selection rules

The intensity of the scattered light  $I_s$  for a given vibrational mode depends on the polarization of the incident and scattered radiations with unit vectors  $e_i$ ,  $e_s$ , respectively, and of the corresponding Raman tensor  $\mathcal{R}$  as [151]

$$I_s \propto |e_i \cdot \mathcal{R} \cdot e_s|^2. \quad (1.17)$$

For a phonon mode to be visible on the first-order Raman spectrum, both its associated Raman tensor has to be non-zero, the mode is then called Raman-active, and the polarization configuration must lead to a non-zero scalar product.

The Raman tensor is a second rank tensor and can be considered symmetric if we neglect the frequencies  $\Omega$  of the phonons compared to light frequencies  $\omega_i$ ,  $\omega_s$ . It is thus linked to the

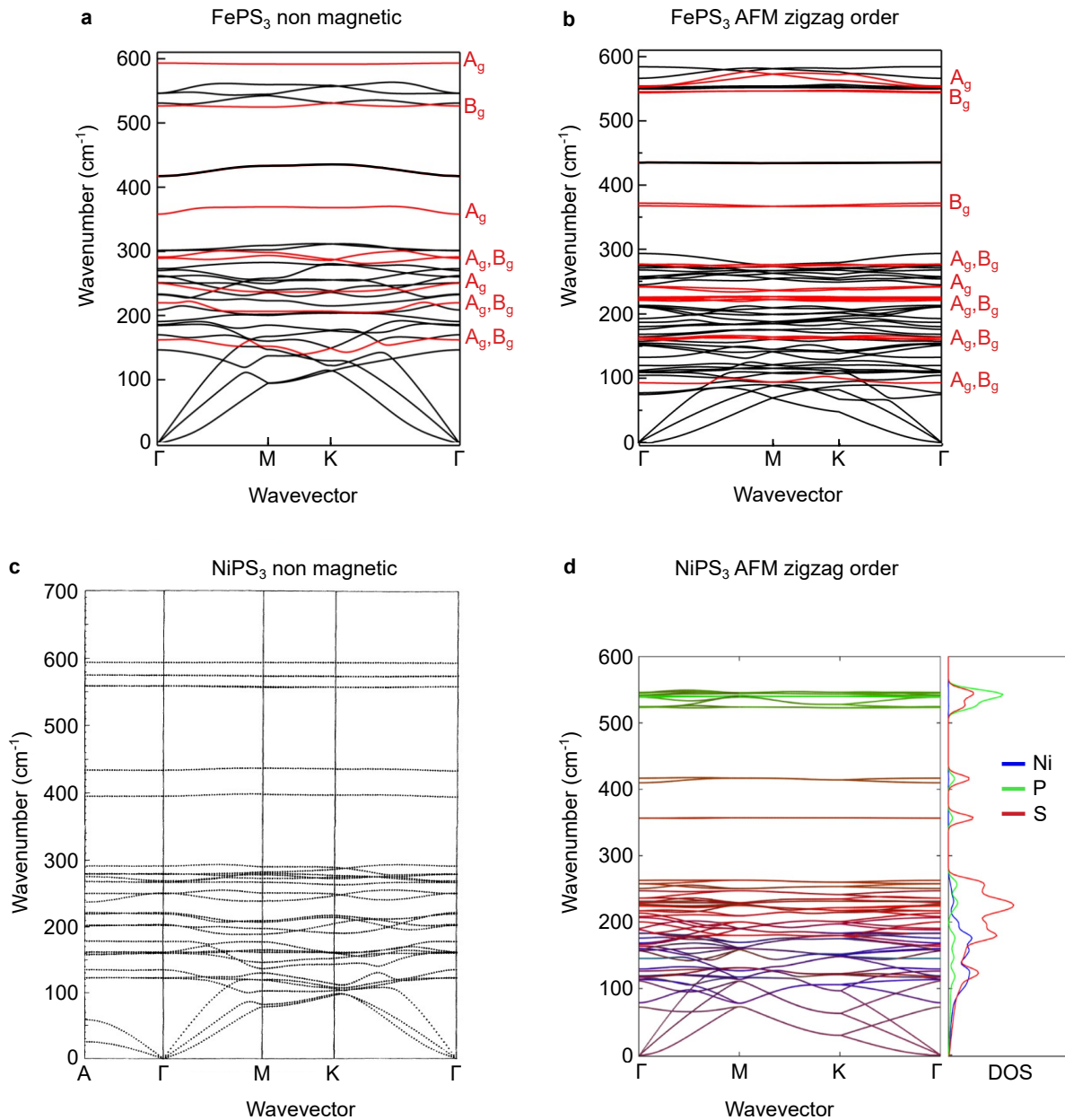


**Figure 1.22: FePS<sub>3</sub> and NiPS<sub>3</sub> phonon dispersion curves between high symmetry points of the Brillouin zone.** **a.** For FePS<sub>3</sub> in its paramagnetic phase. **b.** For FePS<sub>3</sub> in its zigzag antiferromagnetic phase. The red curves represent the phonons experimentally observed using Raman scattering with visible light in [157]. **c.** For NiPS<sub>3</sub> in its paramagnetic phase. **d.** For NiPS<sub>3</sub> in its antiferromagnetic phase. The colors are representing the main atomic contribution to the phonon mode among nickel (blue), phosphorus (green) and sulfur (red) atoms. In the right panel is displayed the partial phonon density of states. **a** and **b** are adapted from [157], **c** from [25] and **d** from [24].

polarizability tensor  $\alpha$  associated with the electron in the crystal by [151]

$$\mathcal{R}_{yz}^x \propto - \left( \frac{\partial \alpha_{zy}}{\partial r_x} \right)_{r=0} \quad (1.18)$$

where  $r$  is the relative displacement amplitude of the three sub-lattices (one sub-lattice per atomic element) and  $x$ ,  $y$  and  $z$  are orthogonal axes which coincide with principal axes of the crystal. The two subscripts on  $\mathcal{R}$  are the polarization directions of the incident and scattered photons, respectively, while the superscript is the axis on which the phonon displacement is considered. As a result, the Raman tensor is non-zero only if the lattice vibration induces a change of polarizability in the unit cell. For unit cells possessing an inversion symmetry, such as the one of  $\text{MPS}_3$ , the Raman tensor is symmetric under inversion and therefore couples only initial and final state of similar parity. The anti-symmetric modes with a "u" subscript (see Tables 1.4,1.5) are thus Raman-inactive, whereas the symmetric modes with a "g" subscript are Raman-active, halving the number of phonon modes visible in the Raman spectrum of  $\text{MPS}_3$  [156].

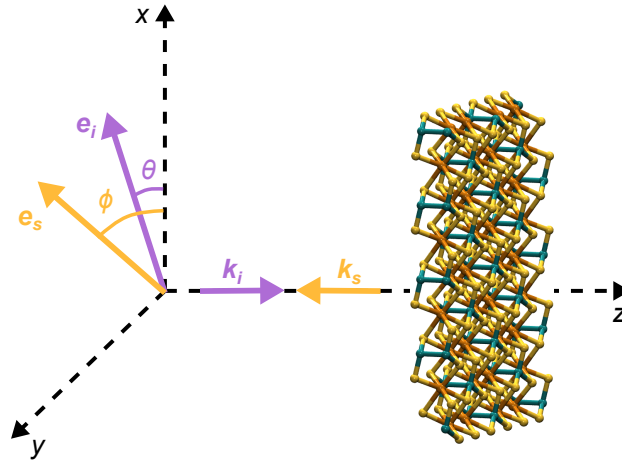


**Figure 1.23:** Scheme of the backscattering configuration used in Raman spectroscopy measurements.  $x, y$  and  $z$  represents the principal axes of the  $\text{FePS}_3$  crystal. The incident light has a wavevector  $k_i$  oriented along the  $z$ -axis and a polarization vector  $e_i$  forming an angle  $\theta$  with the  $x$ -axis. The resulting scattered light has a wavevector  $k_s$  along the  $z$ -axis and a polarization vector  $e_s$  forming an angle  $\phi$  with the  $x$ -axis. Adapted from [155].

The Raman tensors associated with Raman-active vibrational symmetries according to their crystal point group are tabulated in [151] as  $3 \times 3$  matrices. For the  $C_{2h}$  point group, i.e. multi-layer  $\text{MPS}_3$ , the Raman tensors for the  $A_g$  and  $B_g$  active modes are

$$\mathcal{R}(A_g) = \begin{pmatrix} a & \cdot & d \\ \cdot & b & \cdot \\ d & \cdot & c \end{pmatrix} \quad \text{and} \quad \mathcal{R}(B_g) = \begin{pmatrix} \cdot & e & \cdot \\ e & \cdot & f \\ \cdot & f & \cdot \end{pmatrix} \quad (1.19)$$

where  $a - f$  are the major terms and the other terms denoted by "." are expected to be zero on the

basis of symmetry. We are focusing here on the intensities of multi-layer  $\text{MPS}_3$  Raman spectrum components since no monolayer will be investigated in this work.

Our experimental setup is built in the common backscattering configuration (see Fig. 1.23), where both incident and scattered light travel along the  $z$ -axis with their polarization vectors contained in the  $xy$ -plane. The polarization unitary vectors are then expressed by  $e_i = (\cos(\theta), \sin(\theta), 0)$  and  $e_s = (\cos(\phi), \sin(\phi), 0)$  with  $\theta$  and  $\phi$  their angles with the  $x$ -axis, represented in Figure 1.23. We deduce then the following relationships for the scattered intensities

$$I_s(A_g) \propto |a \cos(\theta) \cos(\phi) + b \sin(\theta) \sin(\phi)|^2 \quad (1.20)$$

$$I_s(B_g) \propto |e|^2 |\sin(\theta) \cos(\phi) + \cos(\theta) \sin(\phi)|^2. \quad (1.21)$$

Both  $A_g$  and  $B_g$  modes are allowed in the polarization configuration used in our measurements, meaning that at maximum 15 modes should be visible in the Raman spectrum.

#### 1.4.4 Interpretation of $\text{MPS}_3$ typical spectrum

Raman spectra of  $\text{FePS}_3$  and  $\text{NiPS}_3$  were acquired at room temperature, by experimental methods described in section 1.3.2, on a bulk part of supported  $\text{FePS}_3$  and  $\text{NiPS}_3$  samples (*Ocean* and *PacMan*, see Sample list 1.2.4) to obtain an intense signal (see Fig. 1.24).

For each sample, the Raman spectrum consists of six peaks that are labeled according to the literature (see Tables 1.6 and 1.7) [25, 157, 158]. This number is much lower than the expected maximum of 15 peaks.

The main reason for that is the occurrence of five  $A_g$ ,  $B_g$  degenerate modes that can be assigned from the phonon dispersion bands calculations (see Fig. 1.22) and also from polarization-resolved measurements [14, 95]. Indeed, the degenerate  $A_g$ ,  $B_g$  modes are not polarized due to the opposite symmetry of their  $A_g$  and  $B_g$  components (see Eq. (1.20) and (1.21)), whereas the non-degenerate  $A_g$  modes remain polarized.

The other reason is the frequency ranges considered in our measurements that are excluding one peak in each case: the  $A_g^1$ ,  $B_g^1$  mode for  $\text{NiPS}_3$  that should appear at around  $120 \text{ cm}^{-1}$ , and the  $A_g^8$  mode for  $\text{FePS}_3$  that we should detect around  $579 \text{ cm}^{-1}$  at room temperature. In addition, the two other  $B_g$  expected modes were never reported.

Finally, eight phonon modes are visible in the Raman spectrum of both  $\text{NiPS}_3$  and  $\text{FePS}_3$  at room temperature, even if the  $\text{NiPS}_3$   $A_g^7$ ,  $B_g^7$  mode has a very low intensity and has been rarely reported [32, 158].

The obtained spectra actually resemble to what would have been expected for a  $D_{3d}$  point group representation (see Eq. (1.15)), i.e. the point group for a  $\text{MPS}_3$  monolayer, with three peaks corresponding to  $A_{1g}$  modes and five peaks to  $E_g$  modes (the  $A_{2g}$  are not Raman-active). This indicates a low effect of the monoclinic stacking on phonon frequencies, probably linked to the weak van der Waals interlayer coupling. In some publications [24, 159], the  $\text{MPS}_3$  peaks are then

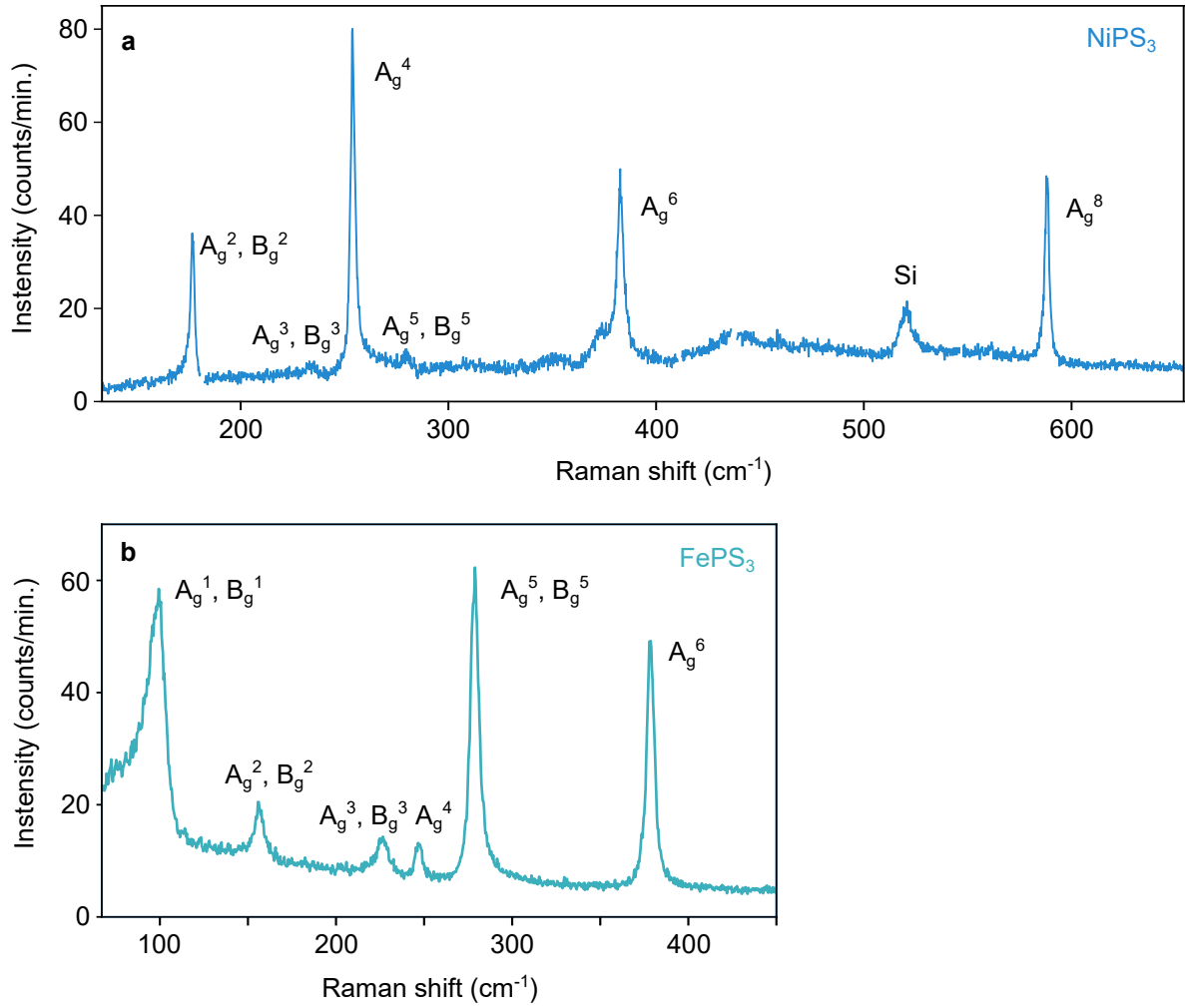


**Figure 1.24: Raman spectra of bulk FePS<sub>3</sub> and NiPS<sub>3</sub> at room temperature.** **a.** Raman spectrum of NiPS<sub>3</sub> for a laser wavelength of  $\lambda = 632.8$  nm. The peak labeled "Si" originates from the substrate. **b.** Raman spectrum of FePS<sub>3</sub> for a laser wavelength of  $\lambda = 532.1$  nm. The peaks are labeled with the associated phonon symmetries (see Tables 1.6 and 1.7).

labeled with the phonon symmetries of the  $D_{3h}$  point group.

The values of the phonon modes frequencies of NiPS<sub>3</sub> and FePS<sub>3</sub> from our study, presented in Tables 1.6 and 1.7, were obtained from fits of the Raman spectra peaks by Voigt profiles (see Section B). There are in very good agreement with those reported in the literature.

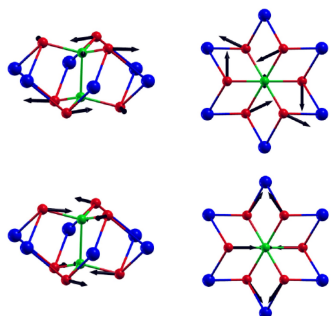
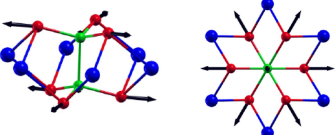
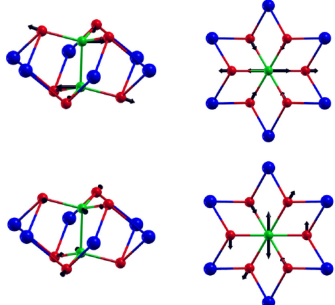
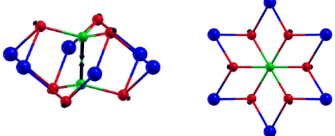
If we now compare the two spectra, we observe that the phonon modes with the same symmetries are located around the same frequencies in each of them, but with a drastic change in their intensities making them appear clearly distinct. In both cases, the peaks with a Raman shift higher than  $200\text{ cm}^{-1}$  are generally attributed to vibrations involving mostly sulfur and phosphorus atoms from the P<sub>2</sub>S<sub>6</sub> unit, whereas the two lower frequency modes are from vibrations including transition metal atoms [24, 25]. This can also be seen on the phonon dispersion curve of Figure 1.22 d where the different atomic contributions to the phonon branches have been highlighted in different colors. Schematic representations of the atomic displacements associated to these Raman-active phonon modes have been proposed in the same paper by Hashemi *et*

*al.* [24], using the  $D_{3d}$  point group irreducible representation, and are reproduced in Tables 1.6 and 1.7. Different schematic representations calculated exclusively for FePS<sub>3</sub> can be found in [157].

In this section, the fundamentals of Raman spectroscopy have been reviewed and the origin of MPS<sub>3</sub> Raman-active phonons has been elucidated. This will become useful in Chapter 2 to understand how magnetic phase transitions are probed with Raman spectroscopy.

Symmetry	Mode frequency	$\text{NiPS}_3$	$\text{FePS}_3$	Atomic displacements viewed from side (left) and top (right)
$A_g^1, B_g^1$	This work Reported Calculated	N.O. N.O. 122	98.4 98 107	
$A_g^2, B_g^2$	This work Reported Calculated	176.8 176.1 160	156.4 158 162, 170	
$A_g^3, B_{\sigma}^3$	This work Reported Calculated	234 233.2 204	226.4 226 209, 220	
$A_g^4$	This work Reported Calculated	254.0 254.2 250	247.0 247 250	

**Table 1.6: Symmetries, frequencies and schematic representation of  $\text{FePS}_3$  and  $\text{NiPS}_3$  Raman-active phonon modes at room temperature.** All the values are in  $\text{cm}^{-1}$ . N.O. signifies that the mode has not been observed experimentally. The comparative values for  $\text{NiPS}_3$  phonon frequencies are from [158] for experiments and [25] for calculations, and the ones for  $\text{FePS}_3$  are from [157] for both experiment and calculations (except for the first mode where the calculated value is from [25]). The representations of the atomic vibrational modes are extracted from [24].

Symmetry	Mode frequency	NiPS <sub>3</sub>	FePS <sub>3</sub>	Atomic displacements viewed from side (left) and top (right)
A <sub>g</sub> <sup>5</sup> , B <sub>g</sub> <sup>5</sup>	This work Reported Calculated	280 279.8 280	278.7 279 290, 291	
A <sub>g</sub> <sup>6</sup>	This work Reported Calculated	382.8 383.7 395	378.6 380 358	
A <sub>g</sub> <sup>7</sup> , B <sub>g</sub> <sup>7</sup>	This work Reported Calculated	N.O. N.O. 559	N.O. N.O. 526	
A <sub>g</sub> <sup>8</sup>	This work Reported Calculated	588.2 588.8 594	N.O. 579 593	

**Table 1.7: Symmetries, frequencies and schematic representation of FePS<sub>3</sub> and NiPS<sub>3</sub> Raman-active phonon modes at room temperature.** All the values are in cm<sup>-1</sup>. N.O. signifies that the mode has not been observed experimentally. The comparative values for NiPS<sub>3</sub> phonon frequencies are from [158] for experiments and [25] for calculations, and the ones for FePS<sub>3</sub> are from [157] for both experiment and calculations. The representations of the atomic vibrational modes are extracted from [24].

## 1.5 Nano-optomechanics of suspended van der Waals materials

### 1.5.1 Dynamics of a circular suspended film

We consider a nanoresonator constituted of a van der Waals material flake suspended over a circular hole as illustrated on Figure 29. The aim here is to describe the mechanical motion of this drum-like resonator.

#### Decomposition in normal vibration modes

The motion of a suspended film can be characterized by a time-dependent displacement vector field. In the case of small amplitude out-of-plane motion, the in-plane motion can be neglected so that the displacement vector field reduces to a scalar field  $\xi(r, \varphi)$  describing the out-of-plane displacement in the  $z$ -direction. The total out-of-plane motion of the membrane can be decomposed into a superposition of its linear eigenmodes as [130, 160]

$$\xi(r, \varphi, t) = \sum_n z_n(t) u_n(r, \varphi) \quad (1.22)$$

where  $u_n(r, \varphi)$  is the  $n$ -th mode spatial profile and  $z_n(t)$  is a function that describes the time dependence of the resonator's motion. We choose to normalize the spatial profiles  $u_n(r, \varphi)$  such that their maximum absolute value is unity, ensuring that  $z_n(t)$  represents the maximum deflection of the mode  $n$ . To describe the total motion of the membrane we will then need to derive the expression of its normal modes spatial profiles  $u_n(r, \varphi)$  and their displacement amplitude  $z_n(t)$ .

#### Normal modes spatial profiles and resonant frequencies

The spatial profiles of the normal modes are obtained by solving the differential equation of the suspended flake motion, that is obtained by minimization of its total energy.

The total energy  $E_{\text{tot}}$  of the suspended film is given by the sum of its kinetic  $E_{\text{kin}}$  and potential energies as  $E_{\text{tot}} = E_{\text{kin}} + U_b + U_s$ , where the potential energy is composed of a bending contribution  $U_b$  and a stretching contribution  $U_s$ . These energies can be expressed as [130, 161]

$$E_{\text{kin}} = \frac{\rho h}{2} \int_{\mathcal{A}} d^2\mathbf{r} \left( \frac{\partial \xi(\mathbf{r}, t)}{\partial t} \right)^2 \quad (1.23)$$

$$U_b = \frac{\kappa}{2} \int_{\mathcal{A}} d^2\mathbf{r} |\Delta \xi(\mathbf{r}, t)|^2 \quad (1.24)$$

$$U_s = \frac{\sigma h}{2} \int_{\mathcal{A}} d^2\mathbf{r} |\nabla \xi(\mathbf{r}, t)|^2 \quad (1.25)$$

where  $\xi(\mathbf{r}, t)$  is the out-of-plane displacement introduced previously with  $\mathbf{r} = (r, \varphi)$ ,  $\mathcal{A}$  is the film area,  $h$  is the film thickness, while  $\rho$ ,  $\kappa$  and  $\sigma$  are the mass density, the bending rigidity defined in Eq. (1.7) and the tension in the film, respectively.

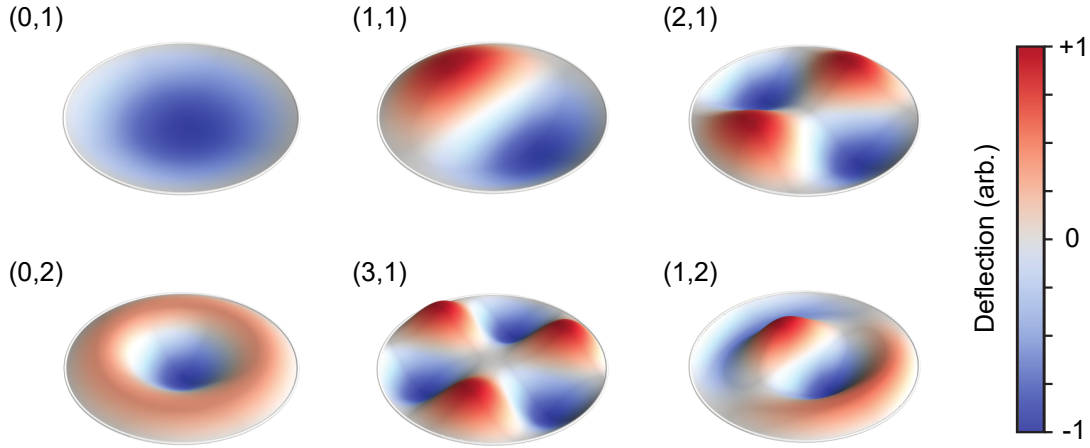


**Figure 1.25:** Calculated spatial profiles of the six first mechanical modes of a circular thin film from Eq. (1.30). The mode  $(m,n)$  presents  $m$  diametrical nodal lines and  $n - 1$  circular nodes.

A variational minimization of the total energy leads to the following differential equation of motion [161]

$$\frac{\kappa}{h} \nabla^4 \xi(\mathbf{r}, t) - \sigma \nabla^2 \xi(\mathbf{r}, t) + \rho \frac{\partial^2 \xi(\mathbf{r}, t)}{\partial t^2} = 0. \quad (1.26)$$

This equation can be solved using the variable separation method and postulating an oscillating solution of the form  $\xi(r, \varphi, t) = \text{Re}(u(r, \varphi)e^{-i\Omega t})$ , with  $\Omega$  being the angular frequency. The equation of motion for the spatial part  $u(r, \varphi)$  can then be written as

$$(\nabla^2 + \alpha_+^2)(\nabla^2 - \alpha_-^2)u(r, \varphi) = 0 \quad (1.27)$$

where

$$\alpha_{\pm}^2 = -\frac{h}{2\kappa} \left( \pm\sigma - \sqrt{\sigma^2 + \frac{4\rho\kappa\Omega^2}{h}} \right). \quad (1.28)$$

The general solution to Equation (1.27) writes [162]

$$u(r, \varphi) = \cos(m\varphi)[A_m J_m(\alpha_+ r) + B_m I_m(\alpha_- r)] \quad (1.29)$$

where  $J_m$  represents the  $m$ -th order spherical Bessel function of the first kind and  $I_m$  the  $m$ -th order modified spherical Bessel function of the first kind [163] with  $\alpha_- r$  as an imaginary argument and  $A_m, B_m$  are normalization constants. However, the function  $I_m$  diverges as  $r \rightarrow 0$ , so it is discarded for physical reasons [160, 162].

Considering the boundary conditions, the edges of the film are clamped at  $r = R$ , with  $R$  its radius, so we should have  $J_m(\alpha_+ R) = 0$ . This implies that the values of  $\alpha_+ R$  must be equal to the  $n$ -th root  $\alpha_{mn}$  of the  $J_m$  Bessel function. The mode spatial profiles are then given by [162, 164]

$$u_{mn}(r, \varphi) = A_m \cos(m\varphi) J_m \left( \frac{\alpha_{mn} r}{R} \right) \quad (1.30)$$

where  $A_m$  is a normalization constant chosen such as that the maximum value of  $u_{mn}(r, \varphi)$  is

unity. The theoretical profiles of the six lower modes thus obtained are shown in Figure 1.25. The corresponding eigenfrequencies are estimated as [161]

$$f_{mn} = \frac{\alpha_{mn}}{2\pi} \sqrt{\frac{\sigma}{\rho R^2} + \frac{\alpha_{mn}^2 \kappa}{\rho h R^4}}. \quad (1.31)$$

### Plate and membrane regimes

In the normal mode frequencies expression of Equation (1.31), we note two terms corresponding to the two limiting behaviors of a thin film: the membrane regime where the behavior of the film is dominated by the tension  $\sigma$  and the plate regime where the behavior of the film is dominated by its bending rigidity  $\kappa$ . We will now check which regime can be used to describe the thin films we are studying.

We can re-express the frequencies of equation (1.31) in order to display the membrane and plate terms as

$$f_{mn} = \sqrt{f_{\text{membrane}}^2 + f_{\text{plate}}^2} \quad (1.32)$$

with [105]

$$f_{\text{membrane}} = \frac{\alpha_{mn}}{2\pi R} \sqrt{\frac{\sigma_s}{h\rho}}, \quad (1.33)$$

$$f_{\text{plate}} = \frac{\alpha_{mn}^2 h}{4\pi R^2} \sqrt{\frac{E}{3\rho(1-\nu^2)}}. \quad (1.34)$$

where we use the expression of the bulk modulus  $\kappa = Eh^3/12(1-\nu^2)$  and replaced the film tension by its surface value  $\sigma_s$  divided by its thickness  $h$ .

In Figure 1.26 is shown the fundamental mode frequency  $f_{01}$  evolution with the film thickness in the case of NiPS<sub>3</sub>. We used the values  $\alpha_{01} = 2.4049$  for the first root of the Bessel function,  $R = 2.5 \mu\text{m}$  for the membrane radius,  $\rho_{\text{NiPS}_3} = 3180 \text{ kg/m}^3$  [165] for the mass density and the values of  $E$  and  $\nu$  calculated in 1.1.3.

As can be deduced from equations (1.33) and (1.34) the plate contribution is linear with the film thickness and dominates at high thicknesses, whereas the membrane contribution goes as  $1/\sqrt{h}$  and dominates at low thicknesses. The crossover region between the two regimes is highly dependent on the film tension  $\sigma_s$ . Here we consider only the fabrication-induced pre-stress  $\sigma_s^0$  at room temperature and no stress resulting from an applied gate voltage. We adjusted the pre-stress value for the model to match the measured frequencies of the suspended NiPS<sub>3</sub> samples studied (*Mordor* and *Balor*, see Sample list 1.2.4) giving  $\sigma_s^0 = 0.2 \text{ N/m}$ , that is of the same order of magnitude as the  $0.1 \text{ N/m}$  estimated for FePS<sub>3</sub> in [26].

We observe that the two NiPS<sub>3</sub> nanodrums studied in this work with thicknesses of 7 and 9.1 nm are well described by the membrane behavior at room temperature. The majority of the measurements on these samples have been performed at temperatures around NiPS<sub>3</sub> Néel

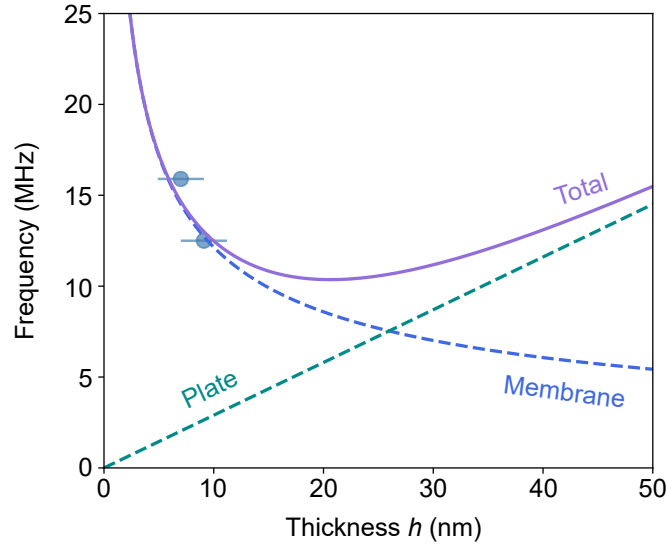


**Figure 1.26:** Comparison between experimental values and theoretical evolution of the fundamental mode frequency with the thin film thickness for NiPS<sub>3</sub> with a pre-stress  $\sigma_s^0 = 0.2$  N/m at room temperature. The blue and cyan dotted lines represent the membrane and plate regimes respectively, while the mauve solid line illustrates the total behavior of the thin film. The two blue dots show the measured frequencies of the two NiPS<sub>3</sub> samples studied in this work (*Mordor* and *Balor*, see Sample list 1.2.4), with the errorbars taking into account a three-layer uncertainty in thickness determination.

temperature ( $T_N \sim 155$  K) or at 4 K. When the temperature is decreased, a thermal strain is induced in the suspended flake that can be expressed as  $\epsilon_r^{\text{th}} = -\alpha_{\text{NiPS}_3} \Delta T$  [26] with  $\alpha_{\text{NiPS}_3}$  the thermal expansion coefficient of NiPS<sub>3</sub>. Since we do not know the value of  $\alpha_{\text{NiPS}_3}$ , we cannot estimate a value for this strain. However, we observe an increase of the thin film resonance frequency with decreasing temperature (see Section 2.2.1), we can deduce that the film contracts, and so, that the thermal expansion coefficient is positive. Decreasing the temperature will then results in an increase of the stress in the film and so a behavior even closer to that of a membrane. We can refer to the work of Šiškins *et al.* [26] that performed similar calculations in the case of FePS<sub>3</sub>, to confirm that the suspended FePS<sub>3</sub> homostructure *Whale* with a 7 nm thickness can also be described by a membrane model. However the behavior of the FePS<sub>3</sub>-based heterostructure *Fantadwich* is harder to classify. Since each material possesses a different Young's modulus, Poisson ratio and mass density, a similar calculation cannot be performed. Moreover it is difficult to predict analytically how the mechanical properties of the different materials will affect each other; finite element simulations could clarify this issue.

### Membrane deflection at the resonance

Now that we have determined the shape of the membrane vibrational modes, we can calculate the deflection  $z_n(t)$  representing the point of maximal deflection.

The dynamical behavior of a point on the membrane for the mode  $(m, n)$  can be described as a

driven damped harmonic oscillator. The corresponding equation of motion is written

$$\ddot{z}(t) + \frac{\Omega_m}{Q}\dot{z}(t) + \Omega_m^2 z(t) = \frac{F(t)}{M_{\text{eff}}} \quad (1.35)$$

with  $\Omega_m$  and  $Q$  the mechanical resonance frequency and quality factor of the considered mechanical mode. The quality factor can be expressed as  $Q = \Omega_m/\Gamma_m$  with  $\Gamma_m/2\pi$  being the damping rate of the mechanical mode.  $F(t)$  is a time-dependent force felt by the resonator. We also introduced the effective mass  $M_{\text{eff}}$  of mode  $(m, n)$  with profile  $u_{m,n}(\mathbf{r})$  that is defined as [166]

$$M_{\text{eff},(m,n)} = \rho h \int d^2\mathbf{r} u_{m,n}^2(\mathbf{r}). \quad (1.36)$$

To take into account that only a fraction of the membrane mass participates in the motion of the mode  $(m, n)$ , the mode profile is integrated over the resonator area, resulting in a effective mass lower than the real mass  $M$  of the membrane. For the fundamental mode we get  $M_{\text{eff},(0,1)} \approx 0.27M$ .

The linear response of the membrane displacement to the force can be expressed in Fourier space as

$$z[\Omega] = \chi_m[\Omega]F[\Omega], \quad (1.37)$$

using the Fourier transform  $f[\Omega] = \int f(t)e^{i\Omega t}dt$ .

The mechanical susceptibility  $\chi_m$  is thus expressed as

$$\chi_m[\Omega] = \frac{1}{M_{\text{eff}}(\Omega_m^2 - \Omega^2 - i\Omega\Omega_m/Q)}. \quad (1.38)$$

The lineshape of  $|z[\Omega]|$  is close to a Lorentzian, with a peak at its resonance frequency ( $\Omega = \Omega_m$ ) presenting a full-width-half-maximum (FWHM) of  $\Omega_m/Q = \Gamma_m$  (see Fig. 1.27 a).

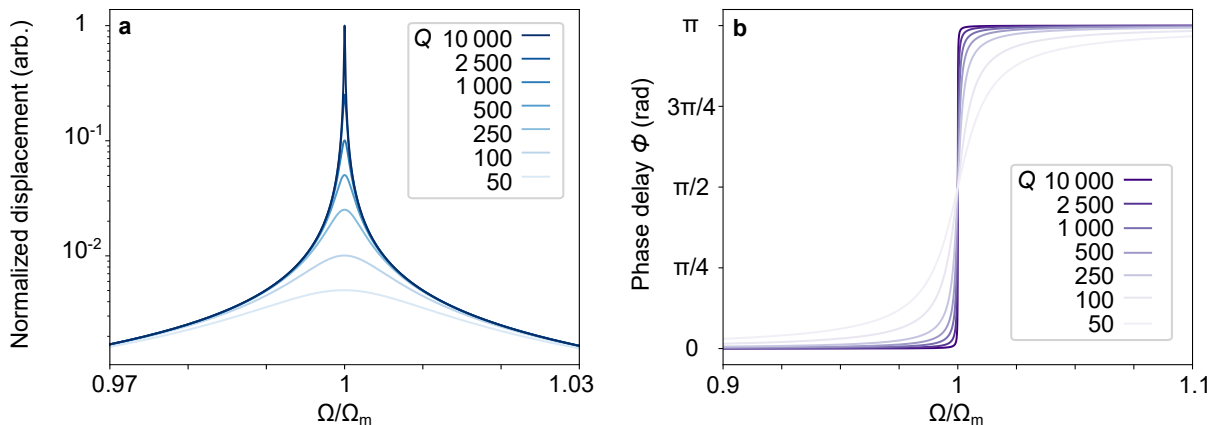


**Figure 1.27: Theoretical plots of the displacement amplitude and the phase of a mechanical mode for frequencies around the resonance and quality factors from 50 to 10 000. a. Normalized displacement amplitude  $|z[\Omega]|$ . b. Phase delay  $\phi$ .**

Close to the resonance, the value of the phase delay  $\phi$  between the oscillator motion and the

driving force changes abruptly from zero to  $\pi$  and equals  $\pi/2$  at the resonance (see Fig. 1.27 b), offering us a complementary probe of the mechanical resonance.

In the following, we will first discuss the case of the membrane Brownian motion, i.e. no external driving force applied, before reviewing the different actuation schemes.

## 1.5.2 Detection of the membrane Brownian motion

### Thermal displacement noise

In the case where no external force is applied, the membrane still moves due to thermal fluctuations. The mechanical mode is driven by stochastic thermal forces that are called Langevin forces. They arise from the thermal coupling of the mechanical resonator to its environment through, for example, random collisions with molecules from the surrounding gas or by coupling to phonons from the substrate at the membrane clamping points [166]. The Langevin force properties are a zero time-averaged value ( $\langle F_{\text{th}}(t) \rangle = 0$ ) and an auto-correlation function  $g_{F_{\text{th}}}$  that writes [160, 167]

$$g_{F_{\text{th}}}(\tau) = \langle F_{\text{th}}(t)F_{\text{th}}(t + \tau) \rangle = 2M\Gamma_{\text{m}}k_B T \delta(\tau) \quad (1.39)$$

where  $\delta$  represents the Dirac delta function. The autocorrelation function  $g_f(\tau)$  describes how a function  $f(t)$  relates to itself at a later time  $t + \tau$  and is defined as

$$g_f(\tau) = \langle f(t)f(t + \tau) \rangle = \lim_{T_0 \rightarrow \infty} \frac{1}{T_0} \int_0^{T_0} d\tau f(t)f(t + \tau). \quad (1.40)$$

As the time dependence of the Langevin force autocorrelation function is governed by a Dirac delta function, it is only non-zero when  $t = \tau$ , and so the Langevin force is said to have no memory effect.

We will now characterize the thermal displacement noise of the membrane, also called Brownian motion, due to these stochastic thermal forces and connect the membrane displacement  $z(t)$  to the autocorrelation function of the Langevin force.

We define the spectral density of the Langevin force as the Fourier transform of the autocorrelation function  $g_{F_{\text{th}}}$  which is written

$$S_{F_{\text{th}}}[\Omega] = \int_{-\infty}^{+\infty} d\tau \langle F_{\text{th}}(t)F_{\text{th}}(t + \tau) \rangle. \quad (1.41)$$

Since the autocorrelation function of the Langevin force is proportional to a Dirac delta function (Eq. 1.39) we obtain

$$S_{F_{\text{th}}}[\Omega] = 2M\Gamma_{\text{m}}k_B T. \quad (1.42)$$

The obtained equation corresponds to the fluctuation-dissipation theorem [133] applied to a damped harmonic oscillator, which writes

$$S_{F_{\text{th}}}[\Omega] = -\frac{2k_B T}{\Omega} \text{Im} \left[ \frac{1}{\chi_m[\Omega]} \right]. \quad (1.43)$$

The quantity to which we will have access via the measurement protocol, is the displacement spectral noise density  $S_z$  that is the Fourier transform of the displacement autocorrelation function. Using Equation (1.37), we can express it as

$$S_z[\Omega] = |\chi[\Omega]|^2 S_{F_{\text{th}}}. \quad (1.44)$$

By replacing  $\chi[\Omega]$  and  $S_{F_{\text{th}}}$  by their respective expressions (Eq. 1.38 and 1.42) we get the displacement noise spectral density at the membrane center as a function of the resonator mechanical parameters

$$S_z[\Omega] = \frac{2\Gamma_m k_B T}{M_{\text{eff}}((\Omega_m^2 - \Omega^2)^2 + \Omega^2 \Gamma_m^2)}. \quad (1.45)$$

We note that the displacement noise spectral density is proportional to the temperature, and inversely proportional to the membrane effective mass.

The variance of the displacement fluctuations is then obtained by the integration of the displacement noise spectral density

$$\Delta z_{\text{th}}^2 = \frac{1}{2\pi} \int_{-\infty}^{+\infty} d\Omega S_z[\Omega] = \frac{k_B T}{M_{\text{eff}} \Omega_m^2}. \quad (1.46)$$

We can then deduce the expected root-mean-square (RMS) displacement ( $z_{\text{th}}^{\text{RMS}} = \sqrt{\Delta z_{\text{th}}^2}$ ) of the membrane center induced by thermal fluctuations. For the fundamental mode of a 10 layer FePS<sub>3</sub> nanodrum (sample *Whale*, see Sample list 1.2.4) with  $M_{\text{eff}} = 0.18$  pg and  $f_m = 4.7$  MHz,  $z_{\text{RMS}}(296 \text{ K}) = 2.28 \text{ \AA}$  and  $z_{\text{RMS}}(T_N = 118 \text{ K}) = 0.80 \text{ \AA}$ .

### Interferometric detection

To detect the motion of the membrane, we need to access its position variations and convert them into an electrical signal that can be treated by our spectrum analyzer (see Section 1.3.2 and Fig. 1.18).

The membrane displacement is measured by optical interferometry, the principle of which is shown on Figure 1.28 a. The sample can be seen as a low finesse Fabry-Pérot cavity, whose two sides are the silicon substrate which can be approximated as a mirror, and the suspended 2D material flake. When the laser is focused on the nanodrum, a standing wave electric field is created in this cavity, the intensity  $I(z)$  of which is modulated by the membrane displacement in two ways: an interference pattern is created by the multiple reflections of the light in the cavity, that will depend on the cavity length, which is modulated by the membrane motion and, in addition, the 2D material absorbs a part of the light proportional to  $I(z)$  when moving across the standing wave, which also modifies the reflected light intensity [166].

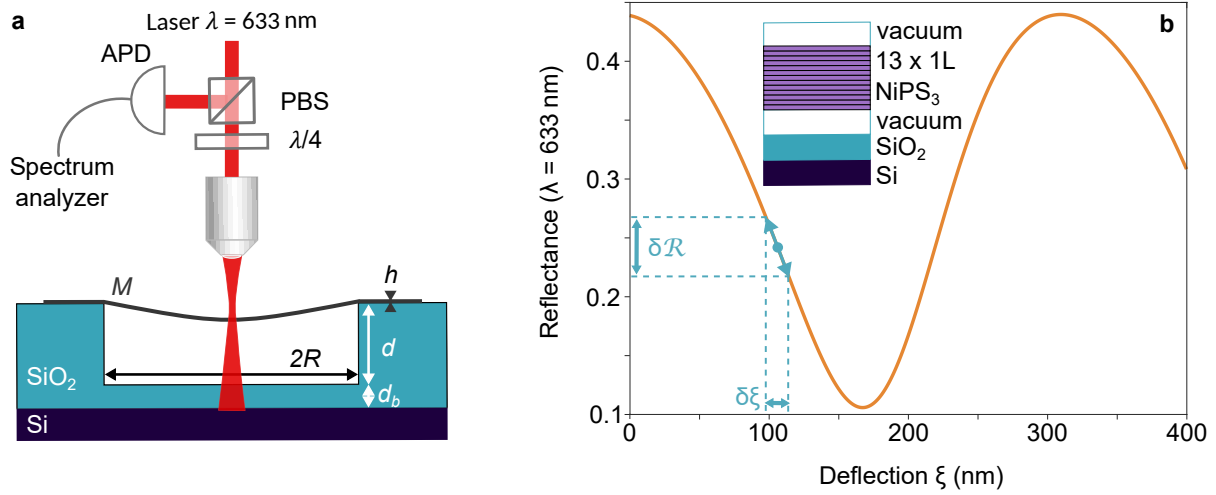


**Figure 1.28: Principle of the membrane motion detection.** **a.** Simplified scheme of the experimental setup for the interferometric detection. A 633 nm wavelength laser is focused on the membrane, the incident light is reflected by both the membrane and the silicon substrate, forming a Fabry-Pérot cavity that allows to encode the membrane motion in the intensity of the reflected light. A circulator composed of a quarter wave-plate ( $\lambda/4$ ) and a polarizing beam splitter (PBS) is used to direct the outgoing light on the photodiode (APD), that converts it in an electric signal transmitted to a spectrum analyzer. **b.** Calculated plot of the reflectance  $\mathcal{R}$  as function of the membrane deflection  $\xi$  for a 13-layer suspended NiPS<sub>3</sub> flake from the model described below. In cyan is depicted the reflectance variation  $\delta\mathcal{R}$  for a deflection variation  $\delta\xi$  around the static deflection point  $\xi_0$  along the reflection curve. In the inset is shown the membrane modeling as layers for the reflectance calculation, the top (vacuum) and bottom (Si) layers are considered as semi-infinite.

To estimate the light intensity reflected by the cavity we will need to calculate the total reflected field  $E_r$  that takes into account all the reflections inside the cavity. For this we consider a normal incident laser beam of wavelength  $\lambda_L$ , resulting in an electric field  $E_0(z, t) = E \exp(-i(\omega t - (2\pi n z)/\lambda_L))$  where  $E$  is the amplitude of the field,  $\omega$  is the laser pulsation and  $n$  is the refractive index of the medium. We model our cavity by successive layers of complex refractive index  $n_i$  with  $i$  the index of the considered layer (see Fig. 1.28 b). From bottom to top we have: the silicon layer than is considered semi-infinite, a 100 nm SiO<sub>2</sub> layer, a vacuum layer whose thickness will be varied to simulate the membrane deflection, 13 NiPS<sub>3</sub> monolayers and a semi-infinite vacuum layer. The NiPS<sub>3</sub> monolayers are supposed to have the bulk properties. We can define an equivalent reflection coefficient  $\rho_{tb}$  for all the layer stack, with the index t for the top layer, here the vacuum, and b for the bottom layer, here the silicon, as  $E_r = \rho_{tb}E_0$ . This equivalent reflection coefficient can be computed by recursive calculation.

We first have to evaluate the equivalent coefficient for the first three layers that are the silicon (0), the SiO<sub>2</sub> (1) and the vacuum (2), considering that the first and last layer are semi-infinite. The equivalent reflection coefficient  $\rho_{20}$  for a medium of thickness  $d_1$  encapsulated by two semi-infinite media is given by [155]

$$\rho_{20} = \frac{r_{21} + r_{10}e^{i2\beta_1}}{1 + r_{10}r_{21}e^{i2\beta_1}} \quad (1.47)$$

where  $\beta_1 = (2\pi n_1 d_1)/\lambda_L$  is the phase difference due to the propagation in medium (1) with  $d_1$  the layer thickness. The coefficients  $r_{ij}$  are the Fresnel reflection coefficients at the interface between the medium  $i$  and  $j$  defined as

$$r_{ij} = \frac{n_i - n_j}{n_i + n_j}. \quad (1.48)$$

The equivalent reflection coefficient  $\rho_{tb}$  can then be evaluated recursively by considering each layer in the stack using the expression [155]

$$\rho_{j+1,b} = \frac{r_{j+1,j} + \rho_{j,b} e^{i2\beta_j}}{1 + r_{j+1,j} \rho_{j,b} e^{i2\beta_j}}, \quad (1.49)$$

This allows us to calculate the membrane reflectance  $\mathcal{R}$  defined as  $\mathcal{R} = |\rho_{tb}|^2$  [168].

To study the evolution of the reflectance with the membrane deflection, we repeat the calculation by varying the intermediate vacuum layer thickness from 400 to 0 nm. The resulting reflectance evolution for a 13 L NiPS<sub>3</sub> membrane suspended over a  $d = 400$  nm hole with a SiO<sub>2</sub> thickness of  $d_b = 100$  nm underneath and illuminated by a  $\lambda = 633$  nm laser is shown on Figure 1.28 b.

The deflection  $\xi$  of the membrane can be decomposed as  $\xi(\mathbf{r}_0, t) = \xi_0(\mathbf{r}_0) + \delta\xi(\mathbf{r}_0, t)$  with  $\xi_0$  its static deflection and  $\delta\xi$  its dynamic deflection at the position  $\mathbf{r}_0$  on the membrane. When the membrane vibrates, its deflection varies around its equilibrium position  $\xi_0$ , creating a deflection variation  $\delta\xi$  that translates into a reflectance variation  $\delta\mathcal{R}$  (see Fig. 1.28 b). The reflectance can then be written as the sum of a static and a dynamic term  $\mathcal{R} = \mathcal{R}(\xi_0) + \delta\mathcal{R}(\delta\xi)$ . For  $\delta\xi \ll \xi_0$ , we can expand the reflectance in terms of  $\delta\xi$

$$\mathcal{R}(\xi_0 + \delta\xi) \simeq \mathcal{R}(\xi_0) + \left. \frac{\partial \mathcal{R}}{\partial \xi} \right|_{\xi_0} d\xi \quad (1.50)$$

and then identify the dynamic term of the reflectance to

$$\delta\mathcal{R}(\delta\xi) = \left. \frac{\partial \mathcal{R}}{\partial \xi} \right|_{\xi_0} d\xi, \quad (1.51)$$

where  $\partial\mathcal{R}/\partial\xi|_{\xi_0}$  is the slope of the reflectance curve at the membrane's equilibrium position. We note that to have an important reflectance variation induced by a small change in deflection (i.e. an efficient displacement detection), the equilibrium position of the membrane should be in a high slope region of the reflectance curve as depicted on Figure 1.28 b. In order to optimize the detection, it is possible to modify the static deflection  $\xi_0$  of the membrane by applying a gate voltage, as will be shown in section 3.1.

The light intensity reflected by the sample is given by  $I_r \propto |E_r|^2 = |\rho_{tb}|^2 |E_0|^2 = \mathcal{R} I_\lambda$ , where  $I_\lambda$  is the laser light intensity. The photodiode collects part of this reflected light, the rest being redirected or absorbed along the optical path, and converts it into a current. In the end, we

measure the photodiode output signal with an oscilloscope, which results in a voltage that can be expressed as

$$V_{\text{APD}} = AP_{\lambda}\mathcal{R} + V_{\text{APD}}^0 \quad (1.52)$$

with  $A$  an experimental proportionality factor in  $V/W$  taking into account the photodiode response, the power lost along the optical path, the laser spot size and the resistive load.  $P_{\lambda}$  is the incident laser power and  $V_{\text{APD}}^0$  is the voltage originating from the dark current of the photodiode. By replacing the expression of  $\mathcal{R}$  we get

$$V_{\text{APD}}(t) = AP_{\lambda}\mathcal{R}(\xi_0) + AP_{\lambda} \left. \frac{\partial \mathcal{R}}{\partial \xi} \right|_{\xi_0} d\xi(\mathbf{r}_0, t) + V_{\text{APD}}^0(t) \quad (1.53)$$

The dynamical component of the photodiode signal is thus proportional to the membrane deflection we want to measure, with a transduction factor  $\beta[\Omega] = A[\Omega]P_{\lambda} \left. \partial \mathcal{R} / \partial \xi \right|_{\xi_0}$ , we also note a instrumental noise coming from the photodiode dark current.

As already shown in section 1.3.3, we can perform spatially-resolved maps of the static part of  $V_{\text{APD}}$  that allows to trace back the spatial evolution of the sample static reflectance  $\mathcal{R}(\mathbf{r}_0)$ . Equations (1.53) is only valid for small oscillation amplitudes  $z(t)$  compared to the membrane deflection  $\xi_0$  which is the case for Brownian motion, and for driven motion within the linear limit.

The output signal of the photodiode is sent to a spectrum analyzer, that measures the power spectral noise density  $S_V$  with a given resolution bandwidth (RBW). We can write the power spectral density read by the spectrum analyzer as

$$S_V[\Omega] = \beta^2 S_z[\Omega] + S_V^{\text{noise}} \quad (1.54)$$

where  $S_V^{\text{noise}}$  is an offset that encapsulates all the instrumental noises.

### Signal calibration

The Brownian motion offers a way to calibrate the displacement of the membrane since (see Eq.1.45)

$$S_z(\Omega = \Omega_m) = \frac{2k_B T}{M_{\text{eff}} \Omega_m^2 \Gamma_m}. \quad (1.55)$$

The value of the displacement spectral density at the resonance can then be evaluated by fitting the detected mechanical mode with the model of Equation (1.45), which gives the parameters  $\Omega_m$  and  $\Gamma_m$ . The temperature is taken as the one measured on the sample holder and the value of the effective mass can be evaluated from the membrane geometry and composition. Nevertheless, there are uncertainties concerning its exact layer number and whether the mode profile matches exactly what is expected for the fundamental mode of an ideal membrane.

A calibrated Brownian motion spectrum for the fundamental mode is shown on Figure 1.29, its

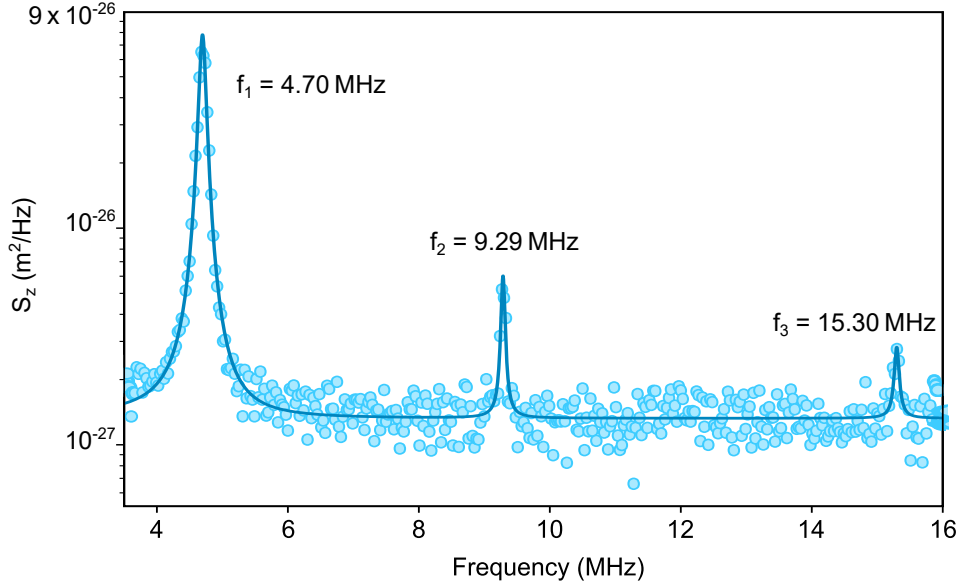


**Figure 1.29:** Brownian motion spectrum at room temperature of a suspended 10 L FePS<sub>3</sub> sample (*Whale*, see Sample list 1.2.4). The dots correspond to the data of the calibrated displacement noise spectral density  $S_z(f)$  and the solid line is a fit to the model of Equation (1.45).

fundamental vibrational mode has a resonance frequency of 4.70 MHz and two higher order modes are observed at 9.29 MHz and 15.30 MHz, respectively. The calibration was performed with the fundamental mode using the fitted damping  $\Gamma_m/(2\pi) = 0.80$  MHz, a temperature of 296 K and an effective mass estimated as  $M_{\text{eff}} \sim 0.18$  pg with  $R = 3$   $\mu\text{m}$ ,  $h = 7$  nm and  $\rho_{\text{FePS}_3} = 3375$  kg/m<sup>3</sup> [165].

The obtained detection noise floor is  $\sqrt{S_z^{\text{noise}}} = 45$  fm/ $\sqrt{\text{Hz}}$  for a laser power of 100  $\mu\text{W}$  before the microscope objective.

The thermal displacement noise being proportional to the temperature, as seen in Equation (1.45), probing the phase transition at low temperature will typically require the acquisition of the displacement noise spectrum for about 15 minutes by temperature point. In order to speed up the acquisition of the nanomechanical properties of the membrane, we will drive its motion.

### 1.5.3 Driven motion

The membrane driven motion is detected with the same interferometric method than the Brownian motion, except that we send the photodiode output voltage to a network analyzer instead of a spectrum analyzer. We are then detecting a

$$z[\Omega] = |\chi_m|(F_{\text{ext}}[\Omega] + F_{\text{th}}) \quad (1.56)$$

Two methods will be used in this work to drive the membrane motion: an electrostatic actuation based on a capacitive coupling between the membrane and the bottom substrate and a laser-induced actuation implying the use of a second laser modulated in intensity.

## Electrostatic actuation

The electrostatic actuation is the main method used to drive the membrane motion in this work, and is commonly used to drive the motion of suspended graphene and transition metal dichalcogenides membranes [19, 33, 169, 170]. A time-varying electrostatic force is induced to the membrane, we will derive here a qualitative model before presenting experimental results.

First, we derive a capacitor model for an ideal membrane regarded as a perfect conductor. Considering the geometry of the sample, it can be seen as a capacitor with two circular parallel plates, one being the suspended membrane and the other the silicon at the bottom of the substrate (see Fig. 1.30 a). A voltage  $V_g(t)$  is applied to one of these plates, the other being grounded, resulting in a voltage difference, and so, an electrostatic force  $F_{el}$ . The membrane can be electrically contacted thanks to its transfer on a gold electrode previously evaporated on the substrate (see Section 1.2).

The equivalent surface capacitance  $C_{eq}$  of this system is composed of the vacuum capacitance  $C_{vac}$  and the  $\text{SiO}_2$  capacitance  $C_{\text{SiO}_2}$  in series and is expressed as  $C_{eq}^{-1} = C_{vac}^{-1} + C_{\text{SiO}_2}^{-1}$ , that gives

$$C_{eq}(\xi) = \frac{\epsilon_0}{d_{eq} - \xi(\mathbf{r}, t)} \quad (1.57)$$

where  $\xi(\mathbf{r}, t)$  is the membrane deflection,  $d_{eq} = d + d_b/\epsilon_{\text{SiO}_2}$  is an equivalent distance between the top of the hole and the Si substrate [20].  $\epsilon_0$  and  $\epsilon_{\text{SiO}_2}$  are the vacuum and  $\text{SiO}_2$  permittivity respectively,  $d$  is the depth of the hole and  $d_b$  is the  $\text{SiO}_2$  layer thickness. The electrostatic energy  $U_{es}$  of this capacitor integrated over the membrane surface is expressed as

$$U_{es} = \frac{\epsilon_0}{2} V_{\text{eff}}^2 \int \frac{1}{d_{eq} - \xi(\mathbf{r}, t)} d^2\mathbf{r} \quad (1.58)$$

where  $V_{\text{eff}} = V_g - V_0$  is the effective voltage felt by the capacitor with  $V_0$  the intrinsic offset voltage, called also neutrality point. The neutrality point is the voltage at which the electrostatic energy cancels out and so does the force applied on the membrane, it is usually close to 0 V but can be higher in case of trapped charges [166].

To derive the electrostatic force felt by the membrane we will consider the parallel plates approximation and so a flat profile for the membrane  $\xi(\mathbf{r}, t) \sim \xi(t)$ . This is true for a membrane radius large compared to the maximum distance to the bottom electrode  $R \gg d + d_b$ , which is always verified, and a membrane deflection small compared to this distance  $\xi \ll d + d_b$ , which is no longer true for high voltages (see Section 3.1.2). The electrostatic force felt by the membrane is then expressed as

$$F_{el}(\xi, t) = -\frac{\partial U_{es}}{\partial \xi} = V_{\text{eff}}(t)^2 \frac{\epsilon_0 \pi R^2}{2(d_{eq} - \xi(t))^2}. \quad (1.59)$$

The applied gate voltage is a sum of a continuous and alternative voltages as  $V_g(t) = V_{\text{DC}} + V_{\text{AC}} \cos(\Omega t)$  with  $V_{\text{DC}} \gg V_{\text{AC}}$ . We can then re-express the electrostatic force by neglecting the

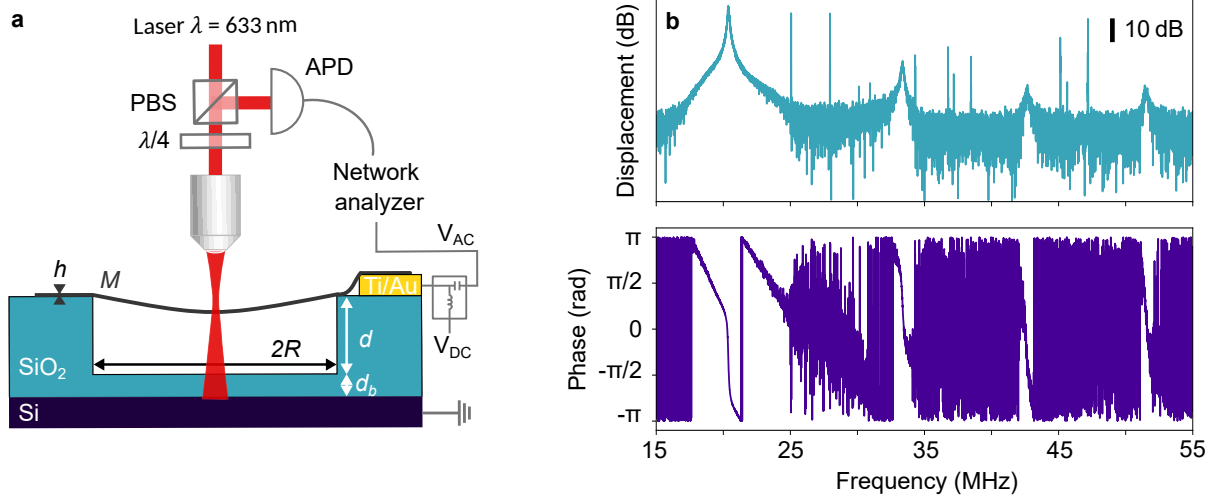


**Figure 1.30: Electrostatically-actuated membrane mechanical response.** **a.** Simplified scheme of the experimental setup for the electrostatic actuation, a more detailed scheme can be found in Figure 1.18. A sum of an alternative  $V_{AC}$  and a continuous  $V_{DC}$  voltage is applied between the bottom of the silicon substrate and the electrode connected to the membrane, forming a capacitor. The resulting electrostatic force is driving the membrane motion. The signal coming from the interferometrical detection is sent to a network analyzer that controls the supplied alternative voltage. **b.** Electrostatically-driven response spectrum of the FePS<sub>3</sub>-based heterostructure *Fantadwich* (see Sample list 1.2.4) at a temperature of 109 K. On the top panel is shown its response in displacement and, on the bottom panel, its response in phase.

quadratic terms in  $V_{AC}$  and the intrinsic offset voltage as

$$F_{el}(\xi, t) \simeq (V_{DC}^2 + 2V_{AC}V_{DC} \cos(\Omega t)) \frac{\epsilon_0 \pi R^2}{2(d_{eq} - \xi(t))^2}. \quad (1.60)$$

The induced electrostatic force can thus be decomposed in two contributions, a static downward force proportional to  $V_{DC}^2$ , that will be considered in more details in Section 3.1.2, and a time-dependent driving force proportional to  $2V_{DC}V_{AC}$ . We can also note that, as the membrane gets closer to the bottom electrode, the force gets stronger.

Since the different vibrational modes of the membrane do not have the same spatial profiles, their overlap with the spatial profile of the driving force has an influence on the efficiency of the actuation, it is usually optimal for the fundamental mode.

In the case of strong electrostatic drive, non-linear effects such as Duffing non-linearities can be achieved as shown in previous works of the team on graphene and TMD resonators [19, 20]. Here, we aim at using the membrane mechanical response as a probe of the magnetic order and will avoid these effects as much as possible to stay in the linear regime.

The AC voltage is sent by the network analyzer with a frequency swept in a range around the membrane resonance frequency  $f_m$  with a given amplitude  $V_{AC}$ . The network analyzer is performing a homodyne detection at the output excitation frequency, that is the one of the alternative driving voltage, such that the photodiode signal is demodulated at this excitation frequency. Figure 1.30 b) shows the electrostatically-induced mechanical response of a FePS<sub>3</sub>-

based heterostructure (*Fantadwich*) at a temperature of 109 K, with  $V_{DC} = 13.5$  V and  $V_{AC} = 22.5$  mV. The fundamental mode appears with a resonance frequency of 20.4 MHz and a quality factor of 160, three higher order modes are also visible with resonance frequencies of 33.3, 42.7 and 51.5 MHz respectively and quality factors ranging from 133 to 189.

The phase is shown on the lower panel of Figure 1.30 b. The sharp shift in the phase at the resonance is useful to discriminate mechanical modes from most parasitic peaks that are not resolved in phase. The phase brings us an additional information to reconstruct the spatial profiles of the mechanical mode (see Sec. 3.3.2).

### Laser-induced actuation

A second method that can be used to drive 2D nanodrum's motion is the laser-induced actuation [26, 33, 105, 171]. A laser modulated in intensity at a frequency close to the mechanical resonance, thanks to an acousto-optic modulator (AOM), is focused on the sample, superimposed to the continuous detection laser (see Fig. 1.18). The pump laser is filtered on the way back such that the resulting reflected signal detected on the photodiode is only coming from the probe laser.

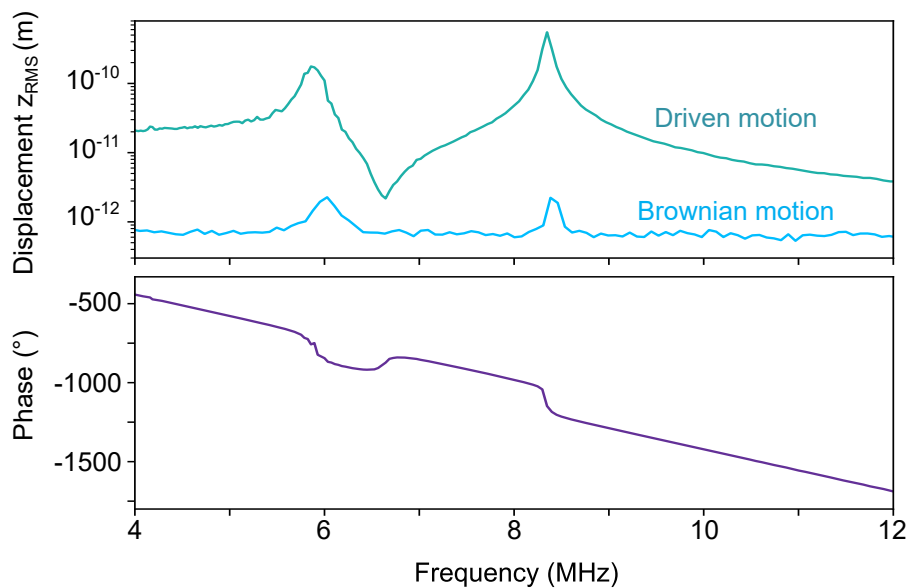


**Figure 1.31: Comparison between the optically-driven motion and the equivalent Brownian motion at room temperature of a 10 L  $\text{FePS}_3$  homostructure** (*Whale*, see Sample list 1.2.4). The top panel shows the calibrated mechanical response of the membrane under laser actuation (in green) and its equivalent Brownian motion (in blue). The bottom panel shows the phase of the laser actuated displacement against the drive frequency.

A typical laser-driven displacement spectrum at room temperature of the 10 L suspended  $\text{FePS}_3$  homostructure (*Whale*, see sample list 1.2.4) is shown on Figure 1.31, presenting two vibrational modes. This spectrum has been calibrated using the transduction coefficient  $\beta^2$  derived from the Brownian motion calibration and taking into account the bandwidth ratio of the instruments. We obtain a maximum root-mean-square amplitude on the order of 20 nm for the laser-induced displacement at a probe laser power of  $P_{633} = 50 \mu\text{W}$  and a pump laser power of  $P_{532} = 12.5 \mu\text{W}$

before the microscope objective. The calibrated displacement for the Brownian motion is shown on the same figure for comparison.

The laser actuation of the membrane motion is caused by two different driving forces: the radiation pressure and optothermal effects.

In the case of the radiation pressure force, each photon reflected by the membrane transfers a momentum of  $|\Delta p| = 2\hbar k$  to it, resulting in a force proportional to the laser power  $P_\lambda$  and sample reflectance  $\mathcal{R}$  as  $F_{\text{rad}}(t) = 2P_\lambda(t)\mathcal{R}/c$ , with  $c$  the speed of light in vacuum [172]. The reflectance can be estimated from the model derived in the previous subsection 1.5.2, using the appropriate laser wavelength for the pump laser (here  $\lambda = 532$  nm).

However, a fraction of the incoming photons can also be absorbed by the membrane. This results in a heat wave that locally contracts and expands the membrane as it is propagating towards the membrane clamping points. This phenomenon implies that the optothermal forces are delayed by a time constant  $\tau$  that corresponds to the characteristic time for the heat to travel out of the resonator [166, 173, 174].

### Influence of detection and drive powers

We will first study the effects of an increase of the probe laser power on the membrane mechanical mode, that will allow us to choose an appropriate detection power. The objectives are to limit the heating of the membrane due to light absorption, and maintain the membrane resonance frequency independent from the measurement protocol.

On Figure 1.32 a are displayed the spectra of the electrostatically-driven motion of the 13 L NiPS<sub>3</sub> homostructure (*Mordor*, see Sample list 1.2.4) taken at 130 K for probe laser powers between 1  $\mu\text{W}$  and 90  $\mu\text{W}$  before the microscope objective, and an electrostatic drive power  $P_{RF} = -20$  dBm. This temperature was chosen because it is in the temperature range that will be covered to probe NiPS<sub>3</sub> phase transition.

The spectra are fitted using the model of equation (1.56) and the peak amplitude, resonance frequency  $f_m$  and damping  $\Gamma_m$  (see Fig. 1.32 b,c,d) are extracted. The peak amplitude is increasing linearly with the laser power until 70  $\mu\text{W}$  where it seems to be starting to saturate. This linear increase is expected from the proportionality between the signal output of the photodiode and the incident laser power (Eq. 1.52). The resonance frequency is linearly decreasing over the entire power range with a slope of -4.1 MHz/ $\mu\text{W}$ , while the damping rate increases linearly at a rate of 1.3 kHz/ $\mu\text{W}$  until 40  $\mu\text{W}$ . For powers higher than 80  $\mu\text{W}$  the mechanical mode shows non-linearities and the values fitted by the Lorentzian model are no longer reliable.

The linear variations of the resonance frequency and the damping rate with increasing probe power indicate an effect of light backaction on the mechanical mode, that is likely due to optothermal effects. Here we observe a dilatation of the membrane due to the laser heating, corresponding to a negative stress and so a decrease of the membrane resonance frequency, that is coherent with a positive thermal expansion coefficient for NiPS<sub>3</sub>.

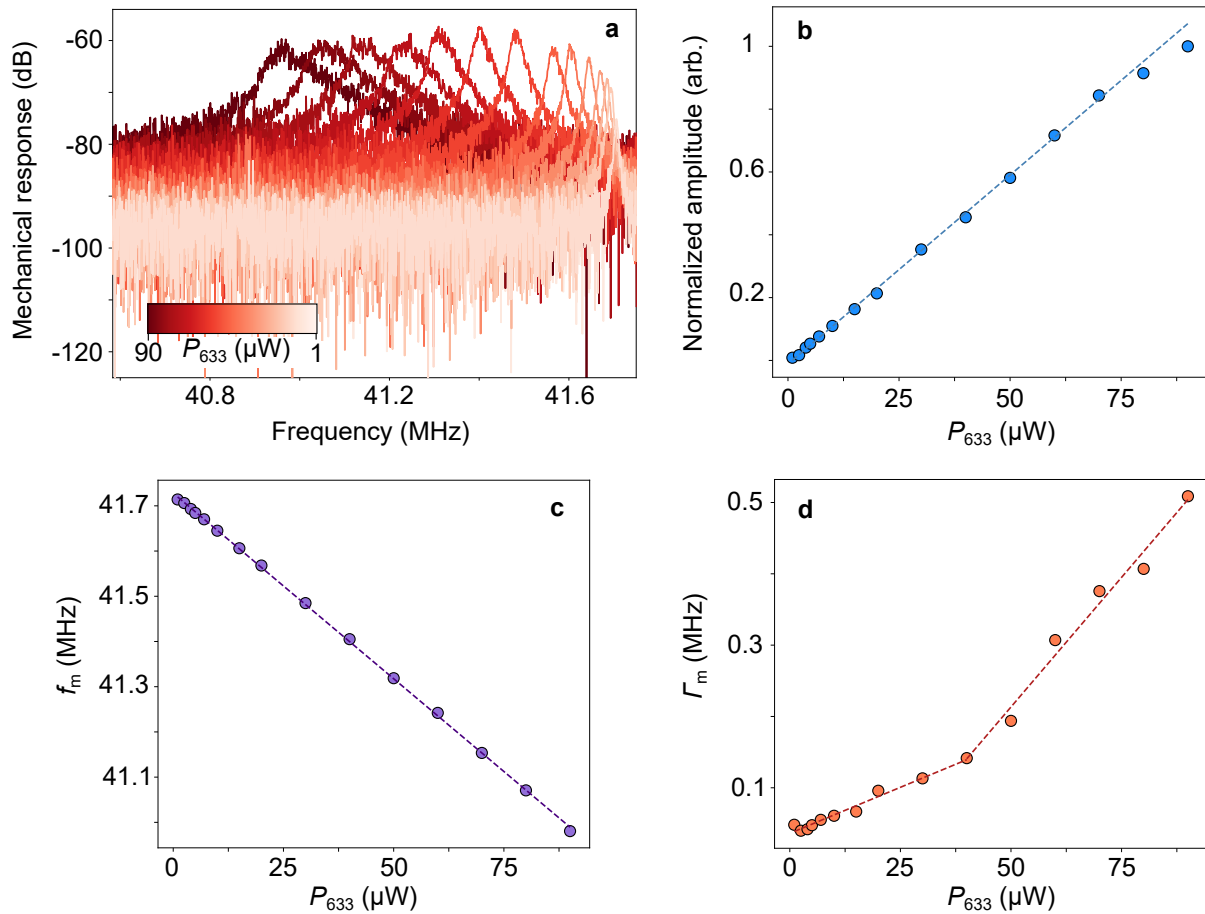


**Figure 1.32: Effects of an increase of the detection laser power on the mechanical mode properties of a  $\sim 13$  L  $\text{NiPS}_3$  sample (Mordor, Sample list 1.2.4) at 130 K. a.** Mechanical response spectra to an electrostatic drive for detection laser power  $P_{633}$  from 1 to 90  $\mu\text{W}$  as measured before the microscope objective. **b,c,d.** Evolution of the mechanical mode fitted amplitude, resonance frequency  $f_m$  and damping  $\Gamma_m/(2\pi)$ , respectively, with increasing detection laser power. The dots are the values extracted from the fits of the spectra. The clearer dots indicate spectra deviating from a Lorentzian profile. The dotted lines are linear fits to the mechanical parameters evolution.

In conclusion, to remain in the linear regime, we should limit ourselves to detection powers below  $40 \mu\text{W}$ , but such a power will still affect the damping and resonance frequency of the mechanical mode. In order to limit optothermal effects, we choose to use a power below  $10 \mu\text{W}$  for  $\text{NiPS}_3$  samples *Mordor* and *Balor*. The  $\text{FePS}_3$  heterostructure *Fantadwich* being composed of different materials, its response to detection laser power is different, in fact it appears to be less sensitive to the probe laser power and we choose to apply a power below  $25 \mu\text{W}$ .

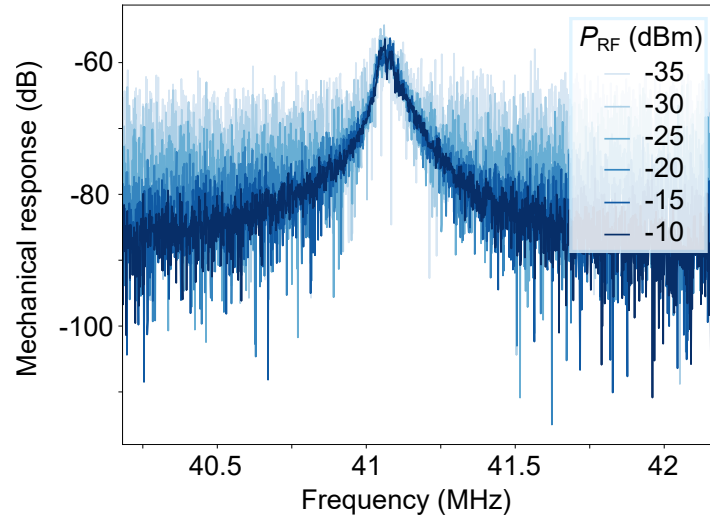


**Figure 1.33:** Mechanical response spectra of the electrostatically-driven suspended 13 L  $\text{NiPS}_3$  homostructure (*Mordor*, see Sample list 1.2) at 130 K for electrostatic drive powers between -35 and -10 dBm, that correspond to peak-to-peak voltages of approximately 6 mV to 100 mV, a DC gate voltage of 25 V and a detection power of  $80 \mu\text{W}$  measured before the objective.

The influence of the electrostatic drive power has also to be taken into account in order to avoid non-linear effects. On Figure 1.33 is shown the mechanical response of the suspended  $\text{NiPS}_3$  homostructure (*Mordor*) under electrostatic actuation at 130 K for increasing drive power  $P_{RF}$ . The frequency and damping of the mechanical mode are almost unaffected by the driving power modification up to -10 dBm which presents a slightly asymmetrical lineshape, that is the sign of non-linear effects emergence. As a consequence, we will set the maximum drive power at -15 dBm for  $\text{NiPS}_3$  samples under electrostatic actuation.

## Chapter conclusion

In this chapter, we reviewed the concepts and methods that will be exploited throughout this manuscript and how they are applied to magnetic van der Waals materials studied in a drum-like nano-resonator geometry.

First, we examined the physical properties of  $\text{FePS}_3$  and  $\text{NiPS}_3$ , the two materials we focus on in this work (see Sec. 1.1). We presented, notably, their different magnetic configurations, with an out-of-plane easy axis for  $\text{FePS}_3$  and an in-plane easy axis for  $\text{NiPS}_3$ , their mechanical properties with their calculated Young's modulus and Poisson ratios and some of their thermodynamics properties with, in particular, the discontinuity observed in their measured specific heats for temperatures close the magnetic phase transition.

Then, we detailed the challenges in the nano-fabrication processes of magnetic few-layer suspended samples (see Sec. 1.2). The substrate pre-patterning process involving laser-lithography, metal deposition and reactive ion etching, in order to implement the electrodes and holes, was described. The mechanical cleavage procedure to obtain few-layer magnetic materials flakes from bulk crystals was explained, followed by a presentation of the two transfer methods used in our case to suspend the exfoliated flakes over the pre-patterned holes.

The next section was dedicated to the experimental setup description (see Sec. 1.3). We presented the two cryostats available for the measurements, notably the one that was the most used in this work, which is a helium closed-cycle cryostat embedded in an optical table and including a cryo-compatible microscope objective. These features ensure high spatial and temperature stability. The excitation and collection optical paths for the Raman spectroscopy and nanomechanics measurements were reviewed. The setup interfacing in *Python* was also presented, including an automatic correction of the spatial drift induced by temperature ramps.

The penultimate section of this chapter was devoted to the presentation of Raman spectroscopy fundamentals, and its application to the materials of the  $\text{MPS}_3$  family at room temperature (see Sec. 1.4). The microscopic mechanisms of Raman scattering were explained in terms of inelastic light scattering by phonons mediated by electrons. The phonons probed at the first order by Raman spectroscopy were shown to be those located at the Brillouin zone center  $\Gamma$ , i.e. with a wavevector close to zero. A number of fifteen phonons modes visible in  $\text{MPS}_3$  Raman spectrum presenting  $A_g$  and  $B_g$  symmetries was determined, thanks to group theory considerations, taking into account the  $\text{MPS}_3$  monolitic stacking, combined with Raman spectroscopy selection rules and illustrated by  $\text{MPS}_3$  calculated phonon dispersions. These predictions were compared to the spectra measured on bulk  $\text{FePS}_3$  and  $\text{NiPS}_3$  supported samples, where only seven phonons modes were observed, mainly due to the degeneracy in frequency of some phonon modes.

Finally, the nano-optomechanical behavior of a drum-like nano-resonator was derived (see Sec. 1.5). The spatial profiles and resonance frequencies of the normal vibrational modes of a circular thin-film were calculated from its energy minimization. The plate and membrane regimes

have been identified from the resonance frequency expression and compared to the resonance frequencies measured on the studied samples, concluding that their dynamic can be described by the membrane regime. Then, we modeled the nano-resonator displacement along  $z$  by a damped harmonic oscillator and derived its linear response in the frequency domain that presents a Lorentzian lineshape at the resonance. We reviewed the interferometric detection scheme of the membrane displacement that is based on the Fabry-Pérot cavity formed by the bottom substrate and the suspended flake. The expression of the thermal displacement noise density was derived and a room temperature calibrated Brownian motion spectrum of a FePS<sub>3</sub> drum-like resonator was shown. Then, we presented the two methods used during this thesis to drive the membrane motion, that are an electrostatic actuation and a laser-induced actuation. Finally, we discussed some results of light backaction on the membrane response, that displays absorption effects with the increase of the probe laser power.

## Chapter 2

---

# Study of magnetic phase transitions

---

In this Chapter we will show that we are able to probe the magnetic order in  $\text{FePS}_3$  and  $\text{NiPS}_3$  suspended membranes by combining nanomechanics and Raman spectroscopy. Demonstrating the phase transition of these magnetic nanodrums and estimating their Néel temperature is the first step towards the strain-tuning of their magnetic properties. We will first study the magnetic phase transition using optomechanics, following a methodology developed separately by Šiškins *et al.* [26] and Jiang *et al.* [27] in 2020. In the first of these works, the magnetic phase transition of  $\text{FePS}_3$  is probed on a bare suspended flake of about 11 layers, we will here investigate it for a 5-layer  $\text{FePS}_3$  flake encapsulated in a van der Waals heterostructure. Magnetic phase transitions of bulk  $\text{FePS}_3$  and  $\text{NiPS}_3$  have been studied using Raman spectroscopy already in the late 80's [175, 176], before the demonstration of magnetic order persistence in monolayer  $\text{FePS}_3$  and bilayer  $\text{NiPS}_3$  in two papers of 2016 [14] and 2019 [32], respectively. Raman spectroscopy has become a standard method to probe locally the magnetic order in magnetic van der Waals materials [44, 115, 177, 178].

### 2.1 $\text{FePS}_3$ phase transition

We will first probe the magnetic order of an approximately 5-layer  $\text{FePS}_3$  flake embedded in the sophisticated heterostructure of the sample *Fantadwich* (see Sample list 1.2.4). The advantages of this sample are that the drum is contacted to the gold electrode thanks to a graphene bilayer ensuring a better electrical contact; and that the  $\text{FePS}_3$  flake is encapsulated, protecting it from an eventual oxidation. It is also the opportunity to demonstrate that the magnetic phase transition is still detectable despite the presence of other materials.

#### 2.1.1 Probed by nanomechanical measurements

We want to monitor the evolution of the resonance frequency and quality factor across  $\text{FePS}_3$  magnetic phase transition expected at 120 K. For this, we record mechanical response spectra

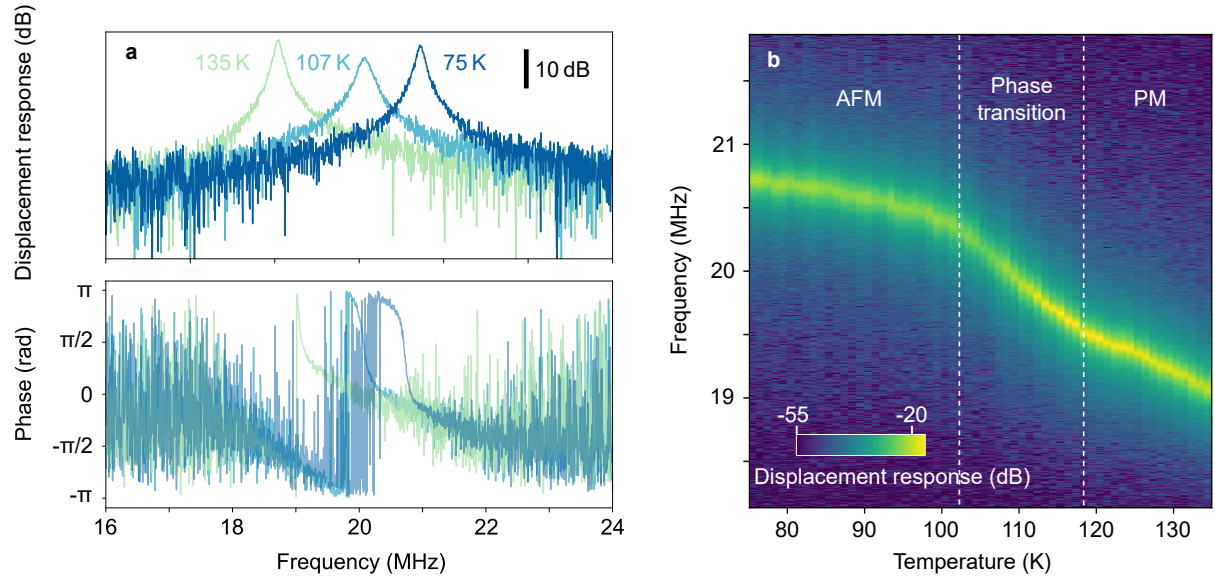


**Figure 2.1: Evolution of the fundamental mode mechanical response with temperature for the FePS<sub>3</sub>-based heterostructure.** **a.** On the top panel is shown the mechanical displacement spectra at 135 K (in green), 107 K (in light blue) and 75 K (in dark blue) for a DC voltage of 16 V. Their respective phases are plotted on the bottom panel. **b.** Colorplot displaying all the mechanical response spectra acquired between 75 and 135 K. The evolution of the resonance frequency with temperature is clearly visible. The dotted lines delimit three regions with different magnetic orders, AFM meaning antiferromagnetic and PM paramagnetic.

of the fundamental mode to an electrostatic actuation at each Kelvin for temperatures between 135 and 75 K (see Fig. 2.1). Three of these spectra are displayed on Figure 2.1 a, two of them recorded at each extremity of the temperature range and one around the middle of it, we first see a frequency shift that is expected due to the contraction of the membrane with decreasing temperature. We also note that the mechanical response at 107 K is broader than the two others. If we now consider all the spectra, we can access to the evolution of the membrane resonance frequency with temperature that can be seen on the colorplot of Figure 2.1 b. The striking feature in this evolution is a break of slope between 103 and 119 K, that indicates the phase transition region.

This slope variation can be explained by identifying the link between the membrane resonance frequency  $f_m$  and its specific heat  $c_v(T)$ . We will first derive the expression in the case of the FePS<sub>3</sub> layer alone, before generalizing it to an heterostructure.

### Principle of the phase transition detection for a homostructure

The fundamental mode resonance frequency for a circular membrane is expressed as (see Eq. 1.33)

$$f_m(T) = \frac{\alpha_{01}}{2\pi R} \sqrt{\frac{E}{\rho(1-\nu)}} \varepsilon(T) \quad (2.1)$$

with  $\alpha_{01} = 2.4049$  the first root of the Bessel function of the first kind,  $R$  the membrane radius,  $E$ ,  $\nu$  and  $\rho$  the Young's modulus, Poisson ratio and mass density of  $\text{FePS}_3$ , respectively (see Section 1.1.3).  $\varepsilon(T)$  is representing the total in-plane strain in the  $\text{FePS}_3$  layer and can be decomposed as  $\varepsilon(T) = \varepsilon_0 + \varepsilon^{\text{th}}(T)$  where  $\varepsilon_0$  is representing the strain at room temperature and  $\varepsilon^{\text{th}}(T)$  the thermal strain induced by the temperature variations. The thermal strain can be expressed as a function of the thermal expansion coefficients that gives, taking into account the substrate contribution [26, 179],

$$\varepsilon^{\text{th}}(T) = - \int_{300\text{K}}^T (\alpha_{\text{FePS}_3}(T') - (\alpha_{\text{SiO}_2}(T') + \alpha_{\text{Si}}(T'))) dT', \quad (2.2)$$

where  $\alpha_{\text{FePS}_3}$  is the thermal expansion coefficient of the  $\text{FePS}_3$ ,  $\alpha_{\text{Si}}$  and  $\alpha_{\text{SiO}_2}$  are those of the silicon and  $\text{SiO}_2$  forming the substrate.

The thermal expansion coefficient can be linked to the specific heat through the Grüneisen parameter  $\gamma_D$  as [134, 180]

$$c_v(T) = 3\alpha_{\text{FePS}_3}(T) \frac{KV_M}{\gamma_D} \quad (2.3)$$

with  $K$  the bulk modulus of  $\text{FePS}_3$  and  $V_M$  the layer molar volume. The Grüneisen parameter is defined as the ratio between the variation of the lattice phonons frequency  $\omega$  and the variation of volume  $V$ , and can also be re-expressed as a function of the Poisson ratio using elasticity theory as [180, 181]

$$\gamma_D = -\frac{V}{\omega} \frac{\partial \omega}{\partial V} \simeq \frac{3}{2} \left( \frac{1 + \nu}{2 - 3\nu} \right), \quad (2.4)$$

it can thus be considered as temperature independent.

Combining the derivative of Equations (2.1) and (2.2) with Equation (2.3) we obtain

$$c_v(T) = 3 \left( \alpha_{\text{Si}}(T) + \alpha_{\text{SiO}_2}(T) - \frac{1}{\mu^2} \frac{df_m^2(T)}{dT} \right) \frac{KV_M}{\gamma_D}. \quad (2.5)$$

The parameter  $\mu$  is equal to  $\frac{\alpha_{01}}{2\pi R} \sqrt{\frac{E}{\rho(1-\nu)}}$ . The quantity  $df_m^2(T)/dT$  is related linearly to the specific heat and will thus reflect its magnetic contribution that is peaked at the Néel temperature (see Section 1.1.4).

## Principle of the phase transition detection for a heterostructure

However, in our case we are not measuring only a suspended  $\text{FePS}_3$  layer, but a van der Waals heterostructure consisting of four different materials. We will consider independent layers without sliding effects nor strain induced by the mismatch of their thermal expansion coefficients. The resonance frequency of the heterostructure depends on weighted sums of the densities and thermal

strains of its constituting materials and can be modeled as [29]

$$f_m(T) = \sqrt{\left(\frac{\alpha_{01}}{2\pi R}\right)^2 \sum_i \frac{1}{h_i \rho_i} \frac{E_i h_i}{1 - \nu_i} \varepsilon_i^{\text{th}}(T) + f_m^2(T_0)} \quad (2.6)$$

where the indices  $i$  range from 1 to 4 and are representing the different materials composing the heterostructure, for example  $h_i$  is the layer thickness of material  $i$ , and  $f_m(T_0)$  is the resonance frequency of the membrane at the initial temperature  $T_0$ . The derivative of the squared resonance frequency is then written as

$$\frac{df_m^2}{dT}(T) = -\tilde{\mu}^2 \sum_i \frac{E_i h_i}{1 - \nu_i} [\alpha_i(T) - (\alpha_{\text{SiO}_2}(T) + \alpha_{\text{Si}}(T))] \quad (2.7)$$

with  $\tilde{\mu} = \left(\frac{2.4049}{\pi d}\right) \frac{1}{\sqrt{\sum_i h_i \rho_i}}$ .

The contribution of each layer to the evolution of  $df_m^2(T)/dT$  with temperature depends on its thickness, elastic constant values and thermal expansion coefficient value at the temperature  $T$ . The highest contributions should then come from the hBN layer, due to its high thickness, and from FePS<sub>3</sub>, thanks to its high thermal expansion coefficient and moderate thickness (see Tables 1.2 and 1.3). Nevertheless, since we do not know precisely the layer number of those materials while the weights of the sum depend dramatically on it, a meaningful value of these contributions cannot be estimated.

Using Equation (2.3), the relation between the membrane resonance frequency and the specific heat is expressed as

$$\frac{df_m^2}{dT}(T) = -\tilde{\mu}^2 \sum_i \frac{E_i h_i}{1 - \nu_i} \left[ c_{v,i}(T) \frac{\gamma_{D,i}}{3K_i V_{M,i}} - (\alpha_{\text{SiO}_2}(T) + \alpha_{\text{Si}}(T)) \right]. \quad (2.8)$$

In suspended heterostructures, we expect the resonance frequency to encapsulate the weighted sum of the specific heats from the different materials forming the membrane, and notably from the magnetic layers.

## Results and discussion

We can extract the suspended heterostructure resonance frequency  $f_m$  by fitting the spectra of Figure 2.1 with the model of Equation (1.56). We obtain its evolution with temperature displayed on Figure 2.2 a, the steeper slope between 101 and 119 K is clearly visible. The derivative of the square of the resonance frequency is then calculated and plotted in Figure 2.2 b. A peak, located in the same temperature range as the steeper slope in the resonance frequency evolution, is emerging on top of a background that is increasing with increasing temperature. This trend is very similar to the calorimetric measurement of bulk FePS<sub>3</sub> specific heat by Takano *et al.* [28] (see Fig. 1.6 a). The background evolution is thus resulting from the specific heat of all the materials composing the heterostructure and is mainly coming from their lattice contributions,

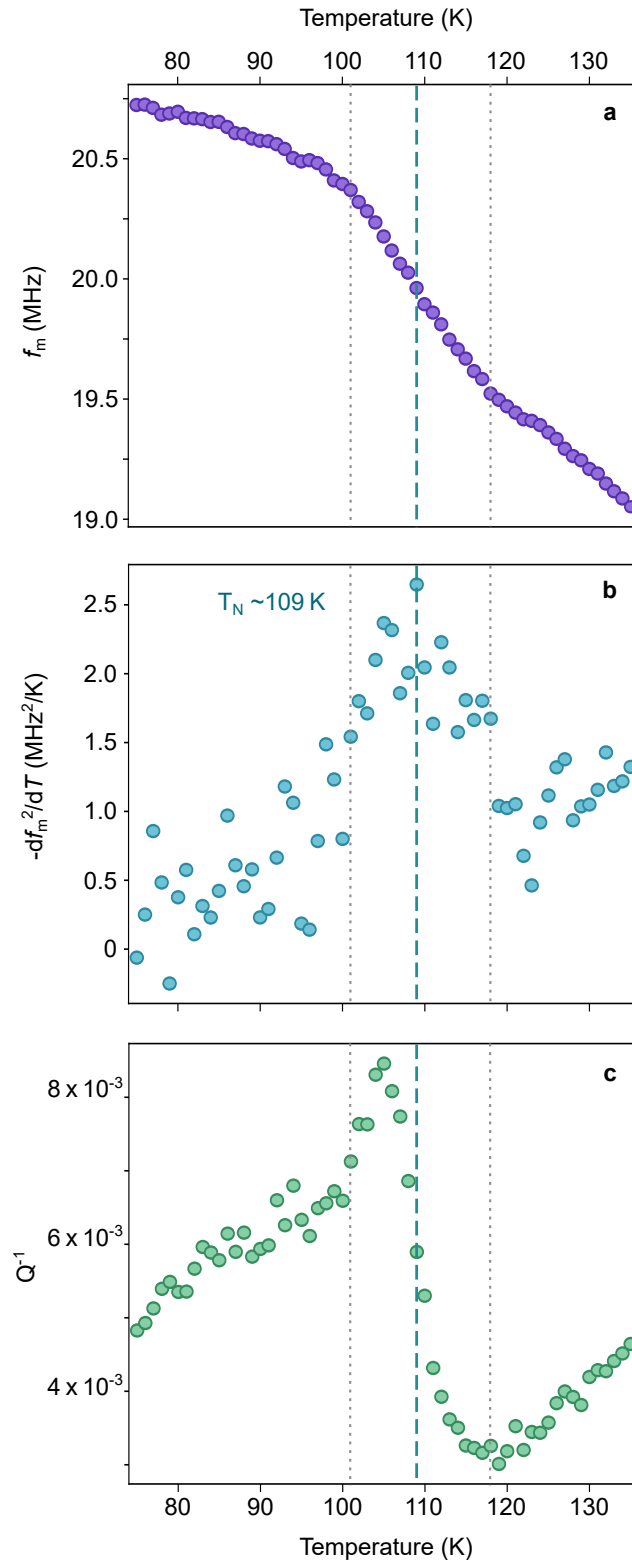


**Figure 2.2:** Estimation of FePS<sub>3</sub> Néel temperature for a 5-layer flake embedded in a heterostructure (*Fantadwich*, see Sample list 1.2.4), from the mechanical mode parameters evolution with the temperature. **a.** Fundamental mode resonance frequency. **b.** Opposite of the derivative with respect to the temperature of the resonance frequency squared. The Néel temperature of the sample can be estimated from the peak maximum. **c.** Inverse of the quality factor. An inflection point is observed at the Néel temperature. The blue dashed line indicates the estimated Néel temperature, while the gray dotted lines delimit the phase transition region.

whereas the peak is originating from the magnetic specific heat of the five layers of FePS<sub>3</sub> (see Section 1.1.4). The top of the peak is therefore indicating the Néel temperature of FePS<sub>3</sub>, that is around 109 K for this sample. We note that the total width of the peak is about 18 K that is comparable to the width of approximately 20 K measured in [28] and is attributed to a structural deformation accompanying the phase transition [91, 117].

On the other hand, the inverse of the mechanical mode quality factor presents an increasing evolution in the phase transition region characterized by an inflection point at the phase transition temperature (see Fig. 2.2 c). This feature is attributed to an increase of the thermoelastic damping near the critical temperature. The thermoelastic damping  $Q_{\text{QED}}^{-1}$  results from the coupling between the strain field and a temperature field and is a significant source of damping in mechanical resonators [182]. It can be written as [182–184]

$$Q_{\text{QED}}^{-1} = \eta \Delta_E \Gamma_D(\Omega, \tau), \quad (2.9)$$

where  $\eta$  is a dimensionless correction pre-factor,  $\Delta_E$  is the relaxation strength and  $\Gamma_D$  is the dissipation peak function. The pre-factor  $\eta$  is a function of the Poisson ratio only and can be considered as temperature independent. The relaxation strength depends on the specific heat and the thermal expansion coefficient as  $\Delta_E = E\alpha^2 T/c_v$ . The dissipation peak term is given by [184, 185]

$$\Gamma_D(\Omega, \tau) = \frac{6}{\zeta_D^2} - \frac{6}{\zeta_D^3} \frac{\sinh(\zeta_D) + \sin(\zeta_D)}{\cosh(\zeta_D) + \cos(\zeta_D)} \quad (2.10)$$

with  $\zeta_D = (\pi/\sqrt{2})\sqrt{\Omega\tau}$ . The thermoelastic damping is then dependent on the thermal relaxation time  $\tau$  that corresponds to the characteristic time for the heat to travel out of the resonator. For a uniformly heated membrane, the thermal relaxation time is given by [186]

$$\tau(T) = \frac{R^2 \rho c_v(T)}{w^2 K_T(T)} \quad (2.11)$$

with  $K_T$  the membrane thermal conductivity,  $R$  its radius and  $w$  a constant related to the membrane geometry. The thermal relaxation time is then proportional to the specific heat and has been demonstrated to exhibit a peak at the magnetic phase transition in the case of FePS<sub>3</sub> in the work of Baglioni *et al.* [185]. This model has been showed to fully reproduce the behavior of the inverse of the quality factor at FePS<sub>3</sub> phase transition [184].

In conclusion, nano-optomechanical measurements allowed us to probe the specific heat of a 5-layer FePS<sub>3</sub>-based suspended heterostructure through the evolution with temperature of both the derivative with respect to the temperature of the squared resonance frequency  $df_m^2(T)/dT$  and the inverse of the quality factor  $Q^{-1}$ . This gives us access to the magnetic contribution to the specific heat and so to the Néel temperature of FePS<sub>3</sub>, that we estimated at 109 K for this 5 layer FePS<sub>3</sub>-based heterostructure. This is about 10 K lower than the expected Néel temperature for bulk FePS<sub>3</sub>, but consistent with the values ranging from 112.7 to 107.9 K measured by Houmes

*et al.* [117] using the same method on several FePS<sub>3</sub> samples. As we will show in the following section, this method can be applied to other magnetic van der Waals materials as long as their magnetic contribution to the specific heat is high enough to be detected.

## 2.1.2 Probed by Raman spectroscopy

### Evidence of the antiferromagnetic phase in bulk FePS<sub>3</sub>

The Raman spectrum of bulk FePS<sub>3</sub> at room temperature has already been discussed in Section 1.4.4. We will now compare it with the one obtained on the same sample (*Ocean*, see Sample list 1.2.4) at low temperature, when FePS<sub>3</sub> is in its antiferromagnetic phase (see Fig. 2.3).

The striking difference between the two spectra is the appearance of four new peaks between 80 and 120 cm<sup>-1</sup> in the antiferromagnetic phase and the vanishing of the (A<sub>g</sub><sup>1</sup>, B<sub>g</sub><sup>1</sup>) mode which was present at room temperature around 100 cm<sup>-1</sup>. The emergence of new peaks below the Néel temperature was first reported in the work of Scagliotti *et al.* in 1985 [187], leading to numerous studies in order to elucidate their origin [14, 95, 115, 175, 176].

The peaks P<sub>1</sub>, P<sub>2</sub> and P<sub>3</sub> are attributed to *zone-folded phonons*. This type of phonons had previously been reported in the mid-70s in europium chalcogenides (EuX, with X = S, Se, Te) [188, 189].

In the case of FePS<sub>3</sub>, the zone-folded phonons appear due to the doubled size of the magnetic unit cell compared to the crystallographic unit cell, both in-plane and out-of-plane, at the onset of antiferromagnetic ordering as already mentioned in Section 1.1.1. Therefore, the inversion center of the magnetic unit cell is now located at the border of two crystallographic unit cells (see Fig. 2.4), implying that some phonons that were antisymmetric to the inversion center (with a *u* subscript) and so Raman inactive in the paramagnetic phase, could now become symmetric to the inversion center (with a *g* subscript) and so Raman active in the antiferromagnetic phase. This can also be seen in the *k*-space as a magnetic Brillouin zone halved compared to the crystallographic Brillouin zone. To obtain this antiferromagnetic Brillouin zone, the paramagnetic Brillouin zone is folded following the arrows drawn in Figure 2.4. The phonons probed by Raman spectroscopy at the first order being those located at the center of the Brillouin zone (see Section 1.4.1), this folding allows to access new phonon modes previously located at the edges, called zone-folded phonons.

Nevertheless, to contribute to this spin-ordering-induced Raman scattering and be visible on the Raman spectrum, the phonon mode has to modulate the exchange interaction or the spin-orbit coupling [176]. For this, transition metal atoms are likely to be involved in the vibration mode, explaining why the zone-folded phonons emerge only in the low-frequency region known to host modes involving iron atoms displacements (see section 1.4.2).

To determine the origin and symmetry of the peaks P<sub>1</sub>-P<sub>3</sub> their measured frequencies have to be identified to the ones calculated at the  $\Gamma$  point for this larger magnetic cell. If we take a look at the dispersion curves in Figure 1.22 **a,b** we see indeed at least five new modes, some of them

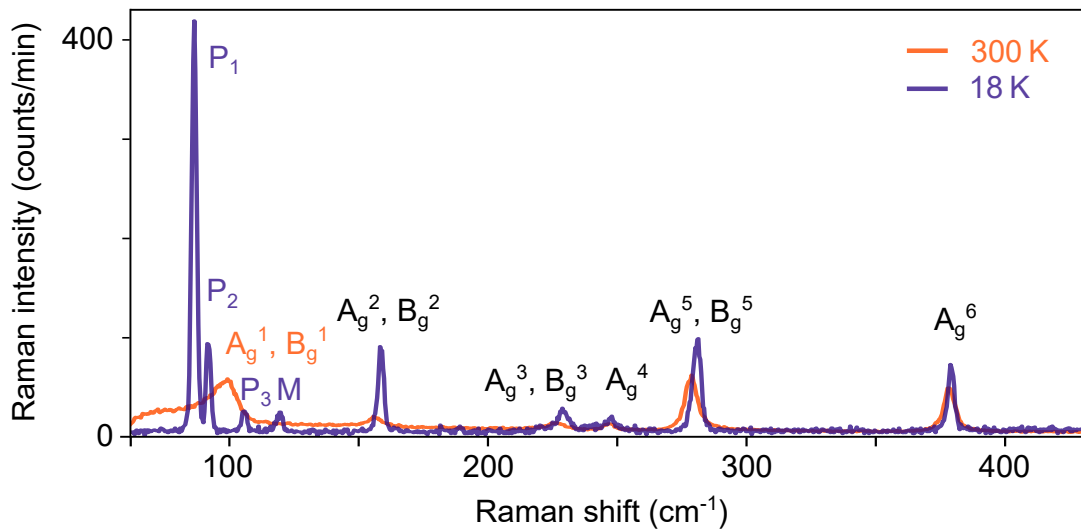


**Figure 2.3:** Raman spectra of bulk FePS<sub>3</sub> (*Ocean*, see Sample list 1.2.4) in its paramagnetic phase at room temperature (in orange) and in its antiferromagnetic phase at 18 K (in purple) acquired with a wavelength of  $\lambda = 532.1 \pm 0.3$  nm. Four new peaks appear in the low frequency region of the Raman spectrum in the antiferromagnetic phase.

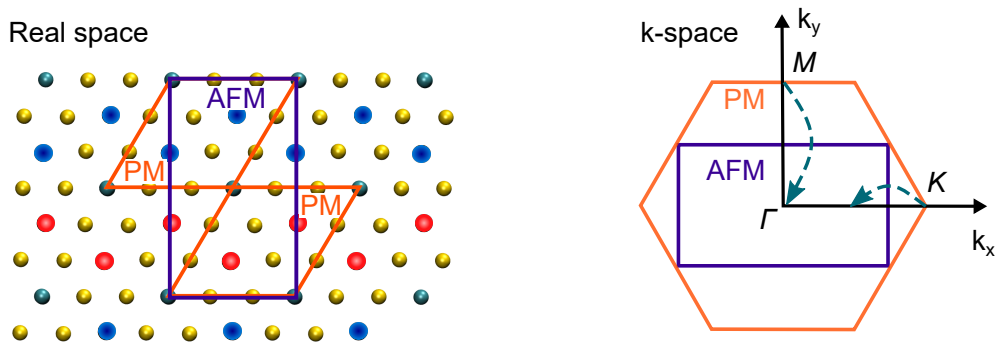


**Figure 2.4:** Schematic on the origin of zone-folded phonons, the doubling of the unit cell size on the onset of antiferromagnetic order induces a halving of the Brillouin zone. The left side shows a FePS<sub>3</sub> layer seen from top, the atoms in blue are Fe atoms with spin down and those in red are Fe atoms with spin up. Two paramagnetic (PM) unit cells are represented in orange and an antiferromagnetic (AFM) one in purple. On the right side are drawn the Brillouin zones in the paramagnetic and antiferromagnetic phases of FePS<sub>3</sub> with their high-symmetry points. The cyan arrows indicate the direction of folding of the paramagnetic Brillouin zone when turning into the antiferromagnetic Brillouin zone.

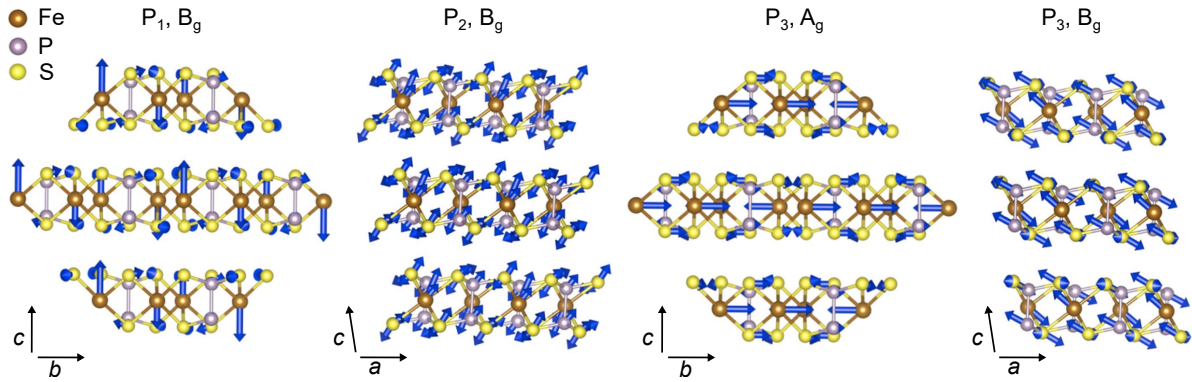


**Figure 2.5:** Scheme of the normal vibrational modes corresponding to the three zone-folded phonons calculated in [177]. The symmetry of the mode is indicated next to its P-label. The modes are represented on three FePS<sub>3</sub> layers seen from side. In brown are the Fe atoms, in purple the P atoms and in yellow the S atoms. The blue arrows represent the direction and amplitude of atoms displacement.

looking degenerate, in the range  $80\text{-}120\text{ cm}^{-1}$  for the antiferromagnetic phase of FePS<sub>3</sub>. Their allocation to a measured peak, and so their point of origin in the paramagnetic Brillouin zone, as proposed in the existing literature, are discussed in the following.

The peak P<sub>1</sub> is unanimously attributed to the folding of a  $M$  point phonon [14, 95, 176].

The peak P<sub>2</sub> is also attributed to a  $M$  point-folded phonon by Sekine *et al.* [176] and Wang *et al.* [95] but to a  $\Gamma$  point phonon by Lee *et al.* [14]. According to Lee *et al.*, that would be the same as the mode visible in the paramagnetic phase.

The peak P<sub>3</sub> has  $M$  and  $\Gamma$  components according to [14], whereas [176] only allocate a  $M$  component to it.

The representations and symmetries of the associated vibration modes calculated by Pawbake *et al.* [177] are shown on Figure 2.5. Two modes are attributed to the peak P<sub>3</sub> because it is not clear from which it originates. We indeed see that all the modes include large displacements of iron atoms, mostly out-of-plane for P<sub>1</sub> and P<sub>2</sub> and the B<sub>g</sub> mode of P<sub>3</sub>, and in-plane for the A<sub>g</sub> mode of P<sub>3</sub>.

We can note that, although the Brillouin zone is halved in the in-plane and out-of-plane directions, the zone-folded phonon are only originating from the in-plane folding, highlighting the weak out-of-plane magnetic interactions in 2D materials [176]. This is emphasized by the measurements performed on monolayer FePS<sub>3</sub> where P<sub>1</sub> and P<sub>2</sub> are still visible, so they clearly do not originate from out-of-plane zone-folding [14, 95].

On the other hand, the peak M presents a more pronounced shift towards the higher frequencies with the decrease of the temperature than the other P-labelled peaks and was thus assigned to a magnon mode in the work of Sekine *et al.* from 1990 [176]. This claim was confirmed in 2020 by magneto-Raman spectroscopy measurements of McCreary *et al.* [115] involving a magnetic field. In an Ising antiferromagnet like FePS<sub>3</sub>, half of the spins are up and the other half are down, forming two sublattices of opposite magnetization  $M_1$  and  $M_2$  along the  $z$  axis. In the ground state, the net magnetization is zero and the two normal magnon modes, one with

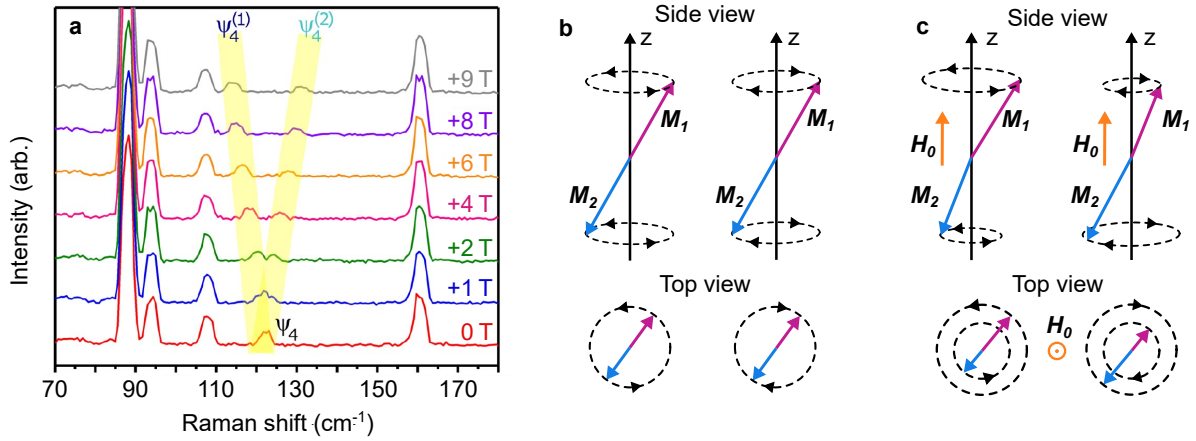


**Figure 2.6: Demonstration of the magnon mode in the Raman spectrum of FePS<sub>3</sub>.** **a.** Raman spectra of FePS<sub>3</sub> at 5 K in function of the applied magnetic field. The peak  $\psi_4$  that splits into two components,  $\psi_4^{(1)}$  and  $\psi_4^{(2)}$ , is the magnon mode. **b.** Scheme of the two magnon normal modes in an antiferromagnet precessing in opposite directions. The vector  $M_1$  (pink),  $M_2$  (blue) represent the magnetization of the spin up, down, sublattice respectively. **c.** Scheme of the two magnon normal modes upon an applied magnetic field  $H_0$  along the  $z$ -axis. Their degeneracy is lifted, the left mode has its energy increasing with  $H_0$  and corresponds to the peak  $\psi_4^{(2)}$ , whereas the right mode has its energy decreasing with increasing  $H_0$  and corresponds to the peak  $\psi_4^{(1)}$ . Adapted from [115].

both magnetization vectors precessing clockwise and both counterclockwise for the other, are degenerate (see Fig. 2.6 b). The application of an out-of-plane magnetic field  $H_0$  causes a Zeeman splitting and lifts this degeneracy (see Fig. 2.6 c), resulting in the splitting of mode M in the Raman spectrum as shown on Figure 2.6 a that demonstrates its magnonic nature.

Another feature of the FePS<sub>3</sub> Raman spectrum in its antiferromagnetic phase is the enhancement of the peak ( $A_g^2$ ,  $B_g^2$ ) intensity compared to the paramagnetic phase. A tentative explanation has been formulated by Sekine *et al.* [176], considering the folding of another M-point phonon with a frequency around  $160 \text{ cm}^{-1}$ . According to the same paper [176], the asymmetric shape and disappearance at low temperatures of the peak ( $A_g^1$ ,  $B_g^1$ ) can be modeled by spin-disorder-induced Raman scattering, coming from short-range fluctuations of spin.

The emergence of zone-folded phonons at the magnetic phase transition of FePS<sub>3</sub> will now be used to determine its Néel temperature in a few-layer suspended sample.

### Determination of the Néel temperature in a suspended FePS<sub>3</sub>-based heterostructure

Raman spectra for temperatures between 80 and 150 K were acquired on a suspended heterostructure (*Fantadwich*, Sample list 1.2.4), that is composed of (from bottom to top) bilayer graphene, 5 layers of FePS<sub>3</sub>, a monolayer of WS<sub>2</sub> and multilayer hBN (see Sample list 1.2.4). As a consequence, in addition to the FePS<sub>3</sub> Raman peaks, four WS<sub>2</sub> peaks are also visible on the Raman spectra of Figure 2.7 a. The FePS<sub>3</sub> modes are labelled the same way as in previous spectra, whereas the WS<sub>2</sub> peaks are left without labels. Since the FePS<sub>3</sub> layer is much thinner than the one showed on Figure 2.3, the low intensity peaks ( $A_g^3$ ,  $B_g^3$ ),  $A_g^4$ ,  $P_3$  and M are no longer visible.

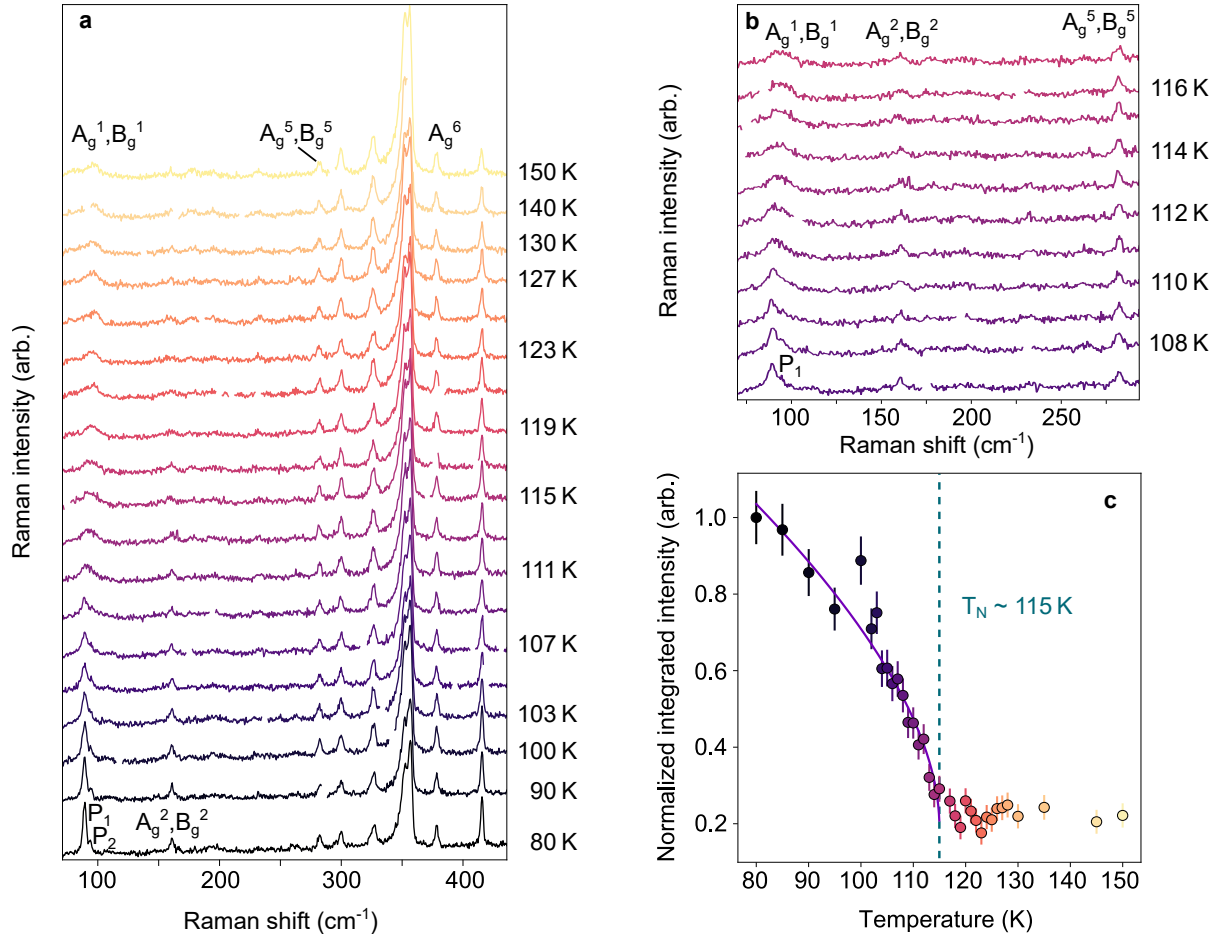


**Figure 2.7: Determination of FePS<sub>3</sub> Néel temperature using Raman spectroscopy.** **a.** Raman spectra of the heterostructure for temperatures from 80 to 150 K. The labelled peaks are originating from FePS<sub>3</sub>, whereas the peaks with no labels are from the WS<sub>2</sub> layer. The peak ( $A_g^1, B_g^1$ ) is progressively replaced by peaks  $P_1$  and  $P_2$  with decreasing temperature. **b.** Raman spectra of the low frequency region (70-290 cm<sup>-1</sup>) for temperatures around the phase transition (109 K to 117 K). The zone-folded phonon  $P_1$  is emerging on top of the ( $A_g^1, B_g^1$ ) peak. **c.** Evolution of  $P_1$  normalized integrated intensity with temperature. The dots correspond to the data, the vertical lines to the error bars and the solid purple line to the fit with the model developed by Suzuki *et al.* [30] for temperatures below  $T_N$ . The phase transition temperature is thus estimated at around 115 K.

We notice, as in the previous part, that the only changes to the Raman spectra are occurring in the low frequency region (below 200 cm<sup>-1</sup>). The peaks P<sub>1</sub> and P<sub>2</sub> emerge gradually from the peak (A<sub>g</sub><sup>1</sup>, B<sub>g</sub><sup>1</sup>) before gaining in intensity. We also note a progressive increase in the intensity of the peak (A<sub>g</sub><sup>2</sup>, B<sub>g</sub><sup>2</sup>) which is not detectable for temperatures above 119 K. These modifications of the peaks intensities appears to be continuous and not abrupt as it was already visible on the nanomechanical measurements (see Fig; 2.2), making the estimation of the Néel temperature more challenging. A zoom on the temperature range where the peak P<sub>1</sub> is appearing, and so does the antiferromagnetic order, is shown on Figure 2.7 b with one spectrum for each Kelvin step. We see that the height of the peak (A<sub>g</sub><sup>1</sup>, B<sub>g</sub><sup>1</sup>) starts to rise at around 114 K and the peak P<sub>1</sub> is clearly visible at 110 K. Again, the evolution is very smooth and continuous and we can only conclude that the magnetic phase transition takes place between 115 K and 111 K.

To get a more quantitative estimation of the Néel temperature we extract the integrated intensity of the peak P<sub>1</sub> and plot it against the temperature (see Fig. 2.7 c). The integrated intensity is obtained by first subtracting the background and then performing a numerical integration on the interval 86.9 - 92 cm<sup>-1</sup>. The resulting values are normalized by the value at 80 K. The errors on the integrated intensities are estimated by propagation of uncertainties (see Appendix A) taking as sources of uncertainty the 0.55 cm<sup>-1</sup> spacing between two points of the Raman spectrum as a reading uncertainty and an estimated error of 3 counts per minute on the intensity of peak. The integrated intensity is approximately constant between 150 and 116 K and starts to rise at 115 K, that is thus estimated as the Néel temperature of this FePS<sub>3</sub> sample.

The evolution of the integrated intensity with the temperature in the magnetically-ordered phase can be modeled considering spin-dependent phonon Raman scattering as in the work of *Suzuki et al.* [30]. They showed that the integrated Raman intensity can be expressed as

$$I(T) = (n_v(T) + 1) \left| R + P \frac{\langle \mathbf{S}_0 \cdot \mathbf{S}_1 \rangle}{S^2} \right|^2 \quad (2.12)$$

where  $n_v$  is the Bose-Einstein factor as expressed in Eq (1.13),  $R$  and  $P$  are the coefficients of the spin independent and dependent parts, respectively, and  $\langle \mathbf{S}_0 \cdot \mathbf{S}_1 \rangle / S^2$  is the reduced nearest neighbor spin correlation function. According to *Lee et al.* [14] the spin correlation function can be approximated as  $\langle \mathbf{S}_0 \cdot \mathbf{S}_1 \rangle / S^2 \sim m^2(T) \sim (T_c - T)^{2\beta}$  near the phase transition temperature, with  $m$  being the reduced magnetization,  $T_c$  the critical temperature (here  $T_c = T_N$ ) and  $\beta$  the corresponding critical exponent.

The resulting fit of our data with this model below  $T_N$  is the purple solid line on Figure 2.7 c. The Bose-Einstein factor was calculated for each point in temperature considering a P<sub>1</sub> phonon frequency of 88 cm<sup>-1</sup>, corresponding to 2.64 THz. The fitting parameters were  $R$ ,  $P$  and  $\beta$ , the temperature being fixed. Several temperature values were tested for  $T_N$  and 115 K was the one giving the best fit result. From the fit results we obtained a  $R/P$  ratio of 3.1. In [30] a positive  $R/P$  ratio is associated with a similar trend for the integrated intensity evolution with the temperature as the one we measured. The value for the  $\beta$  exponent derived from our fit is

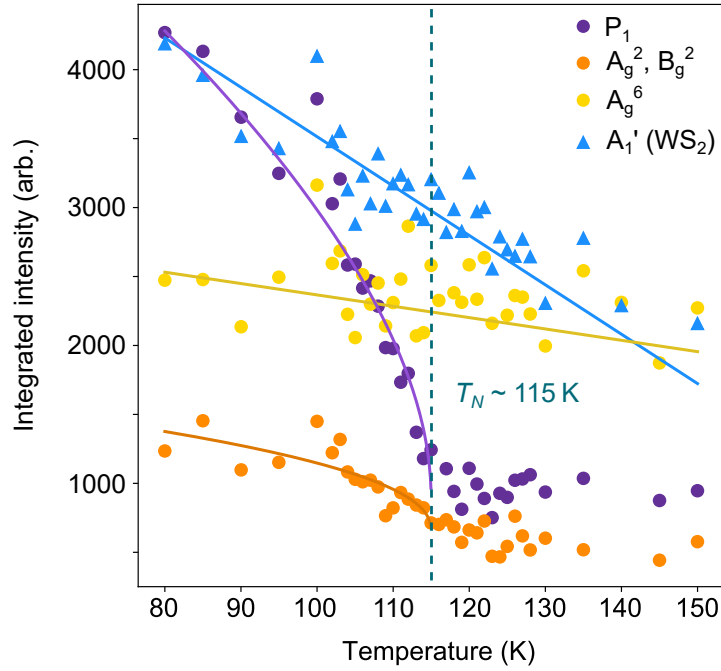


**Figure 2.8:** Integrated intensity evolution with temperature for the peaks  $P_1$  (purple),  $(A_g^2, B_g^2)$  (orange),  $A_g^6$  (yellow) and  $A_1'$  (blue) a peak arising from  $WS_2$ . The data of  $P_1$  and  $(A_g^2, B_g^2)$  are fitted with the model of Suzuki Equation 2.12) (purple and orange solid lines) whereas the data of the peaks  $A_g^6$  and  $A_1'$  are fitted with a linear model (yellow and blue solid lines). The vertical line indicates the estimated phase transition temperature  $T_N$ .

0.21, that is in between the value expected for the three-dimensional Ising model ( $\beta_{\text{Ising}}^{3d} \sim 0.327$ ) and the two-dimensional one ( $\beta_{\text{Ising}}^{2d} = 0.125$ ) [133].

The integrated intensity evolution with temperature for  $P_1$  can be compared with that of other peaks as depicted on Figure 2.8. It shows the greatest change in intensity, with the steepest slope between 115 and 100 K. The variation of the peak  $(A_g^2, B_g^2)$  intensity is weaker than the one of  $P_1$ , but it shows an increase after  $T_N$  and can be fitted using the model of Eq. (2.12), implying that it also arises from spin-dependent Raman scattering. The fixed temperature was also  $T_N = 115$  K and the obtained parameters are  $R/M = 8.13$ , which is also positive, and  $\beta = 0.19$  which is coherent with that found for  $P_1$ . As expected, the peak  $A_g^6$  does not seem to be affected by magnetic ordering and presents an almost flat evolution with temperature. Finally, the peak  $A_1'$  coming from  $WS_2$  and located at around  $415 \text{ cm}^{-1}$  (the last peak on the spectra of Fig. 2.7 a) shows a linear increase in intensity with decreasing temperature and so, does not appear to be related to the magnetic order. The integrated intensities of  $P_1$  and  $(A_g^2, B_g^2)$  peaks are indeed the two suitable quantities to probe antiferromagnetic ordering in  $FePS_3$ .

## 2.2 NiPS<sub>3</sub> phase transition

After developing our measurement protocol on FePS<sub>3</sub>, we went for the phase transition study of NiPS<sub>3</sub>. NiPS<sub>3</sub> has interesting properties like an in-plane magnetic order, a Néel temperature varying with the layer number and an intriguing photoluminescence emission. Moreover, probing its phase transition with nanomechanics promised to be more challenging due to its weaker magnetic contribution to the specific heat than the one of FePS<sub>3</sub>.

We probed the magnetic order of two suspended NiPS<sub>3</sub> homostructure of similar thickness, 10 L (*Balor*) and 13 L (*Mordor*) (see Sample list 1.2.4). The nanomechanics results will be shown for both samples, while only *Mordor*'s Raman measurements will be discussed for the sake of clarity.

### 2.2.1 Probed by nanomechanical measurements

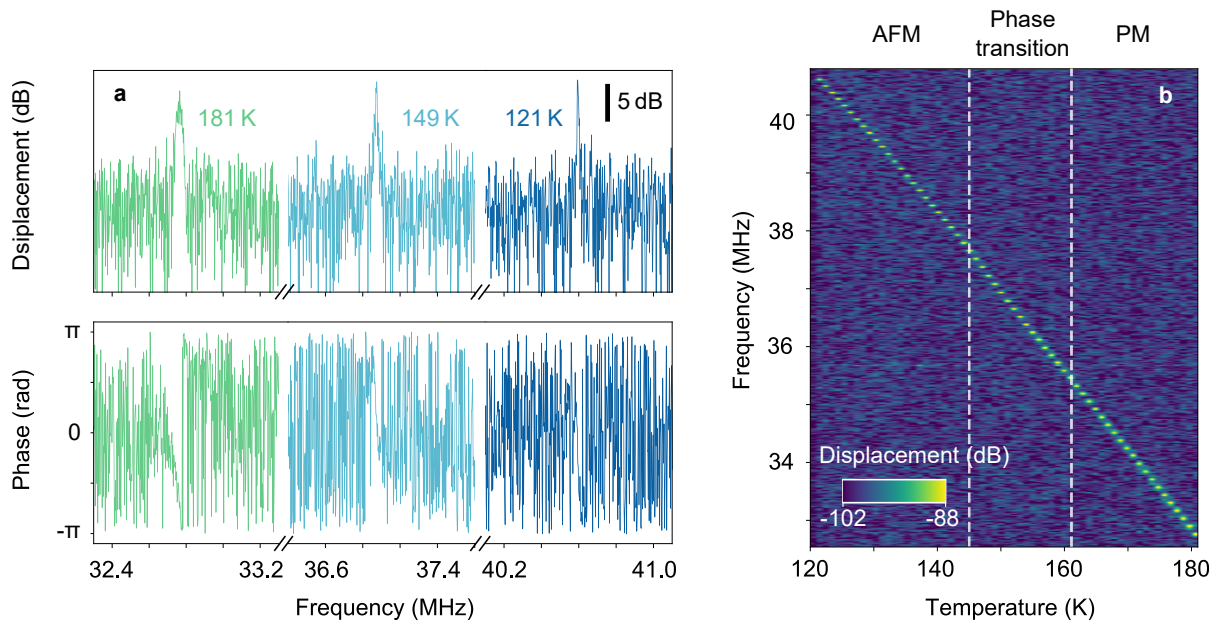


**Figure 2.9: Evolution of the fundamental mode mechanical response with the temperature for the ~ 10 L NiPS<sub>3</sub> sample *Balor*.** **a.** On the top panel is shown its displacement spectra in response to optical forces at 181 K (green), 149 K (light blue) and 121 K (dark blue). The scale bar represents a displacement of 5 dB magnitude. On the bottom panel are shown the corresponding phases. **b.** Colorplot displaying all the mechanical response spectra taken between 120 and 181 K. We can see the evolution of the fundamental mode resonance frequency with the temperature. The dotted lines indicate the separation between the magnetic order configurations, PM and AFM meaning paramagnetic and antiferromagnetic, respectively.

We apply exactly the same method as for probing FePS<sub>3</sub> phase transition in Section 2.1. The mechanical response of the sample is monitored in a temperature range around the expected Néel temperature of NiPS<sub>3</sub> (120-181 K), the resulting displacement spectra are shown on Figure 2.9. We first note that suspended NiPS<sub>3</sub> homostructures have a quality factor about twenty-five times higher than that of FePS<sub>3</sub> heterostructure at the same temperature. This can be explained from

acoustic losses induced by, first, the fabrication process that involves the successive stacking of several layers and, second, by the nature of the heterostructure, that is composed of materials possessing different mechanical properties. NiPS<sub>3</sub> quality factor seems to increase with decreasing temperature, the peak becoming narrower, and does not seem to drop at the phase transition.

On the other hand, the frequency shift induced by the temperature variation is larger, more than 10 MHz for 60 K, than the one observed for the FePS<sub>3</sub> sample *Fantadwich* where it was less than 2 MHz for the same temperature variation. This is again due to the heterostructure nature of the FePS<sub>3</sub> sample whose frequency shift is reduced by the opposite behavior of its constituting materials with the temperature variation: some of them contract while others dilate, inducing stresses of opposite signs (see Eq. 2.6). The mechanical mode frequency of the NiPS<sub>3</sub> resonator is increasing with decreasing temperature, indicating a contraction of the membrane, and so a positive thermal expansion coefficient. However, the change of slope characterizing the antiferromagnetic phase transition is barely visible on the NiPS<sub>3</sub> resonance frequency evolution with temperature, making crucial the calculation of  $df_m^2/dT$ .

As in Section 2.1, the spectra are fitted using the model of Equation (1.38) to extract the mechanical mode resonance frequency  $f_m$  and quality factor  $Q$ . Their evolution with temperature is shown on Figure 2.10, along with that of the derivative of the squared resonance frequency with respect to the temperature  $df_m^2/dT$ . The results obtained for the sample *Balor* using laser-induced actuation are compared to the ones derived from measurements on the sample *Mordor* actuated electrostatically. Laser-induced actuation allows to detect a signal even for low applied DC voltages (here 10 V) to be closer to the intrinsic properties of the membrane, whereas we need to apply at least 18 V to get a sufficient signal with electrostatic actuation on the sample *Mordor*. In both cases we observe a peak in  $-df_m^2(T)/dT$ , originating from the magnetic contribution to the specific heat and indicating the antiferromagnetic transition of NiPS<sub>3</sub> see Eq.( 2.5). We estimate the corresponding Néel temperature as the temperature that coincides with the top of the peak, which gives, considering the uncertainties coming from the peak width,  $T_N \simeq 151 \pm 2$  K for *Mordor* and  $T_N \simeq 148.5 \pm 1.5$  K for *Balor*. If we compare the evolution of  $-df_m^2/dT$  with the temperature to that of the specific heat measured by Pistawala *et al.* [135] (see Fig. 1.6), we first note that the background coming from the lattice contribution seems flatter in our measurements. This could be explained by additional contributions to the specific heat, for example its electronic contribution. Moreover, the peak arising from the magnetic contribution is sharper in our case, but with a comparable width of about 15 K, that is similar to the width of the FePS<sub>3</sub> magnetic contribution peak. However, since no significant lattice deformation has been observed, nor predicted, at the phase transition for NiPS<sub>3</sub> [117].

The most striking feature in the measurements performed on NiPS<sub>3</sub>, compared to the ones carried out on FePS<sub>3</sub>, is the absence of a peak in the inverse of the quality factor evolution with temperature (see Fig 2.10 c,f). A peak in  $Q^{-1}(T)$  at the magnetic phase transition has been demonstrated in Cr<sub>2</sub>Ge<sub>2</sub>Te<sub>6</sub> (CGT) 2D nanodrums [29], showing the relevance of the model of equation (2.9) for other 2D magnetic materials than FePS<sub>3</sub>. However, the peak in CGT inverse

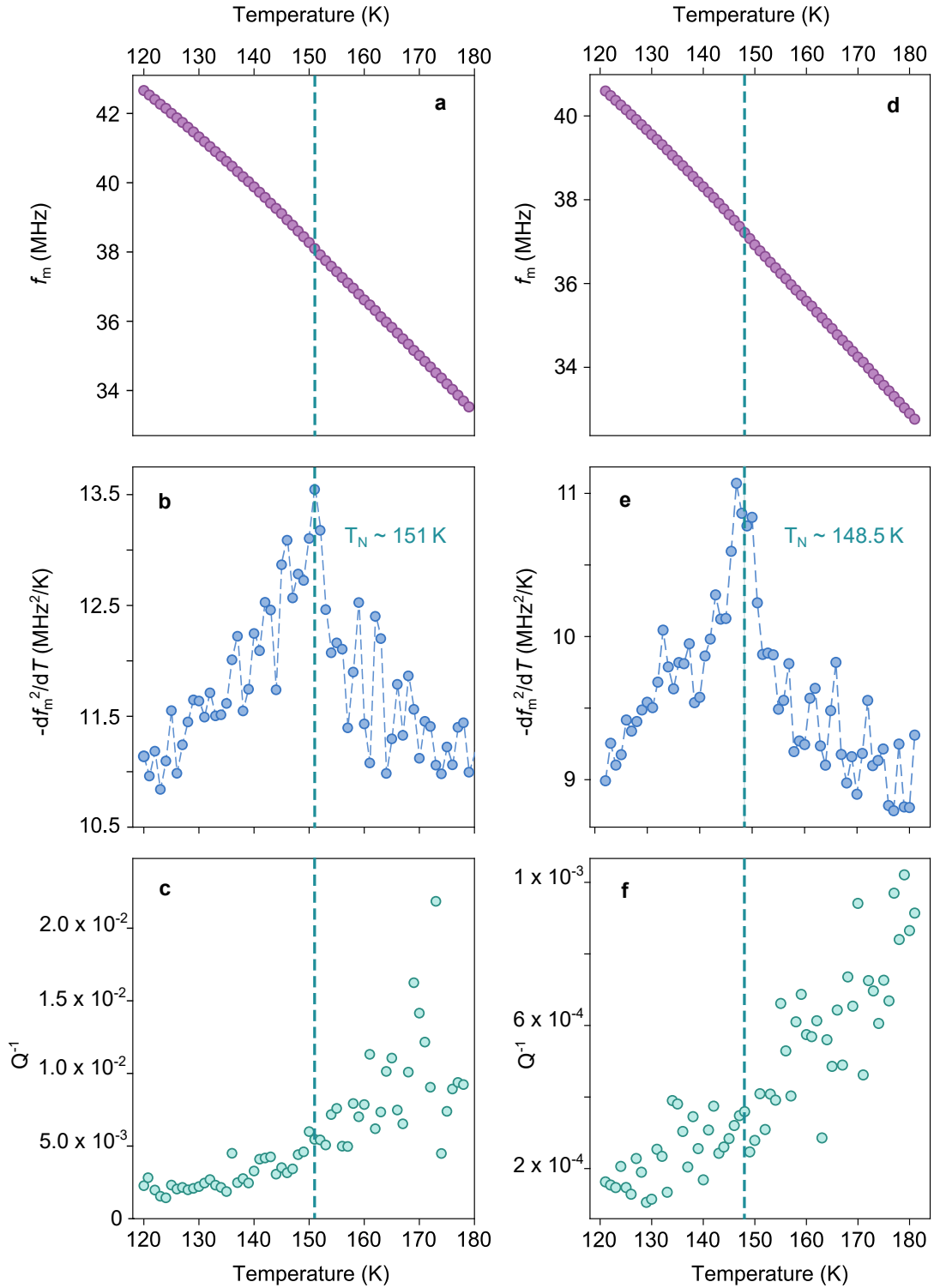


**Figure 2.10: Estimation of NiPS<sub>3</sub> Néel temperature from the mechanical mode parameters evolution with the temperature on the samples *Mordor* and *Balor*.** On the left side are the results of the measurements performed on the sample *Mordor* using an electrostatic actuation and for a DC voltage of 18 V. On the right side are the results of the measurements performed on the sample *Balor* with a laser-induced actuation and a DC voltage of 10 V. The vertical dotted lines indicate the estimated Néel temperature. **a,d.** Fundamental mode resonance frequency  $f_m$  evolution with temperature. **b,e.** Temperature evolution of the opposite of the resonance frequency squared differentiated with respect to the temperature  $df_m^2/dT$ . The top of the peak indicates the Néel temperature of the sample that is around 151 K for *Mordor* and around 148.5 K for *Balor*. **c,f.** Inverse of the quality factor evolution with temperature.

quality factor was already way weaker than the one observed for FePS<sub>3</sub>. Considering that the magnetic contribution to the specific heat of NiPS<sub>3</sub> is lower than the one of FePS<sub>3</sub>, as it is visible on the measured values in Figure 1.6, the contribution from the thermoelastic damping should be weaker in NiPS<sub>3</sub> (Eq. (2.9)). In fact, we focused on measuring a linear response and a stable frequency to derive the quantity  $df_m^2/dT$ , and so, used as low laser power as possible resulting in a less intense signal for which the results of the quality factor fits are more scattered. In order to identify an possible peak in  $Q^{-1}(T)$ , we could try to perform measurements with a better signal to noise ratio, while staying in the linear regime, by tuning the detection and actuation powers.

In conclusion, we showed that we are able to probe the magnetic phase transition of NiPS<sub>3</sub> using nanomechanics despite its lower magnetic specific heat than that of FePS<sub>3</sub>. We obtained consistent estimations of NiPS<sub>3</sub> Néel temperature on two different samples with two different actuation methods. These temperatures are lower than the one of 155 K expected for bulk NiPS<sub>3</sub>, but consistent with the 150.7 K measured by Houmes *et al.* with a similar method [117].

We will now confirm that this phase transition is indeed the expected antiferromagnetic phase transition using Raman spectroscopy.

## 2.2.2 Probed by Raman spectroscopy

### Signatures of the antiferromagnetic order in bulk NiPS<sub>3</sub>

The signatures of the magnetic phase transition in NiPS<sub>3</sub> Raman spectrum will be different from the zone-folded phonons previously mentioned in the case of FePS<sub>3</sub> spectrum (see Section 2.1.2). Only one zone-folded phonon has been recently reported for NiPS<sub>3</sub> in the work of Sun *et al.* [178] at around 30 cm<sup>-1</sup>, that is not visible in our measurements because it is located below the cut-off frequency of the optical filters we used. Nevertheless, another feature linked to the in-plane spin orientation in NiPS<sub>3</sub> was identified by Kim *et al.* [32] in 2019.

To illustrate it, we compare the spectra taken on a bulk part of the NiPS<sub>3</sub> sample *Pac-Man* (see sample list 1.2.4) at room temperature in its paramagnetic phase and at 17 K in its antiferromagnetic phase (see Fig. 2.11). The peaks ( $A_g$ ,  $B_g$ ) that were degenerate at room temperature are now split in their two components  $A_g$  and  $B_g$  in the antiferromagnetic phase. A lifting of degeneracy is usually observed upon the emergence of anisotropy in the system [190], here the source of anisotropy being the magnetic order. Indeed, if we look at the two modes reproduced in Figure 2.12 from which the peak ( $A_g^2$ ,  $B_g^2$ ) originates, we see that they present a different symmetry with respect to magnetic order. The displacements of Ni atoms are along the spin direction for the  $B_g$  mode and orthogonal to it for the  $A_g$  one, resulting in two different frequencies for these modes and so a splitting of the peak in the antiferromagnetic phase. X-ray diffraction experiments performed at 20 K in [32] attested that this splitting does not arise from structural symmetry breaking. Furthermore, the splitting of the ( $A_g^2$ ,  $B_g^2$ ) mode has been now used to characterize NiPS<sub>3</sub> magnetic order in several papers [32, 37, 38, 178].

In the case of the peaks ( $A_g^1$ ,  $B_g^1$ ) and ( $A_g^5$ ,  $B_g^5$ ), since their corresponding vibrational modes do not involve large displacements of nickel atoms as for ( $A_g^2$ ,  $B_g^2$ ) (see Tables 1.6 and 1.7), the connection between their splitting and magnetic order is less clear. The splitting of ( $A_g^5$ ,  $B_g^5$ ) has even been reported as temperature independent in [32], meaning that it is not related to the magnetic phase transition. However, in our measurements, this splitting was not observed at room temperature. A detailed study as a function of temperature could clarify its origin for ( $A_g^1$ ,  $B_g^1$ ) and ( $A_g^5$ ,  $B_g^5$ ) but was not performed due to the low intensities of these peaks.

We also note, as in the FePS<sub>3</sub> low temperature spectra, an enhancement of intensities and sharpening of all the peaks at 17 K compared to room temperature.

We will now investigate the temperature dependence of the ( $A_g^2$ ,  $B_g^2$ ) splitting to estimate the Néel temperature of NiPS<sub>3</sub> in a suspended sample.

### Determination of the Néel temperature in a suspended NiPS<sub>3</sub> membrane

In order to determine the frequency difference between the  $A_g$  and  $B_g$  components of the ( $A_g^2$ ,  $B_g^2$ ) peak, we will exploit their properties regarding light polarization.

The scattered intensities of modes with  $A_g$  and  $B_g$  symmetries as a function of light polarization

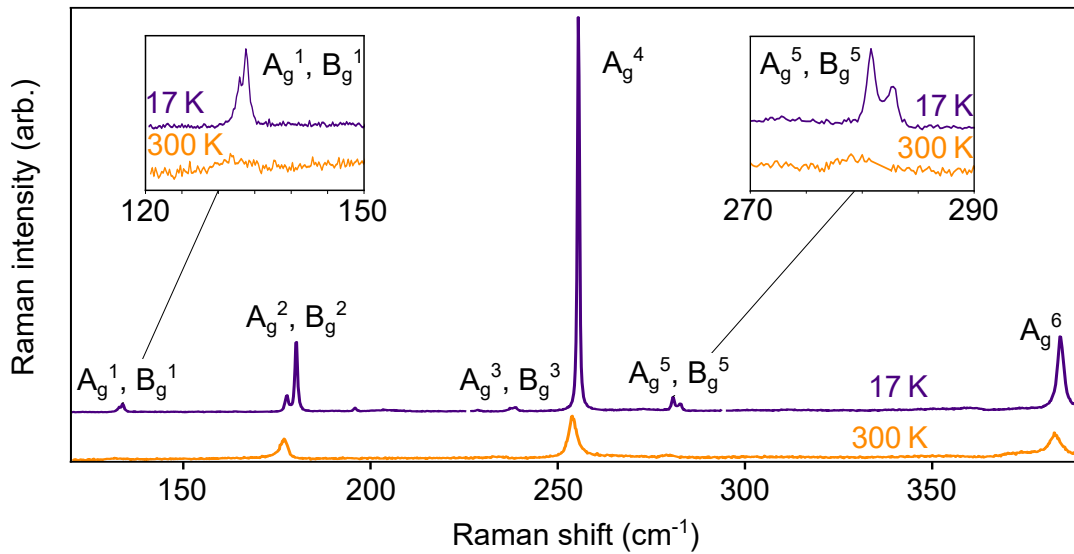


**Figure 2.11:** Raman spectra of bulk NiPS<sub>3</sub> at room temperature in its paramagnetic phase (orange) and at 17 K in its antiferromagnetic phase (purple). Zooms of peaks ( $A_g^1, B_g^1$ ) and ( $A_g^5, B_g^5$ ) are shown in inset. In the antiferromagnetic phase, the ( $A_g, B_g$ ) peaks are split.

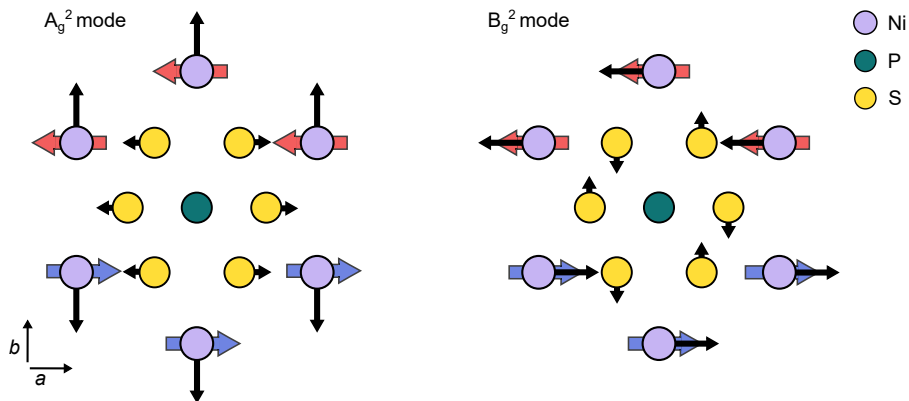


**Figure 2.12:** Schematic representation of the atomic displacements for the  $A_g$  (left) and  $B_g$  (right) components of the ( $A_g^2, B_g^2$ ) mode. The atoms of NiPS<sub>3</sub> are seen from top, the Ni atoms are drawn in mauve color, the S atoms in yellow and the P atoms in cyan. The black arrows represent the atomic motion and the red and blue arrows the spin orientations. The atomic displacements are extracted from [24].

are defined by equations (1.20) and (1.21). We use the notations defined on Figure 1.23 where  $\theta$  is the angle of incident light polarization with the crystal axis  $a$  and  $\phi$  is the angle of scattered light polarization with the same crystal axis. If the polarization of incident and scattered fields are the same ( $\phi = \theta$ ), that will be called the co-polarization configuration and noted  $\parallel$ , the scattered intensities of the A<sub>g</sub> and B<sub>g</sub> modes can be expressed as

$$I_s^{\parallel}(\text{A}_g) \propto |a + (b - a) \sin^2(\theta)|^2 \quad (2.13)$$

$$I_s^{\parallel}(\text{B}_g) \propto 4|e|^2 \sin^2(\theta) \cos^2(\theta) \quad (2.14)$$

with  $a$ ,  $b$  and  $e$  complex components of the associated Raman tensor. We note that in co-polarization configuration the intensity of the modes with A<sub>g</sub> symmetry cannot be canceled for any value of  $\theta$ , whereas the intensity of the modes with B<sub>g</sub> symmetry is zero for  $\theta = p\pi/2$  with  $p$  being an integer. Therefore, by choosing an appropriate value for  $\theta$  we can detect only the A<sub>g</sub> modes on the Raman spectrum. Conversely, if the polarization of the scattered light is orthogonal to the incident one ( $\phi = \theta + \pi/2$ ), that will be called the cross-polarization configuration and noted  $\perp$ , the scattered intensities can be expressed as

$$I_s^{\perp}(\text{A}_g) \propto |b - a|^2 \cos^2(\theta) \sin^2(\theta) \quad (2.15)$$

$$I_s^{\perp}(\text{B}_g) \propto |e|^2 (1 - 2 \sin^2(\theta))^2. \quad (2.16)$$

In this case, the intensity of the modes with A<sub>g</sub> symmetry will be zero for  $\theta = n\pi/2$ , whereas the intensity of the modes with B<sub>g</sub> symmetry will cancel for  $\theta = (2n + 1)\pi/4$ . By choosing an appropriate  $\theta$  angle, it is now possible to measure only B<sub>g</sub> modes in the Raman spectrum. For exemple with  $\theta = 0$  the resulting scattered intensities are

$$I_s^{\parallel}(\text{A}_g) \propto |a|^2 \quad I_s^{\parallel}(\text{B}_g) = 0 \quad (2.17)$$

$$I_s^{\perp}(\text{A}_g) = 0 \quad I_s^{\perp}(\text{B}_g) \propto |e|^2, \quad (2.18)$$

we are thus able to isolate the contributions of A<sub>g</sub> and B<sub>g</sub> modes to the Raman spectrum by measuring in co-polarized and cross-polarized configurations respectively, and extract their respective frequencies.

The Raman spectra acquired on the 15 layers NiPS<sub>3</sub> sample *Mordor* (see sample list 1.2.4) for temperatures between 120 and 165 K are shown on Figure 2.13 a. We see that in the co-polarized configuration (blue spectra) the peak A<sub>g</sub><sup>4</sup> is present, whereas it is absent in the cross-polarized configuration (red spectra), demonstrating that we indeed probe only B<sub>g</sub> modes in the latter configuration. On the other hand, the two lower frequency peaks are present in both cases, confirming their origin as a superposition of A<sub>g</sub> and B<sub>g</sub> modes. When the temperature is decreased

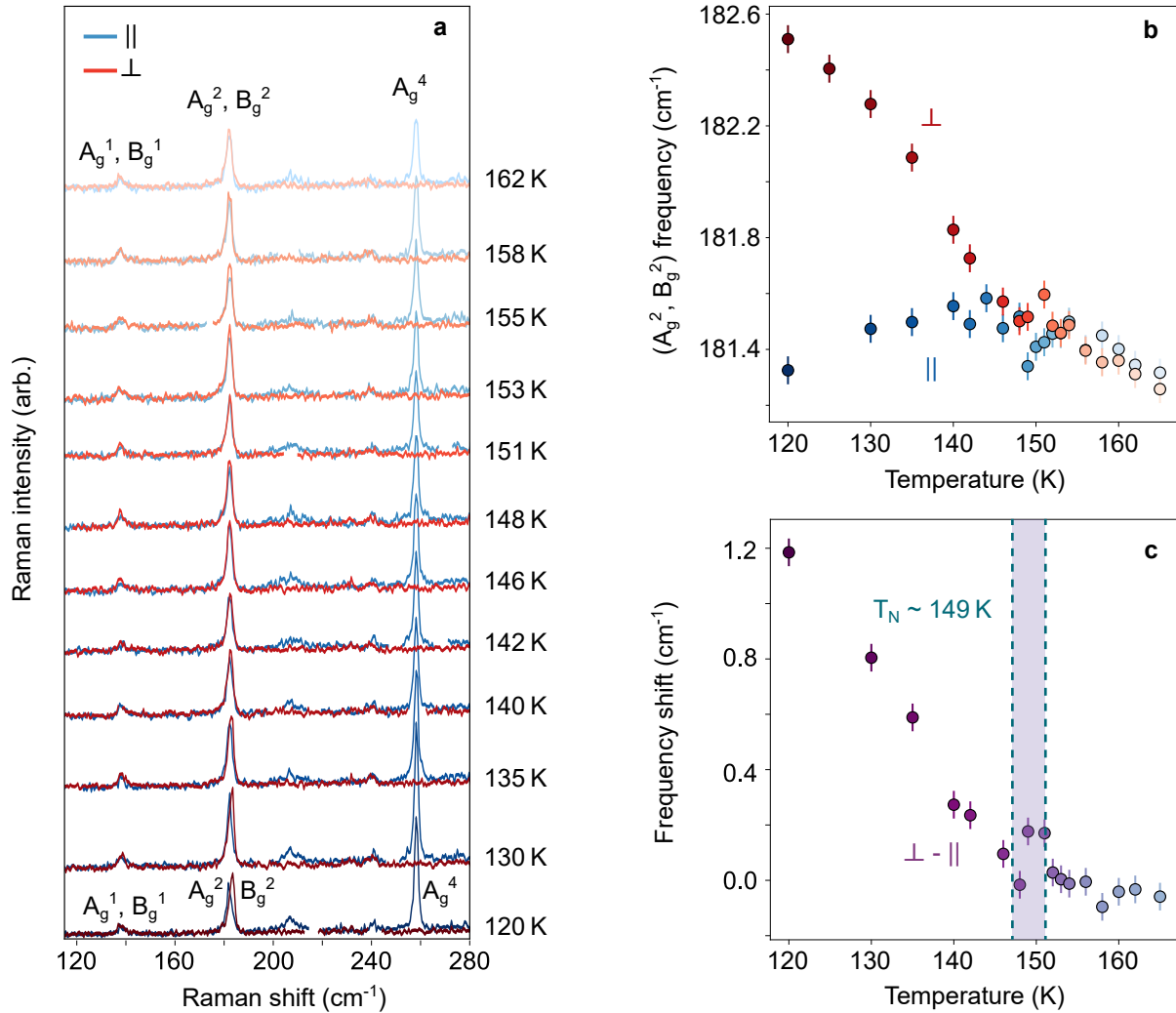


**Figure 2.13: Determination of a 10 L  $\text{NiPS}_3$  suspended homostructure Néel temperature using Raman spectroscopy.** **a.** Raman spectra of about 15 layers  $\text{NiPS}_3$  taken between 120 and 162 K in co-polarized  $\parallel$  (in blue) and cross-polarized  $\perp$  (in red) configurations. A splitting of the  $(A_g^2, B_g^2)$  peak is visible after 146 K. **b.** Evolution of the  $(A_g^2, B_g^2)$  mode frequency with temperature in co-polarization (blue dots) and cross-polarization (red dots). The error bars correspond to the error on the fit. **c.** Evolution with temperature of the frequency difference between the component of  $(A_g^2, B_g^2)$  seen in cross-polarization and the one seen in co-polarization. The increase in the frequency shift value indicates the onset of antiferromagnetic order, the Néel temperature is therefore estimated at around 149 K.

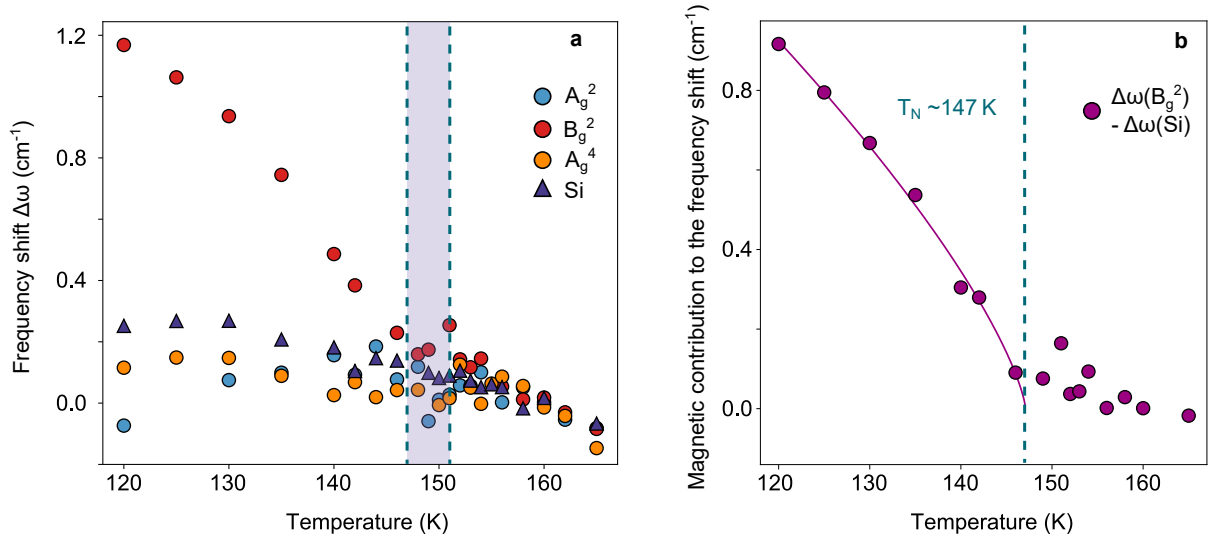


**Figure 2.14: Refining the Néel temperature estimation by considering the frequency shift of several peaks with temperature and the magnetic order contribution to this shift. a.** Evolution of frequency shift with increasing temperature for NiPS<sub>3</sub> and silicon peaks. The frequency shift is obtained by subtracting to the frequency the mean of the frequencies of the three highest points in temperature for each peak. The  $A_g^2$  component of the ( $A_g^2$ ,  $B_g^2$ ) peak (blue dots), the  $A_g^4$  peak (orange dots) and the silicon peak "Si" (purple triangles) are measured in co-polarized configuration. The  $B_g^2$  component of the ( $A_g^2$ ,  $B_g^2$ ) peak (red dots) is measured in cross-polarized configuration. The silicon peak is coming from the substrate. The mauve rectangle represents the phase transition region. **b.** Evolution of the difference between the  $B_g^2$  and Si frequency shifts. Since the Si peak frequency is independent of the magnetic order, the resulting values represent the magnetic contribution to  $B_g^2$  frequency shift. The solid line is a fit by the model for magnetic induced frequency shift of phonons developed in [31]. The corresponding Néel temperature is about 147 K.

below 148 K, the ( $A_g^2$ ,  $B_g^2$ ) peak splits progressively in its two components and at 120 K two distinct peaks are visible, one for  $A_g^2$  in co-polarization and one for  $B_g^2$  in cross-polarization. The evolution of their respective fitted frequencies with temperature is shown on Figure 2.13 b. Above 155 K the two components have the same frequency that increases with decreasing temperature, then between 155 K and 146 K (i.e. in the phase transition region) the peak frequencies seem to fluctuate, before splitting with two distinct behaviors: the  $A_g^2$  mode softens whereas the  $B_g^2$  stiffens. The increase of the frequency difference between the  $B_g^2$  and  $A_g^2$  components shown on Figure 2.13 is the sign of the emergence of the antiferromagnetic order. We can thus estimate a Néel temperature of  $149 \pm 2$  K for this NiPS<sub>3</sub> sample.

To get a deeper understanding of the ( $A_g^2$ ,  $B_g^2$ ) peak splitting, we can observe the frequency shift evolution with increasing temperature for different peaks present in the Raman spectrum of the sample (see Fig. 2.14 a). The frequency shift  $\Delta\omega$  is obtained by subtracting to the mode frequency at a temperature  $T$ , the mean of its frequency for the three highest points in temperature. Its evolution for the  $A_g^2$  and  $B_g^2$  components (blue and red dots respectively) is compared with the one of the  $A_g^4$  mode from NiPS<sub>3</sub> (orange dots) and the silicon peak "Si" (purple triangles) that is coming from the substrate. Since the silicon peak is not affected by the magnetic order in NiPS<sub>3</sub>, its evolution with temperature is only governed by the thermal expansion of the lattice

and anharmonic effects in the crystal that depend on the temperature [151]. We notice that the mode  $A_g^4$  presents an evolution very similar to the one of the silicon peak and so can be considered as independent of the magnetic order as could be expected from its out-of-plane atomic displacements that do not involve nickel atoms (see Table 1.6). On the contrary, the increase of the  $B_g^2$  frequency after the magnetic phase transition indicates an important contribution of the magnetic order to its evolution with temperature. The decrease of the  $A_g^2$  frequency, also indicates a magnetic order contribution but with an opposite effect.

The magnetic contribution to the evolution of the  $B_g^2$  frequency can be thus obtained by subtracting the non-magnetic contributions that are enclosed in the  $A_g^4$  and Si modes evolution. Here we chose to subtract the Si contribution because it is very intense and so its frequency is determined with more precision. The obtained magnetic contribution to the frequency shift of  $B_g^2$  is shown on Figure 2.14 b. It can be fitted by a model developed by Baltensperger and Helman [31] that express the phonon frequency shift induced by magnetic order as

$$\Delta\omega_{\text{mag}} \propto \langle \mathbf{S}_0 \cdot \mathbf{S}_1 \rangle \quad (2.19)$$

with  $\langle \mathbf{S}_0 \cdot \mathbf{S}_1 \rangle$  the spin correlation function. As already mentioned in Section 2.1.2 and according to [32], the spin correlation function can be approximated as  $\langle \mathbf{S}_0 \cdot \mathbf{S}_1 \rangle \sim m^2(T) \sim (T_N - T)^{2\beta}$ , with  $m$  the reduced magnetization and  $\beta$  the corresponding critical exponent. The pink solid line is the fit to our data, that gives a Néel temperature of  $147 \pm 0.5$  K, and a  $\beta$  value of 0.37 that is slightly higher than the ones obtained for bulk NiPS<sub>3</sub> by neutron diffraction or linear dichroism ranging from 0.25 to 0.3 [44, 46, 191].

## Chapter conclusion

In this chapter, we probed magnetic phase transitions in two different materials of the MPS<sub>3</sub> family, FePS<sub>3</sub> and NiPS<sub>3</sub>, using two complementary methods, Raman spectroscopy and nanomechanics. Both approaches were previously employed successfully to this end. Using nanomechanics to detect magnetic order in 2D suspended materials was first demonstrated by Šiškins *et al.* [26] and, separately, by Jiang *et al.* [27] in 2020. Raman spectroscopy has become a popular method to probe magnetic phase transitions in 2D magnetic materials, since its use in proving the persistence of a magnetic order in a FePS<sub>3</sub> monolayer [14, 32, 176, 178].

Here, we combined nanomechanical measurements and Raman spectroscopy on the same setup to investigate the magnetic order in slightly different structures than those already reported: a suspended five-layer FePS<sub>3</sub> encapsulated in a sophisticated van der Waals heterostructure (*Fantadwich*) and two suspended NiPS<sub>3</sub> flakes of 10 L (*Balor*) and 13 L (*Mordor*), respectively (see Sample list 1.2.4).

Through nanomechanics, we monitored the evolution of the nanoresonator fundamental mode of vibration in a temperature range including the expected Néel temperature of the material. The magnetic phase transition is detected thanks to the following considerations:

- the quantity  $df_m^2(T)/dT$ , with  $f_m$  the mechanical mode resonance frequency, is proportional to the membrane specific heat  $c_v(T)$ , Eq. (2.5)
- the magnetic contribution to the specific heat is detected as a peak in  $df_m^2/dT$  evolution with temperature, indicating the Néel temperature
- the evolution of the inverse of the quality factor with the temperature also features an inflection point at the Néel temperature arising from the magnetic specific heat contribution to the thermal damping, Eq. (2.9)

Through Raman spectroscopy, we investigated the evolution of the phonon modes as a function of the temperature. The detection of the magnetic order is characterized by:

- for FePS<sub>3</sub>, new phonons modes detected at the onset of magnetic order, due to the folding of  $M$  point phonons of the Brillouin zone on its  $\Gamma$  point, that is induced by the doubling of the unit cell size at the phase transition (see Section 2.1.2)
- for NiPS<sub>3</sub>, the emergence of the in-plane magnetic order induces an anisotropy for the in-plane degenerate phonons modes involving Ni atoms, that causes a lift of their degeneracy, and so, a splitting of their frequencies.
- in both cases, the evolution with temperature of the zone-folded phonon peak intensities and the frequency splitting can be modeled as proportional to the spin correlation function, itself proportional to the magnetization (see Eq. (2.12) and (2.19))

The Néel temperatures obtained by both methods are shown in Table 2.1.

	FePS <sub>3</sub>	NiPS <sub>3</sub>	
	5 L, encapsulated	13 L	10 L
Nanomechanics	109 ± 1 K	151 ± 2 K	148.5 ± 1.5 K
Raman spectroscopy	115 ± 1 K	147 ± 0.5 K	148 ± 2 K

**Table 2.1:** Summary of the Néel temperatures estimated using Raman spectroscopy and nanomechanics for the samples *Fantadwich*, *Mordor* and *Balor* (see Sample list 1.2.4).

These results are a bit lower than the expected Néel temperatures for the bulk materials that are of 120 K and 155 K for FePS<sub>3</sub> and NiPS<sub>3</sub>, respectively, which is expected for few-layer flakes (see Section 1.1.2).

We note that there are disparities between the Néel temperatures found for the same material using Raman spectroscopy and nanomechanics that cannot be explained by experimental uncertainties (see Table 2.1). However, there are close enough (maximum deviation of 6 K) to be attributed to the same phase transition, demonstrating that nanomechanics measurements are indeed probing the magnetic phase transitions of FePS<sub>3</sub> and NiPS<sub>3</sub>.

The small discrepancies between the estimated values may be accounted for by the differences in the locality of measurement methods. With nanomechanics, we are probing the membrane mechanical mode at a given position, but whose parameters depend on the entire membrane properties. The measured Néel temperature can be thus influenced by local strains or magnetic domains (see Section 4.3.1) situated elsewhere on the membrane than at the point of measurement. By contrast with Raman spectroscopy we are probing the phonons that are located under the laser spot and are thus less sensitive to the global membrane behavior.

To conclude, we demonstrated a robust methodology to probe magnetic order in suspended magnetic van der Waals materials, that could be applied to other materials than FePS<sub>3</sub> and NiPS<sub>3</sub>. This study also allowed us to establish the possibility of detecting the phase transition of a 5 L FePS<sub>3</sub> despite its encapsulation in a sophisticated heterostructure.



## Chapter 3

---

# Towards strain-tuning of mechanical and magnetic properties in suspended homo- and heterostructures

---

In this Chapter, we will investigate how we can reversibly tune the mechanical and magnetic properties of suspended 2D magnetic membranes through strain. This strain will be induced by a gate voltage applied between the membrane and the silicon bottom substrate as already discussed in Section 1.5.3. We will use the experimental probes, that are nanomechanical measurements and Raman spectroscopy, developed in the previous chapters, to track the changes of the membrane mechanical parameters and magnetic properties.

In order to estimate the effects of an increase in strain on the magnetic phase transition, we first need to understand how the strain affects the membrane nanomechanical behavior. In a first part, we will look at the evolution of the membrane mechanical modes and reflectivity with increasing gate voltage for a NiPS<sub>3</sub> homostructure. This will allow us to relate the applied gate voltage to the strain induced in the membrane. As a second step, we will probe the magnetic phase transition of two suspended NiPS<sub>3</sub> homostructures of 10 layers (*Balor*) and 13 layers (*Mordor*) for various gate voltages and so, various induced strains. Finally, the nanomechanical behavior of a FePS<sub>3</sub>-based suspended heterostructure (*Fantadwich*, see Sample list 1.2.4) will be explored at different gate voltages.

### 3.1 Strain-induced effects on a homostructure nanomechanics

We focus first on the study of a homostructure whose behavior is easier to understand and describe than that of a heterostructure. We consider here the consequences of an applied DC gate voltage on 10L and 13L NiPS<sub>3</sub> nanoresonators, *Mordor* and *Balor* (see Sample list 1.2.4). We will first derive a model for an ideal conducting membrane subjected to an electrostatic force to understand

qualitatively the behavior of the suspended homostructures, before estimating the deflection and strain values more quantitatively using the reflectance model presented in Section 1.5.2.

### 3.1.1 Tuning of the membrane's mechanical parameters

#### Static deflection and membrane's profile

We consider, as in Section 1.5.3, a membrane of radius  $R$  and thickness  $h$  suspended over a hole of depth  $d$  (see Fig. 1.30). A gate voltage  $V_g = V_{DC} + V_{AC}(t)$  is applied between the membrane and the p-doped silicon substrate, inducing an electrostatic force  $F_{el}$ , that lead to a deflection  $\xi(r, t)$  of the membrane. The equation of motion is then expressed as [170]

$$M \frac{\partial^2 \xi(r, t)}{\partial t^2} = \pi R^2 \sigma_s \nabla^2 \xi(r, t) + F_{el}(r, t) \quad (3.1)$$

with  $M$  the membrane mass and  $\sigma_s$  its surface stress.

In this Section, we will only consider the membrane static deflection  $\xi(r)$ , resulting from the static contribution to the electrostatic force, written as (see Eq. 1.60)

$$F_{el}^{stat}(r) = \frac{\epsilon_0 \pi R^2}{2(d_{eq} - \xi(r))^2} V_{DC}^2 \quad (3.2)$$

with  $\epsilon_0$  the vacuum permittivity and  $d_{eq} = d + d_b/\epsilon_{SiO_2}$  the effective distance between the membrane and the silicon, taking into account the silicon oxide relative permittivity  $\epsilon_{SiO_2}$  and its thickness  $d_b$ . In this case, the Equation 3.1 is written

$$\pi R^2 \sigma_s \nabla^2 \xi(r) = -F_{el}^{stat}(r). \quad (3.3)$$

To solve this equation we will consider  $d_{eq} \gg \xi(r)$ , and keep only the lowest order term, which gives

$$F_{el}^{stat}(r) = \frac{\epsilon_0 V_{DC}^2}{2d_{eq}^2} \left( 1 + \frac{2\xi(r)}{d_{eq}} + \dots \right) \simeq \frac{\epsilon_0 V_{DC}^2}{2d_{eq}^2}. \quad (3.4)$$

Using the expression of the Laplacian operator in cylindrical coordinates with the boundary conditions  $\xi(R) = 0$  (clamped membrane at the edges) and  $\partial\xi/\partial r(r=0) = 0$  (flat profile at the center), we obtain the expression for the membrane deflection

$$\xi(r) = \xi_0 \left( 1 - \frac{r^2}{R^2} \right). \quad (3.5)$$

For small deflections, the membrane profile resulting from the applied electrostatic force is parabolic with a maximum deflection at the center  $\xi_0$  given by

$$\xi_0 = \frac{\epsilon_0 R^2}{8d_{eq}^2 \sigma_s} V_{DC}^2. \quad (3.6)$$

The membrane deflection is proportional to the square of the imposed DC voltage as is the electrostatic force. It also depends on the stress, that is usually approximated as the pre-stress at zero volt  $\sigma_0$ , which, as we will see later, can be considered as larger than the stress induced by the electrostatic force. This pre-stress can be estimated by modeling the resonance frequency evolution as a function of the gate voltage as we will see in the following. If the deflection becomes so large that the condition  $d_{\text{eq}} \gg \xi(r)$  is no longer met, higher order terms from the series expansion of the capacitance should be considered [192, 193].

### Resonance frequency and quality factor

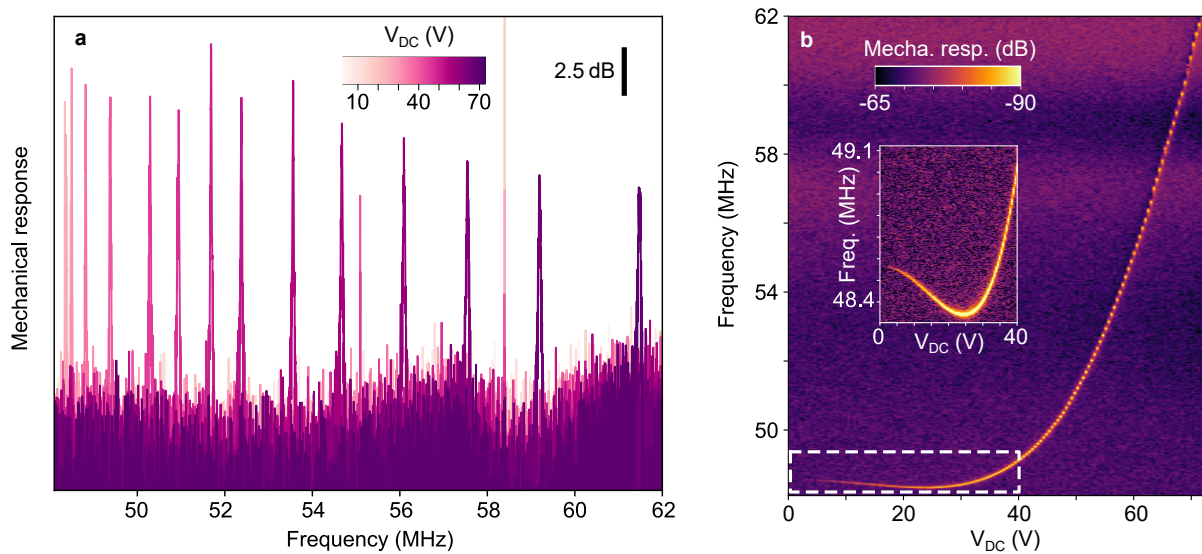


**Figure 3.1: Effects of increasing gate voltage  $V_{\text{DC}}$  on the membrane mechanical mode of a 10 L suspended NiPS<sub>3</sub> (Balor) at 5 K.** **a.** Mechanical response spectra to an electrostatic drive for DC voltages between 0 and 75 V acquired at 5.5 K. A spectrum is plotted every 10 V until 50 V and then each 5 V. **b.** Colorplot representing the mechanical response spectra of **a.** The inset shows a zoom of the low-voltage range indicated by the dashed box.

We can study experimentally the evolution of the mechanical mode resonance frequency and quality factor by acquiring mechanical response spectra to an electrostatic actuation as a function of DC voltage (see Fig. 3.1). We observe that the measured displacement amplitude is first increasing with DC voltage, which is due to the increase of the electrostatic driving force that is proportional to  $V_{\text{DC}}V_{\text{AC}}$  (see Eq. 1.60). The resonance frequency is tuned by 14 MHz, first by decreasing gently by 0.3 MHz up to 24.7 V, after what, it increases abruptly in a parabolic fashion. This behavior can be explained by the competition between elastic and electrostatic energies. The elastic energy  $U_{\text{el}}$  of a membrane undergoing a deflection  $\xi(r)$  is expressed as [192]

$$U_{\text{el}} = \frac{\pi E_{2\text{D}}}{1 - \nu^2} \int_0^R \left[ \varepsilon_0(T) + \frac{1}{2} \left( \frac{d\xi(r)}{dr} \right)^2 \right]^2 r dr \quad (3.7)$$

with the first term in square bracket,  $\varepsilon_0(T)$ , corresponding to the pre-strain at the temperature  $T$

for a zero gate voltage, and the second term to the strain induced by the elongation. By injecting the expression obtained for  $\xi(r)$  in Equation (3.5) and performing the integration we get

$$U_{\text{el}} = \frac{\pi E_{2\text{D}}}{1 - \nu^2} \left( \varepsilon_0 \frac{R^2}{2} + \varepsilon_0 \xi_0^2 + \frac{2\xi_0^4}{3R^2} \right). \quad (3.8)$$

On the other hand, the electrostatic energy  $U_{\text{es}}$  (see Eq. (1.58)) is written as [169]

$$U_{\text{es}} = -\frac{1}{2} C_{\text{eq}} \pi R^2 V_{\text{DC}}^2 \quad (3.9)$$

$$\simeq -\frac{1}{2} \left( C_0 + C' \xi_0 + C'' \frac{\xi_0^2}{2} \right) \pi R^2 V_{\text{DC}}^2 \quad (3.10)$$

where we performed a series expansion of the capacity  $C_{\text{eq}}$  (see Eq. (1.57)) in terms of the membrane deflection at the center  $\xi_0$ .  $C'$  and  $C''$  are thus corresponding to the first and second derivative of the capacity with respect to the deflection,  $dC_{\text{eq}}/d\xi|_{\xi=\xi_0}$  and  $d^2C_{\text{eq}}/d\xi^2|_{\xi=\xi_0}$ , respectively.

The spring constant of the membrane  $k_{\text{m}}$  can then be evaluated from

$$k_{\text{m}} = \frac{\partial^2}{\partial \xi_0^2} (U_{\text{el}} + U_{\text{es}}) \quad (3.11)$$

that allows us to derive the expression of the resonance frequency  $f_{\text{m}}$  as function of the gate voltage [29, 192]

$$f_{\text{m}}(V_{\text{DC}}) = \frac{1}{2\pi} \sqrt{\frac{1}{M_{\text{eff}}} \left( \frac{2\pi\varepsilon_0 E_{2\text{D}}}{1 - \nu^2} + \frac{\varepsilon_0 \pi R^2}{8d_{\text{eq}}^4 \varepsilon_0^2} V_{\text{DC}}^4 - \frac{1}{2} \frac{\varepsilon_0 \pi R^2}{d_{\text{eq}}^3} V_{\text{DC}}^2 \right)} \quad (3.12)$$

where  $M_{\text{eff}}$  is the effective mass of the considered mode. The first term does not depend on the gate voltage and corresponds to the resonance frequency of the membrane at zero gate voltage as it could be derived from Equation (1.33). The second term arises from the additional strain created in the membrane by the electrostatic force, that is increasing as the membrane gets closer to the gate electrode. It results in an evolution of the resonance frequency proportional to  $V_{\text{DC}}^2$  and causes the stiffening observed after 24.7 V (see Fig. 3.1 b). Finally, the third term is at the origin of the softening observed at low voltages and originates from the capacitive electrostatic energy. In the case of large pre-strain, the stiffening term gets weaker and the softening term dominates until high voltages. On the contrary, for low pre-strain there may be no softening at all [33].

This pre-strain can be estimated by fitting our data to the model of Equation (3.12). It is challenging to evaluate the two fitting parameters that are the pre-strain  $\varepsilon_0$  and the effective mass  $M_{\text{eff}}$ , since  $\varepsilon_0$  is appearing in both the resonance frequency at 0 V and the term corresponding to the evolution with strain. We are thus not fitting directly the resonance frequency evolution with DC voltage, but the shift of the squared resonance frequency induced by the gate voltage, which will remove

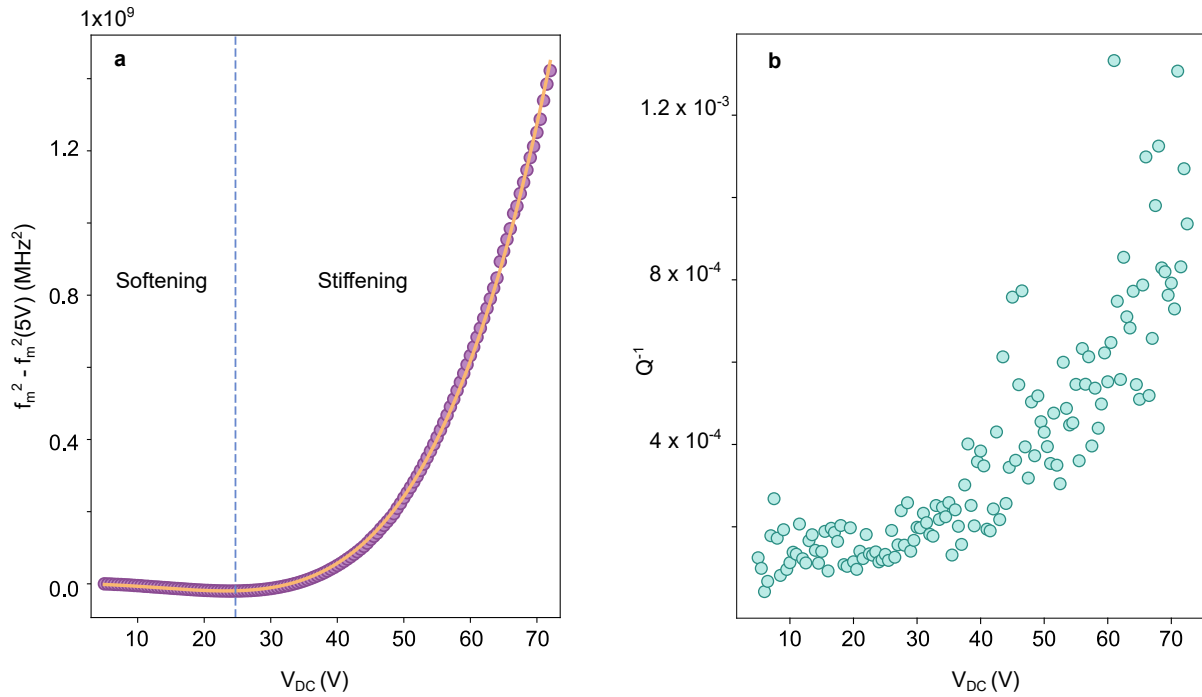


**Figure 3.2: Evolution of the mechanical mode parameters in response to an applied gate voltage  $V_{DC}$  for a 10 L suspended NiPS<sub>3</sub> (Balor) at 5 K.** **a.** Shift of the resonance frequency squared compared to its value at 5 V for an increase in gate voltage. The dots are the data obtained from the fits of the spectra of Figure 3.1, while the solid line is a fit using the model of Equation (3.12). The dashed line at 24.7 V demarcates the softening and the stiffening regimes. **b.** Inverse of the quality factor  $Q^{-1}$  as a function of gate voltage.

the term corresponding to the resonance frequency at 0 V. This provides a better agreement with the data, while keeping  $\varepsilon_0$  and  $M_{\text{eff}}$  as fitting parameters. We use the known parameters of the membrane from its geometry ( $R = 2.5 \mu\text{m}$ ,  $d = 400 \text{ nm}$ ,  $d_b = 100 \text{ nm}$ ) and the values of Young's modulus and Poisson ratio from Table 1.2. The shift in the resonance frequency squared as a function of the DC voltage, with the value at 5 V as a reference, is plotted in Figure 3.2 a alongside with the corresponding fit derived from the model of Equation (3.12).

We note a good agreement between the fit and the data, even in the softening region. We obtained an effective mass  $M_{\text{eff}} = 0.21 \text{ pg}$  that is two times higher than the expected one. The reason could be that the effective mass of the membrane fundamental mode deviates from the ideal one, which could be quantified by mapping and integrating the mode spatial profile (see Eq. (1.36)). The mass of the resonator might also be slightly underestimated because of polymer residues inherited from the transfer process. The resulting pre-stress at 5 K is  $\sigma_0 = \varepsilon_0 E_{2D} / (1 - \nu^2) = 1.02 \text{ N/m}$ , which is higher than the pre-stress of 0.2 N/m estimated at room temperature due to thermally-induced strain.

On the other hand, we observe a drop in the quality factor after 40 V, down to 80 % at 70 V compared to its intrinsic value. This was already reported in nanodrums made of graphene or TMD monolayers and is attributed to electronic Joule dissipation due to the capacitive displacement current generated by the membrane motion [33, 179, 194].

### 3.1.2 Estimation of gate voltage-induced deflection and strain

#### From capacitive model and estimated pre-stress

The membrane deflection can be estimated following the capacitive model derived previously (3.6) (see Fig. 3.3). We note that the predicted deflection at 70 V is about 185 nm, implying that the ratio  $\xi_0/d_{\text{eq}}$  is equal to 0.44, and so, that the approximation  $\xi_0/d_{\text{eq}} \ll 1$  starts to fail. Therefore, extra terms should be introduced to properly describe the membrane behavior around these voltages.

The strain induced by the increase of gate voltage can be estimated from the membrane static deflection as [19, 26]

$$\Delta\varepsilon = \frac{2}{3} \left( \frac{\xi_0}{R} \right)^2. \quad (3.13)$$

The static deflection evolving as the squared DC voltage, the strain will increase as the fourth power of the DC voltage (see Fig. 3.3).

As mentioned in the introduction of this Section, due to the strong hypotheses on the system geometry (parallel plate capacitor) and on its perfect conductivity, while NiPS<sub>3</sub> is considered as a large-gap semiconductor [120], the quantitative results out of this model have to be treated with caution. In the following, we will then estimate the membrane deflection from the reflectance model presented in Section 1.5.2.

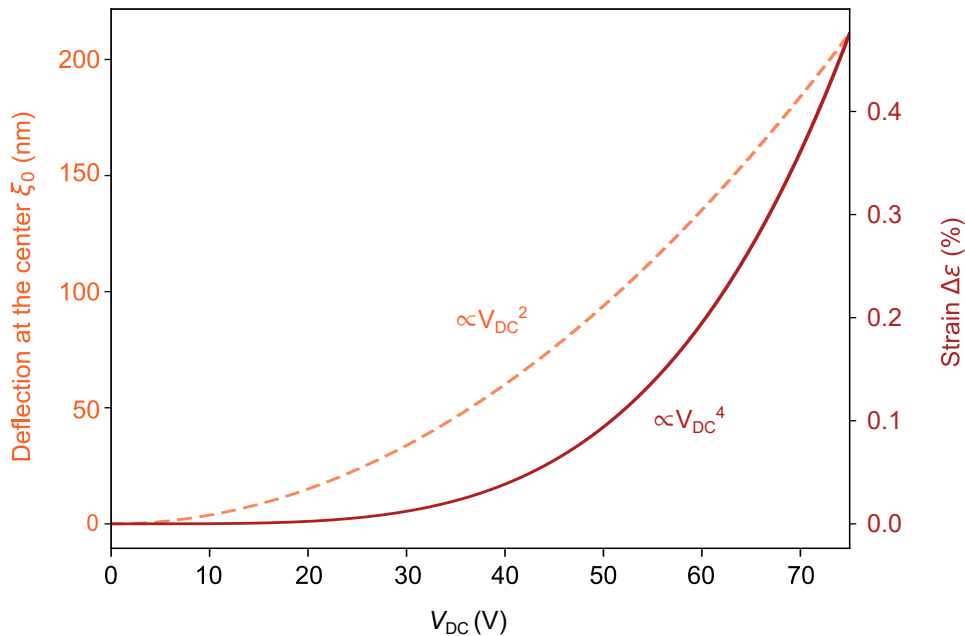


**Figure 3.3: Estimation, using a capacitive model, of the deflection at the membrane center and strain as a function of the gate voltage  $V_{\text{DC}}$  for a 10 L suspended NiPS<sub>3</sub> (*Balor*) at 5 K.** The deflection at the membrane center  $\xi_0$  is plotted by a orange dashed line with its values on the left axis, while the gate voltage-induced strain  $\Delta\varepsilon$  is plotted by a solid red line with its values on the right axis. They are calculated from the model of Equations (3.6) and (3.13), respectively, with  $R = 2.5 \mu\text{m}$ ,  $d_{\text{eq}} = 426 \text{ nm}$  and  $\sigma_0 = 1.02 \text{ N/m}$ . The evolution of the membrane deflection is proportional to the squared gate voltage, whereas the induced strain in the membrane evolves as the fourth power of gate voltage.

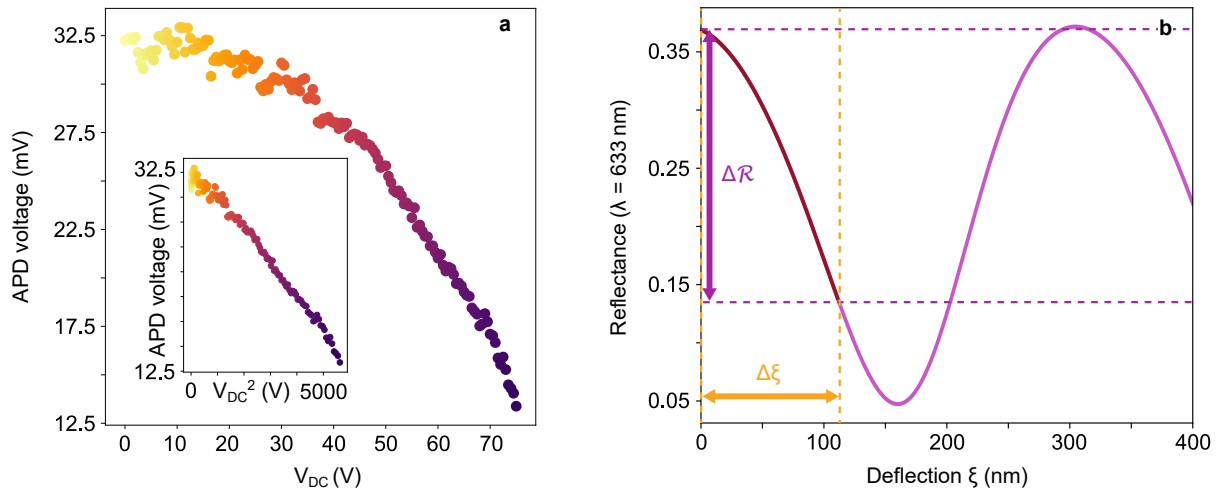


**Figure 3.4: Estimation of the membrane static deflection from the variation of the avalanche photodiode (APD) output voltage for a 10 L suspended NiPS<sub>3</sub> (Balor) at 5 K.** **a.** APD average voltage as a function of the applied gate voltage recorded simultaneously with the spectra of Figure 3.1. In the inset, the same quantity is plotted as a function of the applied gate voltage squared. The APD average voltage output is proportional to the sample reflectance (see Eq. (1.52)). **b.** Calculated reflectance as a function of the membrane deflection (see Section 1.5.2) for a 10 L NiPS<sub>3</sub> nanodrum.  $\Delta\mathcal{R}$  is the reflectance variation for a gate voltage sweep from 0 to 75 V as estimated from the APD output voltage evolution.  $\Delta\xi$  represents the corresponding deflection variation. The red part of the curve is the one traveled by the membrane during the gate voltage sweep.

### From the measured nanodrum reflectance

Another way to estimate the membrane static deflection  $\xi_0$  is to record the output voltage of the avalanche photodiode (APD) at the membrane center.

As we saw in Section 1.5.2, the membrane deflection can be related to the APD voltage through the sample reflectance  $\mathcal{R}$ . Here, we are acquiring the continuous component of the APD voltage (see Eq. (1.52)). The relative APD voltage variation  $\Delta V_{\text{APD}}/V_{\text{APD}}(0\text{ V})$  is then equal to the relative reflectance variation  $\Delta\mathcal{R}/\mathcal{R}_i$ , with  $\mathcal{R}_i$  the initial reflectance at 0 V. The APD voltage variation is shown in Figure 3.4 a for the same voltage sweep as the data displayed in Figure 3.1. A relative APD voltage variation, and so, a relative reflectance variation, of 62% is achieved.

We can derive the evolution of the sample reflectance with the membrane static deflection for a 10 L NiPS<sub>3</sub> nanodrum by calculating its equivalent reflection coefficient (see Fig 3.4 b), taking into account the multiple reflections in the cavity as a function of the vacuum layer thickness between the substrate and the membrane (see Sec. 1.5.2). We assume, in accordance with Equation (3.6), that the deflection is evolving as  $V_{\text{DC}}^2$ , and so, plot the APD voltage as a function of this quantity, as shown in the inset of Figure 3.4 a. We first note that the APD output voltage decreases almost linearly over the entire gate voltage range, which is in good agreement with the reflectance modeling between 0 and 140 nm. We can calculate the reflectance variation during the voltage sweep  $\Delta\mathcal{R} = 0.62 \mathcal{R}_i \simeq 0.23$ , which corresponds to a gate voltage induced deflection of  $\Delta\xi \simeq 111\text{ nm}$  at 75 V.

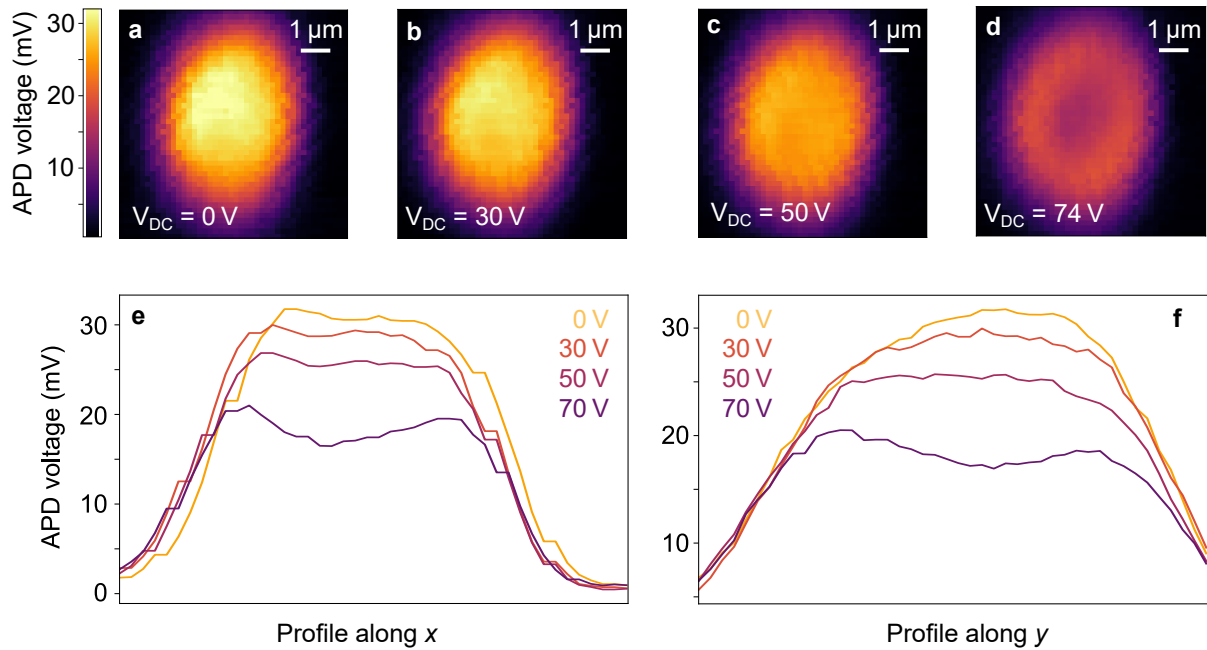


**Figure 3.5: Influence of the gate voltage on the membrane deflection profile seen by laser reflectance.** **a-d.** Spatial maps of the average voltage recorded by the avalanche photodiode (APD) for gate voltages of 0, 30, 50 and 74 V, respectively. The region with the highest APD voltages indicates the membrane area. **e,f.** Evolution of the APD output voltage along  $x$  and  $y$  axis, respectively, retrieved from the middle of the maps for voltages equal to 0, 30, 50 and 70 V.

We perform spatially-resolved maps of the APD output voltage, proportional to the reflectance, to gain information on the membrane spatial profile. Maps acquired for 0, 30, 50 and 74 V, and cuts taken from the middle of these maps along  $x$  and  $y$  axis, are displayed on Figure 3.5.

As shown previously, the changes in the APD output voltage are due to the membrane deformation induced by the applied gate voltage. We see that at zero gate voltage, the membrane has a high reflectance, which is domed-shaped, especially in top left of center. Usually the membranes of this thickness are not flat and present wrinkles induced by the fabrication process, that are visible on the optical pictures (see Sample list 1.2.4). For 30 and 50 V, we note that the reflectance decreases and the membrane becomes flatter. It is only from 60 V that the membrane adopts a parabolic profile, expected from the gate voltage influence, as the one visible on the 74 V map.

## Discussion

The deflection at the membrane center of 185 nm for a 75 V gate voltage predicted by the model combining continuum mechanics and electrostatics is clearly overvalued compared to the deflection of 111 nm for the same voltage estimated from the reflectance variation, confirming the qualitative character of the capacitive model. This is in line with the fact that this model considers a perfect conductor, which is a good approximation for graphene, but not for NiPS<sub>3</sub>, resulting in real values for strain and deflection smaller than those predicted.

A solution to obtain a greater deflection, would be to use a flake of graphene to make the contact

with the electrode, forming a heterostructure, as realized for the FePS<sub>3</sub>-based heterostructure *Fantadwich* (see Sample list 1.2.4). This flake of graphene could also be exploited as a strain sensor thanks to Raman spectroscopy as in a previous work of the team [19], allowing a better estimation of the deflection and strain.

Even if the values derived through the capacitive model are overvalued, it still provides qualitative insights of the membrane parameters evolution and a relevant modeling of the resonance frequency evolution with gate voltage.

In the case of the estimation performed considering the reflectance evolution, the major source of uncertainties is the determination of the reflectance at zero gate voltage  $\mathcal{R}_i$ . The uncertainty on  $\mathcal{R}_i$  has been estimated to be of around 0.02, which results in a uncertainty on the deflection of about 15 nm. According to the reflectance method, the induced static deflection for a gate voltage of 75 V on the 10 L NiPS<sub>3</sub> sample *Balor* at 5 K is of around  $\xi_0 = 111 \pm 15$  nm resulting in a strain of  $\varepsilon = 0.13 \pm 0.02$  % (see Fig. 3.3). This translates in a electrostatically-induced stress  $\sigma_e = 0.16 \pm 0.02$  N/m which is lower than the pre-stress  $\sigma_0 = 1.02$  N/m estimated by the capacitive model (see Subsection 3.1.1).

## 3.2 Influence of strain on NiPS<sub>3</sub> magnetic phase transition

Now that we have determined the influence of a gate voltage increase on the membrane mechanical response, we can investigate its potential for the strain-tuning of the membrane magnetic properties. As a first step, we will review the theoretical background supporting a modification of the Néel temperature resulting from magnetostriction effects. The experimental results on NiPS<sub>3</sub> phase transition probed for different gate voltages will be then discussed.

### 3.2.1 Seen by Landau theory of phase transitions

In this Subsection, we will model FePS<sub>3</sub> and NiPS<sub>3</sub> as uniaxial antiferromagnetic crystals with two sub-lattices whose magnetic moments are anti-parallel. The sub-lattices magnetizations are written as  $M_1$  and  $M_2$ , and their sum  $M$  is zero in the absence of an external magnetic field  $H$ . The vector order parameter for an antiferromagnet is defined as the difference between the magnetization of the two sub-lattices  $L = M_1 - M_2$ , and is therefore equal to zero in the paramagnetic phase.

#### Free energy of an antiferromagnet

Near the Néel temperature  $T_N$ ,  $L$  is small, and thus, according to Landau theory of phase transitions [195], the free energy can be expanded as powers of  $L$  and  $H$  in this temperature range. In the case of a zero external magnetic field ( $H = 0$ ) the antiferromagnet free energy  $F$  is written as [34]

$$F = F_0 + AL^2 + BL^4 + \frac{1}{2}\beta_A(L_x^2 + L_y^2). \quad (3.14)$$

The two first terms after  $F_0$  originate from exchange energy with  $A(T) = a(T - T_N)$ , where  $a$  and  $B(T = T_N)$  are positive constants. The last term derives from anisotropy energy and is expressed considering the crystal principal axis of symmetry along the  $z$ -axis. In the case of an out-of-plane easy-axis antiferromagnet like FePS<sub>3</sub>,  $\beta_A > 0$  and the antiferromagnetic vector  $L$  is along the  $z$ -axis. Whereas, in the case of an easy-plane antiferromagnet like NiPS<sub>3</sub>,  $\beta_A < 0$  and  $L$  lies in the basal plane.

#### Magnetostriction terms

The phenomenon of magnetostriction describes the deformation of a ferro- or antiferromagnetic material caused by a change in its magnetization and, inversely, the magnetization variation induced by an applied strain. The magnetostriction contributes as three extra terms in the total free energy of the system, that are written, by considering  $x$  and  $y$  axis as the principal stress axes, [26]

$$F_{ms} = \zeta_x L_x^2 + \zeta_y L_y^2 + \zeta L_z^2 \quad (3.15)$$

where the terms  $\zeta_{x,y}$  and  $\zeta$  are products of the stress tensor by the fourth rank magnetostriction tensor  $\lambda_{ijkl}$  [34, 117].

### Case of an easy-axis antiferromagnet

In the case of an easy-axis antiferromagnet like FePS<sub>3</sub>, the vector order parameter  $\mathbf{L}$  is oriented along the  $z$ -axis implying  $L_x = L_y = 0$  and  $\beta_A > 0$ . The total free energy is then given by

$$F_{ea} = F_0 + [a(T - T_N) + \zeta]L_z^2 + BL_z^4. \quad (3.16)$$

We can determine  $L_z$  by minimizing the derivative of the free energy  $F_{ea}$ , which gives

$$L_z(T) = \sqrt{\frac{a(T_N - T) - \zeta}{2B}}. \quad (3.17)$$

The Néel temperature is defined as the temperature at which the order parameter  $L_z$  vanishes, so the Néel temperature  $T_N^*$  of a strained easy-axis antiferromagnet is written as

$$T_N^* = T_N - \frac{\zeta}{a}. \quad (3.18)$$

The Néel temperature is thus shifted towards lower or higher values depending on the sign of  $\zeta$  by the applied strain.

### Case of an easy-plane antiferromagnet

In the case of an easy-plane antiferromagnet like NiPS<sub>3</sub>, the vector order parameter  $\mathbf{L}$  is oriented within the plane (neglecting the small out-of-plane component), implying  $L_z = 0$  and  $\beta_A < 0$ . The total free energy is then given by

$$F_{ep} = F_0 + [a(T - T_N) + \frac{1}{2}\beta_A]L^2 + BL^4 + \zeta_x L_x^2 + \zeta_y L_y^2 \quad (3.19)$$

with  $L^2 = L_x^2 + L_y^2$ . We can determine  $L_x$  and  $L_y$  by minimizing  $\partial F_{ep}/\partial L_x$  and  $\partial F_{ep}/\partial L_y$ , respectively, giving

$$L_{x,y} = \sqrt{\frac{2a(T_N - T) - 2\zeta_{x,y} - \beta_A}{4B}}. \quad (3.20)$$

The Néel temperature is defined as the temperature where  $L = 0$ , which is equivalent to  $L_x^2 + L_y^2 = 0$ , giving the Néel temperature  $T_N^*$  of a strained easy-plane antiferromagnet

$$T_N^* = T_N - \frac{(\beta_A + \zeta_x + \zeta_y)}{2a}. \quad (3.21)$$

It depends on the anisotropy coefficient  $\beta_A$  which, since it is negative, results in an increase of the Néel temperature compared to the one of an out-of-plane easy-axis antiferromagnet at zero

strain. The influence of strain is similar to the easy-axis case, except that the variation of Néel temperature will depend on both the magnetostriction coefficients along  $x$  and  $y$  axis. Indeed, since the spins are oriented in the layer plane, they will not have the same sensitivity to the strain along  $x$  or  $y$  directions, which is encoded in the magnetostriction tensor.

In the following, we will investigate this strain-induced Néel temperature modification by probing the magnetic phase transition for different gate voltages using the methods detailed in Chapter 2.

### 3.2.2 Probed by nanomechanical measurements

As in Section 2.2.1, we probe the magnetic phase transition of a suspended NiPS<sub>3</sub> membrane by monitoring the evolution with temperature of its fundamental mode resonance frequency  $f_m$ , giving us access to its specific heat  $C_v(T)$  (see Eq. (2.5)). To study the evolution of NiPS<sub>3</sub> Néel temperature with strain, we will now apply gate voltages from 18 to 50 V.

#### Experimental results

The results obtained for a 13 L NiPS<sub>3</sub> homostructure (*Mordor*, see Sample list 1.2.4) are shown on Figure 3.6. The data acquired at the lowest gate voltage of 18 V are those already discussed in Section 2.2.1.

With the increase of the gate voltage, we note that the resonance frequency rises faster for higher temperatures than lower ones, leading to a non-linear slope for the resonance frequency as a function of the temperature in the paramagnetic region. A similar phenomenon was also observed for FePS<sub>3</sub> in [26]. As a consequence, the slope break in the resonance frequency evolution with temperature, indicating the phase transition region, vanishes progressively with increasing DC gate voltage. We thus rely on the peak in  $df_m^2(T)/dT$ , arising from the magnetic contribution to the specific heat, to determine the Néel temperature of the sample.

With increasing gate voltage, the peak in  $df_m^2(T)/dT$  seems to become broader and less intense, finally appearing as a shoulder emerging from the background. We can, nevertheless, see that it shifts to lower temperatures for higher DC gate voltages, reflecting a decrease of about 3 K in NiPS<sub>3</sub> Néel temperature between 18 and 40 V.

We were not able to measure the Néel temperature shift at 50 V due to a mechanical instability of the vibrational mode occurring from 45 V. This translates as a random drift of the resonance frequency over time, that is visible on the plot as a function of temperature for 50 V (see Fig. 3.6 a). This instability in frequency induces an important noise in  $df_m^2(T)/dT$ , making it impossible to determine the Néel temperature at 50 V and above. This mechanical instability is also observed for the same voltage range, on the other studied 10 L NiPS<sub>3</sub> homostructure (*Balor*).

#### Discussion on the background origin in $df_m^2/dT$

The evolution of  $df_m^2/dT$  between 151 and 185 K, i.e. in the paramagnetic phase, has a linear dependence with the temperature. A possible origin of the appearance of a slope with increasing

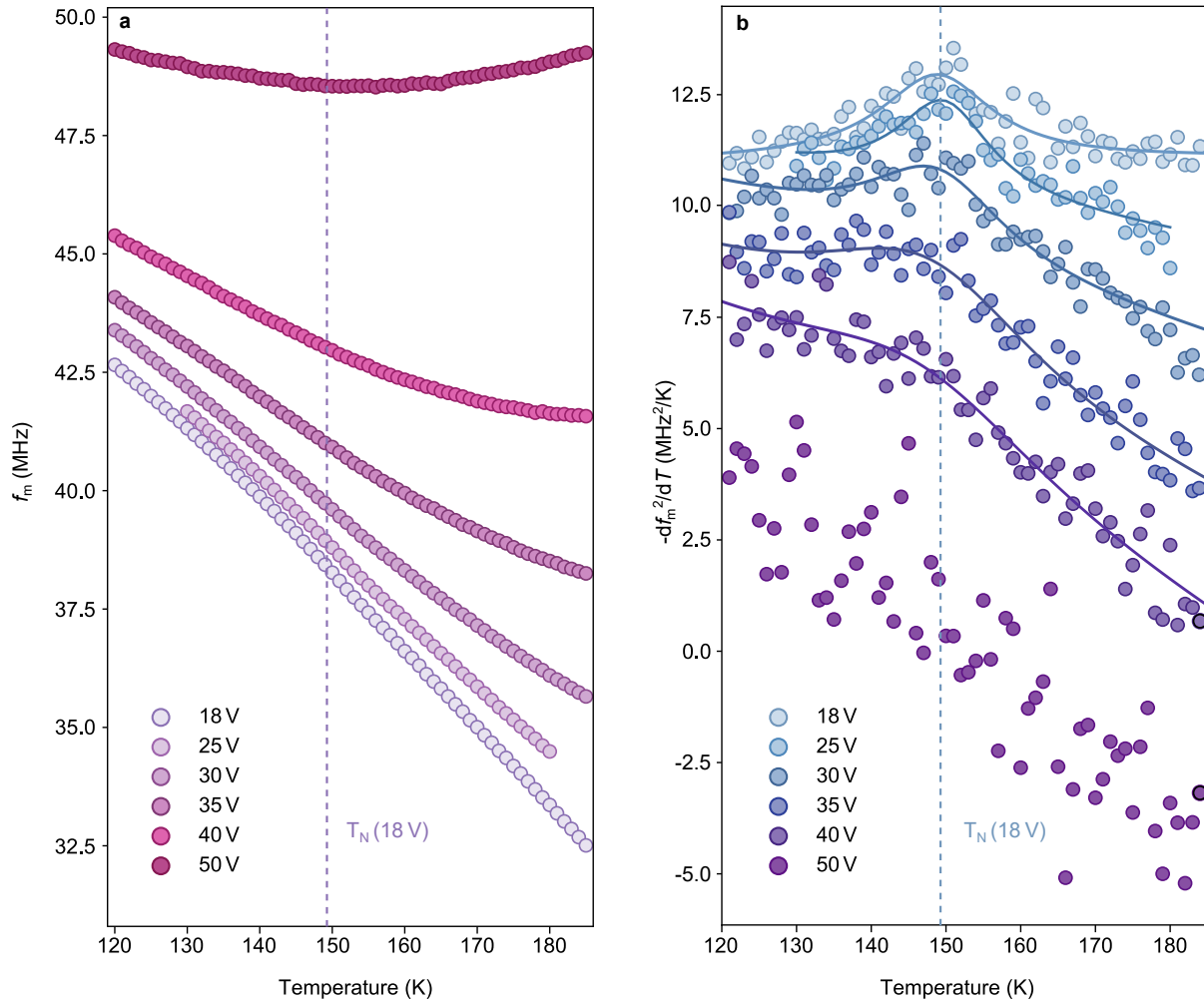


**Figure 3.6: Decrease of the Néel temperature probed on a 13 L NiPS<sub>3</sub> homostructure (*Mordor*) for gate voltages from 18 V to 50 V by nanomechanical measurements. a.** Membrane resonance frequency  $f_m$  as a function of temperature for various gate voltages. **b.** Evolution with temperature of the resonance frequency squared derivative with respect to the temperature  $df_m^2/dT$  for various gate voltages. The solid lines are fits to the data by a Lorentzian plus a background that are used as guides for the eyes. The dashed lines indicates the Néel temperature at 18 V.

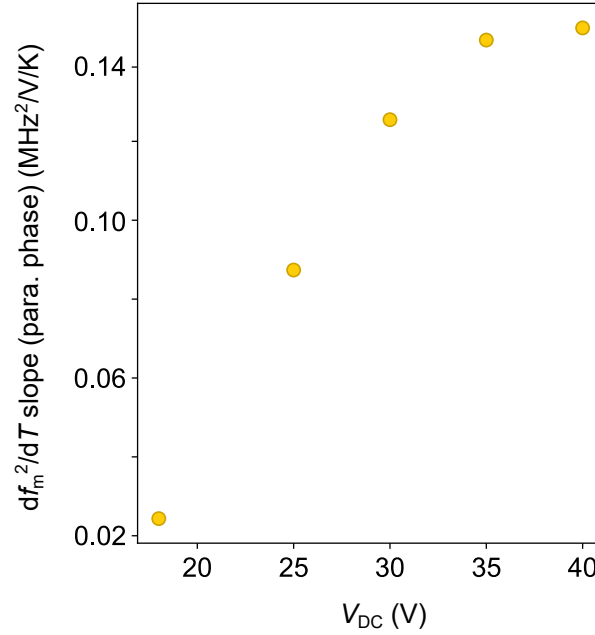


**Figure 3.7: Evolution of  $df_m^2(T)/dT$  background slope in the paramagnetic temperature region with increasing DC gate voltage.** The slope is extracted from the fit by a line of the linear region in  $df_m^2(T)/dT$  between 151 and 185 K. A fit by a square root function does not match the data.

gate voltage is a contribution to  $df_m^2/dT$  from the electronic specific heat  $C_{el}$  whose expression is [134]

$$C_{el}(T) = \frac{\pi^2}{3} k_B^2 g(E_F) T \quad (3.22)$$

with  $g(E_F)$  the electronic density of states depending on the energy of the Fermi level  $E_F$ . The slope of the line would be then proportional to the electronic density of state whose dependence on gate voltage is not trivial (see Fig. 3.7).

### Estimation of the induced strain

We would like to estimate the strain induced in the membrane by the applied gate voltage, leading to this 3 K Néel temperature shift. However, the photodiode signal as a function of the gate voltage was not acquired on this sample, so we cannot use the reflectance calculations directly to estimate the deflection. We will then need to go through the capacitive model and compare the obtained deflection with that previously calculated on the other NiPS<sub>3</sub> sample in Section 3.1.2. We can then extrapolate a deflection value from the reflectance curve of this previously studied sample.

As in Section 3.1, we first acquire the mechanical response to an electrostatic drive as a function of the gate voltage, here for a temperature of 153 K which is in the middle of the temperature range studied for the Néel temperature determination (see Figure 3.8 a).

From the fit of the squared resonance frequency shift with the model of Equation (3.12) we obtain a pre-stress  $\sigma_0 = 0.48$  N/m (see Fig. 3.8 b). This is twice as low as that previously evaluated on the other NiPS<sub>3</sub> homostructure at 5 K. This disparity in the pre-stresses can be explained

by the different temperatures at which the measurements were performed: at 5 K the thermal pre-stress arising from the membrane contraction is more important than at 153 K. A variation in the fabrication-induced stress can also account partially for this difference in pre-stresses. From the fitted pre-stress, we can estimate the evolution with DC voltage of the membrane deflection at the center  $\xi_0$  and strain  $\Delta\varepsilon$  using Equations (3.6) and (3.13), as shown in the inset of Figure 3.8 b. We obtain a maximum deflection of around 200 nm at 50 V corresponding to a strain of 0.42 %.

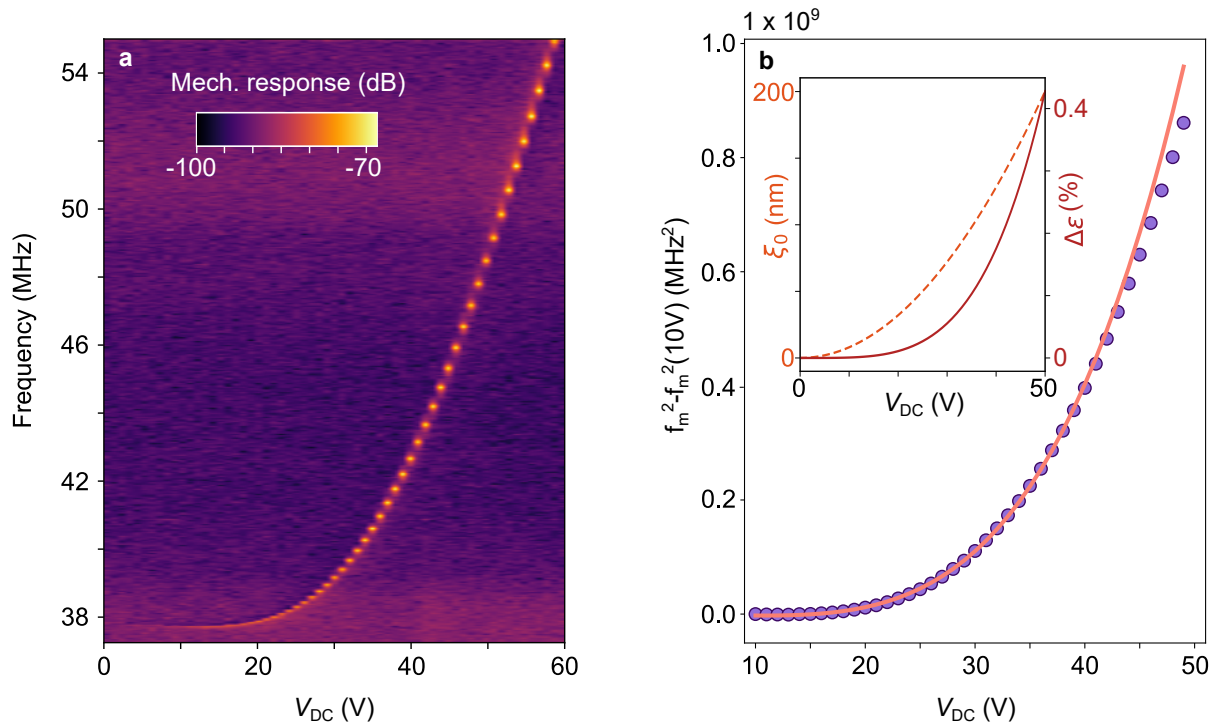


**Figure 3.8: Mechanical response as a function of the gate voltage of a 13 L NiPS<sub>3</sub> homostructure (Mordor) at 153 K.** **a.** Spectra acquired between 0 and 60 V, showing the evolution of the mechanical mode resonance frequency with increasing DC gate voltage. **b.** Shift of  $f_m^2$  compared to its value at 10 V with increasing DC gate voltage. The dots are the data obtained from the fit of the spectra of **a**, while the solid line is a fit using Equation (3.12). The resulting pre-stress and effective mass are  $\sigma_0 = 0.48$  N/m and  $M_{\text{eff}} = 0.35$  pg. In the inset are shown the estimation of the deflection at the membrane center  $\xi_0$  and the strain  $\Delta\varepsilon$  for voltages between 0 and 50 V from Equations (3.6) and (3.13) with a pre-stress  $\sigma_0$ .

As previously discussed in Section 3.1.2, these values are likely to be overestimated, however we need them for comparison with those predicted on the other suspended NiPS<sub>3</sub> sample. We note that a deflection of about 125 nm is predicted on this NiPS<sub>3</sub> sample (Mordor) for a 40 V gate voltage, while a deflection of 125 nm was only predicted at a voltage of 56 V on the NiPS<sub>3</sub> suspended sample studied in the previous subsection. On the reflectance evolution calculated in the previous section for the other NiPS<sub>3</sub> sample (see Section 3.1.2) the deflection at 56 V was of about 45 nm, so by extrapolation, we consider that the deflection value is the same for the current NiPS<sub>3</sub> homostructure under a 40 V DC gate voltage. We conclude that on this 13 L NiPS<sub>3</sub> homostructure (Mordor) at 153 K and for a 40 V gate voltage the membrane deflection at the center is  $\xi_0 \simeq 47$  nm which corresponds to a strain of  $\Delta\varepsilon \simeq 0.023$  %. This strain value is in good agreement with the one of 0.02 % derived in the work of Šiškins *et al.* [26] for a Néel temperature

shift of 3 K in FePS<sub>3</sub>.

### 3.2.3 Probed by Raman spectroscopy

We will discuss here the data obtained on NiPS<sub>3</sub> magnetic phase transition probed by Raman spectroscopy at gate voltages of 0 and 50 V on a 10 L suspended sample (*Balor*, see Sample list 1.2.4). The method used to detect magnetic ordering in NiPS<sub>3</sub> is the same as the one discussed in Section 2.2.2 and is based on the lifting of the degeneracy of the phonon mode ( $A_g^2$ ,  $B_g^2$ ) in the antiferromagnetic phase.

We will first show here that the NiPS<sub>3</sub> homostructure (10 L, *Balor*) studied in this Section presents a different evolution of the  $A_g^2$  and  $B_g^2$  phonon modes with temperature than that of the other NiPS<sub>3</sub> homostructure (13 L, *Mordor*) studied in Section 2.2.2, that will affect the detection of its magnetic phase transition.

#### Experimental results at zero gate voltage

As recalled on Figure 3.9 a, the modes with  $A_g$  symmetry are detected in co-polarization configuration (same polarization for incident and collected fields), whereas the modes with  $B_g$  symmetry are detected in cross-polarization configuration (orthogonal polarization between incident and collected fields) (see Eq. (2.18)). The resulting fitted frequencies for the modes  $A_g^2$  and  $B_g^2$  acquired at zero gate voltage are plotted on Figure 3.9 b as a function of the temperature. We note two major disparities compared to the same plot in the case of the NiPS<sub>3</sub> homostructure (*Mordor*) studied in Section 2.2.2 (see Fig. 2.13 b).

First, the mode with the highest frequency after the splitting is the mode  $A_g^2$ , whereas it was the mode  $B_g^2$  on the other sample. Second, the evolution of the mode frequencies with the temperature is not the same. In the antiferromagnetic phase, the frequency of the mode with the lowest frequency keeps increasing, resulting in a smaller splitting between the two modes, than on the NiPS<sub>3</sub> homostructure (*Mordor*) studied in Section 2.2.2. Moreover, the mode with the highest frequency presents an almost linear evolution with temperature, without the saturation characteristic from its expected dependence in the squared magnetization (see Eq.( 2.19)).

This could be explained by a different relative orientation between the direction of the spins and direction of elongation of the phonon mode. Indeed, as seen in Section 1.1.2, the spins chains in NiPS<sub>3</sub> can take three possible orientations, only one of which is represented on Figure 2.12. If the spins are oriented along one of the other two available directions the frequencies of the phonon modes might be modified in a different way and present a different evolution with temperature.

#### Comparison with 50 V DC gate voltage and Néel temperature estimation

These characteristics are also present on the measurement performed with a 50 V gate voltage as shown on Figure 3.9 c, representing the frequency shift of the phonon modes as a function of the temperature, that is obtained by subtracting to the mode frequency its average at the three

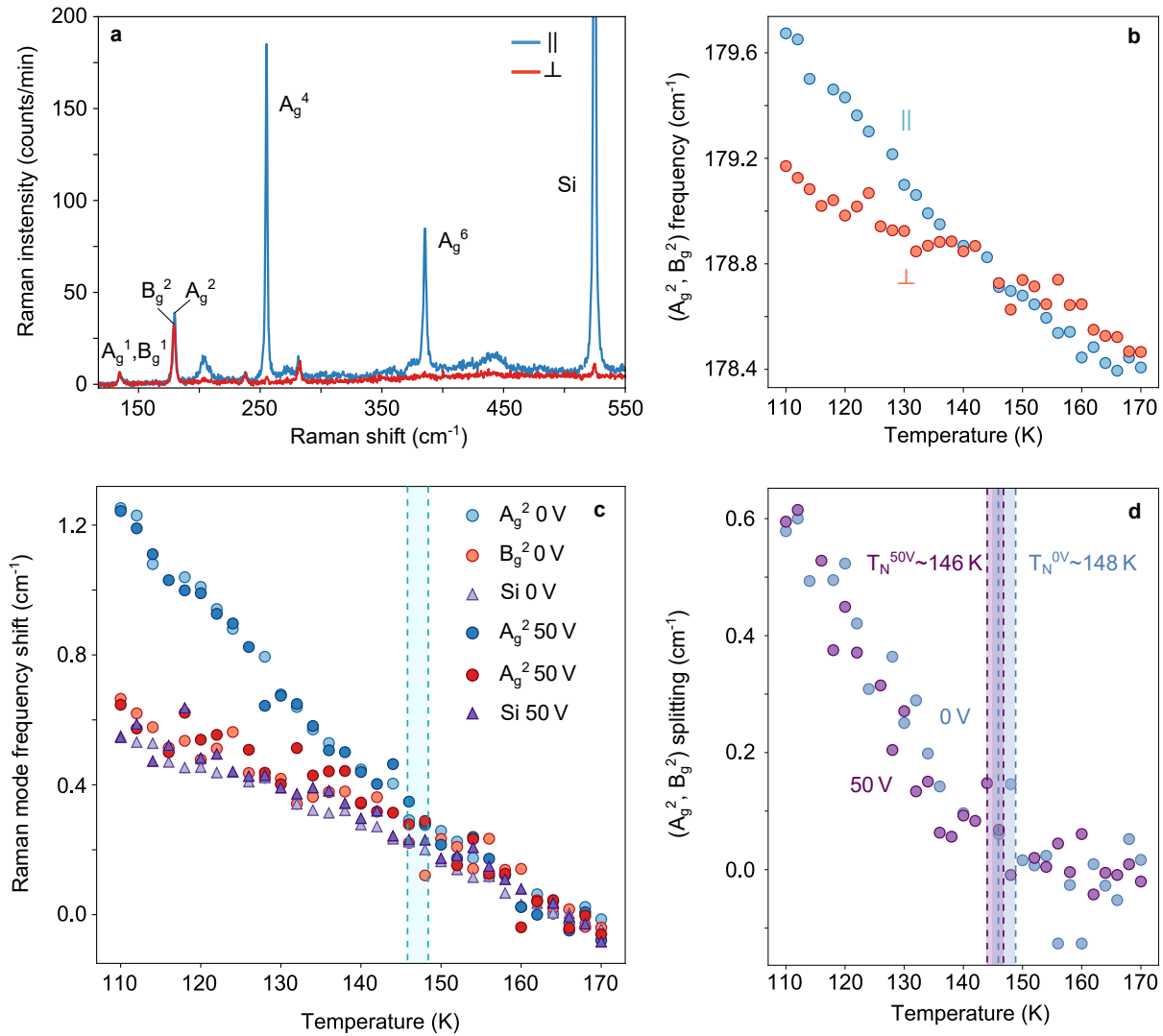


**Figure 3.9: NiPS<sub>3</sub> magnetic phase transition probed by Raman spectroscopy on a 10 L suspended homostructure (*Balor*) at gate voltages of 0 and 50 V.** **a.** Co-polarized (blue) and cross-polarized (red) Raman spectra of NiPS<sub>3</sub> antiferromagnetic phase acquired at 115 K with zero gate voltage. The peaks are labeled according to their corresponding Raman mode symmetries as detailed in Section 1.4.4. **b.** Fitted frequencies of the Raman modes  $A_g^2$  (blue) and  $B_g^2$  (red) as a function of the temperature. **c.** Temperature-dependent shift of NiPS<sub>3</sub> Raman modes  $A_g^2$  (blue dots) and  $B_g^2$  (red dots) and of the silicon Raman mode labeled "Si" (purple triangles) for gate voltages of 0 and 50 V. The light blue window indicates the range for the Néel temperature estimated from the splitting of the modes  $A_g^2$  and  $B_g^2$ . **d.** Frequency shift difference between the modes  $A_g^2$  and  $B_g^2$  as a function of the temperature for gate voltages 0 and 50 V. The blue and purple windows indicates the range for the Néel temperature estimated from the increase in frequency splitting at 0 V and 50 V respectively.

highest temperatures. In addition to the frequency shift of the modes  $A_g^2$  and  $B_g^2$ , we plotted the one of the silicon mode arising from the substrate. This allows us to observe that the  $B_g^2$  mode frequency is shifting with temperature very similarly to the one of the silicon peak, and is thus only weakly affected by the magnetic ordering. To estimate the phase transition temperature, we can thus determine the temperature at which the  $A_g^2$  mode frequency is deviating from the analogous behavior of the  $B_g^2$  mode and silicon peak. We note that the frequency shifts evolution for each phonon mode at 0 V and 50 V are almost superimposed and no appreciable difference can be seen concerning the temperature at which the  $A_g^2$  mode adopts a different behavior. We can only determine a common window of about 3 K around 147 K where the phase transition occurs.

To confirm this temperature range for the magnetic phase transition, the difference in  $A_g^2$  and  $B_g^2$  frequency shifts with temperature is plotted on Figure 3.9 d, in analogy with the Figure 2.13 c. We observe an average splitting of  $0 \text{ cm}^{-1}$  between the two modes until about 148 K, and then an increase of the splitting. As mentioned previously, this increase in frequency splitting does not saturate, unlike in the case of the sample *Mordor*, and thus cannot be fitted by Equation (2.19) to determine more precisely the Néel temperature.

We can, nevertheless, estimate the temperature at which the frequency shift increase starts. For 0 DC gate voltage, we see a frequency fluctuation at 148 K, which can indicate, as seen in Section 2.2.2, the emergence of a magnetic order. We thus mark 148 K as the Néel temperature at zero gate voltage within 3 K. For 50 V gate voltage, the frequency shift is still almost zero at 148 K and its increase starts from 146 K, which we estimate as the Néel temperature in this case, still within 3 K. These temperature intervals are overlapping, therefore we cannot conclude to a clear strain-induced temperature modification, but only that there are some hints to that effect. We could improve the precision of the measurement by acquiring more points around the phase transition, which would also diminish the impact of missing points coming from spectra made unusable due to cosmic rays spikes. It could also be interesting to investigate other magnetic domains on the sample to confirm the influence of the spin orientation compared to phonon mode elongation direction on the phonon frequency shift with temperature.

We will now explore the influence of strain on the mechanical and magnetic properties of a FePS<sub>3</sub>-based magnetic heterostructure.

### 3.3 Magnetic heterostructure nanomechanics

In this Section, we will present and discuss the results obtained by applying a gate voltage on the magnetic heterostructure *Fantadwich* made up of four different materials with varying thicknesses:  $\sim 20$  L hexagonal boron nitride, monolayer  $\text{WS}_2$ , 5 L  $\text{FePS}_3$  and bilayer graphene (see Sample list 1.2.4). We will see that, in contrast to the previously studied  $\text{NiPS}_3$  homostructures, its mechanical modes resonance frequency does not follow the capacitive model presented in Section 3.1. We will thus identify the deviations from this model and investigate their possible origin, in particular by reconstructing the spatial profiles of the mechanical modes. We will finally consider the resulting effects on the detection of the magnetic phase transition by nanomechanical measurements.

#### 3.3.1 Mechanical response evolution for an applied gate voltage

In order to gain a better understanding of the DC gate voltage influence on the mechanical properties of the  $\text{FePS}_3$ -based heterostructure, before investigating its effect on the magnetic phase transition, we first acquired the mechanical mode response to the applied gate voltage that is shown on Figure 3.10.

##### Experimental results

The resulting resonance frequency evolution is very different from the one obtained for  $\text{NiPS}_3$  homostructures (see Figs. 3.1 and 3.8) and is thus deviating from the model presented in Section 3.1. We will analyze step by step the behavior with gate voltage of this sample.

We first focus on the mechanical response obtained for an increasing gate voltage (Fig. 3.10 a) with a positive polarity. We note that the neutrality point, i.e. the DC voltage that compensates the intrinsic offset voltage  $V_0$  and cancels the driving force (see Section 1.5.3), is located around 2 V. Between this neutrality point and 27.4 V, we observe three vibrational modes, all presenting a softening, that occurs on a frequency range of about 5 MHz for the fundamental mode, indicating a high pre-strain in the structure (see Section 3.1.1). This is expected from the stacking of four different layers with different interfacial interactions with each other. At 27.4 V, occurs a first discontinuity, modifying dramatically the number of visible mechanical modes and their frequencies. At 35.9 V, a second discontinuity appears as an inflection point for the two lowest-frequency modes. This second discontinuity does not seem as sharp as the first one, notably for the second highest frequency mode whose frequency is not jumping abruptly, indicating maybe a different origin for it.

If we now compare this evolution to the one obtained for a gate voltage of negative polarity, we see that we get a very close symmetry between the two plots. The negative polarity plot is obtained by grounding the substrate instead of the electrode. The main difference is that the discontinuities are not occurring at the same DC voltages. This is first due to the 2 V shift from the neutrality

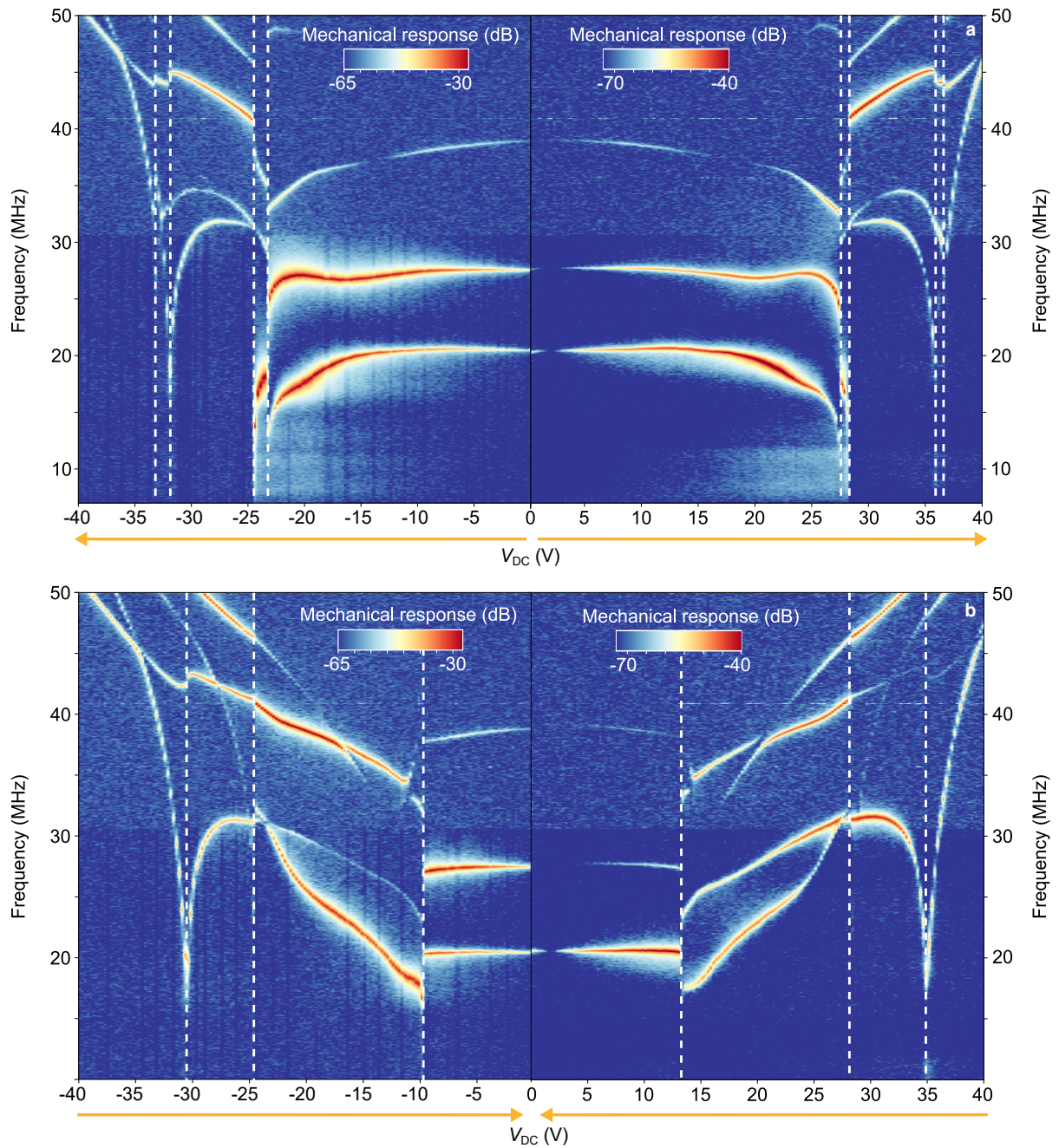


**Figure 3.10:** Mechanical response of the encapsulated 5L FePS<sub>3</sub> heterostructure (*Fantadwich*) to an electrostatic driving force as a function of the gate voltage for positive (electrode grounded) and negative (substrate grounded) polarity at 130 K. **a.** Mechanical response for an increasing DC gate voltage. **b.** Mechanical response for a decreasing gate voltage. We note an hysteretic behavior between increasing and decreasing DC voltages. The dashed lines indicates the major discontinuities visible in the mechanical mode frequency evolution. The orange arrows represent the direction of the voltage sweep.

point, but it is not enough to explain the 4 V gap between the appearances of the discontinuities. This might be caused by a difference in impedance matching between the different electrodes. We also performed the same measurements for decreasing voltages from  $\pm 40$  V to 0 V, displayed on Figure 3.10 b. The results that stands out is a hysteretic behavior of the resonance frequency, that was not present for NiPS<sub>3</sub> homostructures. The main feature is a decrease in resonance frequency accompanied by mode crossovers between 28.2 V and 13.3 V, which was not present in the increasing voltage sweep. At 13.3 V a brutal discontinuity brings back the mode number to three and the frequencies to the ones observed for low increasing voltages, which emphasize a strong pre-strain influence and good reproducibility. Again, there is a very close symmetry between the positive and negative polarities, except for a shift in voltages at which the discontinuities occurs. The difference in detected mechanical mode amplitudes are certainly due to the fact that the measurements were taken at a different time and so at a slightly different position on the membrane.

The membrane mechanical response as a function of gate voltage has been acquired multiple times and for other temperatures (108 K and 75 K), presenting always the same pattern, with slight changes in frequency and voltages according to temperature modifications, indicating a very good reproducibility.

## Discussion

These features are likely originating from the heterostructure nature of the sample that is composed of successively stacked layers, each possessing its own built-in strain. With the application of a DC gate voltage these built-in strains relax, probably inducing layer slipping or layer delamination. Suspended heterostructures formed of a monolayer TMD and mono- or bilayer graphene were already studied by the team and none of them presented such a behavior with gate voltage. This indicates that those discontinuities arise probably from the greater number of layers and likely from the thicker hBN layer on top.

A study of a few-layer hBN/graphene heterostructure pointing towards the layer delamination hypothesis has been performed in 2022 by Sangani *et al.* [35]. They measured a resonance frequency against gate voltage curve for the fundamental mechanical mode presenting some features similar to the ones we obtained. For example, they also observe an initial softening of the resonance frequency followed by an abrupt discontinuity for increasing gate voltage. In addition, they show a symmetric behavior between positive and negative polarities and a hysteresis between increasing and decreasing gate voltages. They attribute these features to the presence of a bubble about 700 nm in size between the hBN and graphene layers that was seen by scanning electron microscopy of the considered sample. The bubble would be caused by a difference in local strain or gas trapped between the two layers. With the increase of strain induced by the gate voltage the bubble would grow and finally lead to the delamination of the two layers. The hysteretic behavior would then results from the separation and adhesion processes of the two layers with voltage increase and decrease, respectively.

The discontinuities observed in this study are clearly analogous to the one we monitored, which support the built-in strain relaxation from the different layers as their origin. However, proving a clear delamination between two layers would need further investigation. For example by studying a simpler heterostructure composed of only two materials and observing an evidence of the modification of proximity effects between these materials upon increasing DC gate voltage [101].

In the following, we will use optical images and mechanical mode reconstruction to explore the modification of the membrane spatial profile around the discontinuities observed in the resonance frequency evolution with gate voltage.

#### 3.3.2 Modification of the membrane spatial profile

To get a better understanding of the observed deviations from an ideal gated membrane behavior, we will monitor the modifications of the static and dynamic spatial profiles of the suspended heterostructure with gate voltage.

##### Imaging the static spatial profile

A way to access qualitatively to the membrane spatial profile is to record directly its optical picture thanks to the imaging camera (see Fig. 1.18). By keeping the imaging lens in front of the beam splitter we can also perform imaging of the sample using laser light. In the case of this FePS<sub>3</sub>-based heterostructure (*Fantadwich*) we found out that laser imaging at a wavelength of 532 nm results in a useful contrast. Indeed, at this wavelength, the membrane appears darker than the rest of the sample, and, contrarily to what we observed at 633 nm, the reflected intensity increases when it is deflected towards the bottom of the substrate (see Fig. 3.11).

On Figure 3.11 a, we see the suspended part of the flake as a dark region at zero gate voltage, and note an area on the membrane top right that is bright, probably resulting from a different shape at this location. This brighter region can be very likely attributed to a wrinkled area, where some layers might not fully adhere to each other as mentioned previously. Between 20 V and 30 V the reflected light patterns appear very different, in good agreement with a redistribution of the strain in the membrane after the discontinuity in the frequency evolution observed at 24.7 V. On the way back to zero DC gate voltage, we note a different profile at 15 V than the one that was visible at 20 V for the increasing voltage sweep, which is consistent with the hysteretic behavior observed on the frequency evolution with DC gate voltage. Finally, at 12 V the membrane suddenly recovers its 0 V profile, again in good agreement with the discontinuity observed at 13.3 V.

Considering the similarities observed between the evolution of membrane reflectivity profile and resonance frequency with gate voltage, we can conclude that the observed discontinuities are indeed resulting from mechanical effects. Also we identified a region on the top right of the suspended heterostructure that seems to follow a different behavior with DC gate voltage and might present a higher built-in strain.

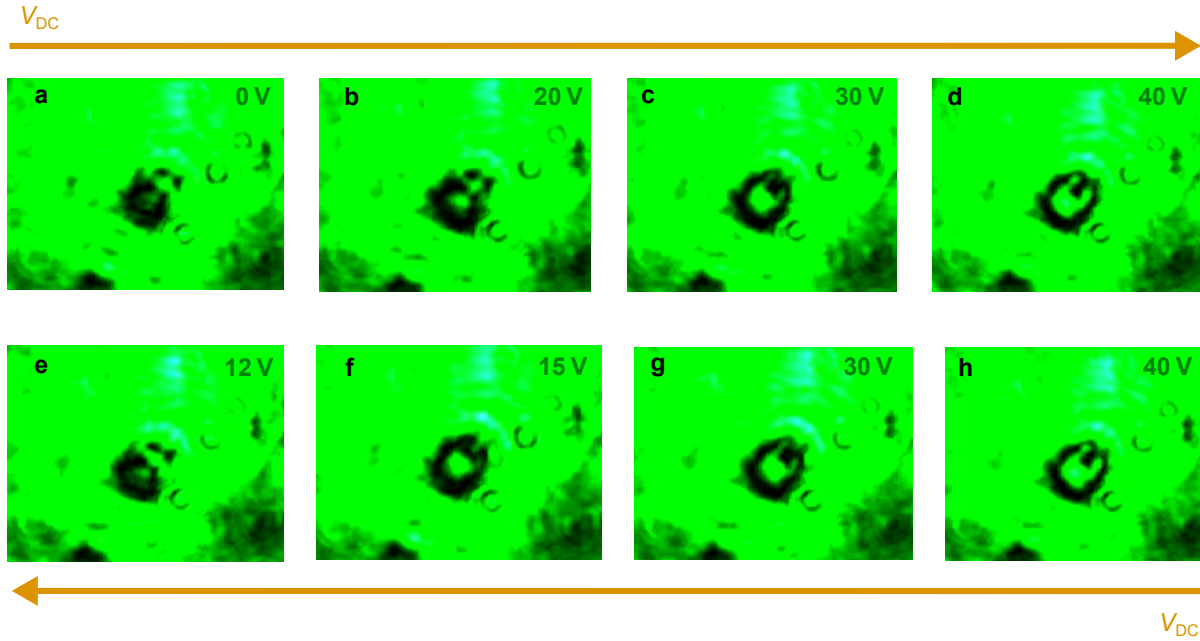


**Figure 3.11: Optical pictures of the FePS<sub>3</sub>-based heterostructure under 532 nm laser illumination at 130 K for various gate voltages. a-d.** For increasing DC gate voltages of 0, 20, 30 and 40 V respectively. **e-h.** For decreasing voltages of 12, 15, 30 and 40 V respectively. At 532 nm the membrane appears darker than the substrate at 0 V and gets brighter when sinking into the hole, contrarily to what we observe at a 633 nm wavelength. The orange arrows represent the voltage sweep direction.

To get more insights on this phenomenon, we will explore quantitatively the evolution of the membrane spatial configuration with gate voltage by the reconstruction of its mechanical modes spatial profiles.

### Reconstruction of mechanical modes spatial profiles

The spatial representations of the mechanical modes are obtained by acquiring the mechanical response to an electrostatic actuation at different locations on the membrane. The resulting spectra are then fitted to obtain the mode amplitude  $z[\Omega_m]$  and resonance frequency  $f_m$  as a function of the position. We can also retrieve the value of the measured phase at the resonance frequency  $\phi_0[\Omega_m]$ , which will allow us to differentiate the membrane regions where a given mechanical mode possesses identical or opposite phases. We then plot the quantity  $z[\Omega_m] \sin(\phi_0[\Omega_m])$ , that will result in the amplitude multiplied by a positive or negative sign depending if the phase is equal to  $\pi/2$  or  $-\pi/2$ . We thus obtain the maps of the mechanical modes shown on Figures 3.12 b-i and 3.13 b-j.

For example, we can take a look at the map of the fundamental mode for a gate voltage of 10 V (see Fig. 3.12 b). The vibrational mode presents two lobes, a blue one that is, by convention, considered to be moving downwards, whereas a smaller one on the top right in red is considered moving upwards. Between these two lobes there is, in pale yellow, a nodal line separating them where there is no motion. We note that it does not look like the expected fundamental mode of an ideal membrane. This could be anticipated from the non-homogeneity of the observed reflectivity

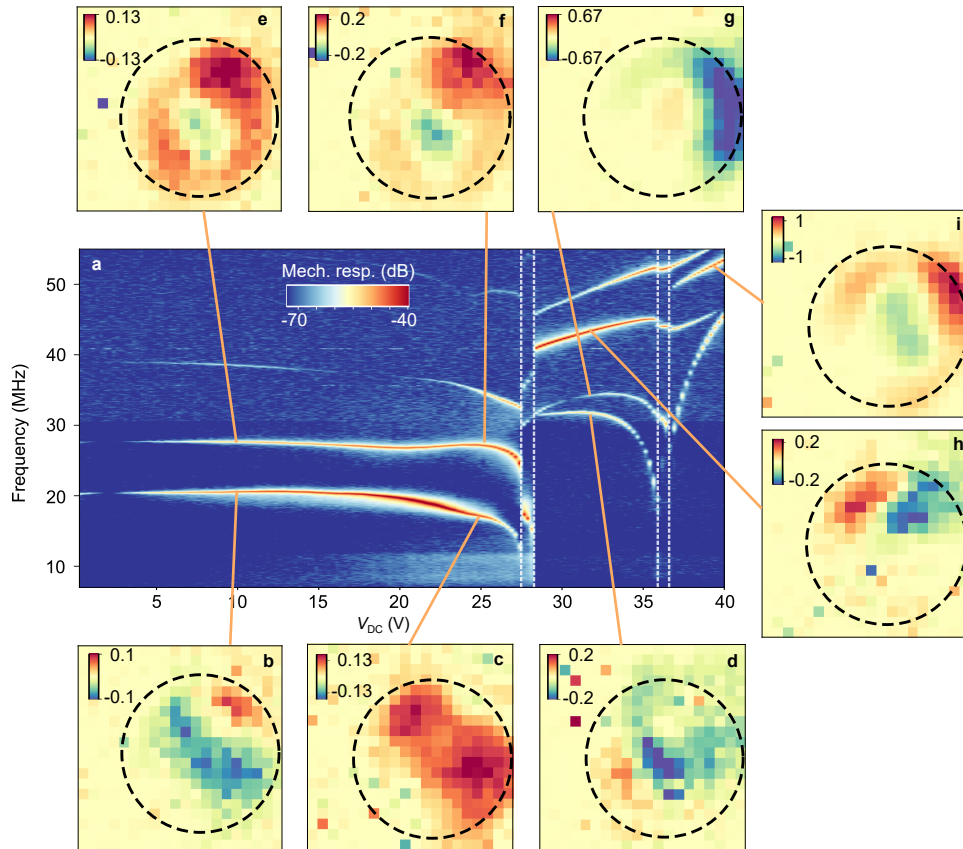


**Figure 3.12: Modification of the mechanical modes spatial profile with increasing gate voltage for the 5 L FePS<sub>3</sub>-based heterostructure at 130 K.** **a.** Colorplot showing the membrane mechanical response as a function of increasing gate voltage. **b,e.** Reconstruction of the two lowest-frequency mechanical modes for a gate voltage of 10 V. **c,f.** Reconstruction of the two lowest-frequency mechanical modes for a gate voltage of 25 V. **d,g-h.** Reconstruction of the three lowest-frequency mechanical modes for a gate voltage of 32 V. **i.** Reconstruction of the third visible mode starting from the lowest frequencies for a gate voltage of 39 V. The displayed quantity is  $z[\Omega_m] \sin(\phi_0)$  that corresponds to the mode amplitude normalized by the largest amplitude of all modes multiplied by the sinus of the phase at resonance. The dashed circles represent the suspended area that has a 5  $\mu\text{m}$  diameter. The maps were measured at a probe laser power  $P_{633} = 40 \mu\text{W}$  before the microscope objective and an electrostatic drive power  $P_{\text{RF}} = -30 \text{ dBm}$ .

profile in laser illumination, where a region of pre-strain has been identified. It has been shown that the presence of wrinkles has a dramatic influence on the mode shape of suspended 2D materials [196]. The higher-order mode at around 28 MHz, still for a gate voltage of 10 V (see Fig. 3.12 e), presents a circular geometry, closer to the theoretical (0,2) mode than the expected (1,1) mode (see Fig 1.25). We note that it displays a higher intensity in the suspected pre-strained region, that was located on the top right of the suspended heterostructure.

The overall profile of the mechanical modes is preserved between DC gate voltages of 10 V and 25 V, whereas none of the modes at 32 V resemble those previously mapped (see Figures 3.12 d, g, h). The first discontinuity in frequency relates then clearly to a drastic reconfiguration of the heterostructure shape. Moreover, at a DC gate voltage of 39 V, so after the second discontinuity, the only mode intense enough to be reconstructed that is the third from the bottom, does again not look like the previously measured modes. It emphasize that the second

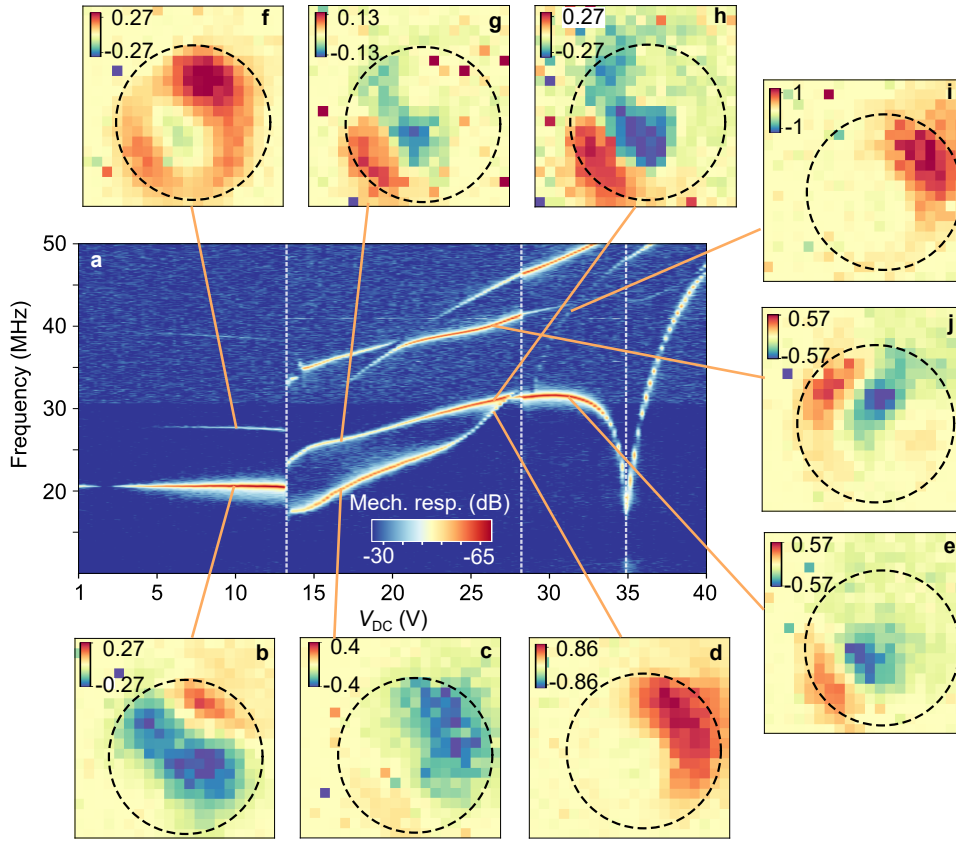


**Figure 3.13: Modification of the mechanical modes spatial profile with decreasing gate voltage for the 5 L FePS<sub>3</sub>-based heterostructure at 130 K.** **a.** Colorplot showing the membrane mechanical response as a function of decreasing gate voltage. **b,f.** Reconstruction of the two lowest-frequency mechanical modes for a gate voltage of 10 V. **c,g.** Reconstruction of the two lowest-frequency mechanical modes for a gate voltage of 17 V. **d,h,j.** Reconstruction of the three lowest-frequency mechanical modes for a gate voltage of 27 V. **i.** Reconstruction of the two lowest-frequency mechanical modes for a gate voltage of 32 V. The displayed quantity is  $z[\Omega_m] \sin(\phi_0)$  that corresponds to the mode amplitude normalized by the largest amplitude of all modes multiplied by the sinus of the phase at resonance. The dashed circles represent the suspended area that has a 5  $\mu\text{m}$  diameter. The maps were measured at a probe laser power  $P_{633} = 40 \mu\text{W}$  before the microscope objective and an electrostatic drive power  $P_{\text{RF}} = -30 \text{ dBm}$ .

discontinuity also arises from a modification of the membrane spatial configuration.

In the case of the mode spatial profiles evolution with decreasing gate voltage (see Fig 3.13 b-j), we observe again that the mode spatial profiles are different before and after each discontinuity. We also note that the mode shapes are globally preserved during the hysteretic behavior between 28.2 and 13.3 V, indicating that the heterostructure spatial configuration is not much modified by it. At 10 V the mechanical modes have recovered their initial shape (see Fig 3.12 b, e), highlighting again the reproducibility of the heterostructure behavior with DC gate voltage.

In conclusion, we have demonstrated that the reported discontinuities in the membrane mechanical response as a function of the gate voltage are the result of changes in its spatial mode profile.

The observed hysteretic behavior between increasing and decreasing voltages sweeps is supported by a preservation of the mechanical mode shapes earned after the discontinuities, even when the voltage is decreased beyond the one at which was occurring the first discontinuity. This

conservation of the mode profiles between 32 and 17 V, indicates only few changes of the membrane spatial profile in this voltage range. If a re-adhesion of the layers was taking place in this interval, in the case of a delamination, the modes shape would probably be modified. This implies that either the re-adhesion occurs instantaneously at 13.3 V or that the discontinuities are caused by a strain redistribution that is more favorable energetically without delamination.

Now that we have a clearer idea of the effect of a applied DC gate voltage on this heterostructure nanomechanics, we can explore its impact on FePS<sub>3</sub> magnetic phase transition detection.

#### 3.3.3 Consequences on the magnetic phase transition

The method to probe magnetic phase transitions in suspended 2D magnets by nanomechanical measurements is the one already discussed in Sections 2.1.1 and 3.2.2. We already reported a Néel temperature of 109 K for the FePS<sub>3</sub>-based heterostructure (*Fantadwich*) with a 16 V applied DC voltage and a strain-induced Néel temperature decrease of around 3 K on the 13 L NiPS<sub>3</sub> homostructure (*Mordor*) for a 40 V applied DC voltage.

Here, we will investigate the consequences of the strain redistribution occurring in the 5 L FePS<sub>3</sub> heterostructure (*Fantadwich*) at the discontinuities observed in its mechanical response evolution with gate voltage, on FePS<sub>3</sub> magnetic phase transition signatures.

The membrane resonance frequency as a function of the temperature has been measured at gate voltages of 10, 25, 32 and 37 V for increasing and decreasing voltage sweeps. For the sake of clarity, we present here selected curves that are representative of the main behaviors observed and that exhibit a sufficiently large signal over the entire temperature range (see Fig. 3.14 a).

We note that the slope of the resonance frequency with temperature increases for higher gate voltages, which is the opposite of what we observed for a 13 L NiPS<sub>3</sub> homostructure and what was reported in [26] for a  $\sim 11$  L FePS<sub>3</sub> homostructure.

More surprisingly, the resonance frequencies of some modes are increasing with increasing temperature. This is likely arising from the competition between the thermal expansion coefficients of the materials composing the heterostructure that possess different signs (positive for FePS<sub>3</sub> and WS<sub>2</sub> but negative for graphene and hBN, see Table 1.3) as shown in Equation 2.6. The behavior with temperature of the vibrational modes might be affected more by one or another layer depending on their spatial profile. Nevertheless the resonance frequency evolution still presents the characteristic break of slope indicating FePS<sub>3</sub> magnetic phase transition, that is even steeper than the one observed at 10 V.

We will now look at the quantity  $df_m^2(T)/dT$  that is proportional to the specific heat (see Eq. 2.5) and thus displays a peak at the magnetic phase transition temperature (see Fig. 3.14 b). We note that the  $df_m^2(T)/dT$  curves from modes which are stiffening with an increasing temperature show a dip rather than a peak.

The striking element is that some of the peaks or dips resulting from the magnetic contribution to the specific heat, are way sharper and of higher intensity than the others, enabling a more precise

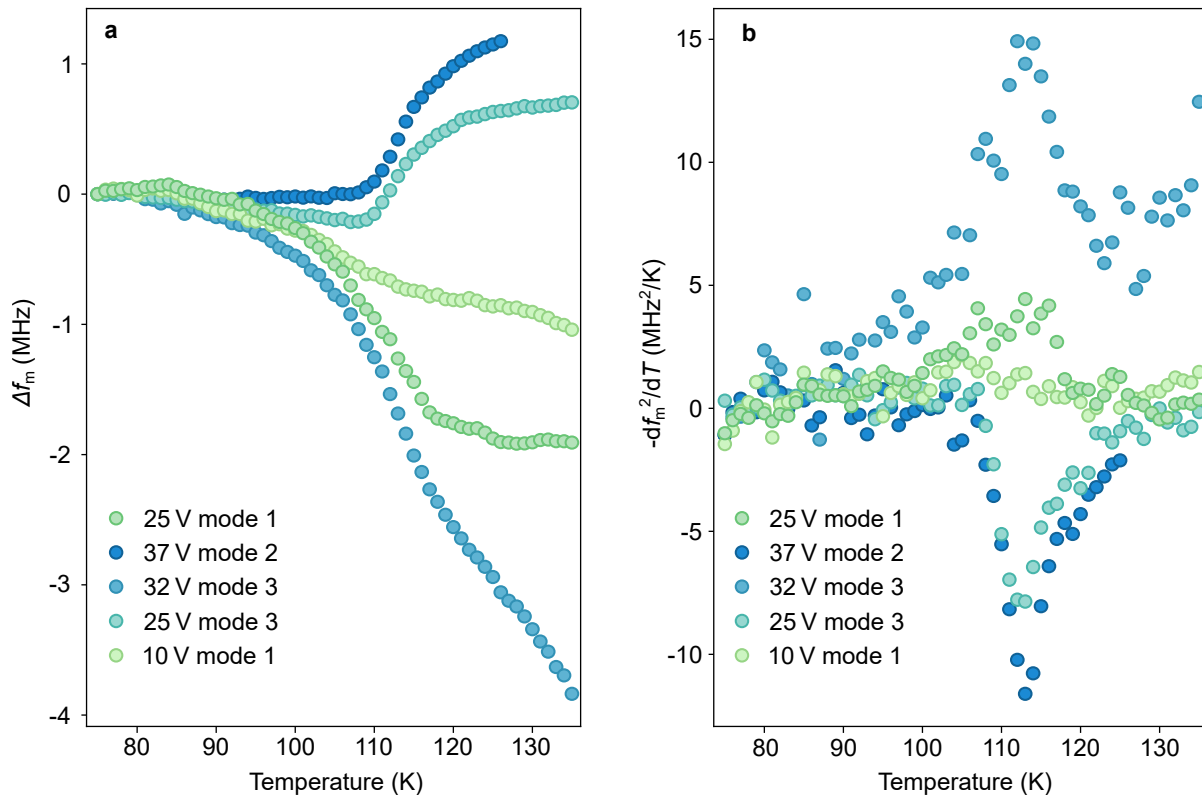


**Figure 3.14: Probing FePS<sub>3</sub> Néel temperature on the suspended heterostructure *Fantadwich* for various voltages.** **a.** Resonance frequency shift  $\Delta f_m$  with respect to the resonance frequency at 75 K, as a function of temperature for various gate voltages. **b.**  $df_m^2/dT$  as a function of the temperature. The top of the peak indicates FePS<sub>3</sub> Néel temperature. The mode number specifies its position starting from the lower frequencies.

determination of the Néel temperature. As a comparison, the peak measured for a 16 V gate voltage in Section 2.1.1 had a height of about 1.5 MHz<sup>2</sup>/K whereas the peak at 32 V possesses a height of about 10 MHz<sup>2</sup>/K. We notice that what these three most intense peaks have in common is that they belong to a voltage range located after the first discontinuity observed in the resonance frequency evolution with DC voltage. In Section 3.2.2, we observed that an increase in gate voltage, and so an increase in strain, is resulting in a decrease in the intensity of the peak in  $df_m^2(T)/dT$ . An increase in the peak intensity implies then that the pre-strain present initially in the FePS<sub>3</sub> layer has been relaxed at 32 V.

We can also look at the evolution of FePS<sub>3</sub> Néel temperature, that is estimated as the temperature corresponding to the top of the peak in  $df_m^2(T)/dT$ , with DC gate voltage. At 10 V the increase in  $-df_m^2(T)/dT$  is very weak and not well defined, we will thus rather consider the Néel temperature of 109 K determined at 16 V in Section 2.1.1 as a starting temperature. We estimate a Néel temperature of around 111 K at 25 V and 113 K at 32 V, which corresponds to a total increase of 4 K.

For an about 11 L FePS<sub>3</sub> homostructure, Šiškins *et al.* [26] have reported a decrease of 6 K in Néel temperature for a 0.045 % increase in strain. In our case, an increase of the Néel temperature would then imply a decrease in the strain in the FePS<sub>3</sub> layer with DC gate voltage.

We note however, that the Néel temperature does not seem to vary much between 32 and 37 V, which could indicate a relaxation of the overall pre-strain and suggest a future decrease of the Néel temperature due to a membrane stiffening.

In conclusion, we report a rise of about 4 K of FePS<sub>3</sub> Néel temperature between 16 and 37 V, which is consistent with a relaxation of the FePS<sub>3</sub> layer pre-strain.

## Chapter conclusion

The goal of this chapter was to show first signatures of controllably modifying the mechanical and magnetic properties of drum-like  $\text{FePS}_3$  and  $\text{NiPS}_3$  nanoresonators. We first investigated the case of a  $\text{NiPS}_3$  homostructure, with the results obtained on 10 L and 13 L samples (*Balor* and *Mordor*, respectively, see Sample list 1.2.4), before exploring the nanomechanical behavior of an encapsulated  $\text{FePS}_3$ -based heterostructure (*Fantadwich*, see Sample list 1.2.4).

In a first Section, we discussed how the applied electrostatic force influences the membrane mechanical properties and estimated the induced deflection and strain.

First, we derived a qualitative model where the sample is considered as a parallel plate capacitor, to describe the global behavior of a suspended membrane to which a DC gate voltage is applied. The main results of this model are, for small membrane deflections:

- the membrane resonance frequency evolution with DC gate voltage includes two terms: a softening contribution that dominates at low gate voltages and a stiffening contribution that becomes significant at high gate voltages, the distinction between these regimes depending on the membrane pre-strain
- the deflection at the center of the membrane is evolving as the squared DC gate voltage
- the strain induced by the electrostatic force is increasing like the fourth power of the DC gate voltage

To estimate quantitative deflection and strain values, we relied on the modeling of the membrane reflectance as a function of its deflection as already discussed in Section 1.5.2. From the acquisition of the photodiode output voltage as a function of the DC gate voltage, we quantified the corresponding membrane reflectance variation from which we obtained an estimate of the membrane deflection.

In a second Section, we investigated the magnetic phase transition of the 10 L and 13 L suspended  $\text{NiPS}_3$  homostructures under strain by three approaches:

- theoretically, by reviewing the Landau theory of phase transitions, including magnetostriction effects, in the case of an antiferromagnet and, which resulted in a prediction of a modification of the Néel temperature by the applied strain
- using nanomechanical measurements, as detailed in Section 2.2.1, we probed  $\text{NiPS}_3$  magnetic phase transition for different DC gate voltage and reported a decrease of  $\text{NiPS}_3$  Néel temperature of about 3 K for a strain estimated at around 0.02 %
- using Raman spectroscopy, following the same protocol to that of Section 2.2.2 we probed  $\text{NiPS}_3$  magnetic phase transition for DC gate voltages of 0 and 50 V, we could not conclude on a clear shift of the Néel temperature, due to a 3 K uncertainty on its estimation

In the last Section, we explored the behavior with applied DC gate voltage of a 5 L FePS<sub>3</sub> encapsulated in a van der Waals heterostructure using three different methods:

- we acquired the membrane mechanical response as a function of the applied DC gate voltage and observed several discontinuities in the resonance frequency evolution, accompanied by a hysteretic behavior between increasing and decreasing gate voltage sweeps, both being reproducible
- we imaged the membrane reflectivity profile by laser illumination, showing its modification between gate voltage values corresponding to the discontinuities seen on the resonance frequency evolution
- we mapped the spatial profiles of the membrane mechanical modes and demonstrated that they are drastically different before and after the DC gate voltages corresponding to the discontinuities seen on the resonance frequency evolution

We concluded that the observed features are indicating a sudden stress redistribution that is likely due to a slipping or a delamination of the layers from which the heterostructure is composed. We finally studied the influence of this exotic behavior with gate voltage on the encapsulated 5 L FePS<sub>3</sub> phase transition. We reported an important increase of the intensity of the magnetic contribution to the specific heat visible in  $df_m^2(T)/dT$  with increasing gate voltage. The resulting sharp peak allows a more precise determination of the Néel temperature that rises of 4 K between 16 V and 32 V. Those findings supports a decrease of the strain in the FePS<sub>3</sub> layer with increasing DC gate voltage, confirming a relaxation of the built-in strain in the layers composing the heterostructure at higher DC gate voltages.

## Chapter 4

---

# Investigation of NiPS<sub>3</sub> photoluminescence: strain-tuning and fine structure

---

NiPS<sub>3</sub> light emission has been first observed by Kang *et al.* in 2020 [36] and is now intensively studied for its intriguing properties and still debated origin [38–41, 43, 197, 198]. In this chapter, we will first review the features which make NiPS<sub>3</sub> photoluminescence (PL) distinctive and discuss its physical origin. We will then benefit from the suspended samples geometry to investigate a property of NiPS<sub>3</sub> photoluminescence that has not been studied until now: its response to strain. Afterwards, we will exploit the linear polarization of NiPS<sub>3</sub> photoluminescence, combined with Raman spectroscopy, to probe antiferromagnetic domains.

### 4.1 An intriguing photoluminescence

NiPS<sub>3</sub> photoluminescence attracts interest because of its narrow linewidth, flake thickness dependency, temperature dependency and linear polarization, which all tend to indicate a correlation with the zigzag antiferromagnetic order. In the following, these properties will be detailed and illustrated by measurements acquired on a supported sample and a 10 L suspended homostructure (*PacMan* and *Balor*, see Sample list 1.2.4).

#### 4.1.1 Characteristic properties

##### Typical spectrum and temperature dependence

On Figure 4.1 a are shown two spectra acquired in an energy range around that of NiPS<sub>3</sub> light emission on a bulky flake of a supported sample (*PacMan*, see Sample list 1.2.4) at 300 K and at 22 K. We clearly see that there is no photoluminescence at room temperature, whereas at 22 K a sharp peak, that we label "X", is visible for an energy of 1.4771 eV, corresponding to 840.0 nm. Its full width at half maximum (FWHM) is resolved at about 0.5 meV which is around five times

narrower than what is observed for transition metal dichalcogenides photoluminescence peak at low temperatures [199]. At energies lower than that of the main peak, we notice a broad band comprising several peaks. It has been shown by Ergeçen *et al.* [200] that those peaks are equally spaced  $253\text{ cm}^{-1}$  apart, which corresponds to the energy of the NiPS<sub>3</sub> Raman mode  $A_g^4$ . From these pump-probe measurements the signal between 1.47 and 1.36 eV has been assigned to a hybridization between  $d-d$  levels of the nickel atom and this Raman active phonon.

Concerning the photoluminescence temperature dependence, it has been reported that the peak X is emerging gradually from 120 K and gets sharper and more intense as the temperature decreases [36, 37, 46]. The fact that the peak appears only when NiPS<sub>3</sub> is in its antiferromagnetic phase suggests that the photoluminescence could be favored by the magnetic order. Moreover, an absorption peak has been observed on bulk NiPS<sub>3</sub>, at an energy corresponding to that of the photoluminescence peak, also emerging progressively from 120 K [36].

### Variation with layer number

When studying thinner NiPS<sub>3</sub> layers, it appears that the photoluminescence is strongly affected by the flake thickness below 10 layers (see Fig. 4.1 b). The peak intensity decreases rapidly with decreasing thickness to become a weak bump for two layers and has been reported to vanish completely at the monolayer level [36, 37]. This extinction of the photoluminescence could be attributed to a weaker magnetic order for this in-plane magnet at the single layer limit, still assuming that light emission and magnetic order are linked. We also note that the peak energy is shifting towards higher values with decreasing thickness.

### A linearly polarized emission

One of the most important properties of NiPS<sub>3</sub> light emission for our work is its linear polarization. To determine the polarization pattern of the photoluminescence, we use one half-wave plate and one polarizer as described in Section 1.3.2. The half-wave plate is placed before the sample to control the incident light polarization, while the polarizer is placed after the sample to select the polarization of the collected light and will be called "analyzer". NiPS<sub>3</sub> photoluminescence having been reported as independent of the incident light polarization [37, 46], we will keep the angle of the half-wave plate fixed and vary only the one of the analyzer. The 0° of the analyzer angle is set as identical to the polarization direction of the incident light. By acquiring spectra for various angles of the analyzer between 0 and 360°, we obtain the polarization pattern of a bulk flake located on the same substrate as a 10 L suspended homostructure (sample *Balor*) (see Fig. 4.1 c,d). We see two lobes separated by extinctions of the photoluminescence peak, indicating a linear polarization with a polarization degree close to unity of  $\rho = (I_{\parallel} - I_{\perp}) / (I_{\parallel} + I_{\perp}) = 0.91$ , with  $I_{\parallel}$  and  $I_{\perp}$  being the photoluminescence intensity parallel and perpendicular to the polarization axis, respectively. The polarization angle  $\theta_0$  can be determined by fitting the photoluminescence maximum intensity evolution with the model  $I_{\parallel} \cos^2(\theta_A - \theta_0) + I_{\perp}$ , where  $\theta_A$  is the analyzer angle,

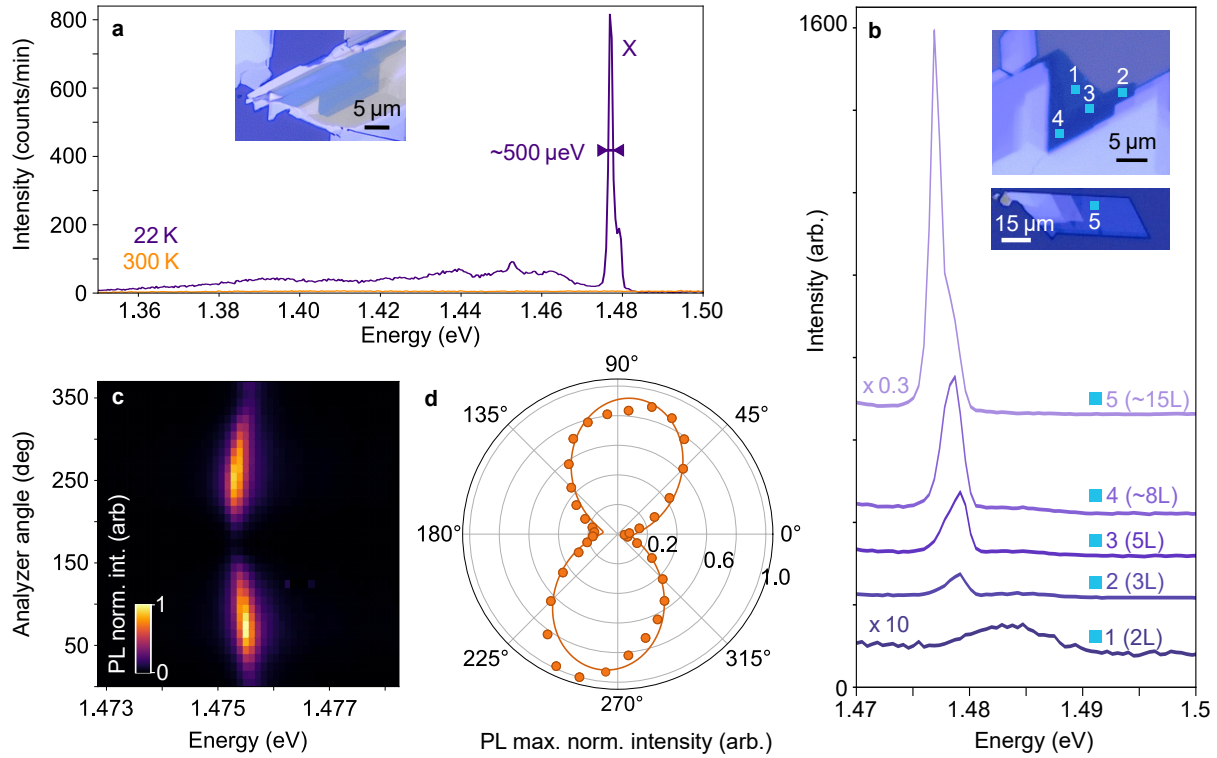


**Figure 4.1: NiPS<sub>3</sub> photoluminescence characteristic properties.** **a.** Photoluminescence spectra acquired at 22 K, in purple, and at 300 K, in orange, on a bulky part of a NiPS<sub>3</sub> supported sample (*PacMan*) visible in the inset. The photoluminescence peak is only visible at low temperatures and has a very narrow width of about 500  $\mu\text{eV}$ . **b.** Spectra of NiPS<sub>3</sub> photoluminescence peak as a function of the flake thickness. The spectra were acquired at various spots on the same supported sample (*PacMan*) which are indicated in the inset. The first number labeling the spectra represents the location at which it was recorded, and in brackets is the associated estimated layer number. The spectra are offset for clarity. **c.** Normalized photoluminescence spectra for various analyzer angles  $\theta_A$  between 0 and 360° acquired on a bulk part of a NiPS<sub>3</sub> homostructure (*Balor*) at 5.5 K. The shift of the peak energy is arising from a measurement artifact. **d.** Polar plot showing the corresponding maximum value of the normalized photoluminescence intensity as a function of the analyzer angle. The data are the dots and the solid line is a fit by the model  $I_{\parallel} \cos^2(\theta_A - \theta_0) + I_{\perp}$ , giving a linear polarization angle  $\theta_0 = 262.6^\circ$ .

that can be derived by calculation of transfer matrices resulting from Jones formalism of polarized light [168, 201]. We thus obtain a polarization angle of  $\theta_0 = 262.6^\circ$  for the photoluminescence of this NiPS<sub>3</sub> bulk flake.

The polarization axis of bulk NiPS<sub>3</sub> photoluminescence was initially demonstrated to be directed along the *b* crystalline axis, that is the one oriented perpendicularly to the spins direction [36] (see Figs. 1.1, 1.3). Subsequently, it has been proven that the photoluminescence polarization rotates accordingly with the spins reorientation induced by a magnetic field [39, 40, 46], confirming its perpendicular orientation to the Néel vector  $\mathbf{L}$  rather than to the *b* axis. This implies the existence of a strong coupling between the spins and the origin of this light emission, a non-linear Zeeman splitting of the peak having been reported in addition to the polarization rotation [39, 40, 202]. On the other hand, the determination of the photoluminescence polarization axis can be used as a probe of the Néel vector orientation.

### 4.1.2 Insights into its origins

The process responsible for NiPS<sub>3</sub> light emission is still under debate and multiple works have tackled this question over the recent years [36–38, 40, 41, 46, 198]. NiPS<sub>3</sub> has been reported as an insulator with an indirect optical bandgap of 1.8 eV [120], that does not match the 1.476 eV energy of the photoluminescence. We will first review the most explored hypothesis concerning NiPS<sub>3</sub> photoluminescence origin, before listing some other possibilities.

#### Zhang-Rice triplet to singlet transition

In the first paper observing NiPS<sub>3</sub> light emission, its origin has been attributed to a transition from a Zhang-Rice triplet (ZRT) state to a Zhang-Rice singlet (ZRS) state [36]. This explanation remains the most often referred to in papers on NiPS<sub>3</sub> photoluminescence [40, 46, 197, 203].

This claim is supported by resonant inelastic X-ray scattering (RIXS) measurements. To understand it, we need to consider the unit NiS<sub>6</sub>, comprising the Ni<sup>2+</sup> nickel ion and its six surrounding sulfur ligands (see Fig. 1.2). The expected ground state of the nickel ion is  $d^8$ , which is its *d* orbital occupied by eight electrons. However, NiPS<sub>3</sub> has been reported to be a charge transfer insulator [36, 120], meaning that the ligands can exchange charges with the metallic atom. From X-ray absorption spectroscopy measurements, it has been shown that the ground state of nickel ions has a predominant  $d^9\bar{L}$  contribution [36]. This corresponds to a configuration where the ligands are transferring one electron to the nickel *d* orbital, leaving a hole in one of the ligands' orbitals, that is represented by the notation  $\bar{L}$ . This state with one hole in the ligands orbitals and one hole in the nickel ion orbitals, that is now Ni<sup>+</sup>, constitutes the Zhang-Rice triplet state, with a spin state  $S = 1$ , which is shown on the left panel of Figure 4.2 a. Its transition to a Zhang-Rice singlet state goes through an intermediate state that is triggered by the excitation of one electron of the *2p* core levels to the nickel *d* orbitals. During this intermediate state, due to a robust spin-orbit coupling, the spin  $S$  is not conserved, only the total spin  $J$  is, which can lead to

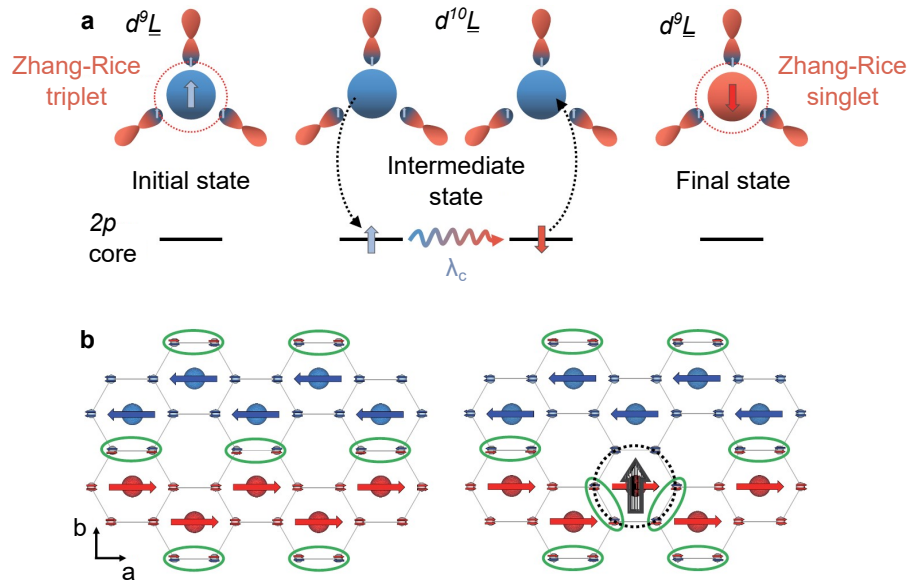


**Figure 4.2: Illustration of the Zhang-Rice triplet (ZRT) to singlet (ZRS) transition and corresponding localized states on the lattice.** **a.** Scheme of the resonant inelastic X-ray scattering (RIXS) process inducing the Zhang-Rice triplet to singlet transition. The disks are representing the nickel  $d$  orbitals, while the three orbitals around it, displaying two lobes, are the ones of the sulfur ligands. The arrows drawn inside these orbitals indicate the spin direction of the holes. In the intermediate state, the dotted arrows correspond to virtual transitions between the  $2p$  core levels and the nickel  $3d$  orbitals with  $\lambda_c$  the core level spin-orbit interaction. **b.** Top view of schematized NiPS<sub>3</sub> antiferromagnetically-coupled spin chains. The bigger, smaller circles are representing nickel, sulfur atoms, respectively. The arrows are indicating the spin directions. The green ellipsoids highlight the sulfur atoms presenting compensated spins. The modification of their number from two before the ZRT to ZRS transition, to four after, induces a local dipole moment represented by a large vertical arrow. Adapted from [36].

spin flip. In this case, the spin of the hole in the nickel  $d$  orbital will change sign, while that of the ligands remains unchanged, leading to a state  $S = 0$  which is the Zhang-Rice singlet state (see Fig. 4.2 a).

The calculated results corresponding to the modeling of this ZRT to ZRS transition have shown very good agreement with the measured RIXS data and lead to a transition energy of 1.476 eV, that corresponds to the observed photoluminescence energy [36]. The light emission would then arise from the formation of the ZRS state.

They were also able to explain the linear polarization of the light emission. The sulfur atoms located at the border between two zigzag spin chains present antiparallel hole spins that cancel (see Fig. 4.2 b). This results in regions of lower hole densities between the spin chains in the ground state (ZRT). However, at the site of a ZRS excitation, due to the spin state  $S = 0$  all the hole spins on the sulfur ligands are reversed compared to the ZRT state, resulting in a lower hole density along the spin chain at this location. This induces an electric dipole orthogonal to the spin chains, and so, parallel to the observed photoluminescence polarization.

To sum up, the Zhang-Rice triplet to singlet transition proposed by Kang *et al.* [36] accounts for NiPS<sub>3</sub> photoluminescence energy and linear polarization orthogonal to the spin chains.

Moreover, a recent work has exploited this formalism to explain the Zeeman splitting of the photoluminescence under a magnetic field [40]. However, the ZRT to ZRS transition does not justify the narrow width of the photoluminescence peak nor the appearance of satellite peaks.

### Nickel ions internal d-d transitions

The photoluminescence of NiPS<sub>3</sub> could also be attributed to an internal *d-d* transition within the nickel ions Ni<sup>2+</sup> [41, 42, 202].

A first argument is that NiPS<sub>3</sub> light emission shares several characteristic properties with the optical transition reported in MnPS<sub>3</sub>, which has been attributed to a Mn<sup>2+</sup> ion *d-d* transition [204]. Indeed, MnPS<sub>3</sub> photoluminescence has also been shown to appear only in its antiferromagnetic phase and to exhibit a rather narrow linewidth of about 1.6 meV. Moreover, MnPS<sub>3</sub> photoluminescence peak presents a splitting similar to that reported of NiPS<sub>3</sub> when exposed to a magnetic field [202].

Secondly, a recent RIXS study has demonstrated a ground state for the nickel ions dominated by a *d*<sup>8</sup> configuration rather than a *d*<sup>9</sup> $\underline{L}$  configuration, that would indicate a Hund's rather than a Zhang-Rice character [41], meaning that the light emission is stabilized by the Hund's exchange interaction. This would imply that the ligands are not involved in the transition giving rise to NiPS<sub>3</sub> light emission, and so, that it would only occur within the *d* orbitals. Similar conclusions have been achieved on nickel dihalides NiX<sub>2</sub> that are also charge transfer insulators including Ni<sup>2+</sup> ions in an octahedral symmetry [42].

### Structural defects

The narrow linewidth of NiPS<sub>3</sub> photoluminescence may suggest an emission from isolated defects, however it has been proved that the emission is homogeneous over micrometers ruling out this possibility [46] (see Fig. 4.11).

Nevertheless, this does not exclude the possibility of structural defects like NV centers in diamond. In their work of 2023, Kim *et al.* [38] suggested homogeneously distributed sulfur vacancies as the origin of NiPS<sub>3</sub> photoluminescence. They based their hypothesis on their observation of a photoluminescence emission only in bulk crystals presenting a sulfur deficiency. In addition, they performed first-principle calculations based on S-vacancy bound excitons, that resulted in a light absorption anisotropic regarding light polarization parallel or orthogonal to NiPS<sub>3</sub> magnetic spin chains. They also justified the presence of the phonon side bands observed between 1.36 and 1.47 eV by the coupling of this localized exciton to phonons, and elaborated a model for this coupling. However, this scenario does not account for the temperature dependence of the PL peak nor the exact energy of the observed light emission.

To conclude, none of these models fully encompasses all the characteristics of NiPS<sub>3</sub> photoluminescence and further investigation is still needed to elucidate its origins.

## 4.2 Study of few-layer NiPS<sub>3</sub> photoluminescence main peak

The properties of NiPS<sub>3</sub> photoluminescence for flakes in the 10-layer thickness range, in which the signal is still quite intense and the membrane behavior is preserved (see Sec. 1.5.1), have so far been little studied [38], the investigations being more focused on bulk crystals or thinner flakes of five to three layers [36, 37, 43, 46, 202]. Here we study NiPS<sub>3</sub> photoluminescence response to an applied strain and its linear polarization orientation for a 10 L homostructure (*Balor*, see Sample list 1.2.4).

### 4.2.1 Evolution with strain

We will first look at the evolution of NiPS<sub>3</sub> light emission as a function of the applied gate voltage, and so, with increasing and decreasing strain, at a temperature of 5.5 K.

For this, we initially record photoluminescence spectra centered on the main peak X at the center of a NiPS<sub>3</sub> nanodrum for various gate voltages between 0 and 80 V (see Fig. 4.3 a). We observe that the photoluminescence intensity and energy are continuously decreasing with the increase of the gate voltage. To quantify these shifts, we fit the peak X by a Voigt profile (see Appendix B) and extract its intensity, energy and linewidth. On Figure 4.3 b is shown the energy shift of the photoluminescence between 0 and 80 V. We observe a maximum decrease of the energy of about 0.18 meV which corresponds to almost half of the peak initial linewidth, that is of 0.4 meV at 0 V on this sample (see Fig. 4.4 b). The peak energy evolution with gate voltage can be nicely fitted by a function proportional to  $V_{DC}^4$ . Since the applied strain is also evolving as the DC voltage to the power four (see Section 3.1.2), it implies that the energy shift is proportional to the gate-voltage induced strain.

We also acquired spectra for decreasing gate voltages between 80 and 0 V and notice that there is an overlap with the energy shift evolution obtained for increasing gate voltages (see Fig. 4.3 b). No hysteretic behavior is visible and the shift is reversible.

To confirm that the observed energy shift is due to strain and not to doping effects, we repeated the measurements on a supported part of the sample located at the same distance to the electrode than the drum center (see Fig. 4.3 b). We note no obvious changes in the supported NiPS<sub>3</sub> photoluminescence spectra with gate voltage. Moreover, the fitted energy evolution is almost flat for both increasing and decreasing gate voltages, indicating that the energy shift on the suspended part of the sample is likely due to the applied strain. The photoluminescence energy shift at 80 V can thus be attributed to a strain of around 0.17 % as estimated from the reflectivity model in Section 3.1.2 for the same sample in identical temperature and voltage conditions. By considering a linear relation between energy shift and strain, we can deduce an energy shift with strain of  $\Delta_\epsilon \simeq 1.1 \text{ meV}/\%$ .

In addition to the energy, we can analyze the evolution of the fitted photoluminescence peak intensity and linewidth with strain as shown in Figure 4.4. The peak intensity decreases of about

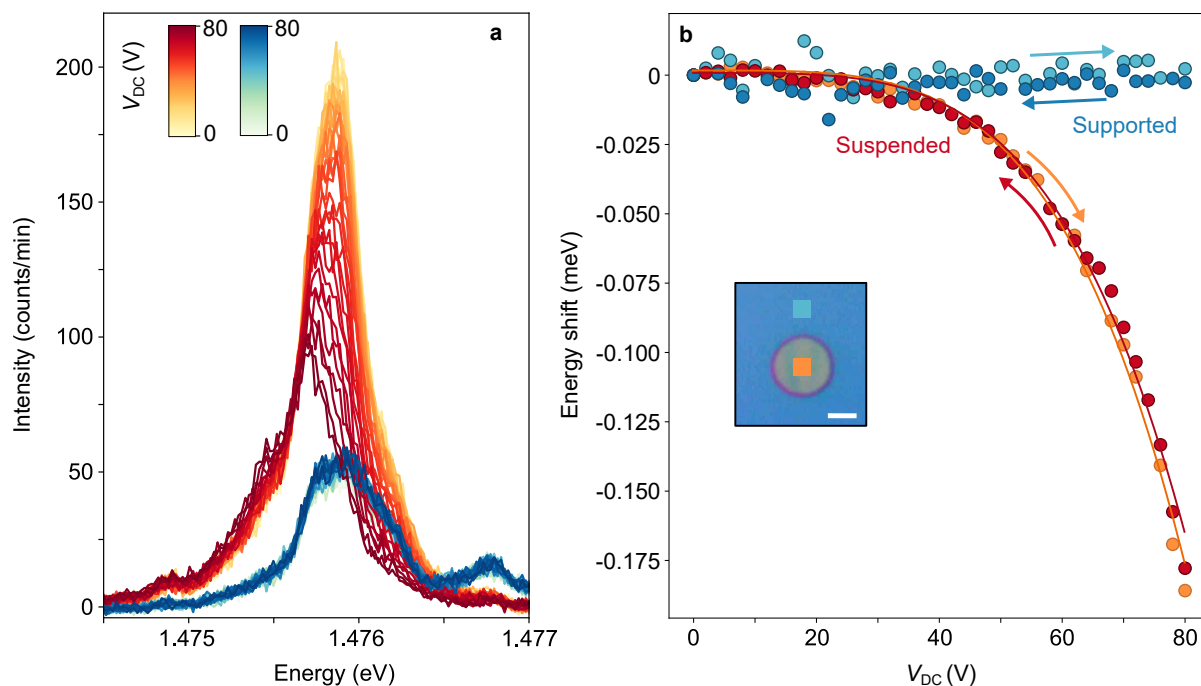


**Figure 4.3: Strain-induced energy shift of NiPS<sub>3</sub> photoluminescence on a 10 L suspended homostructure.** **a.** Zoom on the photoluminescence peak of NiPS<sub>3</sub> for various gate voltages between 0 and 80 V. The spectra plotted in colors ranging from yellow to red are acquired on the suspended flake, whereas those plotted in colors ranging from green to blue are acquired on a supported part of the flake, just above the drum, as shown in the inset of **b**. The photoluminescence of the strained drum is shifting towards lower energies while remaining identical for the supported part of the flake. **b.** Comparison of photoluminescence energy shifts as a function of increasing and decreasing gate voltages between suspended (orange and red) and supported (light and dark blue) spots on the sample. The solid lines are fits to the suspended photoluminescence energy shift with a model  $a_V V_{DC}^4$ , where  $a_V$  is a fitting parameter that is equal to  $-4.3 \times 10^{-9}$  meV/V<sup>4</sup> for increasing voltages and  $-4.0 \times 10^{-9}$  meV/V<sup>4</sup> for decreasing voltages. In the inset is shown an optical picture of the drum with squares indicating the measured suspended and supported spots, the scale bar is 2.5  $\mu$ m.

32 % and the linewidth increases of about 0.2 meV between 0 and 80 V. The data obtained for decreasing gate voltage are again overlapping with those measured for an increasing gate voltage, highlighting the reversibility of the strain-tuning. The intensity evolution fits quadratically, implying that the photoluminescence intensity is proportional to the membrane deflection  $\xi_0$ , which is also evolving as the gate voltage squared (see Sec. 3.1.2). On the other hand, the linewidth is slowly increasing until 60 V, where it rises sharply, probably due to inhomogeneous broadening. Indeed, the laser waist is probing a region of about 800 nm in diameter (see Sec. 1.3), in which, at high voltages, the stress is most likely non-uniform, leading to light emission with different energies. The acquired photoluminescence peak is then averaged over this non-uniform region resulting in a broadening of its linewidth.

To resolve spatially the effects of strain on NiPS<sub>3</sub> light emission, photoluminescence maps of the drum and its surroundings were performed at 0 V and 75 V. Each pixel of the maps corresponds to a parameter of the photoluminescence peak determined from the spectrum acquired at this given position. On Figure 4.5 the difference between the maps obtained at 75 V and those obtained at

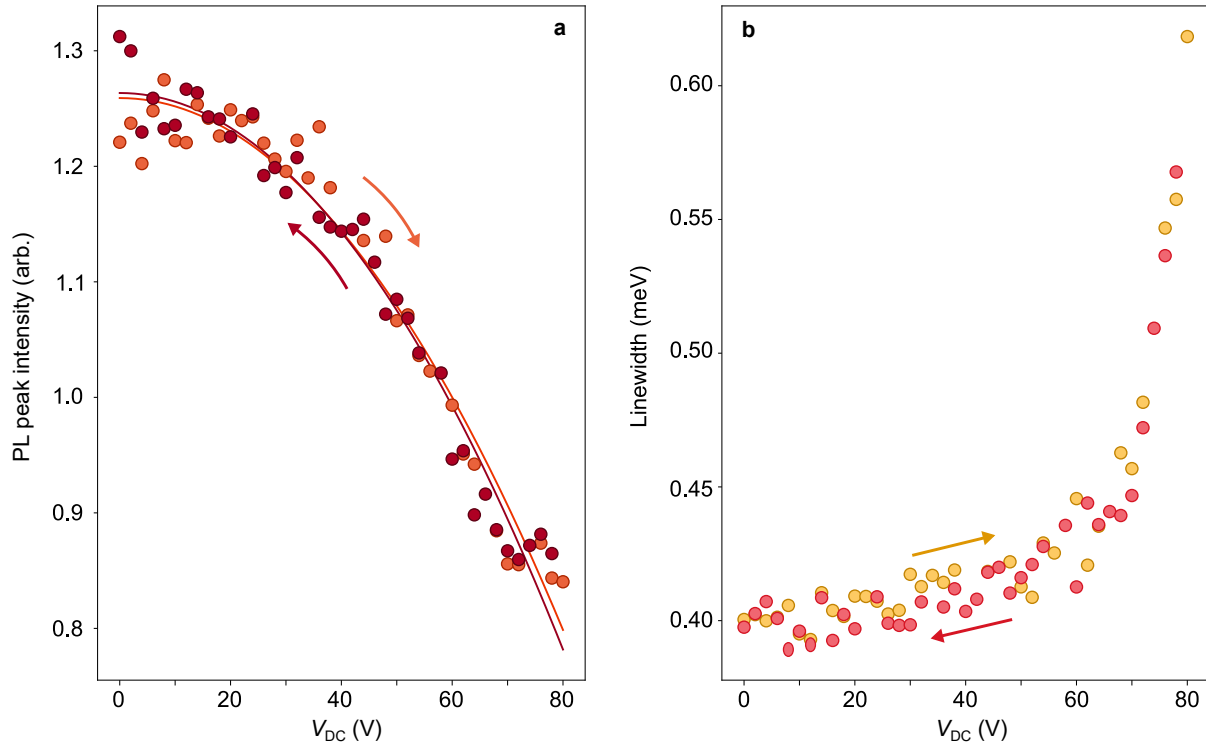


**Figure 4.4: Evolution of NiPS<sub>3</sub> photoluminescence intensity and linewidth with gate voltage on a 10 L suspended homostructure.** **a.** Fitted peak intensity as a function of increasing (orange) and decreasing (red) gate voltages. The solid lines are fits by a  $b_V V_{DC}^2 + c_V$  model where  $b_V$  and  $c_V$  are fitting parameters. **b.** Fitted peak linewidth as a function of increasing (yellow) and decreasing (coral) gate voltages.

0 V is displayed for the integrated PL intensity, the energy and the linewidth.

On both maps, we observe that the major variations arising from the increase of the gate voltage are located within the membrane region that is delimited by dashed circles. This confirms that these are mainly caused by the gate voltage-induced strain on the membrane. We also note that the shift of the parameters seems to be spilled out of the membrane. This is likely coming from the fact that the waist of the laser spot is still detecting part of the photoluminescence emitted by the membrane region even when it is located just next to it.

On the integrated photoluminescence map (see Fig. 4.5 a), we see that the maximum decrease of the peak intensity seems to be located towards the membrane center and that the reduction is rather continuous. This confirms a higher deflection at the membrane center, and is in good agreement with the observed reflectivity profile at 74 V in Section 3.1.2. We also note that there is a slight rise of the integrated photoluminescence on the supported part of the flake at 75 V. This might be due to doping effects and would require additional investigations.

Concerning the map of the photoluminescence energy, we see that the energy variations on the supported region are close to zero indicating a clear effect from strain at the origin of the photoluminescence energy reduction.

On the linewidth map, we note an increase of the linewidth in the lower half of the membrane, with a maximum value of 0.43 meV, which is the double of the values observed at the center. A broader linewidth could indicate a more inhomogeneous strain in this region. Indeed, we see in

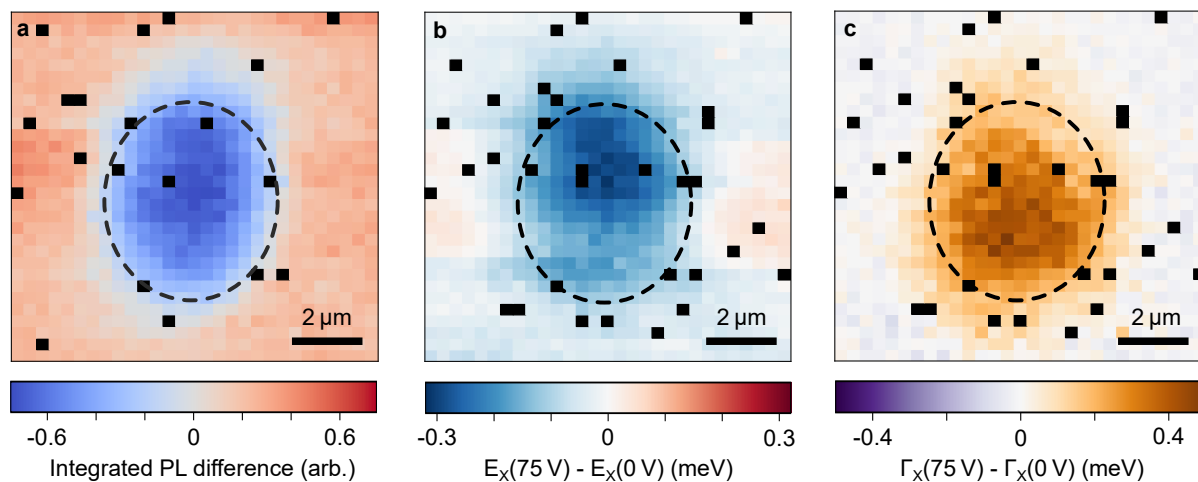


**Figure 4.5: Difference between spatial maps of the photoluminescence peak parameters at 75 and 0 V performed around the suspended part of the flake.** **a.** Difference between the integrated photoluminescence at 75 and 0 V. **b.** Difference between the peak X energy  $E_X$  at 75 and 0 V. **c.** Difference between the peak X linewidth  $\Gamma_X$  at 75 and 0 V. The dashed lines represent the membrane contour determined from the photodiode output voltage map measured simultaneously with the PL maps. The black pixels correspond to spectra made unusable due to cosmic rays spikes.

the same region of the energy map a band of a smaller decrease in energy separating two regions with a greater energy reduction, which could indicate a different strain in this area.

## 4.2.2 A non-trivial polarization dependence

The data from the previous part were acquired at a given analyzer angle, that was chosen for the photoluminescence intensity to be maximal. We will now investigate the orientation of the photoluminescence polarization on the same 10 L NiPS<sub>3</sub> sample (*Balor*, see Sample list 1.2.4), and its evolution with the position and gate voltage. We will first focus on the *drum 1*, which was the one studied in the strain-tuning part, then we will examine the polarization behavior on other spots on the sample.

### Determination of the photoluminescence polarization on drum 1

To identify the linear polarization direction of NiPS<sub>3</sub> light emission we use the protocol described in Section 4.1.1 that consists in collecting photoluminescence spectra for various analyzer angles. The results obtained at the center of drum 1 are shown on Figure 4.6.

The striking element, compared to what we observed on a bulk part of the same sample (see Figure 4.1 c,d) and to what has been reported previously in the literature [36, 37, 46], is the presence of a less intense second peak ( $X_2$ ) that is very close in energy to the most intense one ( $X_1$ ). Both peaks are detected at an analyzer angle of 185°, implying that we observe indeed two different peaks and not the shift in energy of only one peak (see Fig. 4.6 a). At analyzer angles of 125° and 210°, only one of the two peaks is visible, their behavior can therefore be studied separately.

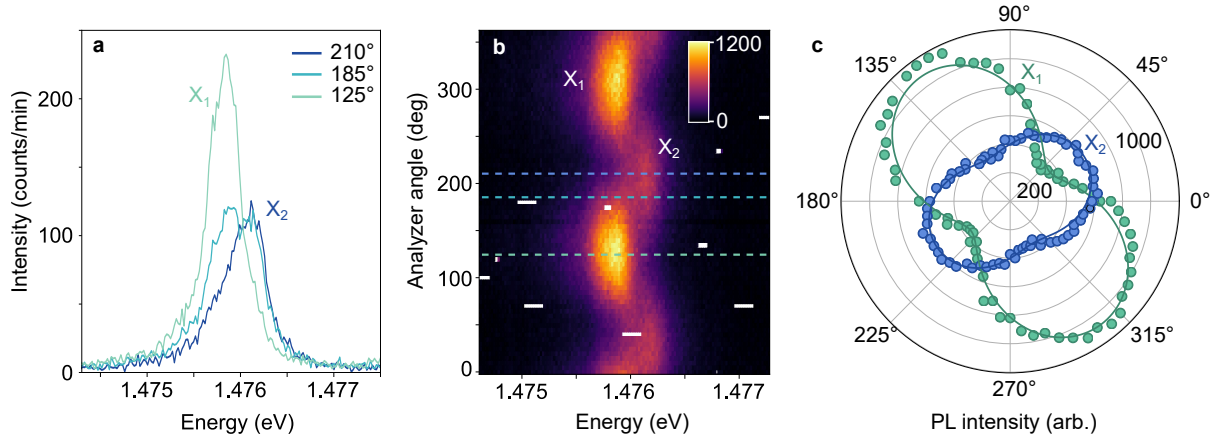


**Figure 4.6: Determination of a 10 L NiPS<sub>3</sub> light emission polarization on the *drum 1* of the sample *Balor* at 5.5 K.** **a.** NiPS<sub>3</sub> photoluminescence spectra for analyzer angles of 125°, 185° and 210°. We see two peaks, labeled X<sub>1</sub> and X<sub>2</sub>, that are both present for an analyzer angle of 185°, whereas only X<sub>1</sub>, X<sub>2</sub> is present at 125°, 210°, respectively. **b.** Photoluminescence spectra for various analyzer angles between 0 and 360°. The colorbar indicates the PL intensity in arbitrary units. The dashed lines indicate the location of the spectra shown in panel **a**. **c.** Polar plot of the maximum photoluminescence intensity in the range  $1.47583 \pm (2 \times 10^{-5})$  eV for X<sub>1</sub> (green) and  $1.47613 \pm (2 \times 10^{-5})$  eV for X<sub>2</sub> (blue). The dots correspond to the data and the solid line to a fit by the model  $I_1 \cos^2(\theta_A - \theta_0) + I_0$ , which gives a polarization angle of 127.1° for X<sub>1</sub> and 208.9° for X<sub>2</sub>.

The complete evolution of peaks X<sub>1</sub> and X<sub>2</sub> intensity with the analyzer angle is shown on Figure 4.6 **b**. Both peaks present two lobes separated by two extinctions, indicating that they are linearly polarized, with a polarization axis of 127.1° for X<sub>1</sub> and 208.9° for X<sub>2</sub> (see Fig. 4.6 **c**). The difference between the polarization angles of peaks X<sub>1</sub> and X<sub>2</sub> is then of about 81.8°. These two peaks with almost orthogonal polarization orientation were also observed on the other NiPS<sub>3</sub> suspended homostructure *Mordor*, which is of a similar thickness<sup>1</sup>.

### Spatial evolution of the polarization on drum 1

To get more insights on the spatial behavior of these two peaks we perform a photoluminescence map on and around *drum 1*. We acquired at the same location a photoluminescence spectrum at an analyzer angle of 140°, at which only peak X<sub>1</sub> is visible, and another one at an angle of 20° at which only peak X<sub>2</sub> is visible. The resulting maps for integrated photoluminescence, energy and linewidth are shown on Figure 4.7.

On the integrated photoluminescence map of the peak X<sub>1</sub> (see Fig. 4.7 **a**), we observe regions with different intensities. A variation of the photoluminescence intensity can be expected on the suspended region due to interference effects in the cavity, however the other regions indicate an inhomogeneity of the peak X<sub>1</sub> photoluminescence. On the optical image of the sample (see Sample list 1.2.4), the area around drum 1 seems to be free from defects or thickness variations, so these inhomogeneities do not arise from visible features on the flake.

<sup>1</sup> The crystal used to fabricate the sample *Mordor* was bought from 2D semiconductors whereas the one for making the sample *Balor* was provided by D. Voiry (see Section 1.2), ruling out a possible origin from the crystal source.

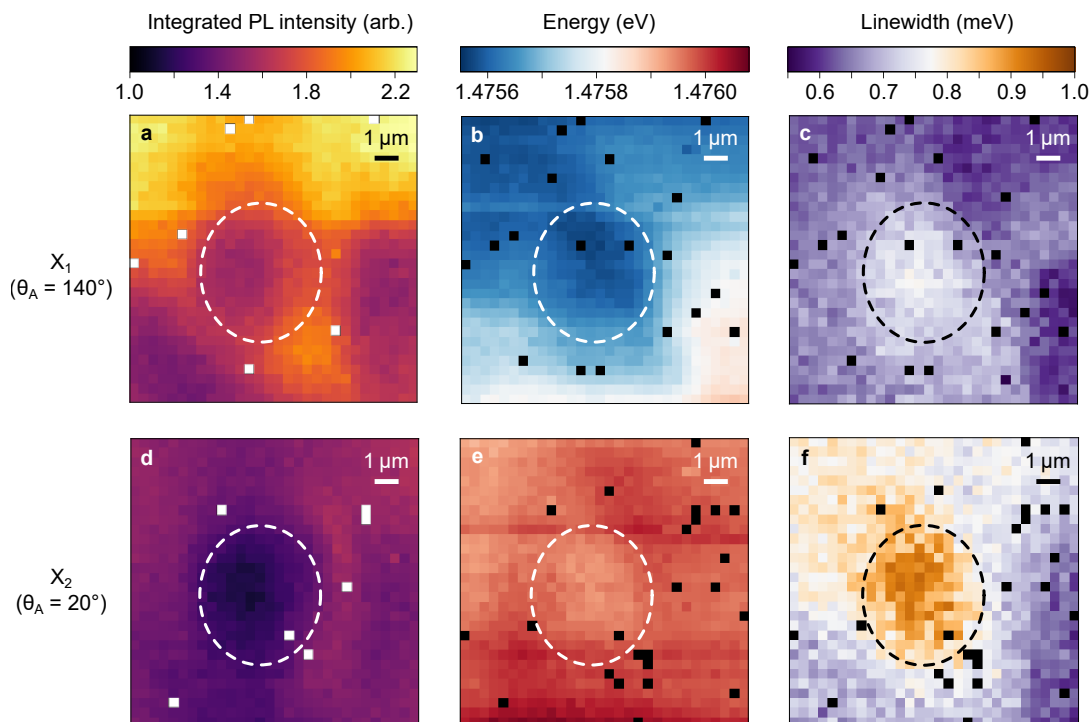


**Figure 4.7: Photoluminescence maps of peaks  $X_1$  and  $X_2$  around *drum 1*.** **a,d.** Integrated PL intensity map of peaks  $X_1$  and  $X_2$ , respectively. **b,e.** Energy map of peaks  $X_1$  and  $X_2$ , respectively. **c,f.** Linewidth map of peaks  $X_1$  and  $X_2$ , respectively. The colorbars are shared between the same mapped parameters of  $X_1$  and  $X_2$ . The value of  $\theta_A$  indicates the analyzer angle at which each map was performed. The dashed circles show the suspended area. The black and white pixels correspond to spectra made unusable due to cosmic rays spikes.

The photoluminescence intensity of  $X_2$  is lower than the one of peak  $X_1$  on the whole map (see Fig. 4.7 **d**), in agreement with what was observed on the polarization determination measurements (see Fig. 4.6). Contrary to  $X_1$  integrated intensity map, only the suspended region is darker, the rest being rather uniform. As a consequence, the two regions where the peak  $X_1$  presents a lower intensity appear clearly on the difference between these two maps (see Fig. 4.8 **a**). Actually, in those darker regions, the peaks  $X_1$  and  $X_2$  have almost the same intensity.

By looking at the photoluminescence energy map of the peak  $X_1$  (see Fig. 4.7 **b**), we note a higher energy in the same areas as those where the intensity was lower. Whereas, the energy of the peak  $X_2$  (see Fig. 4.7 **e**) is again more uniform over the map and has a higher value than the one of the peak  $X_1$ . On the energy difference map (see Fig. 4.8 **b**), we see clearly three regions that correspond to those visible on the integrated intensity map: one with a smaller energy variation of around 0.15 meV at the right of the map, a moderate variation of 0.23 meV in the bottom left region and a higher average variation of 0.33 meV on the rest of the map.

On the photoluminescence linewidth map of the peak  $X_2$  (see Fig. 4.7 **f**) we finally observe some variations related to the previously mentioned regions.  $X_2$  photoluminescence peak is broader on the hole and narrower in the bottom left and right areas in a pattern close to the one observed on the integrated intensity and energy maps of peak  $X_1$ . Whereas the linewidth map of peak  $X_1$  is more uniform (see Fig. 4.7 **c**) with also a slight broadening on the membrane and a narrower

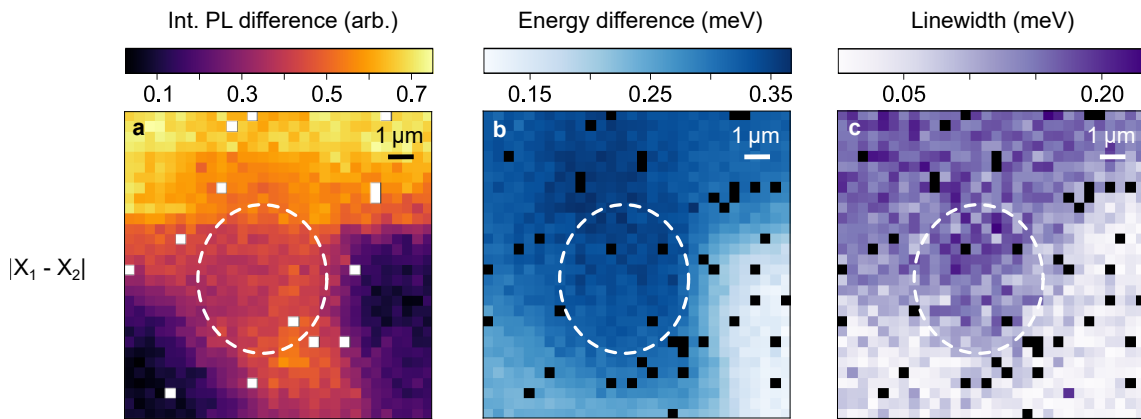


**Figure 4.8: Photoluminescence maps of the absolute value of the difference between the photoluminescence parameters of peaks  $X_1$  and  $X_2$ .** **a.** Integrated PL difference. **b.** Energy difference. **c.** Linewidth difference. The dashed circles show the suspended area. The black and white pixels correspond to spectra made unusable due to cosmic rays spikes.

region on the right of the map, but not on the bottom left. This translates in a more pronounced linewidth difference on the top region of the map including the hole area (see Fig. 4.8 c).

Two conclusions can be drawn from this spatially-resolved study. First, the peaks  $X_1$  and  $X_2$  do not have exactly the same behavior as a function of the position, implying that they are indeed distinct peaks that probably have a distinct origin. Then, three regions where the photoluminescence intensity, energy and linewidth are different can be identified. This inhomogeneity does not seem to result from features visible on the sample optical picture.

### Strain tuning of the light emission viewed along different polarization angles

The evolution of the photoluminescence as a function of strain discussed in Section 4.2.1 was acquired for a single analyzer angle of  $135^\circ$ . Here, we will investigate whether the previously observed behavior is preserved for different collection angles of NiPS<sub>3</sub> light emission.

For this, we perform the same measurement as presented on Figure 4.6 to determine NiPS<sub>3</sub> photoluminescence polarization direction, but for fewer analyzer angles, and reproduce it at various gate voltages between 0 and 80 V.

We first examine an eventual effect of the applied strain on the polarization direction of NiPS<sub>3</sub> photoluminescence (see Fig. 4.9 a). For these measurements we used a 600 gr/mm grating to reduce the acquisition time needed for one spectrum, whereas the measurement of Figure 4.6 was performed with a 1800 gr/mm grating. Reducing the number of the grating grooves induces a decrease in energy resolution, so that peaks  $X_1$  and  $X_2$  can no longer be isolated. We then plot the maximum intensity of the global photoluminescence comprising both peaks  $X_1$  and  $X_2$ , that is why we do not see any extinction. The photoluminescence polarization is then dominated by the one of the peak  $X_1$  that is the most intense. Within the  $20^\circ$  precision of this measurement,

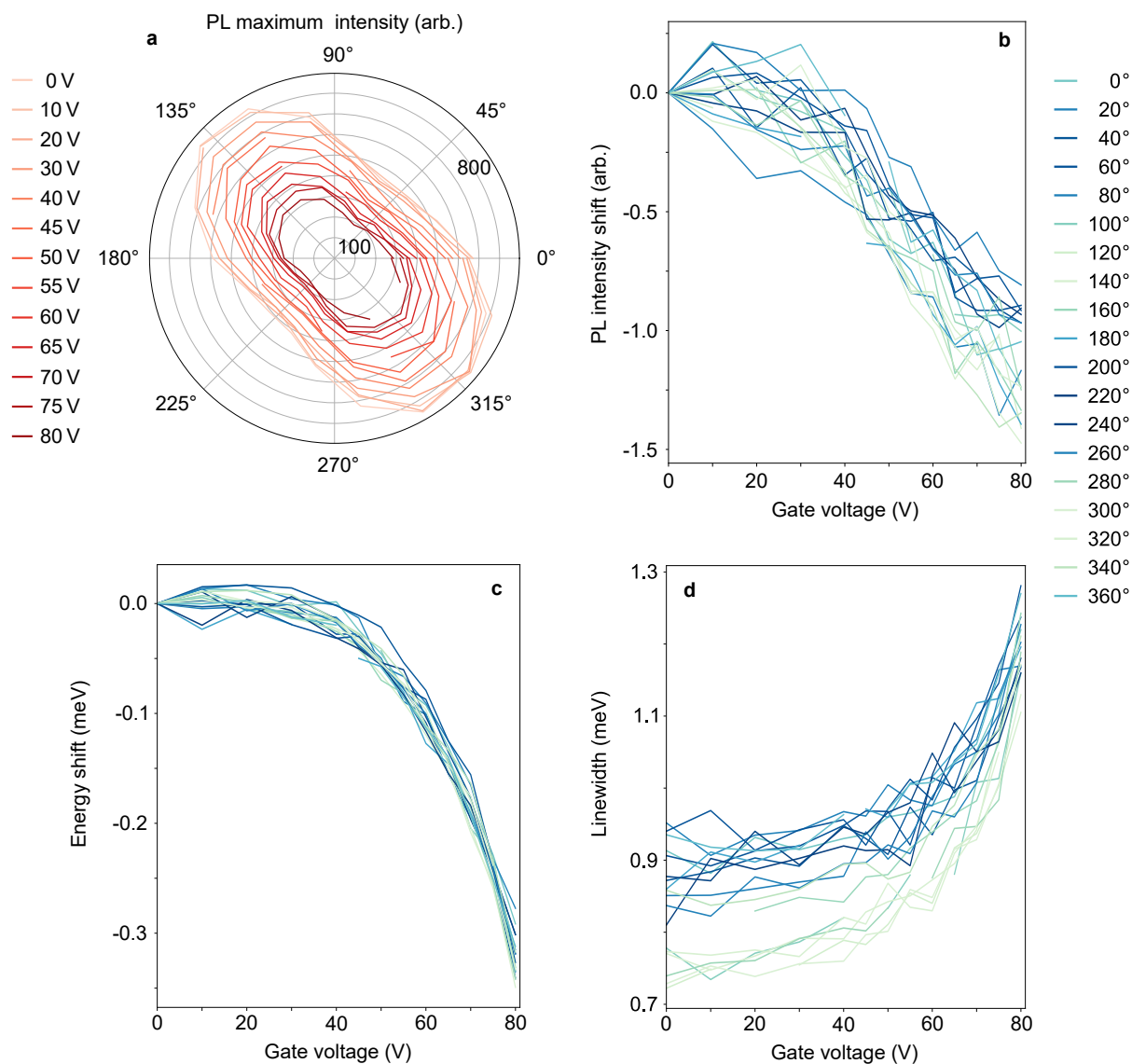


**Figure 4.9: Evolution of NiPS<sub>3</sub> photoluminescence with gate voltage for various emission angles.** **a.** Plot in polar coordinates of the photoluminescence maximum intensity as a function of the analyzer angle for gate voltages between 0 and 80 V. The peaks X<sub>1</sub> and X<sub>2</sub> cannot be separated in this measurement due to the use of a grating with less grooves inducing a lower resolution in energy. **b,c,d.** Shift of the photoluminescence intensity, shift of the photoluminescence energy and photoluminescence linewidth, respectively, as a function of the gate voltage for analyzer angles between 0 and 360°. The color code for these plots is built from the intensity evolution of the photoluminescence peak with the analyzer angle at 0 V. A more intense peak will result in a color close to the green and represents the peak X<sub>1</sub>, whereas a peak with lower intensity will result in a color close to the blue and represents the peak X<sub>2</sub>.

we observe no visible shift of the peak  $X_1$  polarization, that remains of around  $130^\circ$  across the entire gate voltage range. We note that the peak intensity decreases with gate voltage along all the directions of emission.

We now look at the evolution with increasing gate voltage of the photoluminescence parameters for various analyzer angles (see Fig. 4.9 b,c,d).

We observe that the photoluminescence intensities of peaks  $X_1$  and  $X_2$  as a function of the gate voltage (see Fig. 4.9 b) are following a similar behavior, that has been shown to be proportional to  $V_{DC}^2$  (see Sec. 4.2.1). However, the peak  $X_2$  intensity as a function of gate voltage decreases with a smoother slope than that of peak  $X_1$ , and so, reaches smaller intensity shifts. In the case of the photoluminescence energy shifts, all curves overlap quite well, indicating an evolution proportional to  $V_{DC}^4$  for all the emission angles (see Fig. 4.9 c). Finally, we observe that, as reported previously in this section, the peak  $X_2$  is initially broader than the peak  $X_1$ , but after 75 V, the linewidth of  $X_1$  increases more rapidly and reaches similar values to those of the peak  $X_2$  linewidth (see Fig. 4.9 d).

We can therefore conclude that NiPS<sub>3</sub> photoluminescence evolution with strain varies little according to the emission angle considered. Some weaker intensity and linewidth shifts are observed for the peak  $X_2$  compared to the ones of the peak  $X_1$ , that could be due to a different origin for these two peaks as already suggested by the spatially-resolved measurements. However, no significant change in the photoluminescence polarization with strain is reported.

### Polarization evolution at other spots on the sample

For now we studied exclusively NiPS<sub>3</sub> photoluminescence on and around the *drum 1* of the 10 L homostructure *Balor* (see Sample list 1.2.4). Actually, its polarization is not uniform over the whole sample. We will review here some other polarization directions spotted on different locations of the same sample.

In Figure 4.10, are shown the measurements of NiPS<sub>3</sub> photoluminescence as a function of the analyzer angle, and so, the determination of its polarization direction, at three spots on the sample. The data on the left (spot 1) have been acquired on the same flake as *drum 1* and *drum 2* but on a thicker region, where the photoluminescence signal is more intense (see Fig. 4.10 a,d). We therefore see clearly the peaks  $X_1$  and  $X_2$  that appear well separated,  $X_1$  still having a greater intensity than  $X_2$ . However, contrarily to what we measured on *drum 1*,  $X_1$  is polarized at  $80.2^\circ$  and  $X_2$  at  $150.2^\circ$ . The angle between the polarization axes of  $X_1$  and  $X_2$  is of  $70^\circ$  in this region. Since, the spot where this measurement was performed is quite far from *drum 1*, about  $25\ \mu\text{m}$  away, it could be that the crystalline orientation is different in this region. The magnetic order being aligned along the  $a$  crystalline axis, it would be oriented differently than on *drum 1*, and so would the photoluminescence polarization.

The data shown at the center (see Fig. 4.10 b,e) have been measured within a small region next to *drum 2* that might host defects since it is located near a crack (spot 2). It is the only area where we recorded a peak  $X_2$  almost as intense as  $X_1$ . We can therefore better resolve their

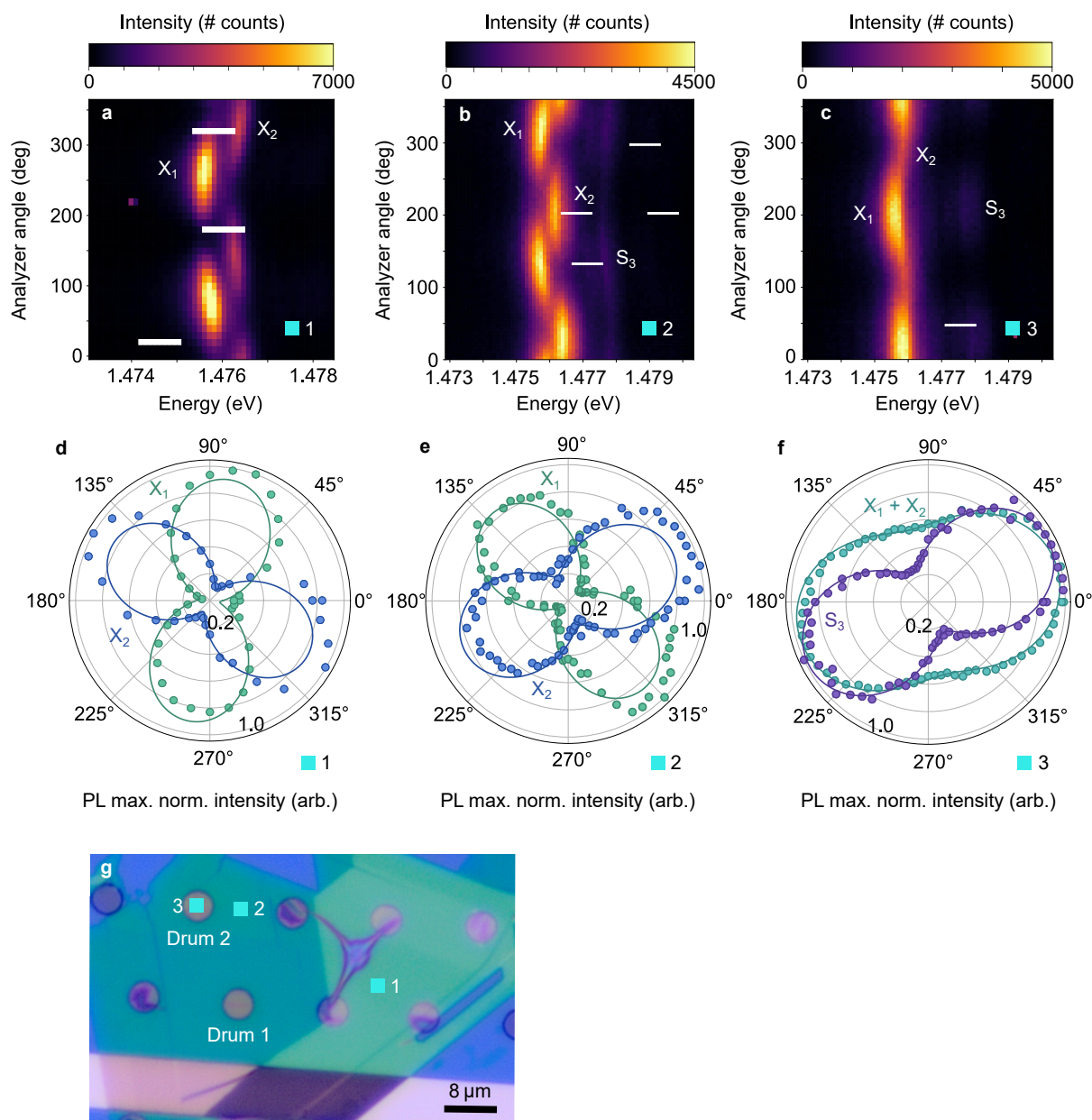


**Figure 4.10: NiPS<sub>3</sub> photoluminescence polarization at other spots in the sample *Balor*.** a-c. Photoluminescence spectra as a function of the analyzer angle. The polarization patterns of three peaks: X<sub>1</sub>, X<sub>2</sub> and S<sub>3</sub> can be observed. The white rectangles are masked pixels due to cosmic ray spikes. d-f. Plot in polar coordinates of the normalized maximum intensity of the peaks visible on the corresponding top panel. The dots correspond to the data and the solid line to a fit by the model  $I_1 \cos^2(\theta_A - \theta_0) + I_0$ . g. Optical picture of the sample indicating the measured spots: **1** is on a thicker region ( $\sim 20$  L) and **2**, **3** on a  $\sim 11$  L,  $\sim 12$  L, region, respectively.

respective polarizations, that are of 131.4° for peak X<sub>1</sub> and 205.0° for X<sub>2</sub>, resulting in angle of 73.6° between the two. These values are very close to the ones of 127.1° and 208.9° found on *drum 1*. We can then conclude that the photoluminescence polarization is the same in these two regions, despite a single layer difference in thickness. On the plot is also visible a peak of lower intensity labeled S<sub>3</sub>, whose polarization seems to follow that of X<sub>1</sub>.

The data displayed on the right are from a measurement performed at the center of *drum 2* (see Fig. 4.10 c,f). We note that the peaks X<sub>1</sub> and X<sub>2</sub> present very close energies in this region and appear almost like a single peak. We can then only determine their global polarization that is dominated by the one of the peak X<sub>1</sub> and equals to 193.6°. The polarization of X<sub>1</sub> on *drum 2* is shifted by 62.2° compared to the one on the spot previously mentioned that is located only about 5 μm below *drum 2*. A single layer thickness difference between these two regions could explain the change in the emission orientation, but this same single-layer difference did not induce any modification between *drum 1* and the region close to a crack (spot 2). Nevertheless, from these results, we deduce that the Néel vector is oriented differently between *drum 1* and *drum 2*. We can, additionally, determine the polarization of the peak S<sub>3</sub>, also visible on *drum 2*, that is of 208.1°.

From these observations, we report that the peaks X<sub>1</sub> and X<sub>2</sub> are polarized differently over the sample. Since the photoluminescence polarization should be orthogonal to the Néel vector, indicating the magnetic order orientation (see Sec. 4.1.1), this implies that there are several Néel vector orientations within the sample, and so, magnetic domains.

The 62.2° angle between two observed polarizations of the peak X<sub>1</sub> is corresponding to the angle between NiPS<sub>3</sub> zigzag axes, and so, between the spin chains mentioned in Section 1.1.2. The Néel vector would then be oriented along a different spin chain direction on *drum 1* and *drum 2* resulting in magnetic domains, that will be spatially resolved in the next section.

We also noticed on the photoluminescence spectra a third peak with a weak intensity, that we labeled S<sub>3</sub>, located near, and on, *drum 2*. Some satellite peaks in the same energy range have already been reported in the literature [36, 202], presenting a behavior similar to the one of peak X<sub>1</sub>.

Finally, we saw that the energy shift between X<sub>1</sub> and X<sub>2</sub> can vary according to the position on the sample, as already shown in the subsection 4.2.2. Also, we observed that the angle between the polarization directions of X<sub>1</sub> and X<sub>2</sub> range from about 70 to 80°.

### Discussion on the origins of peaks X<sub>1</sub> and X<sub>2</sub>

Knowing that the polarization of the photoluminescence has been reported to be orthogonal to the Néel vector orientation, a first possibility is that the peaks X<sub>1</sub> and X<sub>2</sub> could arise from two coexisting magnetic order directions. However, the measured angles between X<sub>1</sub> and X<sub>2</sub> polarization directions are of 70°, 73.6° and 81.8° which is far from the 60° expected from NiPS<sub>3</sub> nematicity (see Sec. 1.1.2). Moreover, in the case of coexisting spin chains with different

magnetic orientations, we could expect that one orientation will result in a light emission at a given energy  $E_{X_i}$  and that the intensity of this emission would be related to the number of spins oriented in this direction. But, what we observe is that the most intense peak  $X_1$  is still the one with the lowest energy, no matter the orientation of its polarization. To investigate more on this hypothesis it would be interesting to monitor the behavior of these two peaks under a magnetic field.

Another possibility would be that the peaks  $X_1$  and  $X_2$  are originating from two different transitions very close in energy, that could be, for example, two  $d-d$  transitions, since no additional transition seems to be predicted by the Zhang-Rice model. The fully polarized peak in the bulk could be explained by the fact that the transition from which  $X_1$  originates would be more favorable in the bulk, while the transition  $X_2$  would be least favorable. The thin bulk case would be a transition regime where both transitions are allowed and visible, with still  $X_1$  being the more efficient. Finally, for flakes below six layers only  $X_2$  would be favorable (see Fig. 4.1 b).

## 4.3 Identification of magnetic domains and characterization of a satellite peak

### 4.3.1 Imaging magnetic domains

#### Photoluminescence mapping of the main peak

To spatially resolve the presumed magnetic domains, we perform photoluminescence maps of a large sample area including *drum 1* and *drum 2*. Three maps were acquired for three analyzer angles separated by 60° each, to cover the three possible orientations of the magnetic order in NiPS<sub>3</sub> (see Sec. 1.1.2). Considering the polarization directions of the photoluminescence peaks previously observed on the sample (see Fig. 4.10), the angles 20°, 80° and 140° were chosen.

The integrated photoluminescence intensity maps of the peak X, that correspond to the integration over an energy range comprising both X<sub>1</sub> and X<sub>2</sub>, are shown in Figure 4.11 c-e. Since the energy shift between X<sub>1</sub> and X<sub>2</sub> is depending on the position on the sample as shown in Subsection 4.2.2, we would not be able to separate their respective contributions over the whole map. The intensity of the peak X will be dominated by that of the peak X<sub>1</sub> that is the highest, except in areas with defects. Since the peak X<sub>2</sub> is also taken into account, we will not observe an extinction of the peak X but only a decrease in intensity at analyzer angles where X<sub>1</sub> is not present.

By looking carefully at the maps, four regions, highlighted in Figure 4.11 d, seem to emerge.

The region **1**, including *drum 1*, has its highest intensity at an angle of 140°, meaning that its polarization direction is close from this angle. This is coherent with the 127° polarization angle observed on *drum 1*.

The region **2**, however, does not appear to have a well defined polarization, likely because both peaks X<sub>1</sub> and X<sub>2</sub> have similar intensities.

The region **3**, comprising *drum 2*, presents a clear polarization close to 20°, which is in good agreement with the polarization of 13.9° determined previously on *drum 2*.

Finally, the region **4** is crossed by several cracks resulting in a quite weak and inhomogeneous photoluminescence. The suspended area, that undergoes a significant pre-strain (see Fig. 4.11 b), shows a low intensity, with a polarization angle close to 80°, whereas the rest of the area seems to have a polarization angle closer to 140°. It is in this region that the measurement of Figure 4.10 b, where X<sub>1</sub> and X<sub>2</sub> have a similar intensity, has been acquired, confirming a photoluminescence polarization along 131°.

The origin of these regions could be partially explained by the different thicknesses of NiPS<sub>3</sub> present on the sample (see Fig. 4.11 b). This can be the most clearly seen on the map acquired at a 20° analyzer angle (see Fig. 4.11 c), where we can distinguish the separation between the 10-layer region from the two others. However, no visible feature on the optical picture of the sample could predict the separation between regions **1** and **2**.

The photoluminescence presents a different polarization in regions **1** and **3**, the region **1** being

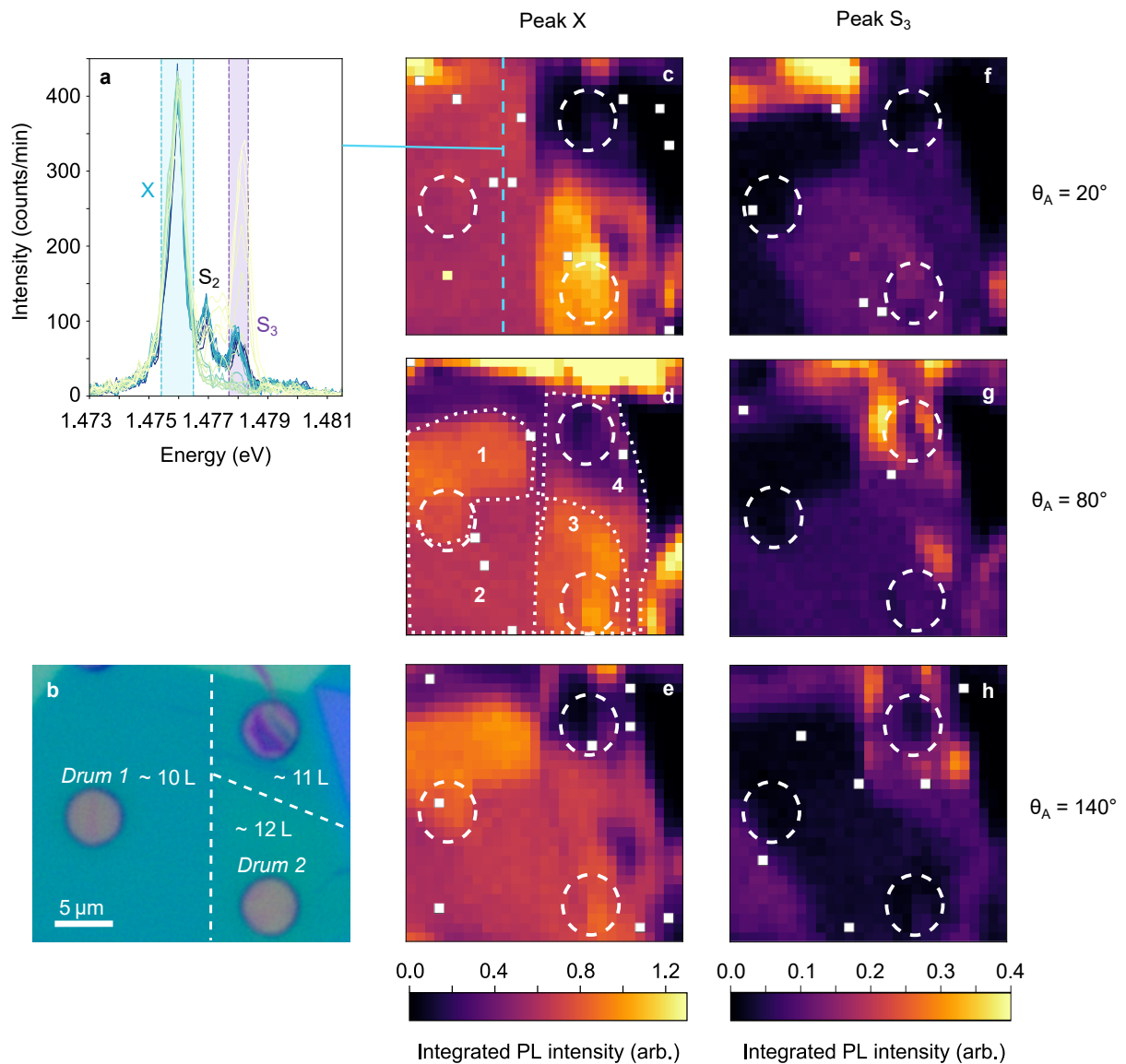


**Figure 4.11: Integrated photoluminescence maps of the sample *Balor* for analyzer angles 60 degrees apart.** **a.** Photoluminescence spectra acquired for an analyzer angle of  $20^\circ$  along the blue dashed line indicated in the panel **c**. The colored rectangles indicate the energy range used for the photoluminescence integration. **b.** Optical picture of the sample corresponding to the mapped region. The dashed lines separate the regions with different thicknesses. **c-e.** Integrated photoluminescence maps of the peak **X** for analyzer angles  $\theta_A$  of  $20^\circ$ ,  $80^\circ$  and  $140^\circ$ , respectively. In panel **d** are highlighted and numbered four roughly homogeneous regions that emerge from these maps. **f-h.** Integrated photoluminescence maps of the peak **S<sub>3</sub>** for analyzer angles  $\theta_A$  of  $20^\circ$ ,  $80^\circ$  and  $140^\circ$ , respectively. The dashed circles represent the position of the 5 μm in diameter drums on the sample.

invisible for a polarizer angle of 20°, while region **3** cannot be seen at 140°. The polarization direction of NiPS<sub>3</sub> photoluminescence having been reported to be perpendicular to the Néel vector in several papers [38, 43, 44, 46], we could then consider these regions as magnetic domains. Nevertheless, we will provide further confirmation of the link between the photoluminescence orientation and magnetic order thanks to Raman spectroscopy.

### Confirmation of the domains orientation by Raman spectroscopy

We have demonstrated in Section 2.2.2 that the NiPS<sub>3</sub> Raman modes  $A_g^2$  and  $B_g^2$  are sensitive to magnetic order. We will now compare their polarization dependence to the one of NiPS<sub>3</sub> photoluminescence, in order to support our findings on the different orientations of NiPS<sub>3</sub> spin chains in *drum 1* and *drum 2* of the sample *Balor* (see Sample list 1.2.4). This approach has been initiated by Kim *et al.* [38] in 2023 and has been successfully employed in recent papers [43, 205].

We perform linear polarization-resolved Raman spectroscopy measurements by varying simultaneously the angles of the incident and collected light to reveal a four-fold symmetry of Raman modes (see Fig. 4.12 a-c, f-h).

We first note that the modes  $A_g^2$  and  $B_g^2$  are polarized at 45° from one another, which is consistent with their opposite symmetry properties (see Sec. 1.4.2).

As shown previously (see Sec. 4.2.2), the photoluminescence on *drum 1* is polarized at an angle of about 127°, implying that the Néel vector, represented by an orange arrow, is oriented orthogonal to it at an angle of around 37° (see Fig. 4.12 d). We see that this Néel vector axis is corresponding to a polarization axis of the Raman mode  $B_g^2$ , and so, to the direction of a minimum in intensity of the mode  $A_g^2$  (see Fig. 4.12 a,b). The polarization of the modes  $A_g^6$  and  $A_g^7$ , which do not involve nickel atoms displacement and are not depending on the magnetic order (see Sec. 1.4.4), is different from the one of the  $A_g^2$  mode and is not linked to the Néel vector direction (see Fig. 4.12 c).

On *drum 2*, since the contribution from the peak  $X_2$  to the photoluminescence emission makes difficult the determination of the direction orthogonal to  $X_1$  polarization axis, we will consider that  $X_1$  has the same polarization as the one of the satellite peak  $S_3$ , that is of 28° (see Fig. 4.10 c,f). We thus obtain a Néel vector oriented at an angle of 118° (see Fig. 4.9 i). Again, we observe a very good agreement between the Néel vector orientation estimated from the photoluminescence polarization and a polarization axis of the  $B_g^2$  Raman mode (see Fig. 4.9 g), as well as a minimum of intensity of the  $A_g^2$  mode (see Fig. 4.9 f).

By comparing the polarization of the Raman modes on *drum 1* and *drum 2*, we see that the  $A_g^6$  and  $A_g^7$  polarizations are preserved, indicating a conservation of the crystalline axis orientation. Whereas the polarization directions of the modes  $A_g^2$  and  $B_g^2$  are rotated between *drums 1* and *2* to follow the magnetic order direction. This indicates clearly that the regions **1** and **3** of the photoluminescence integrated intensity maps (see Fig 4.11 d) present different spin chains orientations, and so, correspond to two antiferromagnetic domains. However, the angle between

### 4.3. Identification of magnetic domains and characterization of a satellite peak

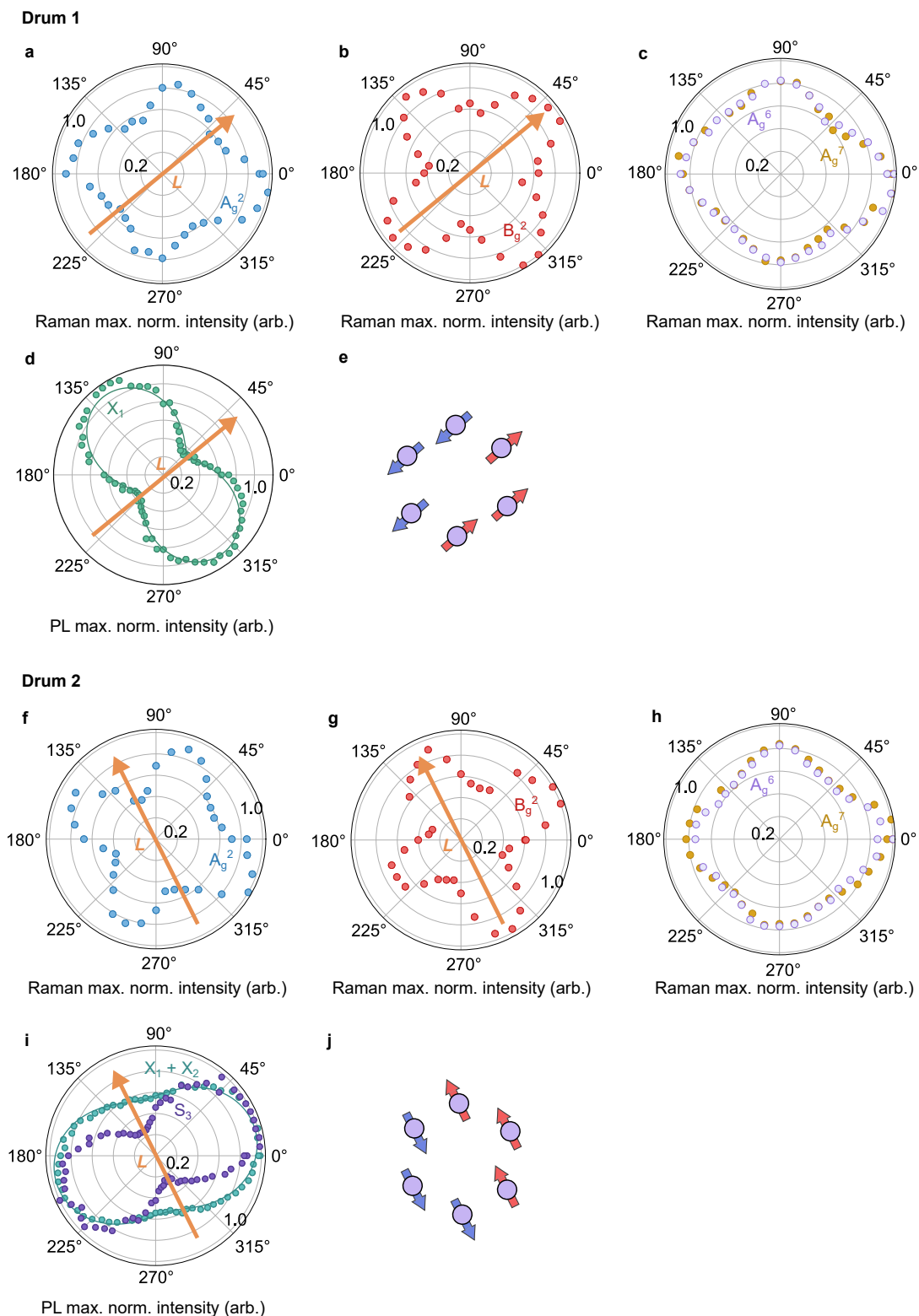


**Figure 4.12: Determination of  $\text{NiPS}_3$  spin chains orientation using both Raman and photoluminescence spectroscopies on *drum 1* and *drum 2* of the sample *Balor*.** The panels **a-e**, **f-j** are showing measurements on *drum 1*, *drum 2*, respectively. **a-c**, **f-h**. Plot in polar coordinates of the maximum normalized intensity as a function of equal polarizer and analyzer angles, which are simultaneously varied, for the Raman modes  $A_g^2$ ,  $B_g^2$  and both  $A_g^6$  and  $A_g^7$ , respectively. **d**, **i**. Polar plot of the maximum normalized intensity of the photoluminescence as a function of the analyzer angle. **e**, **j**. Scheme of a  $\text{NiPS}_3$  hexagonal unit displaying only the nickel atoms, that illustrates the derived spin chains orientation. The orange arrows represent the Néel vector  $L$  direction.

the estimated Néel vectors for these domains is of about 81°, which is far from the expected 60° angle between two spin chains orientations. This discrepancy cannot be explained by experimental uncertainties and would need further investigations on more spots on these domains and on additional samples.

### 4.3.2 Exploration of satellite peak S<sub>3</sub> behavior

Satellite peaks of the main photoluminescence peak have already been reported in the literature, presenting a lower intensity than the main peak and energies ranging from 1.4765 to 1.4790 eV [36, 38, 202]. Usually, one to three of them are observed with some small energy variations, but their behavior was not studied in details and assimilated to that of the peak X.

On the 10-layer NiPS<sub>3</sub> sample *Balor* (see Sample list 1.2.4) we mainly observed two satellite peaks that we labeled S<sub>2</sub> and S<sub>3</sub> (see Fig. 4.11 a) with energies of about 1.4763 and 1.4779 eV. We also detected two other peaks that are mainly located in regions with defects. For the sake of clarity, we will focus only on the peak S<sub>3</sub>, which has the most homogeneous spatial distribution on the sample.

#### Photoluminescence mapping

We go back to the photoluminescence maps performed at three different analyzer angles 60 degrees apart and integrated over the energy range 1.47759-1.47828 eV in which the peak S<sub>3</sub> is present (see Fig. 4.11 f-h).

The striking element of these maps is that the peak S<sub>3</sub> is absent from the region **1** for all the collection polarizations considered. This is very intriguing, and cannot be due to the magnetic order orientation in this region, since part of region **4**, where S<sub>3</sub> is present, is oriented along the same axis as region **1**. Moreover, we observe that the peak S<sub>3</sub> has not the same polarization in the whole region **2**, that appears to be structured in two sub-regions which is not visible on the peak X maps. Since we do not know if the peak S<sub>3</sub> is linked to the magnetic order we cannot conclude about the division of the region in magnetic domains.

Further measurements on other samples need to be performed to check for a similar absence of satellite peaks at specific locations and draw conclusions about its cause. These observations demonstrate that studying satellites peaks can provide complementary information on NiPS<sub>3</sub> photoluminescence and its spatial dependence.

#### Evolution with strain

Since the peak S<sub>3</sub> is present on *drum 2*, whereas it was absent on *drum 1*, we can now study its evolution with DC gate voltage by monitoring the photoluminescence in *drum 2* from 0 to 80 V (see Fig. 4.13).

On the photoluminescence spectra shown in the inset of Figure 4.13 a, both the intensity and energy of peaks X<sub>1</sub> and S<sub>3</sub> are decreasing with increasing DC gate voltage, which was also

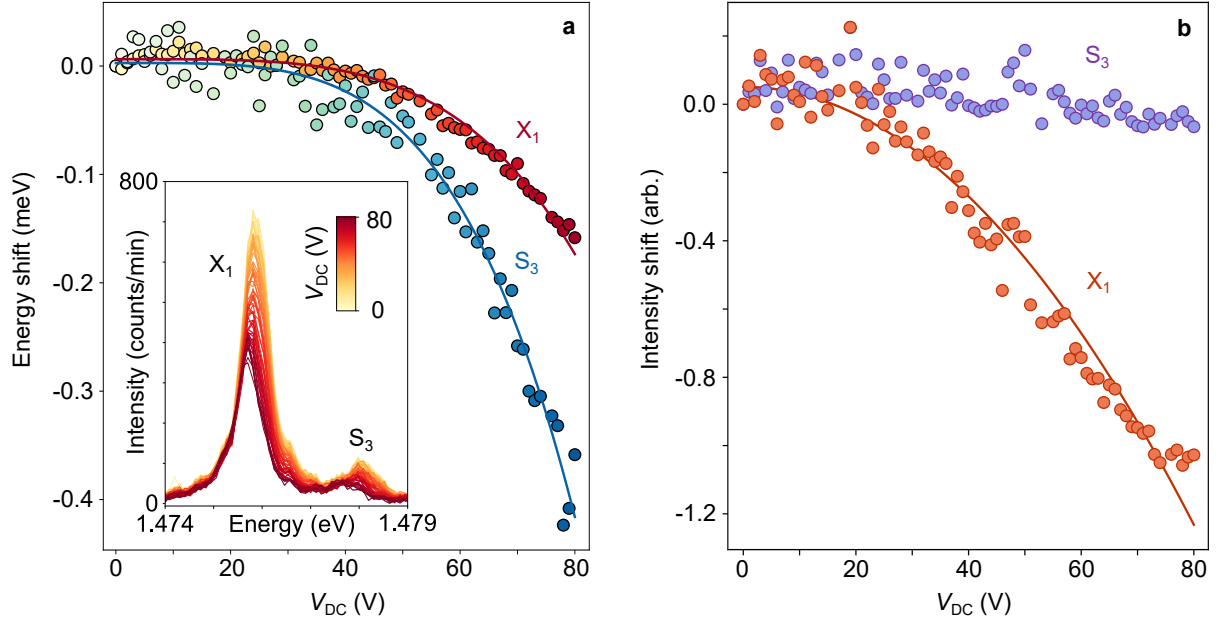


**Figure 4.13: Comparison of the photoluminescence evolution with gate voltage for  $X_1$  and  $S_3$  peaks on *drum 2* of the  $\text{NiPS}_3$  sample *Balor*.** **a.** Energy shift of the photoluminescence as a function of gate voltage  $V_{DC}$  for peaks  $X_1$  (yellow to red) and  $S_3$  (green to blue). The data represented by dots are fitted by a model  $a_V V_{DC}^4$  shown as solid lines with  $a_{V,2} = -4 \times 10^{-9} \text{ meV/V}^{-4}$  for  $X_1$  and  $a_{V,3} = -1 \times 10^{-8} \text{ meV/V}^{-4}$  for  $S_3$ . In the inset are displayed the corresponding spectra showing the evolution of peaks  $X_1$  and  $S_3$  for gate voltage ranging from 0 to 80 V. **b.** Intensity shift as a function of gate voltage for peaks  $X_1$  (orange) and  $S_3$  (mauve). The data of the peak  $X_1$  are fitted by a  $b_V V_{DC}^2$  model, where  $b_{V,2} = -2.0 \times 10^{-4} \text{ V}^{-2}$ .

observed for the peak  $X_1$  on *drum 1* (see Fig. 4.3). The energy shifts result in a maximum energy decrease of 0.16 meV for the peak  $X_1$  at 80 V on *drum 2*. This is a little lower than the 0.18 meV energy shift measured on *drum 1*, but still consistent. However, the energy shift of peak  $S_3$  reaches the value of -0.41 meV at 79 V, that is more than the double of the peak  $X_1$  energy shift. We note that, as for *drum 1*, the photoluminescence energy shifts are well fitted by a model proportional to  $V_{DC}^4$ , indicating that they are proportional to the gate-induced strain (see Sec. 4.2.1). We can then deduce a energy shift with strain of  $\Delta_\varepsilon(S_3) \simeq 2.4 \text{ meV}/\%$  for the peak  $S_3$ .

On the other hand, the intensity shift of  $X_1$  follows a model proportional to  $V_{DC}^2$  (see Fig. 4.13 b) implying that it is proportional to the membrane gate-induced deflection (see Sec. 4.2.1), except at the highest voltages where it seems to saturate, which is consistent with inhomogeneous broadening. This effect was also visible on *drum 1* photoluminescence intensity shift. On the other hand, the intensity shift of  $S_3$  shows only a slight decrease that cannot be fitted by a DC gate voltage squared model.

To sum up, the evolution of photoluminescence peak  $X_1$  with DC gate voltage on *drum 2* is very similar to what was observed for the same peak on *drum 1*. Meanwhile, we demonstrated that the satellite peak  $S_3$  exhibits a different strain-dependent behavior to that of the peak  $X_1$ , characterized by a greater energy shift. These disparities between peaks  $X_1$  and  $S_3$  suggest that they might not have exactly the same origin.

## Chapter conclusion

In this Chapter, we investigated NiPS<sub>3</sub> intriguing light emission properties as a function of spatial position and gate-induced strain on a 10-layer sample (*Balor*, see Sample list 1.2.4) comprising two nanodrums, labeled *drum 1* and *drum 2*.

We first studied the photoluminescence evolution under DC gate voltage on *drum 1* and reported the following results:

- the energy shift is evolving as the fourth power of the gate voltage, and so, is proportional to the induced in-plane strain (see Eqs. 3.13 and 3.6)
- photoluminescence maps showed that the modifications of the photoluminescence properties are localized on the suspended region, proving that those are mainly caused by the applied strain (see Sec. 4.2.1)
- the photoluminescence energy is decreased of about 0.18 meV for a 80 V increase in gate voltage, which corresponds to a induced strain of around 0.17 % (see Sec. 4.2.1)
- no measurable changes of the photoluminescence linear polarization direction with strain were observed (see Sec. 4.2.2)

Then, we went on to determine the linear polarization direction of NiPS<sub>3</sub> photoluminescence and observed that the main photoluminescence peak X is in fact composed of two sub-peaks, that we labeled X<sub>1</sub> and X<sub>2</sub>. We compared the characteristics of these two peaks and made various observations:

- X<sub>1</sub> and X<sub>2</sub> have different polarization directions oriented at about 80° to each other (see Sec. 4.2.2)
- their respective intensities, energies and linewidths show distinct spatial dependencies, determined from photoluminescence maps (see Sec. 4.2.2)
- their separation in energy is not uniform over the sample (see Sec. 4.2.2)

In the last Section of this Chapter, we performed photoluminescence maps on a larger region of the sample, for three polarizations of the collected light at angles 60° apart, to match the three possible orientations of NiPS<sub>3</sub> magnetic spin chains (see Sec. 4.3.1) and obtained the following outcomes:

- several regions presenting a different photoluminescence polarization were observed, which are likely arising from the different thicknesses present on the sample, but also from pre-strain, since some flakes with the same thickness are showing more than one region (see Sec. 4.3.1)

- two of these regions could be assigned to antiferromagnetic domains, whose magnetic spin chains orientations were determined thanks to the consistency between the polarization of the photoluminescence peak X and that of the Raman modes  $A_g^2$  and  $B_g^2$  which are sensitive to the magnetic order (see Sec. 2.2.2)
- an angle of about  $81^\circ$  was reported between the two Néel vectors of these domains instead of the  $60^\circ$  expected, inviting to additional measurements on other samples to get a better understanding of this result

We finally investigated the behavior of the satellite peak  $S_3$ , observed at an energy of about 1.4 meV above that of the peak X, by two approaches:

- we performed photoluminescence maps, which were displaying the same regions than that of peak X, however the satellite peak  $S_3$  appears to be absent in one of these regions, and shows a different polarization dependence in another one
- we studied the response of peak  $S_3$  to an applied gate voltage, demonstrating that its energy shift is also proportional to the induced strain, but with a steeper decrease than the one of peak X (see Sec. 4.3.2)

These observations indicate that the peak  $S_3$  has not exactly the same origin as that of the peak X. Its study can then bring complementary information, notably in the view of the photoluminescence strain-tuning, inviting us to pursue the exploration of these satellite peaks properties.

In order to get more insight into NiPS<sub>3</sub> photoluminescence origins from our results, we could check notably two points: how the strain should be affecting the energy and intensity of the photoluminescence according to a given model (Zhang-Rice triplet to singlet transition, *d-d* transition, structural defects, see Sec. 4.1.2) and if the model is predicting some additional emission peaks that could correspond to  $X_2$  or to the satellite peaks.

Concerning the Zhang-Rice exciton hypothesis, we could intuit that, since the strain is increasing the lattice constant, it would result in a weaker overlap between the metal and ligands orbitals, and so, a decrease of the photoluminescence intensity, that is coherent with our observations. Also, if we consider coexisting magnetic spin chains with different orientations, this would result in two dipoles oriented orthogonally to the spin chains, translating into photoluminescence peaks with different polarizations, that could correspond to  $X_1$  and  $X_2$ . However, we cannot guess if the energies of these peaks would be shifted in relation to each other. Moreover, there is no prediction concerning the satellite peaks in the currently proposed model.

In the case of the sulfur vacancies hypothesis, a modeling of the effect of strain on the energy and intensity of the localized exciton would be needed to reach a conclusion. Nevertheless, we could think of the satellite peaks as other phonon sidebands since those are supposed to follow the polarization of the main peak, which seem to be the case in our measurements [38] (see Fig. 4.10).

---

# Conclusion & perspectives

---

## Conclusion

In this manuscript, we have investigated drum-like resonators made of suspended homo- and heterostructures embedding few-layer magnetic van der Waals materials, namely FePS<sub>3</sub> and NiPS<sub>3</sub>, as a versatile platform to explore the interplay between their mechanical and magnetic properties.

In Chapter 1, we have demonstrated our ability to nano-fabricate few-layer suspended samples made of magnetic van der Waals materials. A sophisticated suspended heterostructure constituted of four different materials was even realized, notably thanks to a lab-built motorized transfer station.

In Chapter 2, we achieved the detection of magnetic phase transitions in suspended magnetic van der Waals materials. A key to this success was the automatized correction of the spatial drift induced during the temperature ramps, that allowed us to perform autonomous measurements over several days. We first probed the magnetic phase transition of a five-layer FePS<sub>3</sub> flake embedded in a heterostructure by combining two methods, one based on Raman spectroscopy, the other on nanomechanical measurements, developed separately in the case of bare FePS<sub>3</sub> [14, 26]. Then, we reported the detection of a magnetic phase transition on two NiPS<sub>3</sub> suspended homostructures, of approximately 10 and 13 layers, by nanomechanical measurements. The magnetic phase transition was confirmed on the same samples by Raman spectroscopy. The Néel temperatures obtained by the two approaches are in good agreement for both materials, demonstrating the robustness of these methods to probe magnetic phase transitions in suspended magnetic van der Waals materials.

In Chapter 3, we presented our first results towards the control by strain of magnetic properties in suspended magnetic van der Waals materials. We reported a decrease of NiPS<sub>3</sub> Néel temperature of about 3 K probed by nanomechanical measurements for an induced radial strain estimated at around 0.02 %.

We also documented the effects of an increase of the electrostatic force applied on the FePS<sub>3</sub>-based van der Waals heterostructure via the DC gate voltage. We observed abrupt discontinuities in the nano-resonator frequency evolution with gate voltage, which were presenting a hysteretic

---

behavior for reversed voltage sweeps and were reproducible. These discontinuities translate into drastic modifications of the spatial profiles of the mechanical modes. We concluded that these features could be attributed either to a redistribution of a high initial pre-strain or to a delamination of two layers composing the heterostructure.

In Chapter 4, we explored NiPS<sub>3</sub> light emission that is assumed to be correlated with the magnetic order [38, 39, 44]. We demonstrated a strain-tuning of the photoluminescence energy of about 1 meV/%. We also imaged magnetic domains, thanks to the orthogonality between the photoluminescence polarization and the magnetic order direction, whose orientations were confirmed by Raman spectroscopy. Additionally, we have observed secondary peaks in the photoluminescence spectrum, whose behaviors as a function of strain and position have been shown to differ from those of the main peak. These observations could shed new light on NiPS<sub>3</sub> photoluminescence origins that are still debated.

From this work, we have succeeded in probing the magnetic properties, and paved the way towards their control, in magnetic drum-like nano-resonators. There are still many paths to explore and degrees of freedom to exploit on these very rich systems, notably by getting closer from their two-dimensional limit.

## Perspectives

### Thickness dependence of NiPS<sub>3</sub> photoluminescence

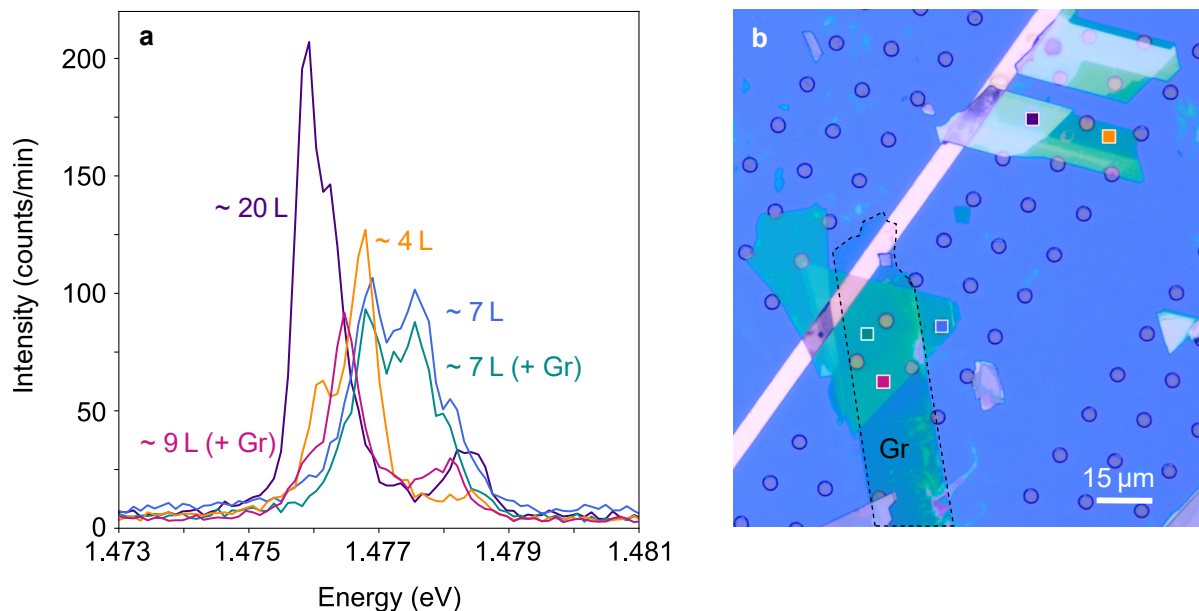


**Figure 4.14: NiPS<sub>3</sub> photoluminescence spectra as a function of the layer number and position on a NiPS<sub>3</sub>/graphene sample.** **a.** Linearly-polarized photoluminescence spectra for various spots presenting different thicknesses. **b.** Optical picture of the corresponding sample. The dashed line indicates a 3 layer graphene flake (Gr). The colored squares show the locations where the spectra of panel **a** have been acquired.

We performed some preliminary measurements on a NiPS<sub>3</sub>/few-layer graphene sample comprising flakes of various thicknesses (see Fig. 4.14). We observe that the number of peaks in the photoluminescence spectra, their energies and intensities vary considerably between flakes less than ten layers thin. Carrying out a similar study as the one shown in Chapter 4, with the determination of polarization, strain dependence and magnetic domains orientation for these different thicknesses would provide meaningful information on the observed disparities in those spectra and, likely, on the origin of the photoluminescence emission.

### Magnetic-field dependent measurements

During the second half of this PhD work, we received a new helium closed-cycle cryostat equipped with optical and microwave accesses, and an electromagnet which can generate a field up to 7 T (see Fig 4.15). Some experimental developments had to be made to mount the sample holder, piezostages and the aspheric lens on the column that is inserted at the center of the magnet. The experimental setup around it had also to be designed and mounted.

This equipment will enable us to exploit an important degree of freedom in our experiments, for example, we will be able to explore the effect of a magnetic field on the specific heat and Néel tem-

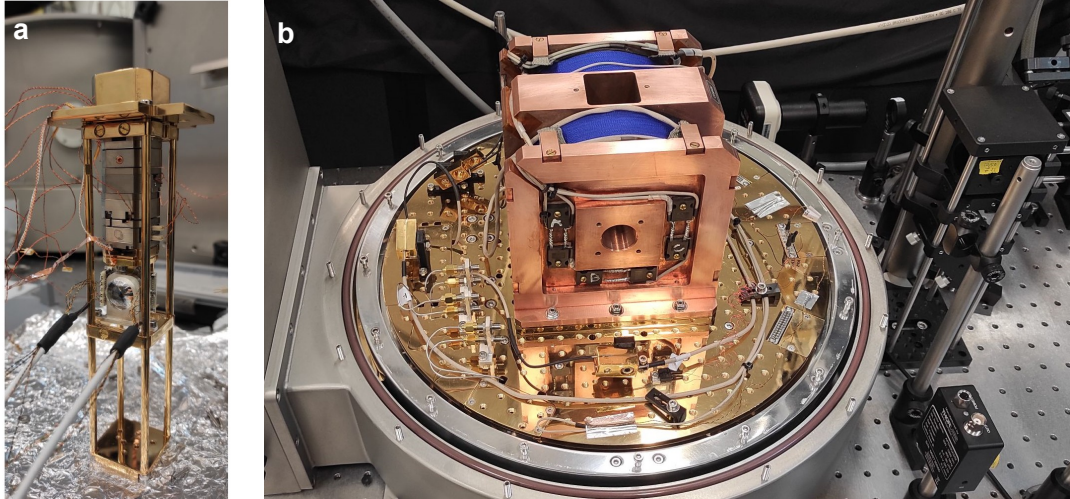


**Figure 4.15: A new closed-cycle cryostat with a magnetic field up to 7 T.** **a.** A column containing the piezostages, an aspheric lens and the contacted sample (on a heated plate for temperature regulation), can be inserted in the square housing visible on top of the electromagnet. **b.** The electromagnet on the gold-plated copper base which can reach a temperature of 4 K. The circular holes in the electromagnet sides allows for optical accesses.

perature of suspended 2D magnets thanks to nanomechanical measurements (see Eq. 2.5) [206]. We will also investigate the evolution of magnetic domains under a magnetic field probed by photoluminescence and Raman spectroscopies (see Sec 4.3.1).

### Feedback cooling and amplification

Feedback cooling is a method employed in the field of cavity optomechanics, notably for the cooling to the quantum ground-state of levitated nanoparticles motion [49], or to a few phonons of the motion of the kilogram mirrors used in gravitational waves detectors [47]. It consists in measuring the displacement  $z$  of the mechanical resonator and reinjecting a damping force proportional to it, with an appropriate phase, thanks to a feedback loop characterized by its gain and phase correction. This will result in an additional damping term that decreases or increases the mechanical mode temperature, depending on the phase of the feedback force [48].

In our case, feedback amplification might be used to increase the quality factor of the suspended membrane mechanical mode without modifying its frequency. This would be useful for probing the magnetic phase transition with a greater precision on the measured resonance frequency shift with temperature, and so, on the Néel temperature determination. We will then monitor the amplified Brownian motion of the membrane, instead of a motion driven by electrostatic or laser-induced forces.

We performed the first tests of feedback amplification on a suspended  $\text{FePS}_3$ -based heterostructure (*Fantadwich*, see Sample list 1.2.4) using an analog electronic board conceived by J. Thoraval (CNRS electronic engineer), that was based on a band-pass filter centered on the mechanical resonance frequency followed by a phase shifter and an amplification stage. The promising

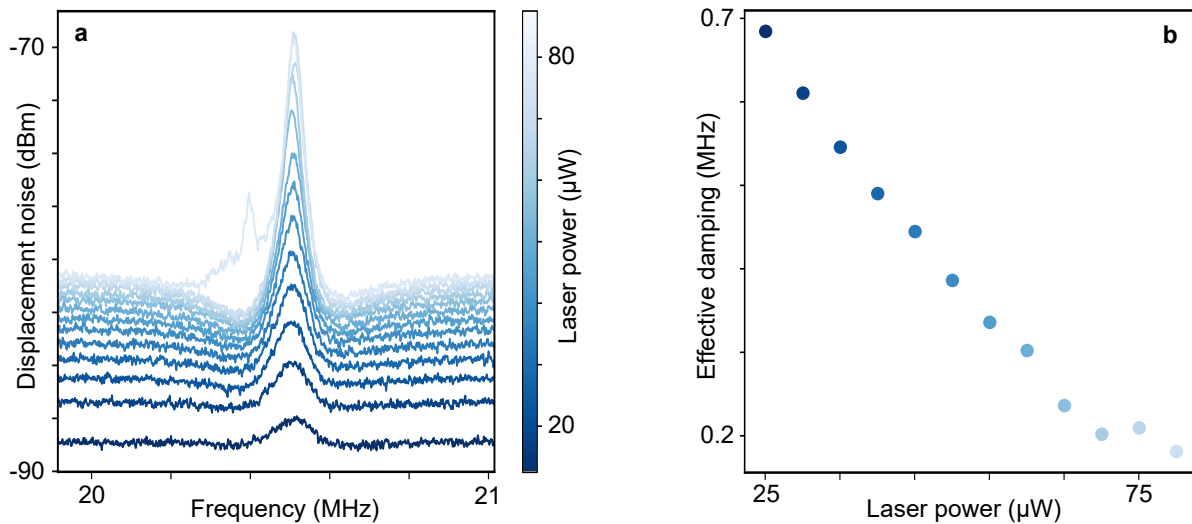


**Figure 4.16: Preliminary results of feedback amplification of the fundamental vibrational mode in a FePS<sub>3</sub>-based heterostructure (*Fantadwich*, see Sample list 1.2.4) at 140 K. **a.** Brownian motion spectra upon feedback amplification for an increasing probe laser power that is controlling the gain. **b.** Effective damping rate of the mechanical mode as a function of the probe laser power, showing a reduction of about 70 %.**

preliminary results obtained at 140 K show a decrease of the effective damping of about 70 % (see Fig. 4.16). However the central frequency of the band-pass filter could not be modified easily in order to follow the mechanical resonance frequency evolution with temperature. To overcome this limitation, a high frequency FPGA board with all digital control of the frequency, gain and phase has been programmed by L. Engel (CNRS electronic engineer) and just awaits to be tested.

### Alloys from MPS<sub>3</sub> compounds

We also plan to investigate Ni<sub>1-x</sub>Fe<sub>x</sub>PS<sub>3</sub> alloys, that present a magnetic anisotropy in between that of an Ising and a XY model depending on the stoichiometry. The anisotropy of such compounds has been shown to switch from in-plane to out-of-plane for  $x \sim 0.1$  [207]. Such crystals grown by flux transport techniques have already been provided by our collaborator D.Voiry from IEM Montpellier. It will be interesting to see how NiPS<sub>3</sub> photoluminescence is affected by the Fe doping and until when it is preserved.

### Longer term perspectives

One of the longer term perspective related to this work is to explore magnetic proximity effects between van der Waals magnets and monolayer semi-conducting transition metal dichalcogenides (TMD), and control them mechanically. The TMD photoluminescence will be affected differently depending on the magnetization direction in the magnetic layer: an out-of-plane magnetization would split the photoluminescence peak between its circular left and right polarizations, indicating a lifting of the valley degeneracy [208], while an in-plane magnetization would result

---

in the appearance of additional peaks that are brightened dark excitons [50, 51]. Due to their ferromagnetic intralayer coupling, the materials from the chromium trihalides family would be more suitable for this study than the antiferromagnets that are the  $MPS_3$ .

Another exciting perspective would be to investigate samples constituted of suspended monolayer magnetic van der Waals materials to reach a two-dimensional magnetic order. We could then tackle the question of the existence of a XY 2D magnet showing no long-range magnetic order, and so, a topological BKT phase transition [9]. Two van der Waals magnets presenting a quasi-XY magnetic order at the few-layer limit are currently considered for this challenge:  $CrCl_3$  and  $MnPS_3$  [209, 210].

# Appendix A

---

## Propagation of uncertainties

---

The quantity  $f$  can be written as

$$f = \bar{f} \pm \delta f \quad (\text{A.1})$$

where  $\bar{f}$  is the best estimation of  $f$  and  $\Delta f$  the standard uncertainty on its value, meaning that the real value of  $f$  lies between  $\bar{f} + \Delta f$  and  $\bar{f} - \Delta f$ .

The standard uncertainty  $\delta f$  of a quantity depending on  $N$  parameters  $(x_1, x_2, \dots, x_N)$ , is expressed as

$$\delta f(x_1, x_2, \dots, x_N) = \sqrt{\sum_{i=1, \dots, N} \left( \frac{\partial f}{\partial x_i} \right)_{x_j \neq x_i}^2 (\delta x_i)^2} \quad (\text{A.2})$$

if the standard uncertainties  $\delta x_i$  on the parameters  $x_i$  are independent [211]. If a standard uncertainty  $\delta x_k$  is way smaller than  $\delta x_j$  the associated term can be neglected in the summation.

In the case of the integrated intensity  $I_{\text{int}}$  calculation by a Riemann summation as used in Section 2.1.2, the peak area is divided in  $n$  rectangles of same width  $h$  and intensity  $I_i$  (for the  $i$ -th rectangle) (see Fig. A.1).

The rectangles area are then summed to obtain the integrated intensity

$$I_{\text{int}} = \sum_i h \times I_i = h \sum_i I_i \quad (\text{A.3})$$

since  $h = (r_n - r_0)/(n - 1)$  is constant for all rectangles with  $r_i$  the Raman shift at point  $i$ . To obtain the standard uncertainty  $\delta I_{\text{int}}$  we apply the formula (A.2) that gives

$$\delta I_{\text{int}} = \sqrt{\left( \frac{\partial I_{\text{int}}}{\partial h} \right)^2 (\delta h)^2 + \sum_i \left( \frac{\partial I_{\text{int}}}{\partial I_i} \right)^2 (\delta I_i)^2} \quad (\text{A.4})$$

$$= \sqrt{\left( \sum_i I_i \right)^2 (\delta h)^2 + n h^2 (\delta I)^2}, \quad (\text{A.5})$$

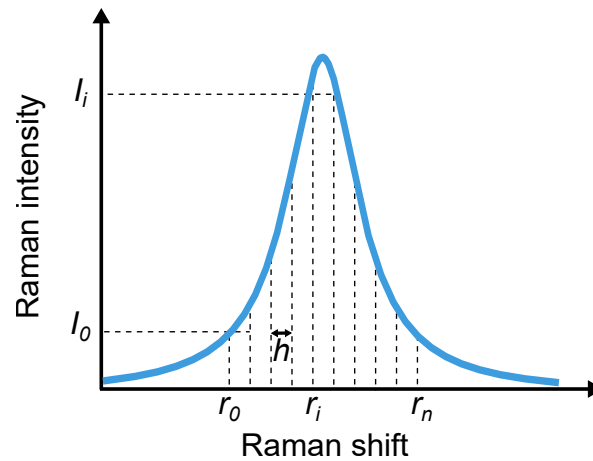


**Figure A.1:** Scheme of the Riemann summation process. The area under the peak is divided in  $n$  rectangles of width  $h$  and height  $I_i$ .

considering the same uncertainty  $\delta I$  for all the intensities, that is evaluated at 3 counts per minute so here 60 counts for a 20 minutes spectrum. The standard uncertainty on the width  $h$  is equal to  $\delta h = 2\delta r / (n - 1)$  with  $\delta r$  the uncertainty on the Raman shift value. We decided to evaluate it as a reading uncertainty since a photon can fall on one pixel or the adjacent one the same way can attribute a value to one or the other graduation on a scale. With a difference of  $0.55 \text{ cm}^{-1}$  between to Raman shift values we have  $\delta r = 0.55 / \sqrt{12}$ . Putting all this together, we get uncertainties between 3 to 7% on the integrated intensity values measured in Section 2.1.2.

# Appendix B

---

## Fit with a Voigt profile

---

The photoluminescence and Raman spectroscopy spectra are both fitted by a Voigt profile  $V$ , which is a convolution between a Lorentzian and Gaussian profiles and writes as [212]

$$V(f) = \int_{-\infty}^{+\infty} \frac{\gamma/\pi}{\gamma^2 + ((f - f_0) - f')^2} \frac{1}{\sqrt{\pi}\sigma} \exp(-((f' - f_0)/\sigma)^2) df' \quad (\text{B.1})$$

where  $f_0$  is the phonon mode frequency or photoluminescence energy,  $\gamma$  and  $\sigma$  are the widths of the Lorentzian and Gaussian profiles, respectively. The corresponding FWHM  $\Gamma_L$  and  $\Gamma_G$  are then expressed as  $\Gamma_L = 2\gamma$  and  $\Gamma_G = 2\sigma\sqrt{2\ln(2)}$  [213].

The Voigt profile can be evaluated by taking the real part of the Faddeeva function  $w(z)$  as [213]

$$V(f) = \frac{2\sqrt{\ln(2)} \operatorname{Re}(w(z))}{\sqrt{\pi}\Gamma_G} \quad (\text{B.2})$$

where

$$z = \frac{2\sqrt{\ln(2)}(f - f_0 + i\Gamma_L/2)}{\Gamma_G}. \quad (\text{B.3})$$

The Faddeeva function is a scaled error function that writes

$$w(z) = e^{-z^2} \left( 1 + \frac{2i}{\sqrt{\pi}} \int_0^z e^{t^2} dt \right) \quad (\text{B.4})$$

and can be easily evaluated using the function `wofz` of the Python *SciPy* package.

Since the Voigt profile is normalized, we use as a fit function the profile  $V^*(f) = AV(f)$ , which is a Voigt profile multiplied by the peak intensity  $A$ .

The parameters obtained from the fit are then the peak intensity  $A$ , its frequency  $f_0$  and the Lorentzian and Gaussian FWHM  $\Gamma_L$  and  $\Gamma_G$ . To recover the Voigt FWHM  $\Gamma_V$  we use the approximated formula  $\Gamma_V \simeq 0.5346 \Gamma_L + \sqrt{0.2166 \Gamma_L^2 + \Gamma_G^2}$  with an accuracy of 0.02 % derived in [212]. The FWHM mentioned in this manuscript are all the Voigt FWHM.



---

# Bibliography

---

1. Mattis, D. C. The theory of magnetism I (Springer Berlin, Heidelberg, 1981) (cit. on pp. [9](#), [43](#)).
2. Uhlenbeck, G. E. & Goudsmit, S. Spinning Electrons and the Structure of Spectra. *Nature* **117**, 264–265 (1926) (cit. on pp. [9](#), [44](#)).
3. Goudsmit, S. La découverte du spin de l'électron. *Journal de Physique* **28**, 123–128 (1967) (cit. on pp. [9](#), [44](#)).
4. Néel, L. Influence des fluctuations du champ moléculaire sur les propriétés magnétiques des corps. *Annales de Physique* **10**, 5–105 (1932) (cit. on pp. [9](#), [44](#)).
5. Williams, H. J., Bozorth, R. M. & Shockley, W. Magnetic Domain Patterns on Single Crystals of Silicon Iron. *Physical Review* **75**, 155–178 (1949) (cit. on pp. [9](#), [45](#)).
6. Cullity, B. D. & Graham, C. D. Introduction to Magnetic Materials (John Wiley & Sons, Ltd, 2008) (cit. on pp. [10](#), [45](#)).
7. Onsager, L. Crystal Statistics. I. A Two-Dimensional Model with an Order-Disorder Transition. *Physical Review* **65**, 117–149 (1944) (cit. on pp. [10](#), [46](#)).
8. Mermin, N. D. & Wagner, H. Absence of Ferromagnetism or Antiferromagnetism in One- or Two-Dimensional Isotropic Heisenberg Models. *Physical Review Letters* **17**, 1133–1136 (1966) (cit. on pp. [10](#), [46](#)).
9. Kosterlitz, J. M. & Thouless, D. J. Ordering, metastability and phase transitions in two-dimensional systems. *Journal of Physics C: Solid State Physics* **6**, 1181 (1973) (cit. on pp. [10](#), [47](#), [198](#)).
10. Legrand, E. & Plumier, R. Neutron diffraction investigation of antiferromagnetic  $K_2NiF_4$ . *Physica Status Solidi B Basic Research* **2**, 317–320 (1962) (cit. on pp. [10](#), [47](#), [48](#)).
11. Kohlhepp, J., Elmers, H. J., Cordes, S. & Gradmann, U. Power laws of magnetization in ferromagnetic monolayers and the two-dimensional Ising model. *Phys. Rev. B* **45**, 12287–12291 (1992) (cit. on pp. [10](#), [48](#), [49](#)).
12. Qiu, Z. Q., Pearson, J. & Bader, S. D. Magnetic phase transition of ultrathin Fe films on Ag(111). *Phys. Rev. Lett.* **67**, 1646–1649 (1991) (cit. on pp. [10](#), [49](#)).

13. Ballentine, C. A., Fink, R. L., Araya-Pochet, J. & Erskine, J. L. Magnetic phase transition in a two-dimensional system: p(1×1)-Ni on Cu(111). *Phys. Rev. B* **41**, 2631–2634 (1990) (cit. on pp. 10, 49).
14. Lee, J.-U. *et al.* Ising-Type Magnetic Ordering in Atomically Thin FePS<sub>3</sub>. *Nano Letters* **16**, 7433–7438 (2016) (cit. on pp. 10, 19, 49, 51, 53, 57, 87, 111, 117, 119, 122, 134, 193).
15. Huang, B. *et al.* Layer-dependent ferromagnetism in a van der Waals crystal down to the monolayer limit. *Nature* **546**, 270–273 (2017) (cit. on pp. 10, 49).
16. Burch, K. S., Mandrus, D. & Park, J.-G. Magnetism in two-dimensional van der Waals materials. *Nature* **563**, 47–52 (2018) (cit. on pp. 11, 50).
17. Kim, P. H. *et al.* Magnetic actuation and feedback cooling of a cavity optomechanical torque sensor. *Nature Communications* **8**, 1355 (2017) (cit. on pp. 11, 51).
18. Metten, D. Etude de propriétés opto-électroniques et mécaniques de membranes de graphène suspendu par spectroscopie Raman. PhD thesis (University of Strasbourg, 2016) (cit. on pp. 11, 51).
19. Zhang, X. *et al.* Dynamically-enhanced strain in atomically thin resonators. *Nature Communications* **11**, 5526 (2020) (cit. on pp. 11, 51, 103, 104, 142, 145).
20. Moczko, L. Suspended van der Waals heterostructures: from optical spectroscopy to opto-electro-mechanics. PhD thesis (University of Strasbourg, 2023) (cit. on pp. 11, 51, 65, 103, 104).
21. Joy, P. & Vasudevan, S. Infrared (700–100 cm<sup>-1</sup>) vibrational spectra of the layered transition metal thiophosphates, MPS<sub>3</sub> (M = Mn, Fe and Ni). *Journal of Physics and Chemistry of Solids* **54**, 343–348 (1993) (cit. on pp. 13, 54).
22. Brec, R. Review on structural and chemical properties of transition metal phosphorous trisulfides MPS<sub>3</sub>. *Solid State Ionics* **22**, 3–30 (1986) (cit. on pp. 13, 50, 53, 55, 56).
23. Castellanos-Gomez, A. *et al.* Deterministic transfer of two-dimensional materials by all-dry viscoelastic stamping. *2D Materials* **1**, 011002 (2014) (cit. on pp. 14, 67, 68).
24. Hashemi, A., Komsa, H.-P., Puska, M. & Krasheninnikov, A. V. Vibrational Properties of Metal Phosphorus Trichalcogenides from First-Principles Calculations. *The Journal of Physical Chemistry C* **121**, 27207–27217 (2017) (cit. on pp. 18, 19, 27, 59, 60, 83–85, 87–91, 129).
25. Bernasconi, M. *et al.* Lattice dynamics of layered MPX<sub>3</sub> (M=Mn,Fe,Ni,Zn; X=S,Se) compounds. *Phys. Rev. B* **38**, 12089–12099 (1988) (cit. on pp. 19, 54, 55, 83–85, 87, 88, 90, 91).
26. Šiškins, M. *et al.* Magnetic and electronic phase transitions probed by nanomechanical resonators. *Nature Communications* **11**, 2698 (2020) (cit. on pp. 23, 60, 63, 94, 95, 105, 111, 113, 134, 142, 146, 148, 151, 162, 163, 193).

27. Jiang, S., Xie, H., Shan, J. & Mak, K. F. Exchange magnetostriction in two-dimensional antiferromagnets. *Nature Materials* **19**, 1295–1299 (2020) (cit. on pp. [23](#), [111](#), [134](#)).
28. Takano, Y. *et al.* Magnetic properties and specific heat of  $\text{MPS}_3$  (M=Mn, Fe, Zn). *Journal of Magnetism and Magnetic Materials* **272–276**. Proceedings of the International Conference on Magnetism (ICM 2003), E593–E595 (2004) (cit. on pp. [23](#), [57](#), [61–63](#), [114](#), [116](#)).
29. Šiškins, M. *et al.* Nanomechanical probing and strain tuning of the Curie temperature in suspended  $\text{Cr}_2\text{Ge}_2\text{Te}_6$ -based heterostructures. *npj 2D Materials and Applications* **6**, 41 (2022) (cit. on pp. [23](#), [114](#), [125](#), [140](#)).
30. Suzuki, N. & Kamimura, H. Theory of Spin-Dependent Phonon Raman Scattering in Magnetic Crystals. *Journal of the Physical Society of Japan* **35**, 985–995 (1973) (cit. on pp. [25](#), [26](#), [121](#), [122](#)).
31. Baltensperger, W. & Helman, J. S. Influence of magnetic order in insulators on the optical phonon frequency. *Helvetica Physica Acta* **41**, 668 (1968) (cit. on pp. [27](#), [28](#), [132](#), [133](#)).
32. Kim, K. *et al.* Suppression of magnetic ordering in XXZ-type antiferromagnetic monolayer  $\text{NiPS}_3$ . *Nature Communications* **10**, 345 (2019) (cit. on pp. [27](#), [57](#), [87](#), [111](#), [128](#), [133](#), [134](#)).
33. Lee, J. *et al.* Electrically tunable single- and few-layer  $\text{MoS}_2$  nanoelectromechanical systems with broad dynamic range. *Science Advances* **4**, 6653 (2018) (cit. on pp. [30](#), [103](#), [105](#), [140](#), [141](#)).
34. Landau, L. & Lifshitz, E. *Electrodynamics of Continuous Media (Second Edition)* (Pergamon, 1984) (cit. on pp. [31](#), [146](#), [147](#)).
35. Sangani, L. D. V. *et al.* Dynamics of Interfacial Bubble Controls Adhesion Mechanics in Van der Waals Heterostructure. *Nano Letters* **22**, 3612–3619 (2022) (cit. on pp. [33](#), [157](#)).
36. Kang, S. *et al.* Coherent many-body exciton in van der Waals antiferromagnet  $\text{NiPS}_3$ . *Nature* **583**, 785–789 (2020) (cit. on pp. [34](#), [35](#), [57](#), [167](#), [168](#), [170](#), [171](#), [173](#), [176](#), [183](#), [189](#)).
37. Hwangbo, K. *et al.* Highly anisotropic excitons and multiple phonon bound states in a van der Waals antiferromagnetic insulator. *Nature Nanotechnology* **16**, 655–660 (2021) (cit. on pp. [35](#), [128](#), [168](#), [170](#), [173](#), [176](#)).
38. Kim, D. S. *et al.* Anisotropic Excitons Reveal Local Spin Chain Directions in a van der Waals Antiferromagnet. *Advanced Materials* **35**, 2206585 (2023) (cit. on pp. [35](#), [40](#), [57](#), [128](#), [167](#), [170](#), [172](#), [173](#), [187](#), [189](#), [192](#), [194](#)).
39. Wang, X. *et al.* Unveiling the spin evolution in van der Waals antiferromagnets via magneto-exciton effects. *Nature Communications* **15**, 8011 (2024) (cit. on pp. [35](#), [40](#), [167](#), [170](#), [194](#)).
40. Song, F. *et al.* Manipulation of anisotropic Zhang-Rice exciton in  $\text{NiPS}_3$  by magnetic field. *Nature Communications* **15**, 7841 (2024) (cit. on pp. [35](#), [167](#), [170](#), [172](#)).

41. He, W. *et al.* Magnetically propagating Hund's exciton in van der Waals antiferromagnet NiPS<sub>3</sub>. *Nature Communications* **15**, 3496 (2024) (cit. on pp. [35](#), [167](#), [170](#), [172](#)).
42. Occhialini, C. A. *et al.* Nature of Excitons and Their Ligand-Mediated Delocalization in Nickel Dihalide Charge-Transfer Insulators. *Phys. Rev. X* **14**, 031007 (2024) (cit. on pp. [35](#), [172](#)).
43. Sun, Z. *et al.* Dimensionality crossover to a two-dimensional vestigial nematic state from a three-dimensional antiferromagnet in a honeycomb van der Waals magnet. *Nature Physics* (2024) (cit. on pp. [37](#), [57](#), [167](#), [173](#), [187](#)).
44. Tan, Q. *et al.* Observation of Three-State Nematicity and Domain Evolution in Atomically Thin Antiferromagnetic NiPS<sub>3</sub>. *Nano Letters* **24**, 7166–7172 (2024) (cit. on pp. [37](#), [57](#), [111](#), [133](#), [187](#), [194](#)).
45. Lee, Y. *et al.* Imaging Thermally Fluctuating Néel Vectors in van der Waals Antiferromagnet NiPS<sub>3</sub>. *Nano Letters* **24**, 6043–6050 (2024) (cit. on p. [37](#)).
46. Wang, X. *et al.* Spin-induced linear polarization of photoluminescence in antiferromagnetic van der Waals crystals. *Nature Materials* **20**, 964–970 (2021) (cit. on pp. [40](#), [133](#), [168](#), [170](#), [172](#), [173](#), [176](#), [187](#)).
47. Whittle, C. *et al.* Approaching the motional ground state of a 10-kg object. *Science* **372**, 1333–1336 (2021) (cit. on pp. [41](#), [196](#)).
48. Cohadon, P. F., Heidmann, A. & Pinard, M. Cooling of a Mirror by Radiation Pressure. *Phys. Rev. Lett.* **83**, 3174–3177 (1999) (cit. on pp. [41](#), [196](#)).
49. Tebbenjohanns, F., Mattana, M. L., Rossi, M., Frimmer, M. & Novotny, L. Quantum control of a nanoparticle optically levitated in cryogenic free space. *Nature* **595**, 378–382 (2021) (cit. on pp. [41](#), [196](#)).
50. Scharf, B., Xu, G., Matos-Abiague, A. & Žutić, I. Magnetic Proximity Effects in Transition-Metal Dichalcogenides: Converting Excitons. *Phys. Rev. Lett.* **119**, 127403 (2017) (cit. on pp. [41](#), [198](#)).
51. Zhang, X.-X. *et al.* Magnetic brightening and control of dark excitons in monolayer WSe<sub>2</sub>. *Nature Nanotechnology* **12**, 883–888 (2017) (cit. on pp. [41](#), [198](#)).
52. Coey, J. M. D. *Magnetism and Magnetic Materials* (Cambridge University Press, 2010) (cit. on pp. [43](#), [47](#)).
53. Coey, J. & Mazaleyrat, F. *History of magnetism* (Elsevier, 2023) (cit. on pp. [43](#), [44](#)).
54. O'Connell, J. FARADAY, MAXWELL, AND LINES OF FORCE. *Journal of the Washington Academy of Sciences* **93**, 1–6 (2007) (cit. on p. [43](#)).
55. Maxwell, J. C. *A Treatise on Electricity and Magnetism* (Cambridge University Press, 2010) (cit. on p. [43](#)).

56. Weiss, P. L'hypothèse du champ moléculaire et la propriété ferromagnétique. *Journal de Physique Théorique et Appliquée* **6**, 661–690 (1907) (cit. on p. 44).
57. Einstein, A. & de Haas, W. J. Experimental proof of the existence of Ampère's molecular currents. *Koninklijke Nederlandse Akademie van Wetenschappen Proceedings Series B Physical Sciences* **18**, 696–711 (1915) (cit. on p. 44).
58. Gerlach, W. & Stern, O. Der experimentelle Nachweis der Richtungsquantelung im Magnetfeld. *Zeitschrift für Physik* **9**, 349–352 (1922) (cit. on pp. 44, 45).
59. Pauli, W. Zur Quantenmechanik des magnetischen Elektrons. *Zeitschrift für Physik* **43**, 601–623 (1927) (cit. on p. 44).
60. Dirac, P. A. M. The quantum theory of the electron. *Proceedings of the Royal Society London A* **117**, 610–624 (1928) (cit. on p. 44).
61. Heisenberg, W. Zur Theorie des Ferromagnetismus. *Zeitschrift für Physik* **49**, 619–636 (1928) (cit. on p. 44).
62. Dirac, P. A. M. Quantum mechanics of many-electron systems. *Proceedings of the Royal Society London A* **123**, 714–733 (1929) (cit. on p. 44).
63. Bloch, F. Zur Theorie des Ferromagnetismus. *Zeitschrift für Physik* **61**, 206–219 (1930) (cit. on p. 44).
64. Slater, J. C. Cohesion in Monovalent Metals. *Physical Review* **35**, 509–529 (1930) (cit. on p. 44).
65. San Miguel, A. & Pallandre, B. Revisiting the Einstein-de Haas experiment: The Ampère Museum's Hidden Treasure. *Europhysics News* (2024) (cit. on p. 45).
66. Néel, L. Propriétés magnétiques des ferrites ; ferrimagnétisme et antiferromagnétisme. *Annales De Physique* **12**, 137–198 (1948) (cit. on p. 44).
67. Bloch, F. Zur Theorie des Austauschproblems und der Remanenzerscheinung der Ferromagnetika. *Zeitschrift für Physik* **74**, 295–335 (1932) (cit. on p. 45).
68. Lenz, W. Beitrag zum Verständnis der magnetischen Erscheinungen in festen Körpern. *Physikalische Zeitschrift* **21**, 613–615 (1920) (cit. on p. 46).
69. Ising, E. Beitrag zur Theorie des Ferromagnetismus. *Zeitschrift für Physik* **31**, 253–258 (1925) (cit. on p. 46).
70. Niss, M. History of the Lenz-Ising Model 1920–1950: From Ferromagnetic to Cooperative Phenomena. *Archive for History of Exact Sciences* **59**, 267–318 (2005) (cit. on p. 46).
71. Kramers, H. A. & Wannier, G. H. Statistics of the Two-Dimensional Ferromagnet. Part I. *Physical Review* **60**, 252–262 (3 1941) (cit. on p. 46).
72. Hohenberg, P. C. Existence of Long-Range Order in One and Two Dimensions. *Physical Review* **158**, 383–386 (1967) (cit. on p. 46).

73. Cortie, D. L. *et al.* Two-Dimensional Magnets: Forgotten History and Recent Progress towards Spintronic Applications. *Advanced Functional Materials* **30**, 1901414 (2020) (cit. on pp. 46, 47, 49).
74. Berezinsky, V. L. Destruction of long range order in one-dimensional and two-dimensional systems having a continuous symmetry group. I. Classical systems. *Soviet Physics JETP* **32**, 493–500 (1971) (cit. on p. 46).
75. Bishop, D. J. & Reppy, J. D. Study of the Superfluid Transition in Two-Dimensional <sup>4</sup>He Films. *Physical Review Letters* **40**, 1727–1730 (1978) (cit. on p. 47).
76. Fisher, M. E. The theory of equilibrium critical phenomena. *Reports on Progress in Physics* **30**, 615 (1967) (cit. on p. 47).
77. Kadanoff, L. P. *et al.* Static Phenomena Near Critical Points: Theory and Experiment. *Reviews of Modern Physics* **39**, 395–431 (1967) (cit. on p. 47).
78. Birgeneau, R. J., Guggenheim, H. J. & Shirane, G. Neutron Scattering Investigation of Phase Transitions and Magnetic Correlations in the Two-Dimensional Antiferromagnets K<sub>2</sub>NiF<sub>4</sub>, Rb<sub>2</sub>MnF<sub>4</sub>, Rb<sub>2</sub>FeF<sub>4</sub>. *Phys. Rev. B* **1**, 2211–2230 (1970) (cit. on p. 48).
79. De Jongh, L. & Miedema, A. Experiments on simple magnetic model systems. *Advances in Physics* **23**, 1–260 (1974) (cit. on pp. 48, 49).
80. Jarnestad, J. in Press release: The Nobel Prize in Physics 2016, The Royal Swedish Academy of Sciences (cit. on p. 48).
81. Bander, M. & Mills, D. L. Ferromagnetism of ultrathin films. *Phys. Rev. B* **38**, 12015–12018 (1988) (cit. on pp. 48, 49).
82. Qiu, Z. Q., Pearson, J. & Bader, S. D. Two-dimensional Ising transition of epitaxial Fe films grown on Ag(100). *Phys. Rev. B* **49**, 8797–8801 (1994) (cit. on p. 49).
83. Koon, N. C., Jonker, B. T., Volkening, F. A., Krebs, J. J. & Prinz, G. A. Direct Evidence for Perpendicular Spin Orientations and Enhanced Hyperfine Fields in Ultrathin Fe(100) Films on Ag(100). *Phys. Rev. Lett.* **59**, 2463–2466 (1987) (cit. on p. 49).
84. Soumyanarayanan, A., Reyren, N., Fert, A. & Panagopoulos, C. Emergent phenomena induced by spin–orbit coupling at surfaces and interfaces. *Nature* **539**, 509–517 (2016) (cit. on p. 49).
85. Sampaio, J., Cros, V., Rohart, S., Thiaville, A. & Fert, A. Nucleation, stability and current-induced motion of isolated magnetic skyrmions in nanostructures. *Nature Nanotechnology* **8**, 839–844 (2013) (cit. on p. 49).
86. Pham, V. T. *et al.* Fast current-induced skyrmion motion in synthetic antiferromagnets. *Science* **384**, 307–312 (2024) (cit. on p. 49).
87. Manuel Bibes, J. E. V. & Barthélémy, A. Ultrathin oxide films and interfaces for electronics and spintronics. *Advances in Physics* **60**, 5–84 (2011) (cit. on p. 49).

88. Solano, J. *et al.* Spin-wave study of magnetic perpendicular surface anisotropy in single crystalline MgO/Fe/MgO films. *Phys. Rev. Mater.* **6**, 124409 (2022) (cit. on p. 49).
89. Díaz, E. *et al.* Energy-efficient picosecond spin–orbit torque magnetization switching in ferro- and ferrimagnetic films. *Nature Nanotechnology* (2024) (cit. on p. 49).
90. Le Flem, G., Brec, R., Ouvard, G., Louisy, A. & Segransan, P. Magnetic interactions in the layer compounds  $MPX_3$  (M = Mn, Fe, Ni; X = S, Se). *Journal of Physics and Chemistry of Solids* **43**, 455–461 (1982) (cit. on p. 49).
91. Jernberg, P., Bjarman, S. & Wäppling, R.  $FePS_3$ : A first-order phase transition in a “2D” Ising antiferromagnet. *Journal of Magnetism and Magnetic Materials* **46**, 178–190 (1984) (cit. on pp. 49, 62, 116).
92. Lines, M. Examples of two dimensional ordered magnetic systems. *Physics Letters A* **24**, 591–592 (1967) (cit. on p. 49).
93. Lines, M. E. Magnetism in Two Dimensions. *Journal of Applied Physics* **40**, 1352–1358 (1969) (cit. on p. 49).
94. Novoselov, K. S. *et al.* Electric Field Effect in Atomically Thin Carbon Films. *Science* **306**, 666–669 (2004) (cit. on pp. 49, 64).
95. Wang, X. *et al.* Raman spectroscopy of atomically thin two-dimensional magnetic iron phosphorus trisulfide ( $FePS_3$ ) crystals. *2D Materials* **3**, 031009 (2016) (cit. on pp. 49, 87, 117, 119).
96. Gong, C. & Zhang, X. Two-dimensional magnetic crystals and emergent heterostructure devices. *Science* **363**, eaav4450 (2019) (cit. on p. 49).
97. Mak, K. F., Shan, J. & Ralph, D. C. Probing and controlling magnetic states in 2D layered magnetic materials. *Nature Reviews Physics* **1**, 646–661 (2019) (cit. on pp. 49, 50).
98. Huang, B. *et al.* Emergent phenomena and proximity effects in two-dimensional magnets and heterostructures. *Nature Materials* **19**, 1276–1289 (2020) (cit. on pp. 49, 50).
99. Jiang, S., Li, L., Wang, Z., Mak, K. F. & Shan, J. Controlling magnetism in 2D  $CrI_3$  by electrostatic doping. *Nature Nanotechnology* **13**, 549–553 (2018) (cit. on p. 50).
100. Qi, Y. *et al.* Recent Progress in Strain Engineering on Van der Waals 2D Materials: Tunable Electrical, Electrochemical, Magnetic, and Optical Properties. *Advanced Materials* **35**, 2205714 (2023) (cit. on p. 50).
101. Ciorciaro, L., Kroner, M., Watanabe, K., Taniguchi, T. & Imamoglu, A. Observation of Magnetic Proximity Effect Using Resonant Optical Spectroscopy of an Electrically Tunable  $MoSe_2/CrBr_3$  Heterostructure. *Phys. Rev. Lett.* **124**, 197401 (2020) (cit. on pp. 50, 158).
102. Zhong, D. *et al.* Layer-resolved magnetic proximity effect in van der Waals heterostructures. *Nature Nanotechnology* **15**, 187–191 (2020) (cit. on p. 50).

103. Bunch, J. S. *et al.* Electromechanical Resonators from Graphene Sheets. *Science* **315**, 490–493 (2007) (cit. on p. 51).
104. Lee, J., Wang, Z., He, K., Shan, J. & Feng, P. X.-L. High Frequency MoS<sub>2</sub> Nanomechanical Resonators. *ACS Nano* **7**, 6086–6091 (2013) (cit. on p. 51).
105. Castellanos-Gomez, A. *et al.* Single-Layer MoS<sub>2</sub> Mechanical Resonators. *Advanced Materials* **25**, 6719–6723 (2013) (cit. on pp. 51, 94, 105).
106. Dolleman, R. J. *et al.* Optomechanics for thermal characterization of suspended graphene. *Phys. Rev. B* **96**, 165421 (2017) (cit. on p. 51).
107. Hernández López, P. *et al.* Strain control of hybridization between dark and localized excitons in a 2D semiconductor. *Nature Communications* **13**, 7691 (2022) (cit. on p. 51).
108. Grasso, V. & Silipigni, L. Low-dimensional materials: The MPX<sub>3</sub> family, physical features and potential future applications. *La Rivista del Nuovo Cimento* **25**, 1–102 (2002) (cit. on p. 53).
109. Petkov, V. & Ren, Y. Critical cation–anion radius ratio and two-dimensional antiferromagnetism in van der Waals TMPS<sub>3</sub> (TM = Mn, Fe, Ni). *Journal of Physics: Condensed Matter* **34**, 175404 (2022) (cit. on p. 55).
110. Ouvrard, G., Brec, R. & Rouxel, J. Structural determination of some MPS<sub>3</sub> layered phases (M = Mn, Fe, Co, Ni and Cd). *Materials Research Bulletin* **20**, 1181–1189 (1985) (cit. on pp. 55, 60, 82).
111. Joy, P. A. & Vasudevan, S. Magnetism in the layered transition-metal thiophosphates MPS<sub>3</sub> (M=Mn, Fe, and Ni). *Phys. Rev. B* **46**, 5425–5433 (1992) (cit. on p. 55).
112. Lançon, D., Ewings, R. A., Guidi, T., Formisano, F. & Wildes, A. R. Magnetic exchange parameters and anisotropy of the quasi-two-dimensional antiferromagnet NiPS<sub>3</sub>. *Phys. Rev. B* **98**, 134414 (2018) (cit. on p. 55).
113. Wildes, A. R. *et al.* Magnetic dynamics of NiPS<sub>3</sub>. *Phys. Rev. B* **106**, 174422 (2022) (cit. on p. 55).
114. Kuntu, D. V. *et al.* Laser-induced demagnetization in van der Waals XY- and Ising-like antiferromagnets NiPS<sub>3</sub> and FePS<sub>3</sub>. *Phys. Rev. Mater.* **8**, 014408 (2024) (cit. on p. 55).
115. McCreary, A. *et al.* Quasi-two-dimensional magnon identification in antiferromagnetic FePS<sub>3</sub> via magneto-Raman spectroscopy. *Phys. Rev. B* **101**, 064416 (2020) (cit. on pp. 57, 111, 117, 119, 120).
116. Kim, T. Y. & Park, C.-H. Magnetic Anisotropy and Magnetic Ordering of Transition-Metal Phosphorus Trisulfides. *Nano Letters* **21**, 10114–10121 (2021) (cit. on pp. 57, 62).
117. Houmes, M. J. A. *et al.* Magnetic order in 2D antiferromagnets revealed by spontaneous anisotropic magnetostriction. *Nature Communications* **14**, 8503 (2023) (cit. on pp. 57, 116, 117, 125, 127, 147).

118. Zhang, X.-X. *et al.* Spin Dynamics Slowdown near the Antiferromagnetic Critical Point in Atomically Thin FePS<sub>3</sub>. *Nano Letters* **21**, 5045–5052 (2021) (cit. on p. 57).
119. Chabre, Y., Segransan, P., Berthier, C. & Ouvrard, G. Fast Ion Transport in Solids (eds Vashishta, P., Mundy, J. & Shenoy, G.) (North Holland, New-York, 1979) (cit. on p. 57).
120. Kim, S. Y. *et al.* Charge-Spin Correlation in van der Waals Antiferromagnet NiPS<sub>3</sub>. *Phys. Rev. Lett.* **120**, 136402 (2018) (cit. on pp. 57, 142, 170).
121. Hu, L. *et al.* Observation of a magnetic phase transition in monolayer NiPS<sub>3</sub>. *Phys. Rev. B* **107**, L220407 (2023) (cit. on p. 57).
122. Zhang, Q. *et al.* Observation of Giant Optical Linear Dichroism in a Zigzag Antiferromagnet FePS<sub>3</sub>. *Nano Letters* **21**, 6938–6945 (2021) (cit. on p. 57).
123. Ni, Z., Huang, N., Haglund, A. V., Mandrus, D. G. & Wu, L. Observation of Giant Surface Second-Harmonic Generation Coupled to Nematic Orders in the van der Waals Antiferromagnet FePS<sub>3</sub>. *Nano Letters* **22**, 3283–3288 (2022) (cit. on p. 57).
124. Landau L. D., Pitaevskii, L. P., Kosevich, A. M. & Lifshitz, E. Theory of Elasticity (Elsevier, 1984) (cit. on p. 58).
125. Lurie, A. & Belyaev, A. Theory of Elasticity (Springer Berlin, Heidelberg, 2005) (cit. on pp. 58, 59).
126. Moakher, M. & Norris, A. N. The Closest Elastic Tensor of Arbitrary Symmetry to an Elasticity Tensor of Lower Symmetry. *Journal of Elasticity* **85**, 215–263 (2006) (cit. on pp. 58, 59).
127. Gould, P. L. & Feng, Y. Introduction to Linear Elasticity, third edition (Springer Cham, 2013) (cit. on pp. 59, 61).
128. Gan, C. K. & Chua, K. T. E. Large thermal anisotropy in monoclinic niobium trisulfide: a thermal expansion tensor study. *Journal of Physics: Condensed Matter* **31**, 265401 (2019) (cit. on p. 59).
129. Xue, M., He, W., Gong, Q., Yi, M. & Guo, W. Nonlinear elasticity and strain-tunable magnetocalorics of antiferromagnetic monolayer MnPS<sub>3</sub>. *Extreme Mechanics Letters* **57**, 101900 (2022) (cit. on p. 59).
130. Schwarz, C. Optomechanical, vibrational and thermal properties of suspended graphene membranes. PhD thesis (Université Grenoble Alpes, 2016) (cit. on pp. 60, 92).
131. Liu, K. *et al.* Elastic Properties of Chemical-Vapor-Deposited Monolayer MoS<sub>2</sub>, WS<sub>2</sub>, and Their Bilayer Heterostructures. *Nano Letters* **14**, 5097–5103 (2014) (cit. on p. 60).
132. Michel, K. H. & Verberck, B. Theory of elastic and piezoelectric effects in two-dimensional hexagonal boron nitride. *Phys. Rev. B* **80**, 224301 (2009) (cit. on p. 60).

133. Diu, B., Guthman, C., Lederer, D. & Roulet, B. *Eléments de physique statistique* (Hermann, 2001) (cit. on pp. [61](#), [97](#), [123](#)).
134. Ashcroft N, W. & Mermin N, D. *Solid State Physics* (Holt, Rinehart and Winston, 1976) (cit. on pp. [61–63](#), [113](#), [150](#)).
135. Pistawala, N. *et al.* Probing electron–phonon coupling in magnetic van der Waals material NiPS<sub>3</sub>: A non-magnetic site-dilution study. *2D Materials* **11**, 025035 (2024) (cit. on pp. [61](#), [62](#), [125](#)).
136. Kumar, D., Singh, B., Kumar, P., Balakrishnan, V. & Kumar, P. Thermal expansion coefficient and phonon dynamics in coexisting allotropes of monolayer WS<sub>2</sub> probed by Raman scattering. *Journal of Physics: Condensed Matter* **31**, 505403 (2019) (cit. on p. [63](#)).
137. Singh, V. *et al.* Probing thermal expansion of graphene and modal dispersion at low-temperature using graphene nanoelectromechanical systems resonators. *Nanotechnology* **21**, 165204 (2010) (cit. on p. [63](#)).
138. Liu, H. *et al.* Optomechanical methodology for characterizing the thermal properties of 2D materials. *APL Materials* **12**, 021126 (2024) (cit. on p. [63](#)).
139. Paszkowicz, W., Pelka, J. B., Knapp, M., Szyszko, T. & Podsiadlo, S. Lattice parameters and anisotropic thermal expansion of hexagonal boron nitride in the 10–297.5 K temperature range. *Applied Physics A* **75**, 431–435 (2002) (cit. on p. [63](#)).
140. Zhang, R.-S. & Jiang, J.-W. Effect of misfit strain on the thermal expansion coefficient of graphene/MoS<sub>2</sub> van der Waals heterostructures. *Phys. Chem. Chem. Phys.* **24**, 156–162 (2022) (cit. on p. [63](#)).
141. White, G., Birch, J. & Manghnani, M. H. Thermal properties of sodium silicate glasses at low temperatures. *Journal of Non-Crystalline Solids* **23**, 99–110 (1977) (cit. on p. [63](#)).
142. Lyon, K. G., Salinger, G. L., Swenson, C. A. & White, G. K. Linear thermal expansion measurements on silicon from 6 to 340 K. *Journal of Applied Physics* **48**, 865–868 (1977) (cit. on p. [63](#)).
143. Parra Lopez, L. E. Tailoring the luminescence of atomically-thin semiconductors at the sub-nanometer scale. PhD thesis (Université de Strasbourg, 2021) (cit. on p. [67](#)).
144. Lorchat, É. Optical spectroscopy of heterostructures based on atomically-thin semiconductors. PhD thesis (Université de Strasbourg, 2019) (cit. on p. [69](#)).
145. Wang, W. *et al.* Clean assembly of van der Waals heterostructures using silicon nitride membranes. *Nature Electronics* **6**, 981–990 (2023) (cit. on p. [70](#)).
146. Jain, A. *et al.* Minimizing residues and strain in 2D materials transferred from PDMS. *Nanotechnology* **29**, 265203 (2018) (cit. on p. [70](#)).
147. Varghese, S. *et al.* Fabrication and characterization of large-area suspended MoSe<sub>2</sub> crystals down to the monolayer. *Journal of Physics: Materials* **4**, 046001 (2021) (cit. on p. [70](#)).

148. Novotny, L. & Hecht, B. Principles of Nano-Optics 2nd ed. (Cambridge University Press, 2012) (cit. on p. 76).
149. Raman, C. V. & Krishnan, K. S. A New Type of Secondary Radiation. *Nature* **121**, 501–502 (1928) (cit. on p. 80).
150. Smith, E. & Dent, G. Modern Raman Spectroscopy – A Practical Approach (John Wiley & Sons, Ltd, 2004) (cit. on p. 80).
151. Loudon, R. The Raman effect in crystals. *Advances in Physics* **13**, 423–482 (1964) (cit. on pp. 80, 82, 84, 86, 133).
152. Klein, M. V. Electronic Raman Scattering. in *Light Scattering in Solids* (ed Cardona, M.) 147–204 (Springer Berlin Heidelberg, 1975) (cit. on p. 80).
153. Yu, P. & Cardona, M. Fundamentals of Semiconductors (Springer Berlin, Heidelberg, 2010) (cit. on pp. 80, 82, 84).
154. Ferrari, A. C. & Basko, D. M. Raman spectroscopy as a versatile tool for studying the properties of graphene. *Nature Nanotechnology* **8**, 235–246 (2013) (cit. on p. 80).
155. Froehlicher, G. Optical spectroscopy of two-dimensional materials : graphene, transition metal dichalcogenides and van der Waals heterostructures. PhD thesis (Université de Strabourg, 2016) (cit. on pp. 81–83, 86, 99, 100).
156. Dresselhaus, M., Dresselhaus, G. & Jorio, A. Group Theory: Application to the Physics of Condensed Matter (Springer Berlin, Heidelberg, 2007) (cit. on pp. 82, 86).
157. Kargar, F. *et al.* Phonon and Thermal Properties of Quasi-Two-Dimensional FePS<sub>3</sub> and MnPS<sub>3</sub> Antiferromagnetic Semiconductors. *ACS Nano* **14**, 2424–2435 (2020) (cit. on pp. 84, 85, 87, 89–91).
158. Wright, D. *et al.* Acoustic and optical phonons in quasi-two-dimensional MPS<sub>3</sub> antiferromagnetic semiconductors. *Applied Physics Letters* **124**, 161903 (2024) (cit. on pp. 87, 90, 91).
159. Kuo, C.-T. *et al.* Exfoliation and Raman Spectroscopic Fingerprint of Few-Layer NiPS<sub>3</sub> Van der Waals Crystals. *Scientific Reports* **6**, 20904 (2016) (cit. on p. 87).
160. Hauer, B., Doolin, C., Beach, K. & Davis, J. A general procedure for thermomechanical calibration of nano/micro-mechanical resonators. *Annals of Physics* **339**, 181–207 (2013) (cit. on pp. 92, 93, 97).
161. Fartash, A., Schuller, I. K. & Grimsditch, M. Thin-film modeling for mechanical measurements: Should membranes be used or plates? *Journal of Applied Physics* **71**, 4244–4248 (1992) (cit. on pp. 92–94).
162. Morse Philip, M. & Ingard Uno, K. Theoretical Acoustics (Princeton University Press, 1986) (cit. on p. 93).

163. *NIST Digital Library of Mathematical Functions*. F. W. J. Olver, A. B. Olde Daalhuis, D. W. Lozier, B. I. Schneider, R. F. Boisvert, C. W. Clark, B. R. Miller, B. V. Saunders, H. S. Cohl, and M. A. McClain, eds. (cit. on p. [93](#)).
164. Graff K., *F. Wave motion in elastic solids* (Ohio State University Press, 1975) (cit. on p. [93](#)).
165. Kocher, M., Jain, A., Ong, S. & Hautier, G. "Materials Project" (cit. on pp. [94](#), [102](#)).
166. Steeneken, P. G., Dolleman, R. J., Davidovikj, D., Alijani, F. & van der Zant, H. S. J. Dynamics of 2D material membranes. *2D Materials* **8**, 042001 (2021) (cit. on pp. [96–98](#), [103](#), [106](#)).
167. Pottier, N. *Physique statistique hors d'équilibre* (EDP Sciences, 2007) (cit. on p. [97](#)).
168. Hecht, E. *Optics* (Pearson, 2016) (cit. on pp. [100](#), [170](#)).
169. Chen, C. *et al.* Performance of monolayer graphene nanomechanical resonators with electrical readout. *Nature Nanotechnology* **4**, 861–867 (2009) (cit. on pp. [103](#), [140](#)).
170. Weber, P., Güttinger, J., Tsioutsios, I., Chang, D. E. & Bachtold, A. Coupling Graphene Mechanical Resonators to Superconducting Microwave Cavities. *Nano Letters* **14**, 2854–2860 (2014) (cit. on pp. [103](#), [138](#)).
171. Schwarz, C. *et al.* Deviation from the Normal Mode Expansion in a Coupled Graphene-Nanomechanical System. *Phys. Rev. Appl.* **6**, 064021 (2016) (cit. on p. [105](#)).
172. Vogel, M., Mooser, C., Karrai, K. & Warburton, R. J. Optically tunable mechanics of microlevers. *Applied Physics Letters* **83**, 1337–1339 (2003) (cit. on p. [106](#)).
173. Morell, N. *et al.* Optomechanical Measurement of Thermal Transport in Two-Dimensional MoSe<sub>2</sub> Lattices. *Nano Letters* **19**, 3143–3150 (2019) (cit. on p. [106](#)).
174. Barton, R. A. *et al.* Photothermal Self-Oscillation and Laser Cooling of Graphene Optomechanical Systems. *Nano Letters* **12**, 4681–4686 (2012) (cit. on p. [106](#)).
175. Balkanski, M., Jouanne, M. & Scagliotti, M. Magnetic ordering induced Raman scattering in FePS<sub>3</sub> and NiPS<sub>3</sub> layered compounds. *Pure and Applied Chemistry* **59**, 1247–1252 (1987) (cit. on pp. [111](#), [117](#)).
176. Sekine, T., Jouanne, M., Julien, C. & Balkanski, M. Light-scattering study of dynamical behavior of antiferromagnetic spins in the layered magnetic semiconductor FePS<sub>3</sub>. *Phys. Rev. B* **42**, 8382–8393 (1990) (cit. on pp. [111](#), [117](#), [119](#), [120](#), [134](#)).
177. Pawbake, A. *et al.* High-Pressure Tuning of Magnon-Polarons in the Layered Antiferromagnet FePS<sub>3</sub>. *ACS Nano* **16**, 12656–12665 (2022) (cit. on pp. [111](#), [119](#)).
178. Sun, Z. *et al.* Dimensionality crossover to a two-dimensional vestigial nematic state from a three-dimensional antiferromagnet in a honeycomb van der Waals magnet. 2024 (cit. on pp. [111](#), [128](#), [134](#)).

179. Morell, N. *et al.* High Quality Factor Mechanical Resonators Based on WSe<sub>2</sub> Monolayers. *Nano Letters* **16**, 5102–5108 (2016) (cit. on pp. [113](#), [141](#)).
180. Sanditov, D. S. & Belomestnykh, V. N. Relation between the parameters of the elasticity theory and averaged bulk modulus of solids. *Technical Physics* **56**, 1619–1623 (2011) (cit. on p. [113](#)).
181. Belomestnykh, V. N. & Tesleva, E. P. Interrelation between anharmonicity and lateral strain in quasi-isotropic polycrystalline solids. *Technical Physics* **49**, 1098–1100 (2004) (cit. on p. [113](#)).
182. Lifshitz, R. & Roukes, M. L. Thermoelastic damping in micro- and nanomechanical systems. *Phys. Rev. B* **61**, 5600–5609 (2000) (cit. on p. [116](#)).
183. Sun, Y. & Saka, M. Thermoelastic damping in micro-scale circular plate resonators. *Journal of Sound and Vibration* **329**, 328–337 (2010) (cit. on p. [116](#)).
184. Šiškins, M. Higher-order phenomena in nanomechanics of two-dimensional material membranes. Dissertation (TU Delft) (Delft University of Technology, 2021) (cit. on p. [116](#)).
185. Baglioni, G. *et al.* Thermo-Magnetostrictive Effect for Driving Antiferromagnetic Two-Dimensional Material Resonators. *Nano Letters* **23**, 6973–6978 (2023) (cit. on p. [116](#)).
186. Dolleman, R. J. *et al.* Optomechanics for thermal characterization of suspended graphene. *Phys. Rev. B* **96**, 165421 (2017) (cit. on p. [116](#)).
187. Scagliotti, M., Jouanne, M., Balkanski, M. & Ouvrard, G. Spin dependent phonon Raman scattering in antiferromagnetic FePS<sub>3</sub> layer-type compound. *Solid State Communications* **54**, 291–294 (1985) (cit. on p. [117](#)).
188. Tsang, J. C., Dresselhaus, M. S., Aggarwal, R. L. & Reed, T. B. Inelastic light scattering in the europium chalcogenides. *Phys. Rev. B* **9**, 984–996 (1974) (cit. on p. [117](#)).
189. Silberstein, R., Schmutz, L., Tekippe, V., Dresselhaus, M. & Aggarwal, R. Magnetic phase-dependent Raman scattering in EuSe and EuTe. *Solid State Communications* **18**, 1173–1177 (1976) (cit. on p. [117](#)).
190. Mohiuddin, T. M. G. *et al.* Uniaxial strain in graphene by Raman spectroscopy: *G* peak splitting, Grüneisen parameters, and sample orientation. *Phys. Rev. B* **79**, 205433 (20 2009) (cit. on p. [128](#)).
191. Wildes, A. R. *et al.* Magnetic structure of the quasi-two-dimensional antiferromagnet NiPS<sub>3</sub>. *Phys. Rev. B* **92**, 224408 (22 2015) (cit. on p. [133](#)).
192. Chen, C. Graphene NanoElectroMechanical Resonators and Oscillators. PhD thesis (Columbia University, 2009) (cit. on pp. [139](#), [140](#)).
193. Davidovikj, D. *et al.* Nonlinear dynamic characterization of two-dimensional materials. *Nature Communications* **8**, 1253 (2017) (cit. on p. [139](#)).

194. Will, M. *et al.* High Quality Factor Graphene-Based Two-Dimensional Heterostructure Mechanical Resonator. *Nano Letters* **17**, 5950–5955 (2017) (cit. on p. 141).
195. Landau, L. On the theory of phase transitions. *Zh. Eksp. Teor. Fiz.* **7**, 19–32 (1937) (cit. on p. 146).
196. Davidovikj, D. *et al.* Visualizing the Motion of Graphene Nanodrums. *Nano Letters* **16**, 2768–2773 (2016) (cit. on p. 160).
197. Li, Y., Liang, G., Kong, C., Sun, B. & Zhang, X. Charge-Transfer-Mediated Exciton Dynamics in Van der Waals Antiferromagnet NiPS<sub>3</sub>. *Advanced Functional Materials* **n/a**, 2402161 (2024) (cit. on pp. 167, 170).
198. Klaproth, T. *et al.* Origin of the Magnetic Exciton in the van der Waals Antiferromagnet NiPS<sub>3</sub>. *Phys. Rev. Lett.* **131**, 256504 (2023) (cit. on pp. 167, 170).
199. Parra López, L. E. *et al.* Single- and narrow-line photoluminescence in a boron nitride-supported MoSe<sub>2</sub>/graphene heterostructure. *Comptes Rendus. Physique* **22**, 77–88 (2021) (cit. on p. 168).
200. Ergeçen, E. *et al.* Magnetically brightened dark electron-phonon bound states in a van der Waals antiferromagnet. *Nature Communications* **13**, 98 (2022) (cit. on p. 168).
201. Theocaris, P. S. & Gdoutos, E. E. *Matrix Theory of Photoelasticity* (Springer Berlin, Heidelberg, 1979) (cit. on p. 170).
202. Jana, D. *et al.* Magnon gap excitations and spin-entangled optical transition in the van der Waals antiferromagnet NiPS<sub>3</sub>. *Phys. Rev. B* **108**, 115149 (2023) (cit. on pp. 170, 172, 173, 183, 189).
203. Belvin, C. A. *et al.* Exciton-driven antiferromagnetic metal in a correlated van der Waals insulator. *Nature Communications* **12**, 4837 (2021) (cit. on p. 170).
204. Gnatchenko, S. L., Kachur, I. S., Piryatinskaya, V. G., Vysochanskii, Y. M. & Gurzan, M. I. Exciton-magnon structure of the optical absorption spectrum of antiferromagnetic MnPS<sub>3</sub>. *Low Temperature Physics* **37**, 144–148. ISSN: 1063-777X (2011) (cit. on p. 172).
205. Chen, J. *et al.* Spin chain orientation and magneto-optical coupling in twisted NiPS<sub>3</sub> homostructures. *Applied Physics Letters* **125**, 113102 (2024) (cit. on p. 187).
206. Ni, Z. *et al.* Magnetic field control of continuous Néel vector rotation and Néel temperature in a van der Waals antiferromagnet. *arXiv*. eprint: 2404.06010 (2024) (cit. on p. 196).
207. Lee, S. *et al.* Chemical tuning of magnetic anisotropy and correlations in Ni<sub>1-x</sub>Fe<sub>x</sub>PS<sub>3</sub>. *Phys. Rev. B* **104**, 174412 (2021) (cit. on p. 197).
208. Lodahl, P. *et al.* Chiral quantum optics. *Nature* **541**, 473–480 (2017) (cit. on p. 197).
209. Dupont, M. *et al.* Monolayer CrCl<sub>3</sub> as an Ideal Test Bed for the Universality Classes of 2D Magnetism. *Phys. Rev. Lett.* **127**, 037204 (2021) (cit. on p. 198).

210. Liao, G., Zhang, S., Cui, P. & Zhang, Z. Tunable meron pair excitations and Berezinskii-Kosterlitz-Thouless phase transitions in the monolayer antiferromagnet MnPSe<sub>3</sub>. *Phys. Rev. B* **109**, L100403 (2024) (cit. on p. [198](#)).
211. Bally, F.-X. & Berroir, J.-M. Incertitudes expérimentales. *Bulletin de l'Union des Physiciens* **104**, 995–1019 (2010) (cit. on p. [199](#)).
212. Kielkopf, J. F. New approximation to the Voigt function with applications to spectral-line profile analysis. *Journal of the Optical Society of America* **63**, 987–995 (1973) (cit. on p. [201](#)).
213. Ida, T., Ando, M. & Toraya, H. Extended pseudo-Voigt function for approximating the Voigt profile. *Journal of Applied Crystallography* **33**, 1311–1316 (2000) (cit. on p. [201](#)).

# Suspended antiferromagnetic van der Waals membranes: optical spectroscopies and nanomechanics to probe and control their magnetic properties

## Résumé

Dans cette thèse, nous présentons l'étude de matériaux de van der Waals magnétiques suspendus au-dessus de trous de diamètre micrométrique, formant des nano-résonateurs mécaniques membranaires, comme une plateforme polyvalente pour explorer les interactions entre leurs degrés de liberté mécaniques et magnétiques.

Dans un premier temps, nous sondons optiquement la transition de phase magnétique d'échantillons de  $\text{FePS}_3$  et de  $\text{NiPS}_3$  de faible épaisseur en combinant spectroscopie Raman et optomécanique. Une contrainte mécanique est ensuite appliquée, dans le but d'observer une modification de la température de transition de phase magnétique induite par des effets de magnétostriction. Enfin, les propriétés de la photoluminescence de  $\text{NiPS}_3$  sont explorées, notamment son comportement sous contrainte et la résolution spatiale de sa polarisation permettant de mettre en évidence des domaines antiferromagnétiques.

Ce travail de thèse met en évidence le potentiel des membranes de van der Waals suspendues pour sonder et contrôler les propriétés physiques de ces matériaux et ouvre vers l'exploration d'effets de proximité dans des hétérostructures magnétiques de van der Waals.

Mots clés : matériaux de van der Waals magnétiques, nanomagnétisme, optomécanique, spectroscopie Raman, spectroscopie de photoluminescence, hétérostructures de van der Waals.

## Résumé en anglais

In this thesis, we present the investigation of suspended magnetic van der Waals materials on micrometric holes, forming drum-like resonators, as a versatile platform to explore the interplay between their mechanical and magnetic properties.

In the first instance, we optically probe the magnetic phase transitions of  $\text{FePS}_3$  and  $\text{NiPS}_3$  few-layer samples combining Raman spectroscopy and optomechanics. Strain is then induced to tune the magnetic phase transition temperature induced by magnetostriction effects. Afterwards, the properties of  $\text{NiPS}_3$  photoluminescence are explored, notably its behavior under strain and the spatial resolution of its polarization that highlights antiferromagnetic domains.

This work sheds light on the potential of suspended 2D membranes for probing and controlling the physical properties of these materials and paves the way for the exploration of proximity effects in magnetic van der Waals heterostructures.

Keywords: 2D magnets, nanomagnetism, optomechanics, Raman spectroscopy, photoluminescence spectroscopy, van der Waals heterostructures